The Variability and Forcing of Ocean Whitecaps and Their Impact on Air-Sea Fluxes

by

Dominic James Salisbury

Submitted in accordance with the requirements for the degree of
Doctor of Philosophy

University of Leeds
School of Earth & Environment

April 2014

Declaration of Authorship

The candidate confirms that the work submitted is his own, except where work which has formed part of jointly authored publications has been included. The contribution of the candidate and the other authors to this work has been explicitly indicated below. The candidate confirms that appropriate credit has been given within the thesis where reference has been made to the work of others.

The publications Salisbury et al. [2013] '*On the variability of whitecap fraction using satellite-based observations, J. Geophys. Res. Oceans, 118, 6201–6222, doi:10.1002/ 2013JC008797*' and Salisbury et al. [2014] '*Global distribution and seasonal dependence of satellite-based whitecap fraction', Geophys. Res. Lett., 41, 1616–1623, doi:10.1002/ 2014GL059246* were jointly authored with Magdalena Anguelova and Ian Brooks.

Content from Salisbury et al. [2013] appears in chapters 2 (background information) 3 (description of dataset and methodology), 4 (results and discussion), and 5 (further results and discussion). Content (mainly results and discussion) from Salisbury et al. [2014] appears primarily in chapters 4 and 6. For both papers, the main dataset used was initially formulated by Magdalena Anguelova and colleagues at the Remote Sensing Division, Naval Research Laboratory, Washington DC, as part of the WindSat mission. The dataset was modified and expanded by the candidate. Analysis was conducted by the candidate. The text of both publications was written by the candidate with input from both coauthors.

This copy has been supplied on the understanding that it is copyright material and that no quotation from the thesis may be published without proper acknowledgement.

"I need my sleep. I need about eight hours a day, and about ten at night."

Bill Hicks (1966–1994)

Acknowledgements

Abstract

The breaking of ocean surface gravity waves is an important phenomenon that affects the dynamics of the upper ocean, development of the wave field, and air-sea exchange processes. As the surface expression of this process, whitecaps provide a visible signature of wave breaking; their areal extent per unit area sea surface—known as the whitecap fraction, W—can be used to quantify the amount and scale of wave breaking. W is traditionally estimated using digital images of the ocean surface and is widely used to represent whitecaps in remote sensing applications, and in the parameterisation of a host of air-sea processes in models. These parameterisations—generally functions of wind speed alone—are based on limited amounts of data, and fail to take into account the known influence of secondary factors on whitecaps.

A novel approach to estimating W using satellite observations has recently been developed, based on passive radiometric measurements of brightness temperature at microwave frequencies. The satellite-based approach enables measurement of W on a global scale, and in a variety of conditions. In this work, the basic characteristics of W estimates at two different radiometric frequencies, W_{10} (10 GHz) and W_{37} (37 GHz), is investigated. The wind speed dependence, global distribution, and seasonal dependence of the estimates are investigated. Comparison is made against estimates obtained from simple, but widely used, wind speed only parameterisations formulated from in situ data. A more direct comparison of radiometric and photographic W estimates, based on ship-satellite matchups, is also made. Both comparisons indicate that satellite-based W has a different wind speed dependence, resulting in estimates that are, on average, higher at low wind speeds and lower at higher wind speeds than parameterisations formulated from in situ, photographic measurements. On a global scale, this results in satellite-based W being more uniform latitudinally than predictions from traditional formulations.

A dataset comprising estimates of W_{10} and W_{37}, together with collocated and concurrent estimates for a variety of forcing parameters, is used to investigate the the influence on W_{10} and W_{37} of secondary forcings, such as the wave field and environmental factors. It is found that on a global scale wind speed describes much of the variability in both W_{10} and W_{37} though the influence of secondary factors on W can be

appreciable (especially for W_{37}). Based on the magnitude of the influence of secondary forcing factors on W_{10} and W_{37}, it is concluded that much of the variability in whitecap fraction is likely due to the behavior of the thinner, decaying foam patches, variability that is not captured by the retrieval using the 10 GHz channel.

Though whitecap fraction offers a pragmatic approach to inferring the magnitude of processes associated with breaking surface waves, it remains an indirect measure with inherent limitations. More fundamental questions regarding the interpretation and use of W are considered. A dynamical model that relates whitecap fraction to breaking wave statistics is used to illustrate the contribution to whitecap fraction due to whitecaps in different lifetime stages. Such a model provides a framework for better relating whitecap fraction to the dynamic, active part of the wave breaking process which is likely more closely linked to processes such as breaking-induced energy dissipation, turbulent mixing, and bubble-mediated gas exchange.

Finally, the implications of use of radiometric estimates for quantifying air-sea processes—specifically production of sea spray aerosol and bubble-mediated gas exchange—is discussed. It is shown that difference between the satellite-based W estimates and those predicted using traditional parameterisations provides an explanation for the consistent geographical biases in sea spray aerosol concentration found in a number of large scale models. The benefit of these novel observations will also extend to predictions of other air-sea processes, and remote sensing applications, that require estimation of W; these benefits will be enhanced if whitecaps and their radiometric signature are more closely related to the physical processes which they are used to quantify.

Contents

List of Figures

List of Tables

Abbreviations

ASIST	**A**ir-**S**ea **I**nteraction & **S**ea-spray in **T**yphoons
AWE	**A**utomated **W**hitecap **E**xtraction
CCN	**C**loud **C**ondensation **N**uclei
CLASP	**C**ompact **L**ightweight **A**erosol **S**pectrometer **P**robe
DOGEE	**D**eep **O**cean **G**as **E**xchange **E**xperiment
ECMWF	**E**uropean **C**entre for **M**edium-range **W**eather **F**orecasts
GDAS	**G**lobal **D**ata **A**ssimilation **S**ystem
HiWASE	**Hi**gh **W**ind **A**ir-**S**ea **E**xchanges
MABL	**M**arine **A**tmospheric **B**oundary **L**ayer
MWS	**M**ean **W**ave **S**lope
NCEP	**N**ational **C**enters for **E**nvironmental **P**rediction
NRL	**N**aval **R**esearch **L**aboratory
SBWR	**S**hip **B**orne **W**ave **R**ecorder
SEASAW	**SEA**-**S**pray, gas fluxes, **A**nd **W**hitecaps
SOLAS	**S**urface **O**cean **L**ower **A**tmosphere **S**tudy
SSA	**S**ea **S**pray **A**erosol
SSM/I	**S**pecial **S**ensor Microwave / **I**mager
SSSF	**S**ea **S**pray **S**ource **F**unction
SST	**S**ea **S**urface **T**emperature
WAGES	**W**aves, **A**erosol, and **G**as **E**xchange **S**tudy

Parameters, Symbols and Units

A	Area of whitecap	m
A_0	Initial area of a laboratory produced whitecap	m^2
A_b	Area of breaking region	m^2
A_max	Maximum area of whitecap	m^2
A_obs	Observational sea surface area	m^2
C_d	Drag coefficient	Unitless
c	Speed of advance of breaking front	$\mathrm{m\ s^{-1}}$
$\vec{c}$	Wave velocity	$\mathrm{m\ s^{-1}}$
c_p	Wave phase speed	$\mathrm{m\ s^{-1}}$
E	Total wave energy	$\mathrm{kg\ m^2\ s^{-2}}$
$\dot{E}$	Rate of energy supplied by wind, per unit sea surface area	$\mathrm{J\ m^{-2}}$
F_ent	Rate of entrainment of air into water	$\mathrm{m\ s^{-1}}$
g	Gravitational constant $= 9.81\ \mathrm{m\ s^{-2}}$	$\mathrm{m\ s^{-2}}$
H_fd	Significant wave height given wind-wave equilibrium	m
H_s	Significant wave height	m
K	Total gas transfer piston velocity	$\mathrm{m\ s^{-1}}$
K_b	Bubble-mediated gas transfer velocity	$\mathrm{m\ s^{-1}}$
K_d	Direct gas transfer velocity	$\mathrm{m\ s^{-1}}$
K_w	Total waterside gas transfer velocity	$\mathrm{m\ s^{-1}}$
L	Cloud liquid water	mm
L_b	Length of an individual breaking front	m
L_total	Total breaking crest length per unit area ocean surface	$\mathrm{m^{-1}}$
MWS	Mean wave slope	Unitless
R	Breaking rate	$\mathrm{s^{-1}}$
T_Phillips	Phillips' 'bubble persistence time'	s

T_b	Wave period of breaking wave	s
T_B	Ocean surface brightness temperature	K
T_{Bf}	Ocean surface brightness temperature due to foam	K
T_p	Peak wave period	s
T_{fd}	Peak wave period given wind-wave equilibrium	s
U	Characteristic speed of energy propagation in lower atmosphere	m s^{-1}
u_*	Wind friction velocity	m s^{-1}
U_{10}	Wind speed at 10-m reference height	m s^{-1}
$U_{10\mathrm{EN}}$	Equivalent neutral wind speed at 10-m reference height	m s^{-1}
U_{dir}	Wind direction	°
V	Columnar water vapour	mm
w	Width of whitecap along crest	m
W	Whitecap fraction	%
z	Depth within foam layer	m
α	Ratio of active breaking time to period of carrier wave	Unitless
δ	Breaking region vertical thickness	m
γ	Ratio of breaking crest speed to underlying wave phase speed	Unitless
ϵ	Energy dissipation rate	W m^{-2}
ϵ	Ocean surface (composite) emissivity	Unitless
ϵ_c	Threshold energy dissipation for whitecap detection	W m^{-2}
ϵ_f	Foam emissivity	Unitless
η_*	Non-dimensional surface elevation	Unitless
Λ	Arc length of breaking crest	m
$\Lambda(c)$	Phillips breaking crest length distribution	m^{-2} s
λ	Wavelength	m
ν_a	Kinematic viscosity of air	m^2 s^{-1}
ν_w	Kinematic viscosity of seawater	m^2 s^{-1}
ρ_a	Density of air	kg m^{-3}
ρ_w	Density of seawater	kg m^{-3}
τ	Characteristic whitecap decay time	s
τ_{Mon}	Monahan's whitecap decay time = 3.53 s	s
τ_{form}	Callaghan's whitecap formation timescale	s

τ_{decay}	Callaghan's whitecap decay timescale	s
τ_{wc}	Callaghan's whitecap timescale	s
τ	Wind stress or air-water momentum flux	kg m^{-1} s^{-2}
Φ	Wave age	Unitless
ω	Wave angular frequency	rads s^{-1}
ω_*	Non-dimensional frequency peak of wave spectrum	Unitless

Chapter 1

Introduction

The oceans cover approximately 71% of Earth's surface area [Bigg, 2003] and form an integral part of the climate system. Their importance—for example, as a major reservoir for heat and carbon—has been known for some time. Several decades ago, before major advances in both our understanding and in computational abilities, it was common for the ocean and atmosphere to be explicitly separated in computer models. Up until the 1980s, wave modellers were simply users of meteorological output products—most often surface winds [Cavaleri et al., 2012]. Likewise, the role of the ocean in determining the state of the atmosphere wasn't fully considered in these early atmospheric models.

In reality, the ocean-atmosphere system is intrinsically coupled. We now understand much more about the complex physical interplay between the atmosphere and the ocean, a result of decades of research to advance weather and climate science. This two-way coupling of wave and meteorological modelling is a vital component of modern coupled-climate models; the ocean must be considered by meteorologists as a strong source and sink of heat, gas, and physical quantities, and it is no longer viable for ocean modellers to simply take atmospheric wind fields as the boundary conditions for their models.

The air-sea interface is a physically important boundary between the surface ocean and lower atmosphere. Here there is a ceaseless two-way interaction between the wind and the surface water; winds generate surface waves while waves modify the airflow resulting in a loss of energy and momentum to the waves. Both the local weather

and the longer-term climate are sensitive to these interactions. However, due to the inherent chaotic and often non-linear nature of the atmosphere-ocean system, it is not possible to explicitly model and numerically predict these processes. It is for this reason that climate models rely on parameterisations of air-sea processes such as wave energy dissipation, and the exchange of momentum, heat, moisture, gases, and particulate matter.

One of the most important physical processes at the air-sea interface is that of surface wave breaking. This process of air-entrainment into the ocean, forming bubbles below and foam patches at the surface (known as whitecaps), modulates the air-sea turbulent exchanges of aerosols, gases, heat and momentum. To successfully quantify these exchanges in weather and climate models, we must be able to make accurate predictions of wave breaking and whitecapping from routinely measured meteorological and oceanographic variables. This is no simple task; wave breaking is a complex and highly non-linear phenomenon. Though much progress has been made in the past two decades, we are not yet able to make accurate predictions of the scale and frequency of occurrence of wave breaking on a global scale.

Wave breaking and formation of whitecaps plays a variety of different roles in air-sea interaction. Bubble entrainment by breaking waves provides an efficient mechanism for the exchange of gases, thus enhancing the total air-sea transfer [Wanninkhof et al., 2009; Woolf, 1997]. It has been argued that the bubble-mediated contribution should scale with whitecap fraction W [Monahan and Spillane, 1984; Woolf, 2005]. Whitecaps are areas where sea spray droplets are actively produced through bubble bursting, and via the wind tearing of wave crests at higher wind speeds [Andreas, 1995; Blanchard, 1963; Monahan et al., 1983], and as such are the main source of primary marine aerosols.

The presence of whitecaps on the ocean surface must also be accounted for in models of the global radiation budget [Frouin et al., 2001], since sea foam layers increase ocean albedo [Koepke, 1984]. Consideration of whitecaps is also required in optical ocean color retrievals due to the masking of water-leaving radiance by foam patches [Gordon and Wang, 1994]. At microwave frequencies, whitecaps mark areas with increased surface emission and brightness temperature [Rose et al., 2002; Smith, 1988; Wentz, 1983]. This has implications for many remote sensing applications, including the use

of satellite-borne radiometric and polarimetric instruments to obtain the surface wind vector [Gaiser et al., 2004; Wentz, 1997; Yueh, 1997].

The primary focus of this study is whitecaps and the whitecap fraction W— a quantity which is widely used as an indirect statistical quantification of wave breaking. In this thesis: (i) the characteristics of satellite-based estimates of the whitecap fraction are assessed, (ii) variability and forcings of W on a global scale are investigated and quantified, (iii) the satellite-based estimates (and their wind speed dependence) are compared to in situ based estimates, and (iv) comments are made on the implications of our findings for air-sea interaction studies. In chapter 2 we provide background material relevant to this study including properties of individual whitecaps, previous work on measurement and parameterisation of W, and details on the role of whitecaps in air-sea interaction.

A major part of this project is analysis of data from a recently developed satellite retrieval of W. By its very nature, the air-sea interface lends itself well to remote sensing. Driven by both technological advance and societal concern, by the early 1980s, several ocean observing satellites were in use. For the first time, it became possible to make measurements on a global scale and monitor the oceans over time. At present, dozens of sensors on a variety of satellites retrieve wave spectral quantities, wind speed and direction, currents and planetary waves, atmospheric water content and rain rate, to name but a few. In chapter 3, a recently developed algorithm to obtain satellite-based estimates of W from passive radiometric measurements of the ocean surface is described, together with the 'whitecap database' that has been compiled in order to study variability in the satellite-based estimates. Additional data used, including ship-based whitecap estimates, are also described.

An accurate parameterisation of whitecap fraction is a requirement for successful modeling of whitecap dependent processes, and for several ocean remote sensing applications. In nearly all current models, W is specified as a simple function of wind speed, $W(U_{10})$ (where U_{10} is the wind speed at a 10 m reference height). In chapter 4, we compare satellite-based estimates with those obtained based on a wind speed only parameterisation, focusing on the global distribution and seasonal dependence. We then explore the wind speed dependence of satellite-based W estimates, and quantify the correlation between wind speed and satellite W. A direct comparison between

satellite-based W estimates with in situ estimates of W from photographic data is also made.

Use of $W(U_{10})$ parameterisations dictates that a reliable estimate of W can only be obtained if it is assumed that wind speed can fully predict whitecap fraction; however, there is substantial evidence that this is not the case [Anguelova and Webster, 2006; Callaghan et al., 2008b; Monahan and O'Muircheartaigh, 1986]. In chapter 5, we draw upon a year's worth of satellite-based W estimates to explore variability in W resulting from secondary factors such the wave field, sea surface temperature, and air-sea stability. The relative importance of such variables in accounting for variability in W is then quantified.

Whitecap fraction estimates are used to predict the magnitude of several air-sea processes associated with wave breaking and bubble-plume production and decay. In chapter 6, the relationship between individual whitecaps, W, and these processes is discussed, with emphasis placed on use of the whitecap method to predict both sea spray aerosol source fluxes and air-sea gas transfer velocities. The implications of a move towards use of radiometric estimates of W, instead of parameterised values, is explored. In light of recent results regarding the whitecap lifecycle, we combine breaking wave statistics with a model for the time evolution of the area of an individual whitecap to explore how this information may be used to resolve different processes contributing to measured W—namely foam associated with active wave breaking, and the residual decaying foam left after a wave breaking event.

In chapter 7, we summarise our findings and draw conclusions, before making recommendations pertaining to the development and future use of satellite-based W estimates, and more generally the interpretation and use of whitecap fraction by the air-sea interaction community.

Chapter 2

Background

2.1 Air-sea interaction and the marine boundary layer

The marine atmospheric boundary layer (MABL) is the part of the atmosphere that is directly influenced by the presence of the ocean surface. At the air-sea interface, the ocean and atmosphere are coupled through a variety physical, chemical, and biological processes occurring over a range of scales (Figure 2.1). This ocean-atmosphere coupling is, to a large degree, controlled by the transfer of momentum via the action of the wind on the ocean surface. A moving atmosphere produces a stress on the ocean surface, resulting in motion within the fluid. Although this motion can take many forms such as surface currents and Langmuir circulations, it most notably produces surface waves with amplitudes dependent upon the strength and duration of the wind forcing. Waves subsequently grow in height and wavelength, and are modulated by breaking and nonlinear interactions [Cavaleri et al., 2012].

The ocean surface generally acts as a barrier to exchanges between the ocean and atmosphere [Rogers, 1995]. However, surface turbulent fluxes provide key pathways through which these exchanges can occur [Bourassa et al., 2010], allowing momentum, energy, moisture, sensible and latent heat, and trace constituents to be transferred between the ocean and atmosphere. In energetic conditions, the excess energy imparted to the wave field, due to the sustained action of the wind, causes waves to break and the air-sea interface to be disrupted. In such conditions, wind-driven surface turbulent
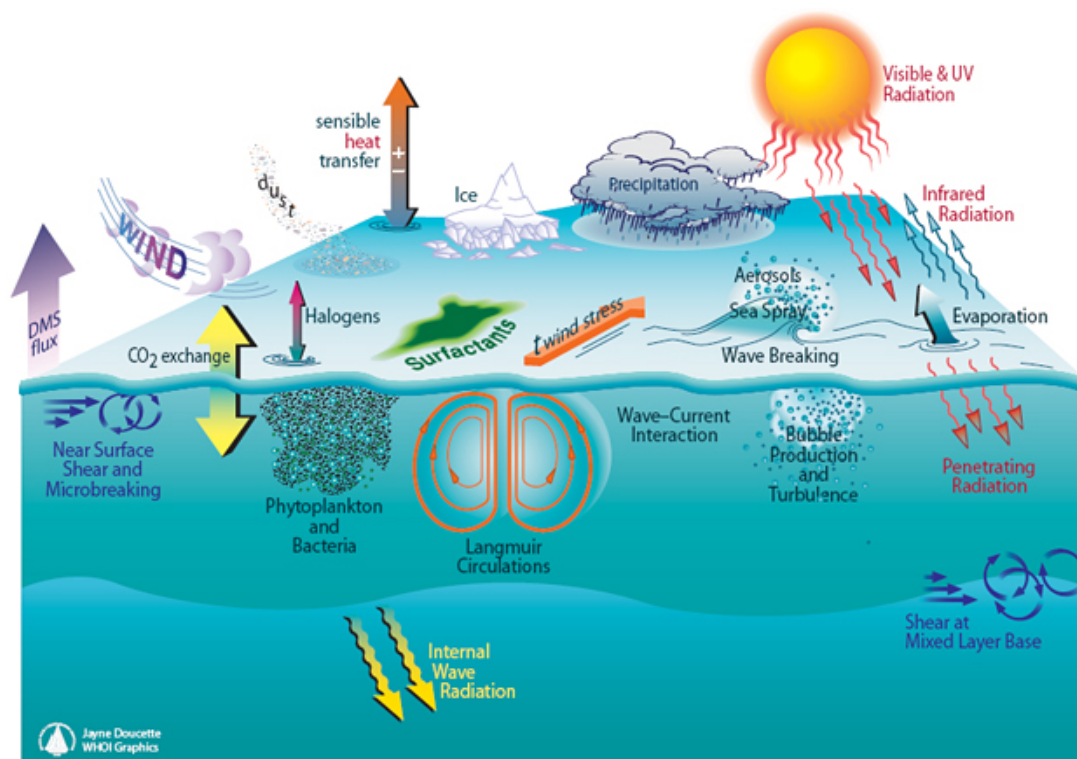
FIGURE 2.1: Schematic of the main physical, chemical, and biological processes occurring at the air-sea interface (taken from http://www.whoi.edu/cms/images/ ooi_oceanAtExchange_en_70189.jpg).

fluxes can be greatly enhanced. These exchange processes have a critical role in weather and climate, and so predicting them is of vital importance.

2.1.1   Wind-driven ocean surface waves and their breaking

Surface ocean wave generation is primarily driven by the action of the wind on the ocean surface in a process that is now largely understood [Janssen, 1991]. Wind blowing across a flat surface couples the two layers via a thin viscous layer. This leads to a two-fluid shear instability with growing undulations that steer the wind over the waves. This results in differential surface pressures that increase the transfer of energy and momentum from the wind to the waves and drives wave growth [Cavaleri et al., 2012].

The presence of waves at the ocean surface can have a significant impact on on the local atmospheric boundary layer. This is due to the sea state dependence of momentum transfer from the air to the wave field. Overall, waves act to enhance the surface drag which leads to a reduction in wind speed. Importantly, this drag depends of the shape of the waves; steep waves extract more momentum from the airflow than smoother, less

steep waves. As growing waves associated with young wind seas are steeper than old wind seas (or swell-dominated seas), the roughness is said to be sea state dependent. Therefore, the evolution of the wind is in part determined by the wave field. This can have wider impacts on atmospheric circulation and climate [Cavaleri et al., 2012], with global climate models performing significantly better when this two-way coupling is included [Garfinkel et al., 2011].

Eventually, due to a combination of sustained input of energy from the wind and wave-wave interactions, certain waves will grow so steep that they break. Breaking is of vital importance to a host of upper ocean processes: it is the main mechanism for wave energy dissipation, modulates momentum transfer from the wind to ocean currents, enhances vertical mixing in near-surface water, affects the exchange of heat and trace gases, is a source of underwater noise, and is involved in the generation of aerosols by bursting bubbles.

However, breaking is an intermittent, random process and occurs at scales ranging several orders of magnitude; from small micro-breakers, to large breaking waves that generate large amounts of turbulence that is injected into the surface waters. As neatly summarized by Zhao and Toba [2001], 'Wave breaking is a highly nonlinear process and its quantitative estimation is difficult, both experimentally and theoretically.' Quantification requires both detection and measurement of breaking events, both of which are challenging tasks [Babanin, 2011]. Although techniques (including analytical methods and contact measurements) to directly detect and measure breaking have greatly evolved over the past few decades, the post-breaking signature of wave breaking remains the most practical and efficient means for detection and quantification of breaking. In particular, the visual signature of breaking (assuming air entrainment)—whitecaps—remains the most common method to investigate the breaking of ocean surface waves.

2.2   Oceanic whitecaps

One consequence of surface wave breaking is that air is entrained into the seawater, forming clouds of bubbles, which subsequently rise to the surface forming patches of foam, known as whitecaps. In this thesis we distinguish these surface layers of sea

foam (whitecaps) from sub-surface bubble plumes and sea spray droplets suspended closely above the surface, though all three are the result of breaking surface waves and can be classified as sea foam. Callaghan et al. [2013] define the term 'whitecap' as the surface expression of wave breaking that persists for a length of time over which it can be visually distinguished from the background water.

2.2.1   Whitecap formation and evolution

Although individual whitecaps are in constant temporal evolution (as illustrated in Figure 2.2), it is possible to define two distinct phases of a whitecap's life-cycle [Monahan and Lu, 1990]. During the active breaking stage, air is entrained into the water column at the wave crest (Figure 2.2a), with associated generation of underwater noise due to bubble formation and fragmentation [Callaghan et al., 2013; Deane and Stokes, 2002]. As the leading wave crest progresses forwards, it continues to entrain air (Figure 2.2b). The resulting surface expression is a dense layer of foam, termed active (or stage A) whitecap, with a visible albedo of around 0.5 [Whitlock et al., 1982]. The characteristic whiteness is due to light scattering through the air-water mixture.
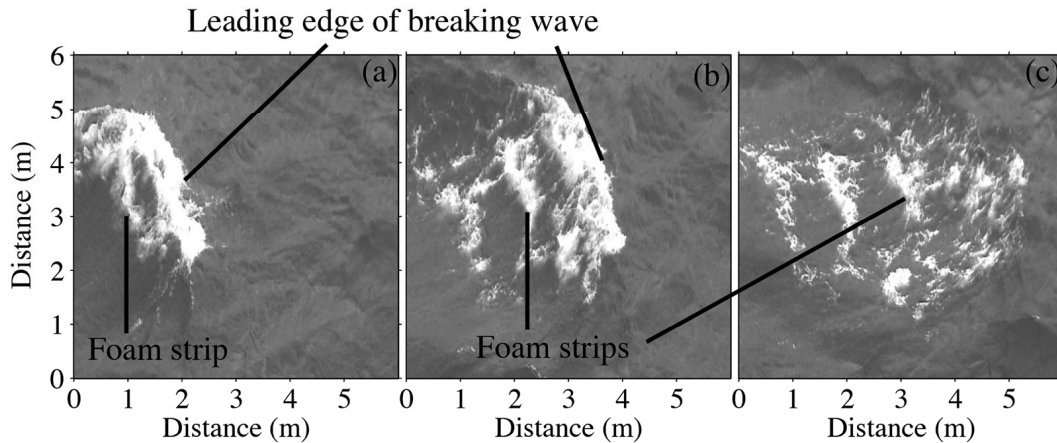
FIGURE 2.2: (a-c) Temporal evolution of an individual oceanic whitecap (left to right). Successive images are separated in time by 750 ms, with the first image acquired 1.2 s after the onset of breaking (taken from Callaghan [2013]).

Following active air-entrainment, the whitecap enters its second phase (stage B) as bubbles in the sub-surface plume rise to the surface due to buoyancy and turbulent forces. Once at the surface, the lifetime of risen bubbles is dictated by a combination of seawater chemistry (e.g., salinity, saturation levels of dissolved gases), turbulent forces, thin film fluid drainage, and stabilizing or destabilizing forces [Callaghan, 2013]. The

surface foam layer as a whole gradually decays—a result of thinning of the bubble raft due to bubble bursting—leading to a reduction in albedo (Figure 2.2c). The foam layer persists as long as there is a sufficient flux of bubbles to the surface; usually this is of the order of seconds. In some instances, foam can persist on the surface for much longer, perhaps several minutes. One example is the stable, thread-like structures associated with confinement of foam patches by Langmuir vortices [Sharkov, 2007].

2.2.2 Physical description of whitecaps

2.2.2.1 Mechanical structure

A layer of sea foam on the ocean surface is an air-water mixture in which air bubbles are inclusions. The properties of such a mixture depend on a set of variables that describe this 'medium': bubble dimensions (characterized by radius and wall thickness), bubble concentration or size distribution $N(r)$, foam layer thickness t, and foam void fraction f_a (fraction of unit ocean volume occupied by air). These micro and macro characteristics represent the specific mechanical structure of sea foam [Anguelova and Gaiser, 2013].

Within the foam layer, the dimensions of the densely packed bubbles gradually change with depth. Figure 2.3 shows the structure of a typical foam layer; the photo was taken during an experiment in 2004 with the foam layer created in a large outdoor basin filled with salt water (35 psu) [Padmanabhan et al., 2007]. In the upper part of the layer, thin-walled bubbles contain little seawater (dry foam). Moving down through the foam layers, the bubbles become smaller and thicker-walled resulting in decreasing air content (wet foam). The consequence of such vertical stratification is that foam characteristics acquire a large range of values, with a vertical profile; for example, the void fraction can range from 100% at the air-foam interface to 1% at the foam-water interface [Anguelova, 2008].

In the open ocean, foam layer thickness, δ, can range from 1–20 cm for active whitecaps and 0.1–1 cm for residual foam [Anguelova and Gaiser, 2011]. Foam layer thickness is thus distributed [Reul and Chapron, 2003], being dependent upon the meteorological and oceanographic forcings of new foam formation, and the lifetime stage of the foam.
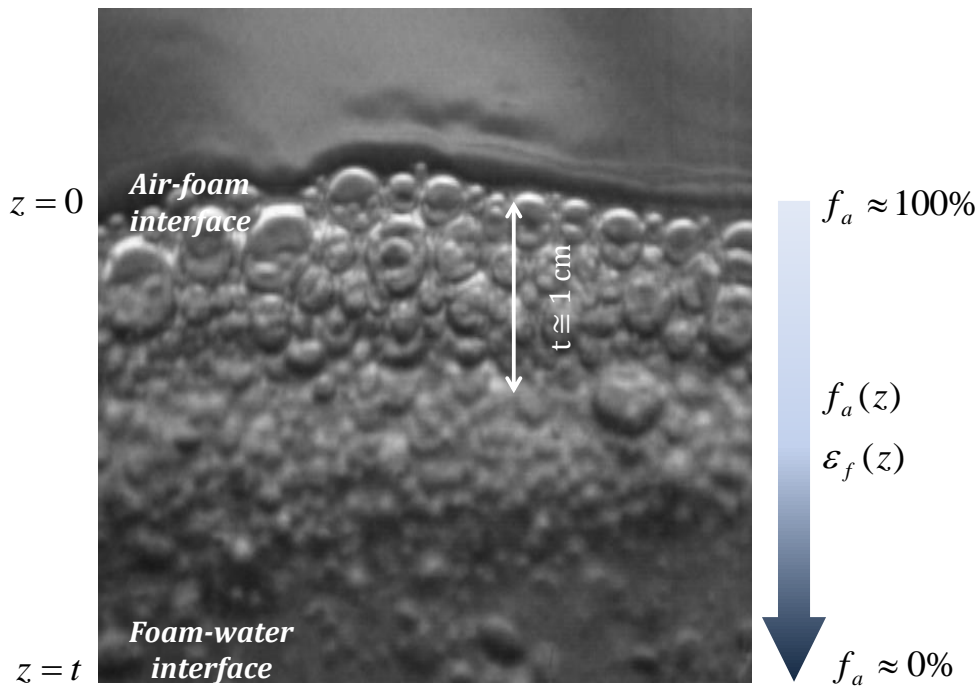
FIGURE 2.3: Schematic of a vertically stratified surface foam layer. Photo by Bill
Asher (Applied Plysics Laboratory, University of Washington)

2.2.2.2   Dielectric properties and remote sensing signature

The dielectric properties of sea foam determine the absorption, scattering, and trans-
mission of electromagnetic radiation through it, and so determine its radiative prop-
erties and remote sensing signature. The most important quantity in this context is
the foam complex dielectric constant (relative permittivity) ϵ_f. This dictates all other
dielectric properties of sea foam [Anguelova and Gaiser, 2011]. As the microstructure
of the foam layer has a vertical profile, so does the dielectric constant i.e., $\epsilon_f(z)$, where
z is the depth in the foam layer.

The visible signature of whitecaps is well known to the casual observer of the ocean
surface in the presence of breaking waves. Whitecaps are highly reflective at visible
frequencies and their presence at the ocean surface increases its albedo. The reflectance
of sea foam varies with both the thickness of the foam layer and it's mechanical prop-
erties. The irradiance reflectance (in the visible range) of a thicker foam layer with
tens of layers of bubbles can reach 55% [Whitlock et al., 1982]. To account for this
dependency, an effective reflectance can be introduced which accounts for changes in

optical properties with whitecap lifetime; Koepke [1984] estimated this quantity to be 22% in the visible.

At microwave wavelengths, sea foam has a high blackbody-like emissivity [Aziz et al., 2005; Nordberg et al., 1971; Rose et al., 2002], suggestive of foam being a highly absorptive medium. For remote sensing applications, the bulk of the registered radiation emanates from a thin layer known as the skin depth—defined as the medium thickness over which the electromagnetic radiation decreases by a factor $1/e$. This depth in seawater varies from around 0.5 mm to 10 mm, and is frequency dependent. The microwave remote sensing of whitecaps is discussed in detail in chapter 3.

2.2.3   Properties of individual whitecaps

2.2.3.1   Geometry

Whitecaps can occur over a range of scales and with a variety of geometries. However, it is widely acknowledged that for quasi-steady (as opposed to unsteady) breaking ocean surface waves the overall geometry may be assumed to be statistically self-similar. It is therefore possible to describe the geometry of an individual whitecap through scaling laws. In the geometry considered by Duncan [1981], the whitecap forms at the turbulent region growing on the forward face of an individual spilling (rather than plunging) breaker.

Figure 2.4 depicts the breaking region forming on the forward crest of spilling wave of wavelength λ and phase velocity $\bar{c}$. δ is the breaking region vertical thickness and Λ is the arc length of the breaking front. Duncan [1981] found that (i) all the laboratory produced waves have breaking regions with the same aspect ratio $A_b/L_b^2 \approx 0.1$ where $A_b = \delta L_b$ is its area and L_b^2 its length in the direction of propagation, and (ii) the ratio of breaking area length and the breaking wave's wavelength is the same for all conditions, $L_b/\lambda \approx 0.3$.

Bortkovskii [1987] reported on the aspect ratio of individual whitecaps (with areas of 5–10 m^2) using photographic data from the literature. It was found that the width of the whitecap along the wave crest w and L_b followed closely $w/L_b = 2.15$.
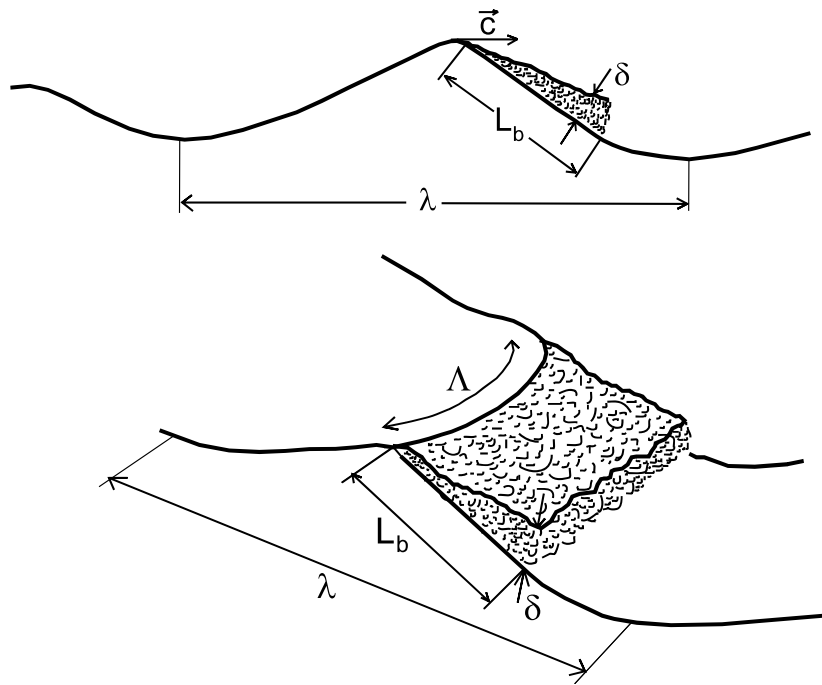
FIGURE 2.4: Schematic of a quasi-steady spilling breaker, moving from left to right (from Reul and Chapron [2003]).

2.2.3.2   Time-evolution of area

The property of whitecaps of most interest to this study is the areal extent. A single frozen image of the sea surface would yield a distribution of whitecap areas, some of which would correspond to active whitecaps and others to residual foam patches. Individual oceanic whitecaps have typical mean areas ranging from tens of centimeters (as reported by Snyder et al. [1983] in shallow coastal waters at low wind speeds) to tens of meters for dominant breakers; mean areas have been cited to be several meters [Bortkovskii, 1987]. The distribution of individual crests and strip-like structures were parameterized as gamma distributions by Bondur and Sharkov [1982] from aerial photography of the ocean surface; through dividing whitecap formations into 'crests' (corresponding to active whitecaps) and 'stripe-like structures' (stage B foam), it was found that at moderate wind speeds (6–11 m s^{-1}) the mean areas of individual crests and foam stripes increases from ∼0.5 m^2 to ∼1.2 m^2 and from ∼20 m^2 to ∼30 m^2, respectively, as wind speed increases. More recently, Kleiss and coworkers analyzed aircraft video recordings of breaking waves to obtain the distribution of foam patch area. It was found that the probability density function of whitecap areas follows closely a power law relationship of the form $A^{-1.8}$ [Kleiss, 2009]. Callaghan et al.

[2012] investigated the distribution of maximum foam patch area $A_{\max}$ of individual whitecaps. The largest whitecap resolved in the study had a maximum area of 26 m^2 but for the majority of whitecaps $A_{\max} < 10$ m^2.

Monahan and Zietlow [1969], based on laboratory measurements of simulated whitecaps, introduced an exponential decay model to describe the time evolution of the surface area of an individual whitecap subsequent to formation:

$$A(t) = A_0 \exp(-t/\tau) \tag{2.1}$$

where τ is the e-folding decay time (or characteristic whitecap decay time). In this model, τ is constant across a range of whitecap scales i.e., it has no dependence on A_0, the initial area of the laboratory produced whitecap. In such a model, the rate of change of an individual whitecap's area is independent of its size, and is simply the quotient of the area at a time t, and τ:

$$dA/dt = \frac{-A(t)}{\tau}. \tag{2.2}$$

It can be seen from equation 2.1 that the time-averaged areal extent of an individual whitecap is dependent upon its decay rate τ. There exists large variation in reported decay times. Estimates for the mean lifetime of foam patches have been reported by several authors, although only some make a distinction between active breaking crests and residual foam patches. Estimates range from fractions of a second [Kondo et al., 1973] to tens of seconds [Bondur and Sharkov, 1982]. The large variation in estimates from these early studies is likely due in part to differences in image collection and processing, as well as image resolution.

In the laboratory study of Monahan and Zietlow [1969], the decay rate was measured as 2.54 s for fresh water whitecaps and 3.85 s for salt water whitecaps. The salt water decay rate was measured as 3.53 s in a subsequent study by Monahan and colleagues [Monahan et al., 1982, 1986]. For some time, this value was taken as the standard characteristic decay rate and was used in a variety of applications such as in estimating the SSA source flux.

Using digital images of whitecaps, Callaghan [2013] characterised the evolution of whitecap area by considering distinct growth and decay phases, based on the appearance of a well-defined peak in the whitecap area time series which allows the area to be operationally separated into a linear formation phase and an exponential decay phase. A whitecap formation timescale for an individual whitecap (τ_{form}) is defined as

$$\tau_{\text{form}} = \frac{1}{A_{\text{max}}} \int_{t=-\infty}^{t=0} A(t)dt \tag{2.3}$$

where A_{max} is the maximum surface area of the whitecap reached at $t = 0$. The decay timescale for the individual whitecap is defined as

$$\tau_{\text{decay}} = \frac{1}{A_{\text{max}}} \int_{t=0}^{t=\infty} A(t)dt. \tag{2.4}$$

Combining these timescales gives the whitecap timescale (τ_{wc}) for an individual whitecap: $\tau_{\text{wc}} = \tau_{\text{form}} + \tau_{\text{decay}}$.

The whitecap decay timescales was investigated by Callaghan et al. [2012] using the same data set of digital images. It was found that τ_{decay} scales with A_{max}, such that

$$\tau = K_0 A_{\text{max}}^{k_1}, \tag{2.5}$$

where mean values for index K_1 is approximately 0.43, and factor $K_0 = 1.97$. Individual whitecap decay rates can vary by a factor of 20, and though an area-weighted average whitecap decay time can be defined, it will be different between different observational periods with different environmental forcing conditions. These results support the earlier findings of Jessup et al. [1997] who observed that the decay rate scales with the strength of breaking, with larger whitecaps taking longer to decay.

The temporal evolution of the area of three evolving individual oceanic whitecaps is illustrated in figure 2.5, using time-series of area evolution obtained from analysed digital images [Callaghan, 2013]. Note that in this figure, $t = 0$ defines the time at which the whitecap has reached its maximum area A_{max} and the point at which the growth phase ends and the decay phase begins. The three whitecaps show a similar evolution of area, characterised by a linear growth phase, followed by an exponential decay phase.
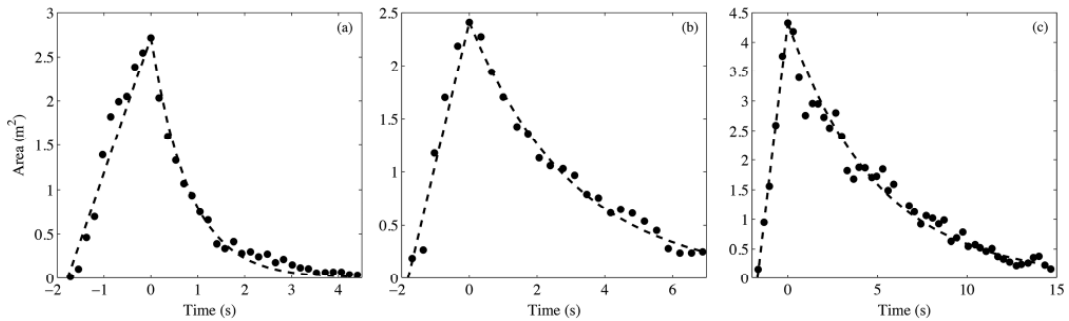
FIGURE 2.5: The evolution of whitecap area for three different breaking waves, each with different values for τ_{form} and τ_{decay}. Figure taken from Callaghan [2013]

2.3   The whitecap fraction, W

2.3.1   Definition of W

The whitecap fraction W is defined as the spatial fraction of the sea surface covered by whitecaps at any instant in time:

$$W = \frac{\sum_i A_i}{A_{\mathrm{obs}}} \tag{2.6}$$

where A_i is the area of an individual whitecap and A_{obs} is the total ocean surface area of the scene. Using this instantaneous definition, A_{obs} should be large enough to contain a sufficient number of whitecaps (so that the measured W is representative of the actual coverage), but should be sufficiently restricted to satisfy the requirement of spatial uniformity of the wave field Massel [2007]. Note that 'whitecap fraction' is used interchangeably throughout the literature with 'whitecap coverage', and that both can be given as a fraction or percentage. Throughout this text, we use the term whitecap fraction, and give as a percentage.

Using a steady-state approximation, Monahan [1971] related the whitecap fraction to the area of an individual whitecap, given by equation 2.1. In such a model, the statistics of the area of a given whitecap are independent of the whitecap number distribution. Assuming whitecaps with a mean initial area of $\overline{A}_0$, the whitecap area formed per unit time and unit area is $\overline{A_0}R$, where R is the breaking rate per unit area of water surface ($\mathrm{s}^{-1}\ \mathrm{m}^{-2}$). This quantity is balanced by the rate of whitecap area decay per unit sea

surface area; following from equation 2.2 this quantity is given by W/τ. Rearranging for W, we have

$$W = \overline{A_0}R\tau. \tag{2.7}$$

It follows that an increase in W can result from larger waves breaking, a higher frequency of breaking, or a longer whitecap decay time.

Alternatively, the whitecap fraction can be defined by taking into account the time-dependence of whitecap area. Following Callaghan [2013], for a given observational area and time period T, in steady state conditions, W can be written as

$$W = \frac{\sum_i \int A_i(t)dt}{A_{\text{obs}}T}. \tag{2.8}$$

The time integral in the numerator can be rewritten as

$$\int A_i(t)dt = A_{\text{max},i}(\tau_{\text{form}} + \tau_{\text{decay}}) = A_{\text{max},i}\tau_{\text{wc},i} \tag{2.9}$$

and when substituted into equation 2.8 yields

$$W = \frac{\sum_i A_{\text{max},i}\tau_{\text{wc},i}}{A_{\text{obs}}T}. \tag{2.10}$$

The whitecap timescale therefore plays an important role in determining the whitecap fraction. Importantly, variable growth and decay timescales are likely a major source of variability in W estimates between data sets. Furthermore, variable foam decay time will affect primary marine aerosol production, and energy dissipation estimates from breaking waves [Callaghan et al., 2012].

2.3.2   Relation of W to wave breaking and energy dissipation

Whitecap observations provided one of the first means of observing and quantifying wave breaking. It should be noted that W quantifies the post-breaking signature of wave breaking and therefore deviates from a measure of the strength, scale, and frequency of breaking because (i) contributions to W are from all breaking scales (with this information on relative contributions lost when W is evaluated), and (ii) W includes residual foam cover Massel [2007] which is affected by post-breaking processes.

As Kleiss and Melville [2010] summarise: 'Whitecap [fraction] and the breaking rate provide bulk representations of the amount of breaking, without any indication of the scales of waves that are breaking and dissipating energy. Information about the scales of breaking waves is of fundamental importance for the development of more rational models of air-sea mass, momentum, and energy transfer and mixed layer dynamics.' However, this information is not currently attainable on a global scale i.e., from routine model output or satellite measurements, and whitecaps remain the most conveniently observable indication of breaking surface waves [Hwang, 2012]. Further, the relation between the scale and severity of breaking and W is equivocal; for example, the same whitecap fraction can result from different frequencies of occurrence of breaking waves, depending on the scale and severity of the breaking events [Babanin, 2011].

For air-sea interaction processes (such as gas transfer) where dissipation of wave energy is the primary concern, one must critically assess how suitable W is as a representation of (i.e., a quantity directly proportional to) energy dissipation. We have seen above that W is dependent on post-breaking processes—the decay of residual foam, for example. Even if these factors do not play a role, the dependence of W on energy dissipation is not clear. By definition, the total energy flux from the wind to the waves (and therefore total energy dissipation rate in a quasi-stationary case) is

$$\langle \epsilon \rangle = \tau U \tag{2.11}$$

where

$$\tau = \rho_a u_*^2 = \rho_a C_d U_{10}^2 \tag{2.12}$$

is the wind stress imposed at the surface, U is a characteristic velocity of energy propagation in the lower atmosphere, u_* is the air-side friction velocity, ρ_a is the air density, and the drag coefficient is defined as $C_d = u_*^2/U_{10}^2$. According to the above relationships, the wave energy dissipation is related to some wind speed cubed, though the precise details of the relationship depend on the choice of characteristic wind speed U [Babanin, 2011]. However, these relationships do not imply that $W \sim U^3$, though some authors have enforced a cubic dependence of W on U_{10} in their parameterisations. The parameterisation of W in terms of wind quantities and wave energy dissipation rate is discussed in more detail in section 2.6

2.3.2.1   The Phillips spectral framework for wave breaking and whitecaps

Recently there has been a renewed interest in the work of Phillips [1985] (the Phillips framework), in which a theory for equilibrium range wind wave interaction was formalised. In this work, a new statistical measure was introduced which offers a scale-dependent description of wave breaking. The scale of a breaking wave is ideally specified by its wave number, but this can be difficult to measure in the field. As a surrogate, Phillips [1985] proposed using the breaker speed c, which is related to the wave number via the deep water dispersion relation. The Phillips distribution $\Lambda(c)$ (m^{-2} s), is defined such that $\Lambda(c)dc$ is the average total length per unit sea surface area of breaking fronts propagating with speeds in the range $(c, c + dc)$. This parameter can also be defined to account for a directional spread in the horizontal, but here we focus on the scalar distribution. It follows that the average total length of breaking crests per unit area ocean surface is

$$L_{\text{total}} \equiv \int_c \Lambda(c)dc \tag{2.13}$$

with units of m^{-1}. The distribution was originally predicted by Phillips [1985] using a spectral model of wave energy dissipation for wind and waves in equilibrium. More recently, the distribution has been measured empirically using video or infrared recordings of breaking waves (see Callaghan et al. [2012]; Kleiss and Melville [2010]; Melville and Matusov [2002]), and obtained from a spectral wave model [Leckler et al., 2013].

The relevance of the Phillips framework for this study is that it provides a semi-empirical approach to obtaining a relationship between whitecap fraction and the energy and momentum balances of surface gravity waves. Moments of the crest length distribution define various statistics for breaking waves; the first moment of $\Lambda(c)$ defines the fraction of the surface area 'turned over' by breaking fronts per unit time [Phillips, 1985]

$$R = \int_c c\Lambda(c)dc \tag{2.14}$$

which is related to heat and gas exchange between the ocean and the atmosphere [Jessup et al., 1997]. R can also be interpreted as the breaking frequency at a fixed point, and so has units of inverse seconds. The quantity under the integral sign defines the area swept by breaking wave crests of incremental wave speed dc per unit are per unit time, $A = c\Lambda(c)dc$ (s^{-1}). Phillips [1985] combined equation 2.14 with a timescale

T_{Phillips} to obtain an expression for W:

$$W = T_{\text{Phillips}} \int_c c\Lambda(c)dc. \tag{2.15}$$

Phillips [1985] defined this timescale as an 'average bubble persistence time', setting it as a constant though noting that it likely varied with water surface temperature and other environmental factors.

The fifth moment of the distribution determines the breaking-induced energy dissipation:

$$\epsilon(\vec{c})d\vec{c} = bg^{-1}c^5\Lambda(\vec{c})d\vec{c} \tag{2.16}$$

where b is the 'breaking strength' proportionality factor [Drazen et al., 2008; Phillips, 1985; Romero et al., 2012], and g the acceleration due to gravity. Combining equations 2.15 and 2.16 one can obtain an expression relating W to the energy dissipation rate:

$$W = gT_{\text{Phillips}}b^{-1} \int_c c^{-4}\epsilon(\vec{c})d\vec{c}. \tag{2.17}$$

The term $\epsilon(\vec{c})d\vec{c}$ can be expressed as the spectral rate of energy loss from wave components in the equilibrium range of the wave spectrum [Phillips, 1985]. Using such an expression, one can integrate equation 2.17 over a suitable range of breaking front velocities ($c_{\min}$,$c_{\max}$). In the result of this integration appears the total (i.e., integrated) energy dissipation rate $\int_c \epsilon(\vec{c})d\vec{c} = \langle\epsilon\rangle/p_w$ where ρ_w is the density of water [Phillips, 1985]. A final expression relating W to $\langle\epsilon\rangle$ is obtained:

$$W(\langle\epsilon\rangle) = \frac{gT_{\text{Phillips}}}{4b\rho_w} \frac{\langle\epsilon\rangle}{c_{\min}^4 ln(c_{\max}/c_{\min})}. \tag{2.18}$$

The merit of such an expression is that the whitecap fraction is determined by the kinematics and dynamics of the breaking waves via c and $\langle\epsilon\rangle$. However, the nature of this framework results in an expression with several other parameters that are not well constrained; to obtain W, one requires $\langle\epsilon\rangle$ estimates (or measurements), as well as values for b, $c_{\min}$ and $c_{\max}$, and T_{Phillips}. Estimates of b, $c_{\min}$ and $c_{\max}$ are given in the literature, but these parameters generally show a large variation between studies.

In the original formalism set out in Phillips [1985], the factor T_{Phillips} is somewhat ambiguous. Reul and Chapron [2003] suggest that choice of the factor T_{Phillips} can—to

first order—discriminate between different stages of whitecap evolution i.e., between active and residual coverage. Based on a model of an individual breaker, the persistence time of the generated foam layer is not constant, but scales with the period of the underlying carrier waves: $T_{\mathrm{Phillips}} = aT_b = a2\pi c/g$, where a is a constant of proportionality.

2.4   Measurement of whitecap fraction

2.4.1   In situ observations

Estimates of whitecap fraction have traditionally been obtained from in situ measurement of the ocean surface via photographic or video imagery [Anguelova and Webster, 2006; de Leeuw et al., 2011]. Measurements have been made from aircraft, ships, and fixed platforms (e.g. Bobak et al. [2011]; Callaghan and White [2009]; Sugihara et al. [2007]). W is generally estimated as an average value of a range of individual measurements of W over a time period short enough that forcing remains constant ($\sim$30 minutes). Typically, estimates from video measurements are an order of magnitude lower than those from photographic measurements taken in comparable conditions; the exact reason for this difference is unknown but could be related to image resolution.

Early observations of wave breaking and measurements of whitecap fraction include those of Munk [1947], Blanchard [1963], Gathman and Trent [1968], and Cardone [1969]. Although there were some exceptions (e.g., the study of Munk [1947] where the number density of foam patches were reported), the majority of these studies reported estimates of W obtained through manual processing of photographs. These were used in conjunction with wind speed measurements to obtain some of the first empirical relationships between whitecaps and wind speed (section 2.6).

Over subsequent decades, dozens of observational data sets from field campaigns were published, with a trend of increasing data volume due to a move from film to digital photography, and use of automated systems to extend the period of measurement. Anguelova and Webster [2006, Table 2] give a chronological listing of whitecap fraction data sets spanning nearly 50 years, from 1952–2000. Individual W estimates from these data sets are plotted against corresponding U_{10} estimates in Figure 2.6.
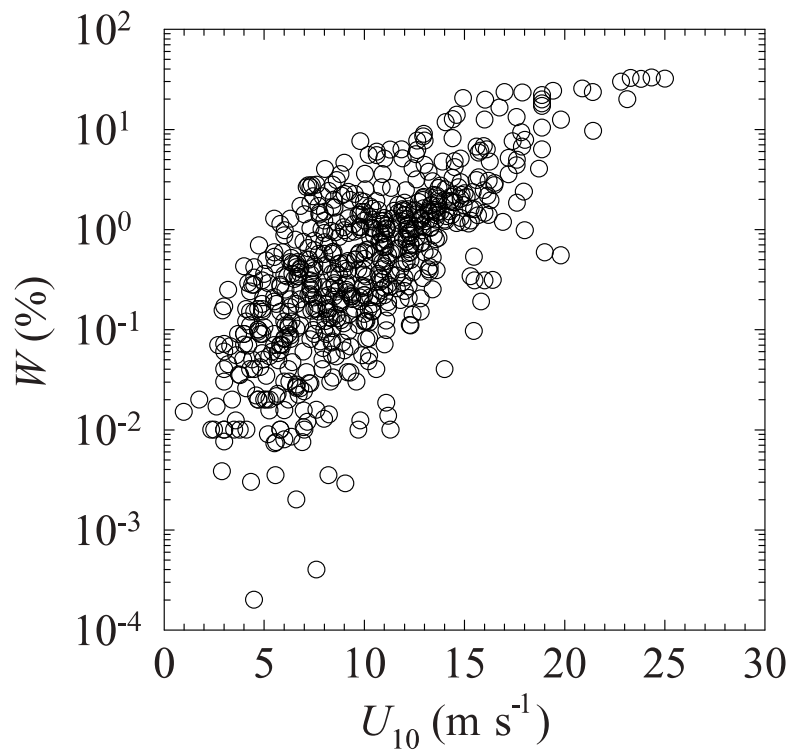
FIGURE 2.6: Scatter plot of individual W estimates from photographic data as a function on U_{10}. Figure taken from Anguelova and Webster [2006]

Of the 28 data sets documented in Anguelova and Webster [2006], only a small selection focus on measurements made in the open ocean where the ocean waves are not fetch limited (namely those of Spillane et al. [1986] and Stramska and Petelski [2003]). The data sets used by Monahan and O'Muircheartaigh [1980], and Bortkovskii [1987] contain a mixture of open ocean and coastal measurements. In subsequent years, two more open ocean datasets have been published, those of Callaghan et al. [2008a] and [Moat et al., 2009]. Practically, coastal measurements are easier to obtain, but both the physical and environmental conditions pertinent to coastal sites will affect the wave breaking mechanism and the whitecap fraction. For example, one might expect relatively higher W values in coastal zones due to the effect shallowing in the surf zone has on slowing and steepening swell waves. On the other hand, fetch-limited conditions occur more frequently in coastal regions and so W could be expected to be relatively lower than that for open ocean regions under comparable wind forcing.
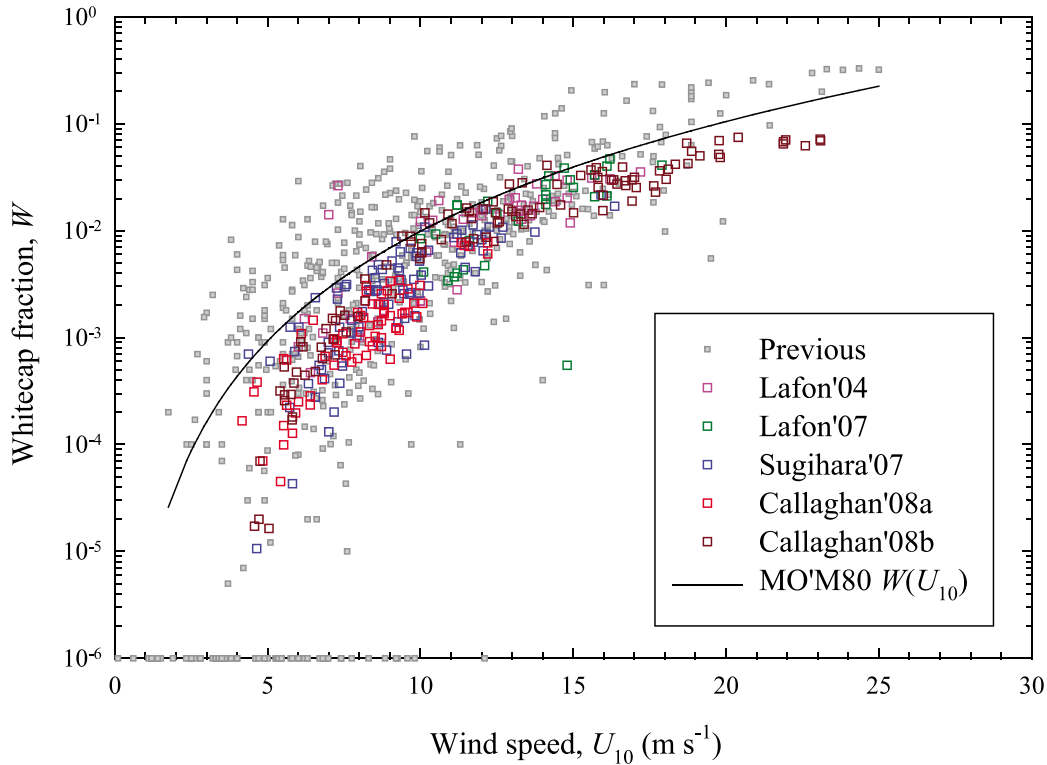
FIGURE 2.7: W estimates as a function of U_{10} from five new datasets (colours), and previous photographic studies (grey). W estimates less than or equal to 1×10^{-6} are omitted. The line represents the formulation of Monahan and O'Muircheartaigh [1980], equation 2.20. Figure taken from de Leeuw et al. [2011].

2.4.1.1   Variability between W estimates from different data sets

Figure 2.7 shows W against U_{10} for five recent data sets (that of Lafon et al. [2004], Lafon et al. [2007], Sugihara et al. [2007], Callaghan et al. [2008a], and Callaghan et al. [2008b] [colours]), together with all previous photographic estimates [de Leeuw et al., 2011] (grey). In this figure, estimates of W from video recordings are omitted as they are thought not to be as accurate as those by film photography [Lewis and Schwartz, 2004]. Also shown is the widely used Monahan and O'Muircheartaigh [1980] relationship, denoted MM80 henceforth (see section 2.6.1).

As can be seen, the pooling of many historical data sets results in large scatter in W when plotted solely in terms of wind speed. Part of this variability is likely due to the use of different measurement techniques; this is especially true of earlier data sets where data volume is generally much lower, and measurement techniques less consistent. It has been shown by Callaghan and White [2009] that to obtain an individual estimate of W with a fractional error of a few percent from sea surface images with a limited

field of view, one needs to average over order hundreds of individual photographs (or video frames) within an interval short enough to have constant forcing. Analysis of an insufficient number of images—as was the case in many of the earlier studies—can lead to nonconvergent W estimates with larger uncertainties, contributing to data scatter [Callaghan and White, 2009].

The more recent data sets show a clustering of W estimates when plotted as a function of U_{10}. This clustering is indicative of improvements to the extraction of W from photographic data and increases in data volume, although it should be acknowledged that the clustering may in part be due to the similar image processing methodology adopted in these recent studies.

Aside from the reduced scatter in recent data sets, it is clear that there is a general trend of lower W estimates (at a given wind speed) than the older historical data. The Monahan and O'Muircheartaigh [1980] relationship acts as a sort of upper bound for W estimates at a given wind speed. Furthermore, it appears that the wind speed dependence is also different; at low wind speeds ($U_{10} < 7 \text{ m s}^{-1}$), the new measurements are suggestive of a faster rate of increase of $W(U_{10})$ than MM80, whereas at higher wind speeds ($U_{10} > 15 \text{ m s}^{-1}$) the rate of increase seems to level off, with W estimates plateauing.

The almost order-of-magnitude scatter that remains is likely an indication that factors other than wind speed play a role in determining whitecap fraction. Thus, there is a need for global, consistent measurement of W, with sufficient documentation of relevant oceanographic and meteorological conditions— something which hitherto has not been achieved.

2.4.1.2   Limitations of in situ measurement

In situ observations, while instrumental in gaining knowledge of whitecapping so far, have their limitations. Sampling frequency and data volume may be low, with as few as five individual photographs having been used to construct a $W(U_{10})$ parameterisation [Blanchard, 1963]. The number of individual W estimates obtained per study has

increased dramatically since the earliest studies with a move from film to digital photography, and use of automated systems to extend the period of measurement [Moat et al., 2009].

Most studies are limited spatially, with observations from platforms and ships offering measurements only in environmental conditions pertinent to the given location. Nearly all existing datasets were obtained in coastal, or fetch-limited waters [Anguelova and Webster, 2006]. The only open ocean datasets are those presented in Bortkovskii [1987], Bondur and Sharkov [1982], the more recent study of Callaghan et al. [2008a], and to some extent Reising et al. [2002] and Stramska and Petelski [2003]. Furthermore, only one study has been conducted in the Southern Hemisphere (from the POLEX-YUG campaign, reported in Bortkovskii [1987]). Thus, existing datasets significantly under represent open ocean conditions, specifically those encountered in regions of the Southern Ocean where sea conditions are influenced by persistent winds over long fetches [Anguelova and Webster, 2006]. Another bias may result from the small amount of data obtained in warm waters; measurements have generally been conducted in cold waters where sea surface temperatures are lower than $\sim17^{\circ}$C. It is plausible that the seawater temperature (or more fundamentally, the kinematic viscosity ν_w) could alter whitecap fraction due to changes in wave breaking kinematics and the behaviour of bubbles comprising the surface foam layer (section 2.5.2).

Temporal coverage is limited by the measurement period—often of the order of days, and usually no longer than several weeks. There are likely to be seasonal changes in whitecap fraction at a given location, due to changes in wind patterns and other forcings. Hitherto, an in-depth analysis of temporal changes in whitecap fraction over the course of a whole year has remained elusive.

A further weakness of this method is the subjective choice of the intensity threshold used in the processing algorithm to extract the 'white areas'. On a related note, it is known this method works better for stage A whitecaps (dense, recently formed foam layers from an active breaking wave) due to there more intense 'whiteness' in comparison with the more grey stage B (residual surface foam) whitecaps. Therefore, stage B whitecaps may not always be well quantified using photographic images.

2.4.2   Satellite-based estimates of whitecap fraction

Both the large variability in whitecap fraction and the limitations of traditional measurement approaches necessitates a new method for obtaining global W estimates. Remote sensing of the ocean surface can capture both spatial and temporal variability of W, and better quantify its dependence on meteorological and oceanographic forcings.

The first direct implementation of a method to estimate W from remote sensing measurements is described in chapter 3. This method, in contrast to in situ measurement, does not require the resolving and counting of individual whitecaps. Rather, what is of interest is how much the average emission of a given ocean area changes with appearance of whitecaps, and how well these changes can be retrieved from measured data [Anguelova and Webster, 2006]. Importantly, a more comprehensive study of variability in W becomes viable if estimates are supplemented with accompanying estimates or measurements of different forcing variables.

2.5   Factors affecting whitecap fraction

In the previous section, it was shown that decades of measurements of W have indicated significant scatter in estimates of W at a given wind speed, leading to suggestion that factors other than wind speed play a role in determining W. This should come as no real surprise; W is a function of the size and frequency of breaking waves, and the characteristic rate at which an individual whitecap decays. Therefore, any physical factor that could affect either of these quantities will have an impact on the measured whitecap fraction. For example, both A and R will primarily be a function of the wave field, whereas τ will also be dependent upon factors that influence foam lifetime. In this section, we review the literature regarding the influence of forcing factors on W.

2.5.1   Influence of the wave field

Stramska and Petelski [2003], working with data obtained in the North Atlantic, categorized measurements of W by the corresponding wave conditions; this was achieved by comparing measured significant wave height, H_s, with that expected for a fully

developed sea given the measured wind speed [Pierson et al., 1955]; the data points were classified as representing an undeveloped sea state when the observed H_s was at least 0.5 m less than the expected H_s for a hypothetical fully developed sea. The 0.5-m criterion was chosen due to the relatively low accuracy of the H_s estimates. They concluded that at a given wind speed, a developed sea should result in a slightly higher whitecap fraction than that of an undeveloped sea, suggesting that the wind duration or fetch is an important factor in determining W. The results of this analysis are shown in Figure 2.8.
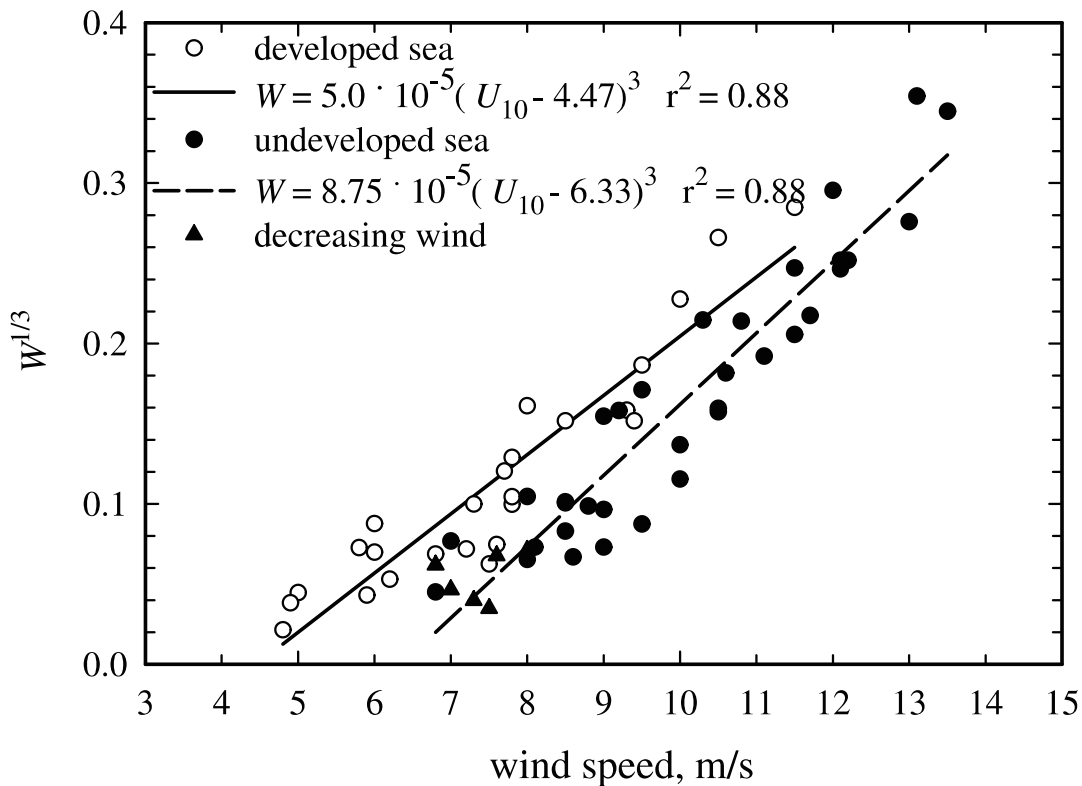
FIGURE 2.8: Variation in W due to degree of wave development (taken from Stramska and Petelski [2003]). See text for details of the classification used.

It can be seen that for a given wind speed, a developed sea resulted in a slightly higher whitecap fraction than that of an undeveloped sea. The authors thus conclude that wind history is an important factor; winds blowing in the same direction over a prolonged period of time will lead to developed seas. Additionally, wind history (or wave development) should account for some of the variation in W. This wind history influence may be contributing some of the difference in W by geographic location; to use the authors' example, wind in trade winds regions is likely to vary less over a

period of time, leading to developed seas and higher whitecapping in comparison to polar waters where atmospheric conditions can be highly variable.

Sugihara et al. [2007] found evidence that whitecaps are produced most actively under the condition of a pure wind sea, and that W is suppressed by swell, indicating that whitecapping is primarily a result of breaking wind waves. The authors also report that in conditions of a pure wind sea, at a given value of U_{10}, W increases with wave age, supporting the conclusions of Stramska and Petelski [2003].

In contrast to the above two studies, Lafon et al. [2007]—by analysing photographs taken in a coastal environment—found that there is a peak in W at an intermediate wave age, and that W is likely to be lower both above and below this point i.e., in growing or fetch-limited seas, or under swell-dominated conditions.

Callaghan et al. [2008b], focusing on a fetch-limited coastal region, observed that: (i) scatter in W was reduced when seas were mixed (i.e., when the spectral intensity of wind waves is of the same order of magnitude as the swell) rather than swell-dominated, (ii) swell-dominated seas result in overall lower values of W than mixed seas (as in Sugihara et al. [2007]) and (iii) the presence of a tidal current can augment W estimates depending on the relative direction of the tidal current and the waves.

Most recently, Goddijn-Murphy et al. [2011] provided evidence that, at a given wind speed for higher winds ($U_{10} > 10 \text{ m s}^{-1}$), W is slightly larger in conditions of developed seas (mostly associated with decreasing winds) as opposed to developing seas (increasing winds), as shown in Figure 2.9a. Callaghan et al. [2008a], using the same dataset of W estimates, had previously reached the same conclusion, reporting higher values of W in cases of decreasing winds (developed seas). In the study of Goddijn-Murphy et al. [2011], it was also concluded that whitecap fraction is generally reduced in swell conditions compared to wind sea conditions in cases of cross swell (angle between direction of wind and swell waves between $\pm45^{\text{o}}$ and $\pm135^{\text{o}}$) (Figure 2.9b). Perhaps a more important conclusion from the [Goddijn-Murphy et al., 2011] study is that a grouping of sea state according to wave development, wind history, or the composition of wind and swell waves was not observed when ECMWF or QuikSCAT data was used.

It can prove difficult to isolate the effect of the wave field because of inherent correlations between wind speed and measures of the degree of wave development. Many
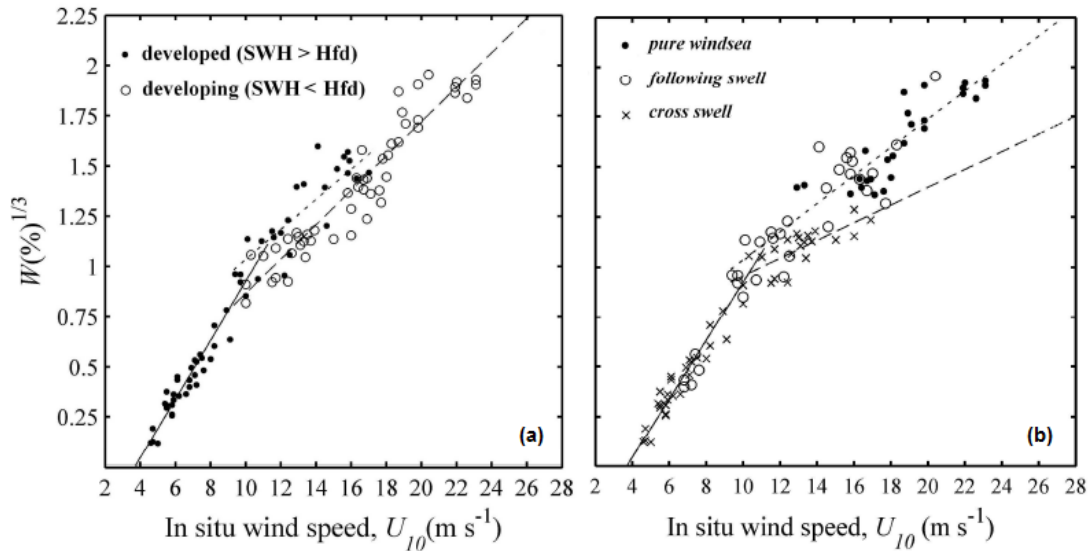
FIGURE 2.9: The effects of (a) wave development, and (b) wave field conditions, on whitecapping. (a) Developed seas—indicating bigger waves—are associated with enhanced W at a given wind speed, while cross swell can suppress W at moderate wind speeds (b). Figure adapted from Goddijn-Murphy et al. [2011]

different measures of sea state have been adopted; these vary in how exactly the degree of wave development should be defined in terms of readily available measurements. Both Stramska and Petelski [2003] and Sugihara et al. [2007] consider the effect of wave development on W; however, the classification of Stramska and Petelski [2003] is based on significant wave height only, which may include contributions from swell, while Sugihara et al. [2007] used directional frequency wave spectra to separate swell-dominated from pure wind seas. This makes a direct comparison of their results questionable.

On a practical level, individual in situ data sets are likely to span only a narrow range of possible wave conditions due to the temporal and spatial limitations of an individual field campaign, so that a direct comparison of results may not be viable.

2.5.2   Influence of other environmental factors

Aside from the wave field, many other factors—acting alone or in combination—have the potential to enhance or suppress W. It has proven difficult to quantify the dependence of W on sea surface temperature (SST). Only a handful of studies of whitecap fraction variability consider this effect, and furthermore, where data for SST does exist, conditions are often limited to a small range of temperatures. Monahan and O'Muircheartaigh [1986] suggest that SST has an influence on whitecap fraction, the

effect being twofold. First, they found evidence that the exponent of a $W(U_{10})$ power law fit increased with increasing SST. The authors reason that the true cause of this result is the inherent correlation between SST and average duration of high wind events; at higher latitudes (lower SSTs), the average duration of these events is shorter, leading to a wave spectrum that is not fully developed. Second, the authors propose that W should increase with increasing SST because of the reduction in water viscosity; a lower viscosity results in less viscous dissipation, with a larger fraction of energy available for dissipation through wave breaking and whitecapping.

Bortkovskii [1987] classified W–U_{10} fits by SST, and found no apparent trend in the parameters; however, the total whitecap fraction (i.e., the sum of active and residual foam) was found to increase with increasing SST. Thus result may, however, have been largely influenced by the inclusion of a cold water (SST $< 5^\circ$C) data set. Both Wu [1988] and Stramska and Petelski [2003] report no systematic trends in W with SST.

In summary, although several studies show increasing W with increasing SST (decreasing water viscosity), there is little agreement as to the physical bases of this dependence [Lewis and Schwartz, 2004, section 4.5.3.1].

Atmospheric stability is thought to affect whitecapping through its influence on how the air over the sea interacts with waves. In unstable conditions, there can be significant deviations from the standard logarithmic wind profile describing the steady lower boundary layer. This effect can be difficult to take into account, and can result in biases in U_{10} and thus W–U_{10} dependencies. It is also possible that an atmospheric stability type signal in W data may actually be a result of correlation between stability and other factors, such as SST.

The air-sea temperature difference $\Delta T = T_a - T_s$ is generally used as a proxy for atmospheric stability; a negative ΔT represents unstable conditions, a positive ΔT stable. Monahan and O'Muircheartaigh [1986] find evidence for greater values of W under unstable conditions than stable conditions at the same wind speed, with W increasing by nearly 10% per $^\circ$C, at a fixed wind speed. Wu [1988] concluded that W will increase as conditions become more unstable, based on an hypothesized relationship between the drag coefficient and ΔT. However, Stramska and Petelski [2003] found no evidence of a relation between ΔT and W at a given wind speed.

Monahan and Woolf [1988] quantified the stability effect on active and residual white-cap fractions separately. Estimates using their empirical expressions show that the largest changes resulting from stability effects would be on stage A whitecapping with an increase of a factor of 7 as the temperature difference between air and water increases from 0°C to 10°C; the increase in stage B whitecap fraction would be a factor of 2.4.

Again, there is no general consensus as to the effects of atmospheric stability on W; those trends have been observed are small relative to the spread of data.

Whilst the salinity difference between freshwater and saltwater can have a large effect on the persistence of bubble plumes (and thus W) [Monahan and Zietlow, 1969], the effect is expected to be much more subtle over the relatively small range of salinity variations encountered in the open oceans; it was demonstrated by Peltzer and Griffin [1987] that changes to foam lifetime due to salinity are insignificant in the open ocean. Another factor to consider is the role of salinity in changing bubble sizes which could affect the remote sensing signature of the whitecaps, though this effect is not well understood. More pertinent to this study is inclusion of the effects of salinity by considering the role it plays in determining water viscosity—a parameter which essentially combines the effects of SST and salinity.

The role surface-active substances (surfactants) play in modulating W in the open ocean has yet to be evaluated, although some laboratory studies do exist [Garrett, 1967; Peltzer and Griffin, 1987; Scott, 1986]. Recently, Callaghan et al. [2013] confirmed that the presence of surfactants acts to stabilize surface bubbles and so increase whitecap decay times. As the concentration of surfactants is known to vary markedly over the global oceans [Falkowski et al., 1998; McClain et al., 2004], it is plausible that presence of such material can significantly affect residual whitecap fraction.

2.6   Parameterisation of whitecap fraction

2.6.1   Wind dependent parameterisation

Although numerous factors control whitecap formation and lifetime, wind speed is the first-order controlling factor for wave breaking and the formation of whitecaps,

and being readily measured, is often used to parameterize whitecapping through an empirical expression, $W = f(U_{10})$. Nearly all of these relationships are expressed as a power law of the form aU_{10}^b with the exponent b typically close to 3 [Anguelova and Webster, 2006]. One of the earliest $W(U_{10})$ parameterisations was that of Monahan [1971] in which $W \propto U_{10}^{3.4}$.

The power-law dependency of W on U_{10} has been the subject of much debate. Cardone [1969] hypothesized that whitecaps manifest the dissipation of excessive energy transferred from the air flow to the waves. Later, Wu [1979, 1988] argued this on analytical grounds by noting that W can be related to the rate of energy supplied by the wind (per unit sea surface area) i.e., $W \propto \dot{E}$. $\dot{E}$ can be expressed as a product of the wind stress (τ) and surface drift current V, so that

$$W \sim \dot{E} = \tau V \sim (C_{10}U_{10}^2)(C_{10}^{1/2}U_{10}) \sim U_{10}^{3.75}, \tag{2.19}$$

after substituting in the common expressions for wind-stress and wind-induced surface drift current. Using data obtained in the Atlantic Ocean by Monahan [1971] and the Pacific Ocean by Toba and Chaen [1973], the whitecap fraction was expressed in terms of the 10 metre wind speed as $W = 1.7 \times 10^{-6} U_{10}^{3.75}$. The exponent in such a relationship is derived from the argument above (rather than being derived through curve fitting), whereas the constant is related to the foam persistence, itself related to the water temperature and atmospheric stability. Monahan and O'Muircheartaigh [1980] later expressed reservations about this 3.75 power law, citing variation in the power-law dependencies of relationships derived from different data sets and a general need for an optimal empirically-based expression based on a statistical analyses.

Thirty wind speed dependent empirical expressions (published between 1971 and 2004) are listed in Table 1 of Anguelova and Webster [2006]; the majority of these are wind speed only parameterisations i.e., $W(U_{10})$, and the remaining expressions are functions of wind speed and an additional factor. Most of the whitecap data sets published subsequent to the study have been used primarily to explore the dependency of W on U_{10}, but also friction velocity, u_* [de Leeuw et al., 2011].

As numerous $W(U_{10})$ parameterisations exist within the literature, it is often a matter of preference as to which formulation should be utilized in applications where W needs to be specified. Despite being one of the earliest formulations, the Monahan

and O'Muircheartaigh [1980] relationship (obtained using the robust biweight fitting technique on a combination of field data reported in Monahan [1971] and Toba and Chaen [1973]) has been widely adopted in the parameterisation of sea spray aerosol production in models:

$$W(U_{10}) = 3.84 \times 10^{-4} U_{10}^{3.41}, \tag{2.20}$$

where W is in %. The highest wind speed recorded in the combined dataset is 16.6 m s^{-1}, but a maximum wind speed above which (2.20) is no longer suitable, is not explicitly defined. However, the parameterisation is widely extrapolated to much higher wind speeds.

The Callaghan et al. [2008a] relationship is a recent formulation resulting from analysis of whitecap data obtained during the 2006 Marine Aerosol Production (MAP) campaign in the North East Atlantic. By assuming that W can be related to U_{10} with a power law of the form $W = a(U_{10} + b)^3$, a linear regression on $W^{1/3}$ against U_{10} was performed, resulting in the following relationships:

$$
\begin{aligned}
W(U_{10}) &= 3.18 \times 10^{-3}(U_{10} - 3.70)^3; \quad 3.70 < U_{10} \leq 11.25 \text{ m s}^{-1}, \\
W(U_{10}) &= 4.82 \times 10^{-4}(U_{10} + 1.98)^3; \quad 9.25 < U_{10} \leq 23.09 \text{ m s}^{-1},
\end{aligned}
\tag{2.21}
$$

where W is percentage total (i.e., stage A plus stage B) whitecap cover. Note that data has been divided into two overlapping groups according to the measured wind speed, with a regression performed on each group.

In the study of Goddijn-Murphy et al. [2011], analysis of the MAP whitecap data set was extended through use of in situ, model, and satellite data for wind and waves. The following $W(U_{10})$ relationship is reported when NASA QuikSCAT satellite wind speed measurements are used:

$$W(U_{10}) = 11.5 \times 10^{-3} U_{10}^{1.86}. \tag{2.22}$$

2.6.2   Inclusion of wave state

A strong dependency of W on wave field characteristics has been demonstrated in numerous studies (e.g., [Kraan et al., 1996; Ross and Cardone, 1974; Zhao and Toba, 2001]). The wave field influence can be included in a parameterisation of W in different

ways. First, $W(U_{10})$ relations for different wave conditions can be proposed; this approach has been used by Stramska and Petelski [2003] and Callaghan et al. [2008a] (section 2.5.1) to account for the degree of wave development due to wind duration. Second, W can be parameterised in terms of u_* which itself can be estimated using a wave-state dependent roughness scheme ([Hwang, 2005]). Third, one can replace U_{10} as the independent parameter and instead work with a wave or wind-wave parameter; we review efforts on this last approach next.

2.6.2.1 Energy dissipation models

Ross and Cardone [1974] proposed that whitecap fraction should be proportional to the rate of energy dissipation from the wave field. By estimating the total (i.e., integrated) energy dissipation rate using the Phlliips equilibrium range theory [Phillips, 1985] applied to wave buoy observations, Hanson and Phillips [1999] found that use of this parameter in a standard power-law description of W decreased data scatter by two to three orders of magnitude compared to wind speed parameterisation.

The utility of such a formulation relies on the availability of directional wave spectrum information from which the wind sea part of the spectrum can be isolated (e.g., using the spectrum integration method of [Hwang et al., 2012]), before ϵ is calculated. Addressing this concern, Hwang and Sletten [2008] expressed the energy dissipation of wind-generated waves in terms of readily measurable, bulk quantities—wind speed, significant wave height, and peak wave frequency—as

$$
\begin{aligned}
\epsilon &= \alpha \rho_a U_{10}^3 \\
\alpha &= 0.2 \omega_*^{3.3} \eta_*
\end{aligned}
\tag{2.23}
$$

where ρ_a is the density of air, and α is a wave parameter determined using non-dimensional values for the frequency peak of the wave spectrum ω_*, and the surface elevation η_*. Applying equation 2.23 to an extensive database of whitecap observations results in the following relationship:

$$
W = 0.014(\epsilon - \epsilon_c),
\tag{2.24}
$$

with threshold energy dissipation for whitecap detection ϵ_c between 0.013 and 0.038 W m^{-2}.

2.6.2.2   Wave age

Kraan et al. [1996] found a relationship between the stage A whitecap fraction W_A—as opposed to total W which quantifies both active and decaying whitecaps—and wave age, defined as $\xi = c_p/u_*$ where c_p denotes the phase velocity of the dominant waves, and is equal to g/ω_p. The authors find that W_A scales with the inverse square of wave age, though data scatter was high.

Guan et al. [2007] include a theoretical analysis of wave breaking dissipation models in their discussion of whitecap coverage models. They conclude that single-parameter models are insufficient to explain the variability of whitecap fraction, and propose a model parameterised in terms of the wave age, $\beta_* = g/(u_{(*)}\omega_p)$ where g is the acceleration due to gravity and ω_p is the spectral peak angular frequency. The result is a $W \propto \beta_*^{-2}$ relationship, the same scaling as found by Kraan et al. [1996]. Lafon et al. [2004] suggest a similar relationship, although the power-law exponent and constants of the exact relationship are slightly different due to the different data sets used.

2.6.2.3   Wave Reynolds numbers

Zhao and Toba [2001] investigated the correlation between W and several different variables, including a breaking-wave parameter,

$$R_{\mathrm{B}} = \frac{u_*^2}{\nu_a \omega_p}, \tag{2.25}$$

which was originally proposed by Toba and Koga [1986]. Here, v_a the kinematic viscosity of air, and w_p the spectral peak angular frequency of wind waves. This non-dimensional parameter represents both a wind-forcing and wave property dependence, and through fitting to a combination of various data sources, find that $W = 3.88 \times 10^{-7} R_{\mathrm{B}}^{1.09}$. Another parameter considered was the wave age $\beta = g/w_p u_*$, where g is the acceleration due to gravity. Several whitecapping data sets were pooled for this study, and analysed using the method of least squares. The breaking-wave parameterisation above performed best, whilst a $W \sim \beta$ relationship had quite a low

correlation coefficient. The authors conclude that although a wave-age dependence does exist, it cannot be used to parameterise the whitecap fraction itself, and that R_{B} can effectively describe wave-breaking behaviour for wind-waves in local equilibrium with the wind.

A similar non-dimensional wind-wave variable, the so-called breaking-wave Reynolds number, has been proposed to give improved predictions of gas transfer velocities [Woolf, 2005], but the model is tuned to fit range of empirical parameterisations and has not been validated.

$$R_{\mathrm{Hw}} = \frac{u^* H_{\mathrm{s}}}{\nu_{\mathrm{a}}}, \tag{2.26}$$

where H_s is the significant wave height, and ν_{a} the viscosity of air. Woolf [2005] later adapted this parameter by exchanging the viscosity of air for that of water; this slight alteration is an attempt to characterise the turbulence in the upper ocean, and is also more consistent with an analysis of the temperature sensitivity of wave breaking. It has been suggested that such a variable may be more successful than U_{10} alone in accounting for variability in W.

There is continued effort to fit both new and existing field data with improved empirical models. In the majority of recent W data sets, measures of the wave field have been documented enabling W to be parameterised as a function of different wind-wave, or wave variables. However, neither the use of friction velocity, nor inclusion of wave field measures in parameterisation of W, have led to the reduction in scatter that was perhaps indicated by previous studies [Goddijn-Murphy et al., 2011].

2.7   Whitecaps and the production of sea spray aerosol

One of the most important consequences of wave breaking and whitecap formation is the production of sea spray droplets through bubble bursting, and via the wind tearing of wave crests at higher wind speeds [Andreas, 1995; Blanchard, 1963; Monahan et al., 1983]. Sea spray aerosol (SSA) can be defined as 'a suspension, in air, of particles that are directly produced at the sea surface' [de Leeuw et al., 2011]. It is a key aerosol constituent over much of the Earth's surface, and is central to description of Earth's aerosol burden [Lewis and Schwartz, 2004]. Globally, the mass flux of SSA is estimated to be 0.01–1×10^{14} kg yr^{-1} [Textor et al., 2006]. SSA particles often dominate

Role	Description	References
Function readily as CCN (Indirect radiative forcing)	Due to hygroscopicity and size. Determine number concentration and size distribution of marine drops, in turn affecting clouds and their reflectance	[Andreae and Rosenfeld, 2008; Twomey, 1991]
Scattering of electromagnetic radiation (Direct radiative forcing)	Dominant contribution to light scattering by aerosols in most ocean regions. Cooling influence cited as 0.08-6 Wm^{-2} [†]	[Dobbie et al., 2003; Lewis and Schwartz, 2004; Quinn et al., 1996]
Absorption of IR radiation	Warming through absorption of thermal infrared radiation	[Reddy et al., 2005]
Interaction with atmospheric gases & particles	Serve as sink for condensable trace atmospheric gases and for smaller aerosol particles. Important role in many chemical reactions and cycles, e.g. the marine sulphur cycle	[Lewis and Schwartz, 2004] - section 2.1.5.2, [O'Dowd and de Leeuw, 2007]
Contribution to heat and water vapour transfer	Bubbles and spray essentially increase oceanic surface area, enhancing transfer of both heat and moisture. This is true for coarse SSA ($D_p > 10$ μm), at 'high' wind speeds (> 20 ms^{-1})	[Andreas, 1995; Andreas and Monahan, 2000; Fairall et al., 1994]

TABLE 2.1: Physical and chemical roles of SSA in the marine environment. [†] Estimate from Lewis and Schwartz [2004]

the mass concentration of marine aerosol, especially away from continental sources of anthropogenic aerosols and dust. As such, the chemistry and physics of the marine environment are sensitive to the SSA concentration.

Table 2.1 lists the major roles that SSA plays once it is present in the marine boundary layer. Many of these processes are inherently linked to one another—more so with the

various feedbacks that come into play. In recent years, there has been a shift in the literature to more inclusive studies of SSA (and other natural aerosols) and their role in the climate system. Without this comprehensive understanding, we lack a sufficient framework in which to better quantify the influence of anthropogenic aerosols on the climate system, and their role in climate change. The effects of anthropogenic aerosols have been identified as the greatest uncertainty in radiative forcing of climate change over the industrial period by the Intergovernmental Panel on Climate Change (IPCC) [Houghton et al., 2001, page 8]. In order to decrease this key uncertainty, we must first better understand the interplay between natural aerosols and the climate system.

2.7.1 Production of sea spray aerosol

Bursting bubbles in the oceans are the main production mechanism for SSA particles (e.g., Blanchard [1963]; Deane and Stokes [2002]; Lewis and Schwartz [2004]; Modini et al. [2013]; Woodcock [1948]). During the bursting process, two types of drops are produced [Resch et al., 1986] (Figure 2.10). Film drops are produced when the bubble cap (or film) fragments with the resulting drops ejected over a wide range of angles relative to the vertical. The number and size distribution of the film drops produced largely depends on the size of the bursting bubble; one bubble can produce as many as a thousand drops, with radii spanning five orders of magnitude—from 0.1 micrometers to several hundreds of micrometers, though most are < 1 μm [de Leeuw et al., 2011]. In the subsequent stage of bursting, a vertical jet forms in the middle of the cavity left by the bubble. On breaking up, the jet produces up to 10 jet drops which are ejected close to vertically and can reach heights of ∼20 cm [Blanchard, 1983]. The majority of SSA particles in the atmosphere with radii between 1 and 25 μm are likely jet drops [de Leeuw et al., 2011].

Larger drops can be formed via an alternative mechanism—the tearing of wave crests by the wind. These so-called spume drops can be transported vertically with the wind, and have sizes ranging from tens of micrometers to several millimeters.
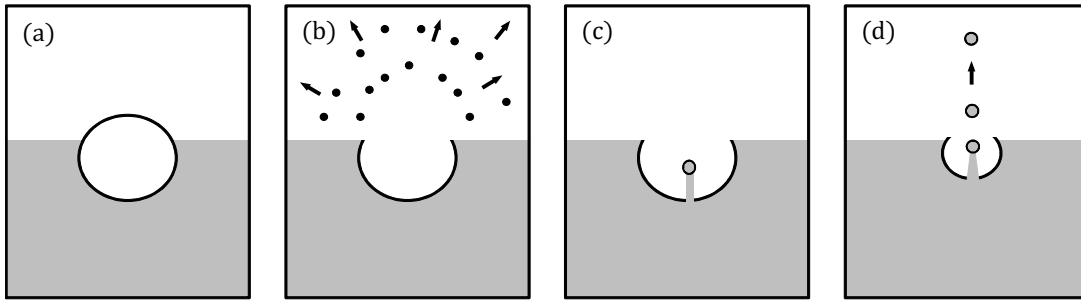
FIGURE 2.10: Drop formation from bubble bursting. (a) A bubble rising from below reaches the surface with formation of a bubble film, which will burst to produce film drops (b). (c) The cavity left by the bubble decreases in size as it is filled by the surrounding liquid with the formation of several jet drops from the breakup of the jet (d). Figure modified from Lewis and Schwartz [2004].

2.7.1.1 Sizing convention and size distributions of sea spray aerosol

Upon injection into the lower atmosphere, the behaviour of SSA and their relative importance in a host of different processes is a function of the particle size and composition. To facilitate this description of their behaviour, here we label SSA particles by their equilibrium radius at a reference relative humidity of 80%, r_{80}. Characterizing size using r_{80} provides an unambiguous description of the amount of solute present in the drop that is independent of local conditions, and is a physically relevant size, with 80% relative humidity (RH) being typical over the oceans [Lewis and Schwartz, 2004]. At this relative humidity, SSA particles are almost always present as liquid drops.

The smallest particulate matter ejected from a bursting bubble have radius of order 0.1 micrometers, whilst the largest particles are visible with radii of several millimeters. Small particles ($r_{80} \leq 1$ μm), having a residence times of the order of days, play a vital role in the climate system both directly through the scattering of solar radiation [Haywood et al., 1999], and indirectly by acting as cloud condensation nuclei, and thus affecting cloud albedo [Andreae and Rosenfeld, 2008]. Larger particles ($r_{80} \geq 25$ μm), despite having short residence times of the order of seconds, can affect interfacial fluxes of sensible and latent heat at high wind speeds [Andreas et al., 1995, 2008], and are believed to affect the intensity of tropical cyclones [Andreas and Emanuel, 2001].

Several different size distributions can be formed once particles have been classified into discrete size ranges. If one assumes (wrongly) that the solute composition of all SSA particles, independent of their size, is that of seawater—which is near constant over the oceans—then the size distribution of SSA number concentration constitutes a complete

description of the aerosol [Lewis and Schwartz, 2004]. The number concentration can be obtained by counting the number of SSA particles in a known volume of air in each of the given size ranges, and is usually presented as valid for a given wind speed, or wind speed range. The resulting distribution can be represented as $n(r_{80}) \equiv dN/d\log r_{80}$, where particles are classified into intervals of $\log r_{80}$. This method of representing size distributions is used for two reasons. First, counting the number of particles in different size intervals is usually the first step in formulation any size distribution, regardless of the final representation. Second, the choice of $\log r_{80}$ as the size interval of SSA particles allows the size distribution to be reported over a wide range of sizes, and ensures the size distribution of a quantity has the same units as the quantity itself [Lewis and Schwartz, 2004]. The size distribution most relevant to this study is the size-dependent production flux of SSA (section 2.7.2).

2.7.1.2   Composition and chemical description of sea spray aerosol

Knowledge of the chemical composition of marine aerosols as a function of their size is needed to evaluate their role in the global climate system. Aerosol in the marine environment (in areas remote from continental sources) is to a large degree of marine origin, and not aged continental aerosol [Fitzgerald, 1991]. The size-dependent composition of marine aerosol reflects several factors, including (i) the original composition of the particle injected into, or on formation in, the atmosphere, and (ii) the chemical modification of particles during their residence in the atmosphere. For SSA, this means a concentration that is primarily determined by the chemical nature of the seawater in which they have their origin, and by any subsequent chemical interactions with other aerosol or gases (see O'Dowd and de Leeuw [2007]). Particles found in the marine environment can be highly variable, with complex chemical signatures; a single aerosol particle may consist of one species, or it may be a mixture of several distinct chemical compounds [Saltzman, 2009]. As bulk seawater is largely a sodium chloride / magnesium sulphate brine, large SSA particles (with short atmospheric residence times) share this chemical signature. Smaller particles, with longer residence times, are susceptible to mixing non-sea-salt and organic containing particles, and so will exhibit a much more diverse chemistry.

It is known that organic material (mostly colloids and aggregates exuded by phytoplankton) present at the surface can be incorporated into SSA through the bursting mechanism. In biologically productive waters, sea spray particles (especially those with $r_{80} \leq 1$ μm) can be considerably enriched in these substances. As early as 1948, Woodcock [1948] showed that bubble bursting in areas with high concentrations of plankton (in red tide) could result in 'irritants' being carried into the atmosphere. Blanchard [1963] documented that organic matter can be enriched in sea spray, and Hoffman and Duce [1976] made measurements of the organic content of sea spray in laboratory studies.

Recently, there has been considerable effort to understand in more detail the role that wave breaking, whitecap formation, and bubble bursting plays in the transfer of organic matter from the ocean surface into the atmosphere (e.g., see de Leeuw et al. [2011]; Monahan and Dam [2001]; O'Dowd et al. [2004, 2008]; Vignati et al. [2010]). With use of more sophisticated instrumental methods, quantification of the organic mass fraction of SSA from field measurements [O'Dowd et al., 2004; Yoon et al., 2007] and laboratory studies [Facchini et al., 2008; Fuentes et al., 2010; Keene et al., 2007] has been possible.

2.7.2 Inferring the production flux of sea spray aerosol

To quantify the various roles that SSA plays in the climate system, knowledge of the size-dependent production flux of SSA particles is required. Its numerical representation is the sea spray source function (SSSF) which can be formulated as:

$$f(r_{80}) \equiv \frac{dF(r_{80})}{d\log_{10} r_{80}}, \tag{2.27}$$

where $f(r_{80})$ denotes the number of particles in a given infinitesimal range of the common logarithm of r_{80}, injected into the lower atmosphere per unit area, per unit time. $F(r_{80})$ is the total number flux of particles with size less than r_{80} [de Leeuw et al., 2011]. Given this definition of the production flux, it is clear that this quantity will vary over scales the size of individual breaking waves. To formulate this quantity for use as an input to global climate models for example, the production flux is averaged over areas and times sufficiently large that rapid fluctuations caused by individual breaking waves are smoothed out [de Leeuw et al., 2011]. At this point it is worth

noting the distinction made between an interfacial flux (for which the height is zero), and an effective flux at a given height (typically taken as 10 m above mean sea level). Hereinafter, this distinction will be made through use of appropriate subscripts; F_{int} for an interfacial flux, F_{eff} for an effective flux.

To account for all possible factors capable of influencing the production flux, the expression in equation 2.27 should be extended so that it becomes a function of the driving variables, and not just a function of aerosol radius. Identifying the relative importance of these variables—and then developing new and improved flux parameterisations— requires a complete understanding of the controlling processes [de Leeuw et al., 2011]. One would expect wind speed, as the dominant factor controlling wave generation, to have a significant effect on the production flux and the vast majority of SSSFs are in terms of U_{10}. Other physical parameters that have been considered as possibly more directly linked to SSA production include the wind stress on the surface, τ, and the whitecap fraction, W.
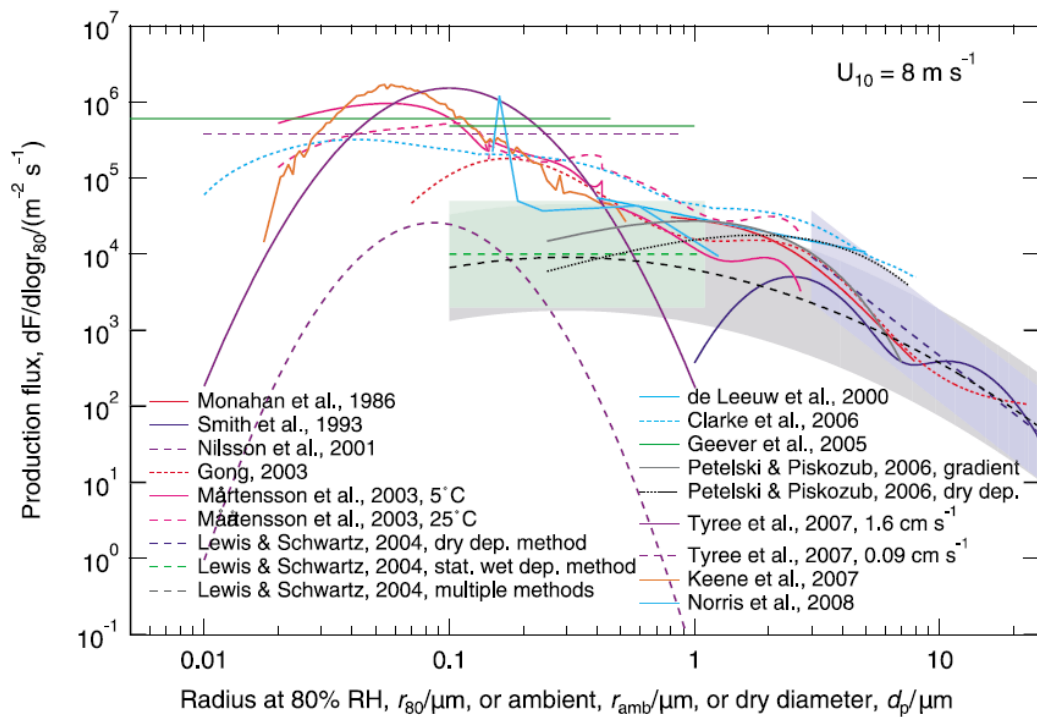
FIGURE 2.11: A selection of parameterisations of the size-dependent SSA production flux from the literature, evaluated for $U_{10} = 8$ m s^{-1}. Also shown are central values (curves) and uncertainty bands (shaded areas) presented in the review of Lewis and Schwartz [2004]; green denote measurements made by investigators using the statistical wet deposition method, blue for all steady state deposition estimates, and grey for an average of all available methods. Figure taken from de Leeuw et al. [2011]

Numerous parameterisations of the SSA source flux have been published in the literature. Figure 2.11 shows a selection of these SSSFs, and illustrates the range and spread of the formulations, evaluated at a wind speed of 8 m s^{-1} which is close to the global average. Various methods can be used to obtain a SSSF and the method used is significant factor in the end result. One must distinguish between the different methods used before we can make a clear comparison between the results. Included in this figure are results from studies using the dry deposition method, statistical wet deposition method, the steady state dry deposition method, as well as those using the whitecap method and eddy-covariance method—the two methods most relevant to this study. Despite these differences, the sizable spread between different SSSFs has a physical basis, namely, a failure to consider any of the several other factors affecting the production flux, for example sea state and wave field variability, atmospheric stability, and sea surface temperature.

2.7.2.1 Eddy-covariance method

Eddy-covariance is the most direct method for measuring turbulent fluxes. However, the technique can be challenging to apply to SSA particles mainly because of low number concentrations resulting in poor counting statistics. Whilst this technique has been widely used to compute gas fluxes, only a handful of studies have attempted measurements of SSA fluxes (de Leeuw et al. [2007]; Geever et al. [2005]; Nilsson et al. [2001]; Norris et al. [2012, 2008]). Many early studies lacked any size resolution and indeed no means of distinguishing SSA particles from other species. Whilst the accuracy and resolution of measurement systems (condensation nuclei counters and scattering spectrometers, for example) has subsequently evolved, the technique is still extremely tricky to get right. However, eddy-covariance remains the most direct method of measuring production flux of SSA over the open ocean.

The eddy-covariance technique aims at resolving the fluctuation in the quantity of interest—in this case the SSA number concentration (N) and the vertical wind velocity (w)—into mean values, $\overline{N}$ and $\overline{w}$, and turbulent fluctuations, N' and w' [Nilsson and Rannik, 2001]. This decomposition allows determination of the net vertical flux due to turbulent diffusion, $\overline{N'w'}$, usually averaged over 20–30 minute periods. The choice of averaging period is a subject of much debate, but should be long enough that

individual gusts or breaking waves do not influence the results, and short enough so that environmental conditions do not change significantly during the period [Lewis and Schwartz, 2004]. Uncertainties in time-averaged flux estimates are due to both the stochastic nature of turbulence [Rannik and Vesala, 1999] and discrete counting of aerosol particles [Fairall, 1984].

The measured $\overline{N'w'}$ (a net of upward and downward fluxes) are actually lower than the source flux F, due to the downward fluxes of SSA particles from both dry deposition and gravitational settling. The relationship is

$$\frac{dF_{\text{eff}}}{d\log r_{80}} = \overline{w'(\frac{dN}{d\log r_{80}})'} + \overline{(\frac{dN}{d\log r_{80}})} \times [v_{\text{dd}}(r_{80}) - v_{\text{grav}}(r_{80})], \qquad (2.28)$$

where the final term on the right hand side denotes the difference between the dry deposition flux and the gravitational flux.

2.7.2.2 The whitecap method

The whitecap method—first described by Blanchard [1963]—is widely used to predict SSA source fluxes. The source function of Monahan et al. [1986] obtained using this approach, and subsequent modified forms (e.g., Gong [2003], and Jaeglé et al. [2011]) are routinely used in global chemical transport models such as GLOMAP ([Spracklen et al., 2005]) and GEOS-Chem ([Gantt et al., 2012]). The interfacial production flux is inferred by scaling an estimate of the production flux per unit area white-cap $dF_{\text{wc}}(r_{80})/d\log r_{80}$ often derived from laboratory measurements, by the whitecap fraction W:

$$\frac{dF_{\text{int}}}{d\log r_{80}} = W \times \frac{dF_{\text{wc}}}{d\log r_{80}}. \qquad (2.29)$$

Traditionally, in the absence of global measurements of W, estimates of W are obtained using a $W(U_{10})$ parameterisation, so that the total flux of particles $dF_{\text{int}}(r_{80})/d\log r_{80}$ is a function of U_{10}, implying that wind speed (alone) determines the magnitude of the SSA source fluxes. The shape of the distribution (i.e., the variation of the source flux with particle size) is dictated by the second term in equation 2.29.

Two methods of generating laboratory whitecaps have been employed. Here we focus on the discrete whitecap method (DWM) (as opposed to the continuous whitecap

method) pioneered by E. C Monahan and colleagues [Monahan et al., 1982, 1986]. In these experiments, the increase in the number concentration of SSA particles per unit logarithmic interval of r_{80}, $\Delta n(r_{80})$, from a single laboratory breaking wave with initial white area A_{wc} enclosed in a tank of air volume V was measured. Aerosols were counted and sized using a particle spectrometer. From this information, the size-resolved distribution of total number of aerosol particles produced by bursting bubbles during the entire lifetime (visible and post-visible stages) of a simulated whitecap is

$$\frac{dE_{\mathrm{wc}}}{d\log r_{80}} = \frac{\Delta n(r_{80})V}{A_{wc}}. \tag{2.30}$$

To determine the rate of production of SSA particles in the open ocean, one needs to extrapolate these laboratory findings. To do so, the production flux per unit white area $dE_{\mathrm{wc}}/d\log r_{80}$ can be combined with W/τ_{decay} where τ_{decay} is the characteristic e-folding time of the simulated whitecap with a value of 3.53 s from their experiments:

$$\frac{dF_{\mathrm{int}}}{d\log r_{80}} = \frac{W}{\tau_{\mathrm{decay}}} \times \frac{dE_{\mathrm{wc}}}{d\log r_{80}}. \tag{2.31}$$

A key assumption of the DWM was that under steady state conditions, the rate of decay of whitecap area per unit area sea surface is equal to the rate of whitecap area formation per unit sea surface (see Monahan [1971]). It is also assumed that (i) all whitecaps, regardless of their size, decay exponentially with the same decay time, (ii) the whitecap timescale should only consider the decay time, and (iii) that the shape and magnitude of $dE_{\mathrm{wc}}/d\log r_{80}$ is typically constant; Monahan et al. [1986] recognized that in reality this term will vary with the characteristic of the breaking wave producing the whitecap [Callaghan, 2013]. The production flux per unit white area will also vary with the properties of the water (e.g., salinity, temperature, and surfactant concentration), which will affect both the bubble population and the resulting aerosol size and composition on bursting (see for example the laboratory studies of Keene et al. [2007]; Mårtensson et al. [2003]; Modini et al. [2013]; Zábori et al. [2012]).

2.8 Whitecaps and air-sea gas exchange

Air-sea gas exchange—the movement of gases both from the atmosphere into the oceans and from the oceans into the atmosphere—plays an important role in the biogeochemical cycles, atmospheric chemistry, marine productivity, climate, and human health. In particular, the flux of gases such as oxygen, dimethylsulphide, carbon dioxide, and volatile iodocarbons (VICs) across the interface is of importance. These exchanges are quantified by the air-sea flux which is driven by the concentration gradient between the two phases and a kinetic (or rate) term, known as the gas transfer coefficient (or velocity).

In addition to the direct diffusion of gases across the air-sea interface and transfer driven by microbreaking, the breaking of air-entraining surface waves plays a role in the air-water exchange of gases (e.g., Keeling [1993]; Merlivat and Memery [1983]; Monahan and Spillane [1984]; Woolf [1997]). The breaking event itself generates turbulence which generally enhances transfer at the surface [Monahan and Spillane, 1984; Woolf, 1995], whilst the injection and surfacing of bubbles disrupts the surface microlayer and so reduces or removes the barrier to air-sea exchange. However, for poorly soluble gases—such as CO_2—the greatest influence is from bubble-mediated transfer, which is defined as the net transfer of gas across the surface of bubbles while they are submerged and advected by motions in the upper oceans [Woolf and Thorpe, 1991]. Though these mechanisms are physically different, and are each influenced by different physical and environmental forcings, it is accepted that combined influence of wave breaking and bubbles on air-sea gas exchange becomes increasingly important at high wind speeds [Wanninkhof et al., 2009]. The evolution of a single bubble after entrainment is shown in Figure 2.12; black arrows indicate interfacial and bubble-mediated exchange.

The contribution of bubble-mediated exchange to the total transfer velocity for a gas depends on its solubility, as shown in Figure 2.13. The contribution is larger for weakly soluble gases such as CO_2; in the figure, the grey shaded region represents additional, bubble-mediated transfer for CO_2. Bubble-mediated exchange for more soluble gases, such as dimethyl sulphide (DMS), is smaller, because bubbles quickly come into equilibrium with the bulk seawater so that a bubble takes place in the exchange only for a fraction of its lifetime. In this case, direct transfer across the surface, via molecular and turbulent diffusion, is dominant.
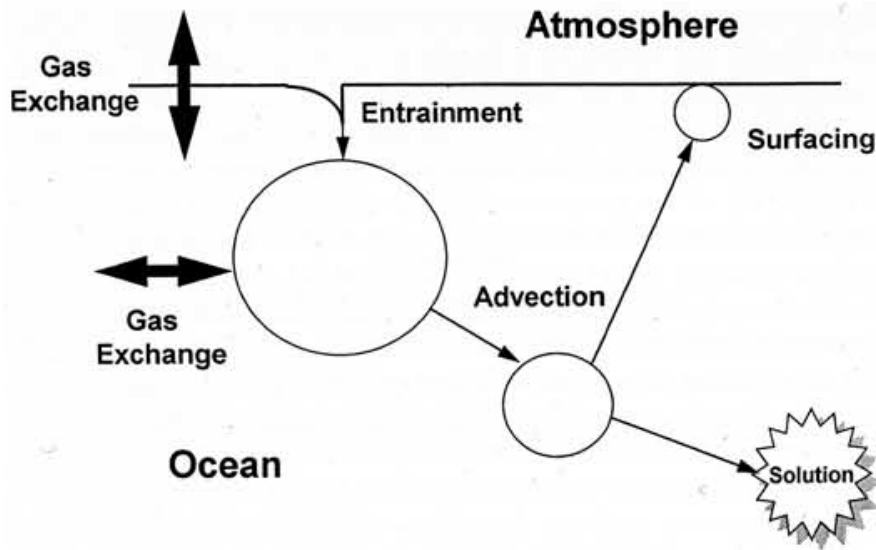
FIGURE 2.12: Schematic illustrating the different mechanisms of air-sea gas transfer and bubble evolution following entrainment into the upper ocean. (Figure taken from Woolf [1997])

2.8.1 Modelling bubble-mediated exchange

A common starting point in the modeling of bubble-mediated gas exchange is to consider the total waterside transfer velocity K_w to be a linear sum of two contributions [Woolf, 2005]—the non-breaking fraction (or 'direct transfer') with transfer velocity K_d and the bubble-mediated fraction with transfer velocity K_b,

$$K_w = K_d + K_b, \tag{2.32}$$

based on the fact that these two processes occur in parallel. Though the dependence of K_d on its various forcings is not yet fully understood, it is generally accepted that direct transfer will scale with u_* (as wind stress is the primary source of turbulence and roughness at the ocean surface), but the mean square slope $\langle s^2 \rangle$ has also shown good agreement with gas transfer rates [Jähne et al., 1987]. As for bubbled-mediated transfer, Woolf [1997] proposed a model in which K_b is proportional to the whitecap fraction W i.e.,

$$K_b = aW, \tag{2.33}$$
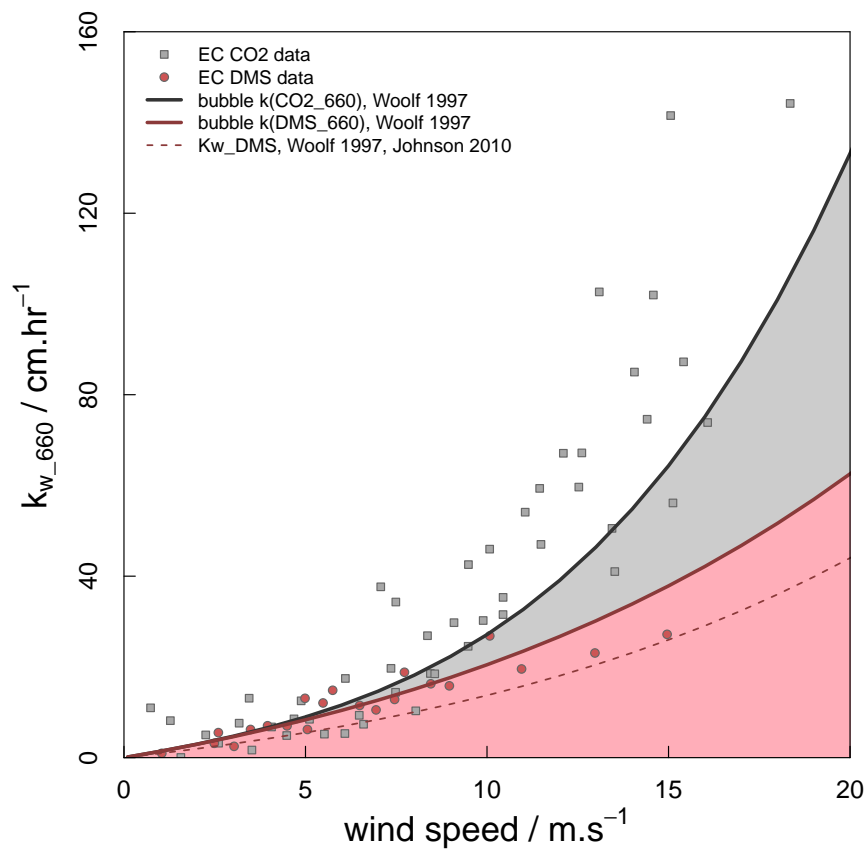
FIGURE 2.13: The magnitude of the bubble effect on the normalised (Schmidt number of 660) transfer velocity for the relatively soluble DMS compared to less soluble CO_2. Pink dots show eddy covariance estimates of the DMS transfer velocity, and grey sqaures those for CO_2. Also shown are estimated transfer velocities using the scheme of Woolf [1997] for CO_2 (solid black line) and DMS (dark pink solid line). The pink shaded region represents the diffusive transfer, which is approximately equal for the two gases. The grey shaded area represents additional bubble-mediated transfer for CO_2. Figure by M.T. Johnson, shared under creative commons license at http://dx.doi.org/10.6084/m9.figshare.92419.

where a is a coefficient which depends on the solubility of the gas. Therefore, K_w may be described by a hybrid model:

$$K_w = K_d(u_* \text{ or } \langle s^2 \rangle) + K_b(W),\qquad(2.34)$$

following [Woolf, 1997]. Note that here we acknowledge (i) that both mechanisms depend on the Schmidt number, Sc; (ii) that bubble-mediated exchange further depends on the solubility of the gas, and (iii) that part of the contribution to to direct transfer may actually be related to W. An expression for K_b in terms of physiochemical variables remains elusive, despite the efforts of modelling studies (Memery and Merlivat

[1985]; Woolf [2005]; Woolf and Thorpe [1991]) and laboratory measurements (Asher et al. [1996]; Woolf et al. [2007]). This is largely due to the complicated dependence of K_b on the solubility and molecular diffusion constant of the gas.

2.8.2   Quantifying role of whitecaps in gas-exchange

Both laboratory and field studies have found both correlation between gas transfer and the areal extent of breaking waves, and a large enhancement of gas fluxes due to breaking waves and bubble entrainment [Asher et al., 1996; McNeil and D'Asaro, 2007]. However, direct quantification of the role of breaking waves and bubble production is a tricky task, as it is almost impossible to separate the different contributions to gas-exchange in field measurements. As summarised by Wanninkhof et al. [2009]: 'The role of breaking waves at high wind speeds is recognized as important, but as yet there remains no reliable way to accurately quantify the effect of breaking waves on gas exchange.'

It has been argued that the role of breaking waves and bubbles should manifest as non-linearity in the total gas transfer velocity K. If K_d is assumed constant with U_{10}, the departure from a linear dependence is likely to be largely a result of bubble-mediated exchange [Woolf, 2005]. To validate this claim, one would have to rule out a possible non-linear enhancement of K_w due to microscale breaking and/or a homogeneous increase in upper ocean turbulence associated with wave breaking.

Field data has generally been used to explore the dependence of K_w on breaking waves through inclusion of this dependence in a wind speed parameterisation of the total gas transfer velocity. A functional form for K_w was obtained by [McGillis et al., 2001]:

$$K_w = a + bU_{10}^3. \tag{2.35}$$

Several $K_w(U_{10})$ relationships of this form have been published in the literature (e.g., McGillis et al. [2001, 2004]; Wanninkhof and McGillis [1999]), each with their own wind speed dependence ranging from linear (e.g., Liss and Merlivat [1986]) to cubic (e.g., Wanninkhof and McGillis [1999]). The advantage of these formulations is that K_w can be estimated using only U_{10} fields. Thus, they have been widely used to calculate regional and global-scale fluxes. However, the resulting estimates of K_w are sensitive to

the wind speed data used and applying these relationships over temporal and spatial scales with varying winds can lead to incorrect application of the relationships and discrepancies in comparisons of different flux estimates [Wanninkhof et al., 2009].

In the same way that wind speed alone is not expected to account for variability in W on a global scale, it is recognised that various other forcings need to be considered to accurately predict air-sea gas fluxes through their influence on both interfacial and bubble-mediated transfer. These include the wave field and wave energy dissipation, sea surface temperature, buoyancy fluxes, surfactants, fetch, and rain, among others [Wanninkhof et al., 2009].

Based on the large spread in experimental estimates and different wind speed only parameterisations of the transfer velocity for poorly soluble gases, Woolf [2005] proposed a sea state dependent model of gas transfer building on the hybrid model (equation 2.32) with $K_b \sim W$. To account for the sea state dependence of the whitecap fraction, W is parameterised in terms of the roughness Reynolds number R_{Hw} (equation 2.26). Thus, model predicts transfer velocities that increase not only with wind speed, but with fetch, through the dependence of R_{Hw} on H_s; at a given wind speed, H_s is larger for more developed seas, and so too therefore are W and K_{w}.

Whether W is implicitly or explicitly part of a transfer velocity model, without direct estimates one must rely on parameterisation of W. The use of direct measurements of W that can capture at least some of these influences, rather than simple parameterisations, is likely to improve the prediction of air-sea gas fluxes on regional and global scales.

Chapter 3

Data Sources and Methodology

3.1 Satellite-based estimates of whitecap fraction

3.1.1 Whitecaps and ocean surface remote sensing

It has been recognized for some time that the presence of whitecaps affects the electromagnetic (EM) signature of the ocean surface in various portions of the electromagnetic spectrum (section 2.2.2.2). This has a direct impact on remote sensing of the ocean surface [Anguelova et al., 2009b], for example in the use of passive microwave radiometers to obtain the sea surface wind vector [Bettenhausen et al., 2006] and sea surface salinity [Camps et al., 2005]. Consideration of whitecaps is also required in optical ocean color retrievals due to the masking of water-leaving radiance by foam patches [Gordon and Wang, 1994]. In such applications, forward models to correct for the effects of foam can be implemented.

Here, our interest is restricted to passive remote sensing of the ocean surface. Quantification of the influence of whitecaps on passive microwave measurements can be achieved by combining a surface emissivity model (e.g., Nordberg et al. [1971]; Smith [1988]) with satellite measurements of brightness temperature T_B (e.g., as in the work of Pandey and Kakar [1982] and Wentz [1983]). Such an approach enables one to quantify the influence—under given meteorological conditions—of whitecaps on the satellite signature of a large sea-surface area [Monahan and O'Muircheartaigh, 1986]. A more comprehensive approach to correcting for the influence of whitecaps involves

the use of a physically-based model. It was this work, within the framework of the WindSat mission [Gaiser et al., 2004], which led to the Naval Research Laboratory (NRL) developing a method to obtain whitecap fraction estimates from satellite-based observations.

At the same time, increasing interest in the role that whitecaps play in air-sea interaction processes prompted work to more accurately parameterise whitecap fraction and its variability. To capture this variability, W needs to be measured globally and throughout the year, something not achievable with in situ photographic measurements. With the advent of new satellite technologies over the past few decades, it is now possible to estimate W on a global scale using routine satellite measurements.

3.1.2 Passive microwave remote sensing of whitecaps

Microwave radiometry is a well developed passive remote sensing technique (as opposed to active or radar remote sensing) that uses the natural emissivity of the ocean surface in its various states—smooth, roughened by small and large scale waves, and covered with sea foam [Ulaby et al., 1981, chap. 4]. Use of microwave frequencies is preferential because atmospheric interference can be more easily corrected for in this region of the spectrum [Gordon and Wang, 1994]. Detection of whitecaps by space-borne remote sensors is through the microwave radiation emanating from the surface foam layer. The depth of the layer contributing to the microwave signature varies with the frequency detected by the radiometer, ranging from less than a millimeter at 37 GHz to several centimeters at 6 GHz. This penetration depth is dictated by the foam layer structure and the resulting dielectric properties of the bubble layer. It is worth noting that satellite retrieval of whitecapping using passive microwave radiometry does not require resolving individual whitecaps which have a characteristic length scale $\mathcal{O}(10$ m$)$. As Anguelova and Webster [2006] state: '...what is of interest is how much the average emission of a given ocean area changes with whitecaps appearance and how well these changes can be retrieved from measured data.'

3.1.3   The $W(T_B)$ algorithm

3.1.3.1   Physical concept

The brightness temperature of a partially foam covered surface may be decomposed into foam-free and foam-covered regions, following the model of Stogryn [1972]. The composite surface emissivity e, is just the composite of two contributions; the rough sea emissivity, e_r, in areas free of whitecaps $(1 - W)$, and the foam emissivity e_f, in the remaining foam-covered regions, W;

$$e = e_r(1 - W) + e_f W, \tag{3.1}$$

After simple rearrangement, W can be calculated from

$$W = \frac{e - e_r}{e_f - e_r}. \tag{3.2}$$

Although this model appears simple, the development of an inversion algorithm to obtain W estimates from remotely sensed data is complex. In equation 3.2, e is obtained from satellite radiometer measured T_B with appropriate atmospheric correction. Both e_r and e_f are computed using analytical or empirical models. The rough sea emissivity, e_r, is computed using a 'two-scale' emissivity model [Johnson, 2006; Yueh, 1997], which accounts for changes of emissivity due to Bragg scattering from short gravity and capillary waves. This emissivity should be completely free of the effects of foam and so purely a result of changes due to roughness. The model is tuned so that the output of the two-scale model represents e_r only. The foam emissivity, e_f, can be obtained using analytical or empirical models (discussed in the following sections).

3.1.3.2   Initial implementation

A feasibility study by Anguelova and Webster [2006] demonstrated a method of estimating W from routine satellite measurements of T_B at 19 GHz, horizontal polarization. This initial algorithm used T_B observations from the Special Sensor Microwave Imager (SSMI/I) [Wentz, 1997], a radiometer flown on satellite platforms F8 to F17 of the United States Department of Defense since 1987 and operating at four frequencies

between 19 GHz and 85 GHz. The algorithm for estimating W combines satellite T_B observations with models for the rough sea surface and foam-covered areas (whitecaps). In addition, an atmospheric model is used to remove the influence of the atmosphere from the satellite measured top-of-atmosphere T_B, in order to obtain the changes in T_B at the ocean surface; this is usually termed the atmospheric correction. Wind speed U_{10}, wind direction U_{dir}, SST at the ocean surface, and atmospheric variables such as water vapour (V) and cloud liquid water (L) are necessary as input to the atmospheric, roughness, or foam models. In this initial implementation, the foam emissivity was obtained with the Fresnel formula for foam reflectivity using foam permittivity with a constant void fraction. Though various models and many variables are involved in the algorithm estimating W, for simplicity, the computational procedure as a whole will be denoted the $W(T_B)$ algorithm.

3.1.3.3 Development of the $W(T_B)$ algorithm: The 'WindSat version'

This initial implementation of the $W(T_B)$ algorithm has recently been improved in several respects [Anguelova et al., 2009a]. Use of independent data sets in the $W(T_B)$ algorithm has been possible due to newly available T_B observations since 2003—in addition to those of SSM/I—from the microwave radiometric sensor WindSat (Figure 3.1), onboard the Coriolis satellite [Gaiser et al., 2004]. WindSat operates at five frequencies, between 6 GHz to 37 GHz, thus providing more T_B data suitable for remote sensing of whitecaps than SSM/I [Anguelova and Gaiser, 2011]. The Coriolis satellite completes 14 orbits per day, with ascending (northbound Equator crossing) and descending (southbound Equator crossing) passes at local times of approximately 1800 and 0600, respectively. There are 80 pixels within the WindSat swath with an approximate spacing of 12.5 km across the swath and along the spacecraft track [Bettenhausen et al., 2006]. With the designed sampling procedures and data processing at the lowest level, each pixel within the WindSat swath represents a T_B (or W) value averaged over an area of 50 km × 71 km. Each W value resulting from such an intrinsic spatial averaging of satellite instantaneous samples is analogous to the temporal averaging required to produce stable W values from instantaneous photographic data (section 2.4.1). WindSat T_B data at higher swath resolutions (i.e., pixel value averaged over an area of 35 km × 53 km or 25 km × 35 km) are also available, but here W

estimates at the low resolution are used because the increased computational expense
of using a lower resolution product are not counter-balanced by gains from their use.

FIGURE 3.1: Photograph of the WindSat payload (taken from http://www.nrl.navy.
mil/WindSat/Description.php).

Use of WindSat T_B data in the $W(T_B)$ algorithm allows independent use of SSM/I
data (V and L) for the atmospheric correction. In addition, more physically robust
models for rough and foam-covered surfaces are now employed [Anguelova and Gaiser,
2013; Bettenhausen et al., 2006; Johnson, 2006], and the input variables U_{10}, U_{dir},
and SST to the atmospheric, roughness, and foam models in the $W(T_B)$ algorithm
are also compiled from independent sources. This development has likely reduced
self-correlations between different input variables within the algorithm.

The updated computational procedure for obtaining satellite W is shown in Figure 3.2,
with 'modelling' procedures coloured green and 'measurement' procedures coloured
blue. Model or satellite input data are shown in white. Note that this chart gives
a general concept for the $W(T_B)$ algorithm, but specific implementations may dif-
fer. Ocean surface brightness temperature $T_B(\text{WS})$ is obtained from WindSat top-of-
atmosphere T_B measurements by solving a radiative transfer equation (which includes
an atmospheric correction stage with use of SSM/I data for V and L). The WindSat
forward model is used to obtain $T_B(2s)$, the ocean surface brightness temperature due
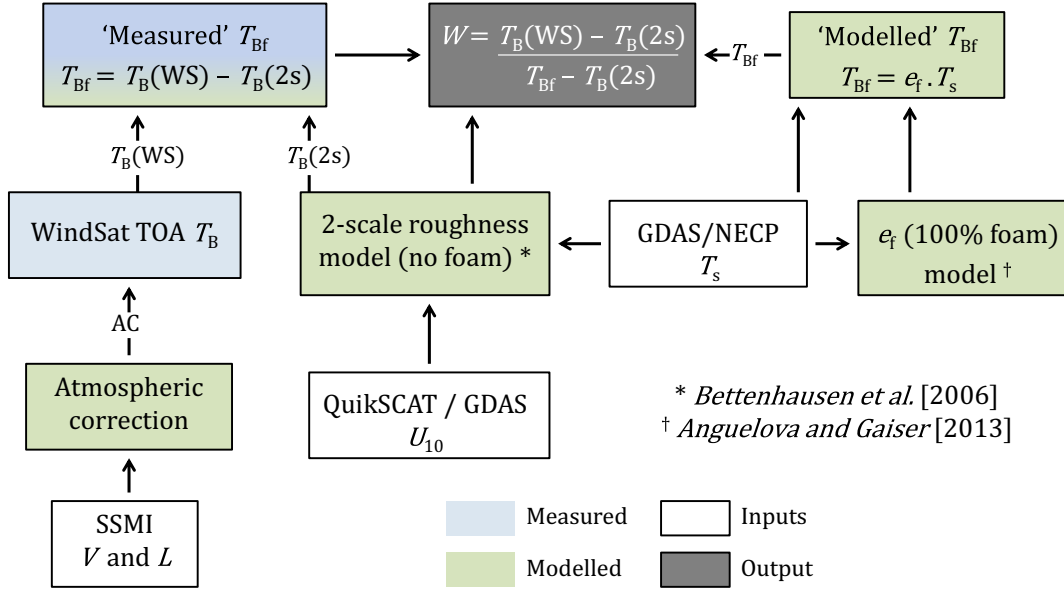
FIGURE 3.2: Flow-chart illustrating measurement and model input to the retrieval
algorithm for computation of whitecap fraction.

to rough surface only (i.e., without including foam effects). Taking the difference be-
tween $T_B(\mathrm{WS})$ and $T_B(\mathrm{2s})$, one obtains 'measured' T_{Bf}; this differencing minimizes the
uncertainty due to atmospheric correction.

The brightness temperature due to foam is obtained as $T_{\mathrm{Bf}} = e_f.T_s$, where T_s is
obtained from model output and e_f is the foam emissivity; this quantity is obtained
from a physically-based radiative transfer model [Anguelova and Gaiser, 2013] and
corresponds to the emissivity of an area 100% covered in foam. Referring back to
equation 3.2 we now have all the emissivity terms, though cast in terms of brightness
temperature rather than emissivities:

$$W = \frac{T_B(\mathrm{WS}) - T_B(\mathrm{2s})}{T_{\mathrm{Bf}} - T_B(\mathrm{2s})}, \qquad (3.3)$$

which is equivalent to equation 3.2.

3.1.3.4 Current state of the project

The data used in this study is obtained by running v.1.96 of the $W(T_B)$ algorithm, which was finalised in 2007. The improvements to the algorithm described above have reduced the somewhat noticeable differences between trends in the satellite and photographic measurements (Figure 3.3). The new WindSat implementation gives a more realistic behaviour than the initial implementation described in Anguelova and Webster [2006], when comparing to a $W(U_{10})$ relation from photographic data (that of Monahan and O'Muircheartaigh [1980]), although the data still diverges at both high and low wind speeds.
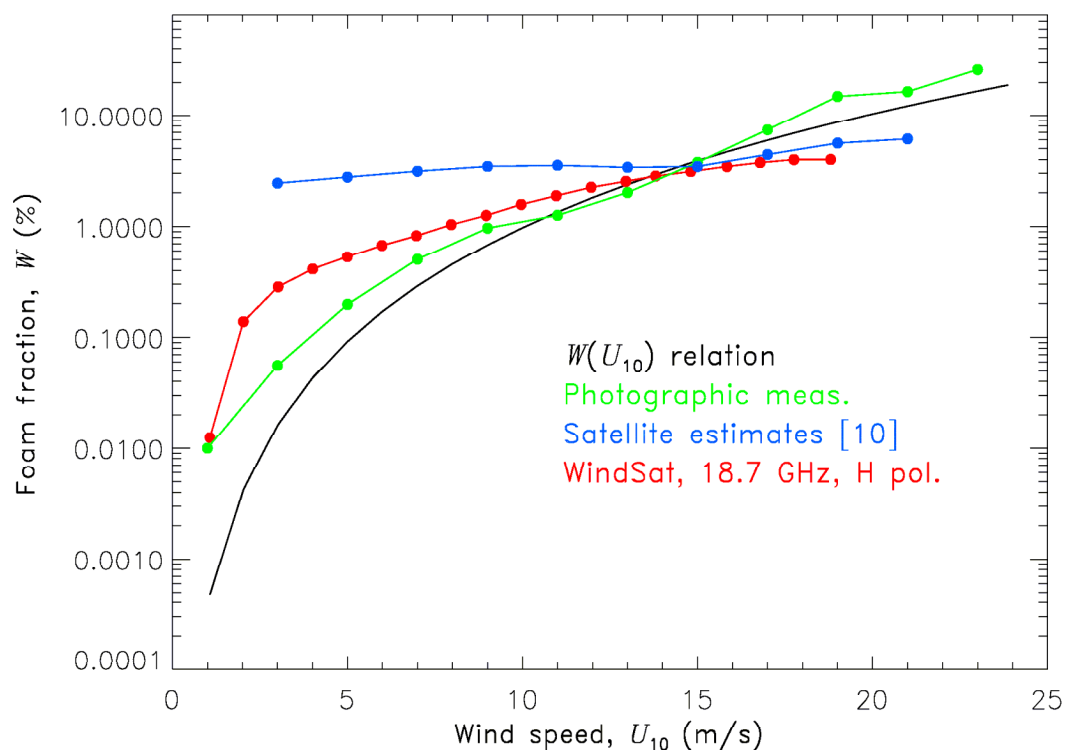
FIGURE 3.3: W as a function of U_{10} highlighting the difference in behaviour for the updated retrieval algorithm (red curve) compared with an earlier version of the retrieval algorithm (blue curve, [Anguelova and Webster, 2006]), and how these compare with a fit to photographic data (yellow curve), and the Monahan and O'Muircheartaigh [1980] $W(U_{10})$ relationship, (equation 2.20, black curve). Figure taken from Anguelova et al. [2006]).

Presently, development of the $W(T_B)$ algorithm continues at NRL. W estimates were initially obtained for 2006 and various months of 2007 and 2008 (prompted by work on

validating satellite estimates with in situ photographic data from ships). The process-
ing of data for subsequent years has stalled due to both the failure of QuikSCAT in
November 2009, and processing changes associate with input data from SSM/I. These
developments could not easily be accommodated with the current version of the algo-
rithm. Further, these changes prompted more radical changes to the forward model,
which has been in constant development at NRL since 2007. As of March 2013, further
work to improve the $W(T_B)$ algorithm has been funded; the revised SSM/I input data
will be incorporated, a suitable source for wind vector data will be identified, and the
revised forward model implemented.

3.2   Compiling a whitecap database

Whitecap fraction estimates were obtained by running the $W(T_B)$ algorithm (v1.96)
for all five WindSat frequencies and both horizontal and vertical polarizations at a
swath resolution of 50 km $\times$ 71 km. All available WindSat orbits for 2006 with both
ascending and descending passes were used. A subset of this vast pool of raw swath data
for whitecap fraction was then used to compile a more tractable database of satellite-
based W estimates, accompanied by six meteorological and oceanographic variables;
hereafter we refer to this database as the 'W database'. The compilation of the W
database involved three main activities: (i) devising a criterion to choose a subset of
all W data; (ii) gridding the W values from swath resolution into regular global maps;
and (iii) matching additional variables to the gridded W values.

3.2.1 W estimates

The W database includes estimates of W at two frequencies—10 GHz and 37 GHz,
horizontal polarisation; the horizontal polarisation radiometric measurements are more
sensitive to changes in wind speed and breaking events than vertical polarisation. The
choice to work with only these two frequencies, instead of all five frequencies available
from WindSat, is based on two considerations. First, the $W(T_B)$ algorithm for satellite-
based W estimates is still a work in progress. This W database is an intermediate stage
in the $W(T_B)$ algorithm development which can be used to evaluate the utility of the
W data, and identify how best to improve the $W(T_B)$ algorithm. On a related note,

it was deemed that the overall quality of calibration was lower for measurements at some frequencies (including those from the 6 GHz channel). Second, recent work on the electromagnetic properties of sea foam, including the penetration depth of different microwave frequencies trough sea foam [Anguelova and Gaiser, 2011], shows that each radiometric frequency has a different sensitivity to different stages of the whitecap. While all WindSat frequencies would react to foam thicker than 1 cm, as the frequency decreases from 37 GHz to 6 GHz, its sensitivity to thinner foam decreases. The lower limit of detectable foam thickness for 37 GHz is around 1 mm; for 10 GHz it is 4 mm; and for 6 GHz it is around 1 cm. Because thick foam is associated with the active whitecaps while thin foam characterizes residual whitecaps [Anguelova and Gaiser, 2011], we expect that W estimates at 10 GHz will predominantly be representative of active, stage A (section 2.3.1), whitecaps and to some extent residual foam (stage B) when it is thicker, e.g., at higher wind speeds. At 37 GHz, W estimates will represent total whitecap cover (stages A and B). Therefore, the frequency dependence of whitecap fraction offered by W_{10} and W_{37} provides a way to at least roughly differentiate between active and residual whitecaps and infer how the various relationships are affected by the whitecap lifetime stages.
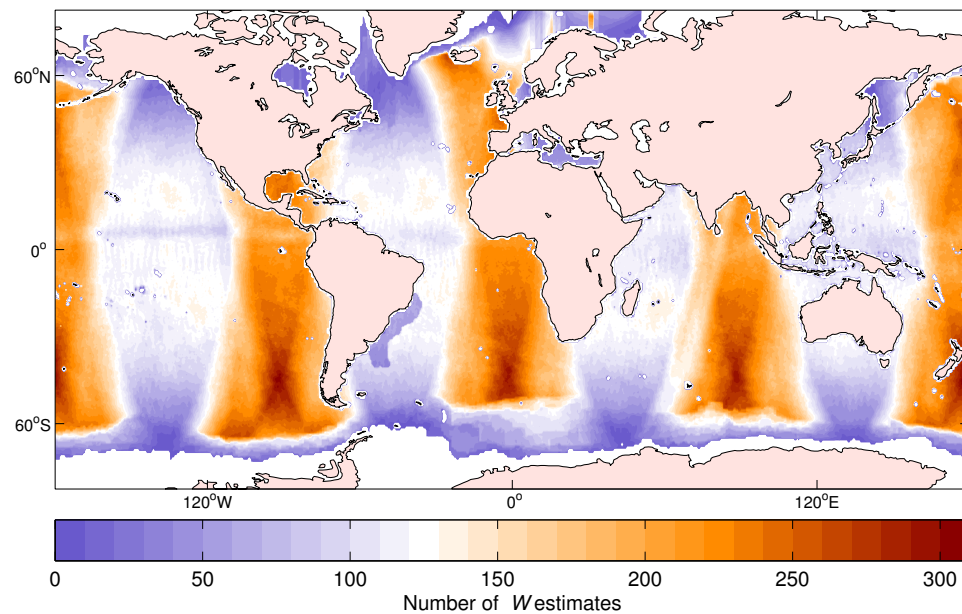
FIGURE 3.4: Cell-by-cell number of 'daily' W estimates obtained for 2006.

The swath W values at 10 GHz and 37 GHz were gridded onto a 0.5º × 0.5º grid. For each grid cell, an average value of all swath W samples falling within the cell is calculated. These cell-averages for each frequency, hereafter referred to as W_{10} and

W_{37}, represent a mean estimate of whitecap fraction for the cell at the local time of the satellite overpass. The total number of these individual (i.e., daily) W estimates over a given time period varies from cell to cell, due to the availability of data used at any stage of the $W(T_B)$ algorithm; the resulting somewhat uneven distribution of W estimates for the whole of 2006 is show in Figure 3.4). The area south-east of Brazil with a noticeably lower count is an area where microwave measurements are affected by reflected X-band emissions from geostationary communication satellites.

Figures 3.5a and 3.5b present daily global maps of W_{10} and W_{37} along both ascending and descending passes for 1 October, 2006. The spatial coverage provided by WindSat's orbits can be seen as can the gaps of missing data within a single swath which are the result of the patchy spatial matching between WindSat and QuikSCAT (section 3.2.2). Complete swaths exemplify the good spatial coverage resulting from match-ups with GDAS data. Figures 3.5c and 3.5d show monthly maps for October 2006.
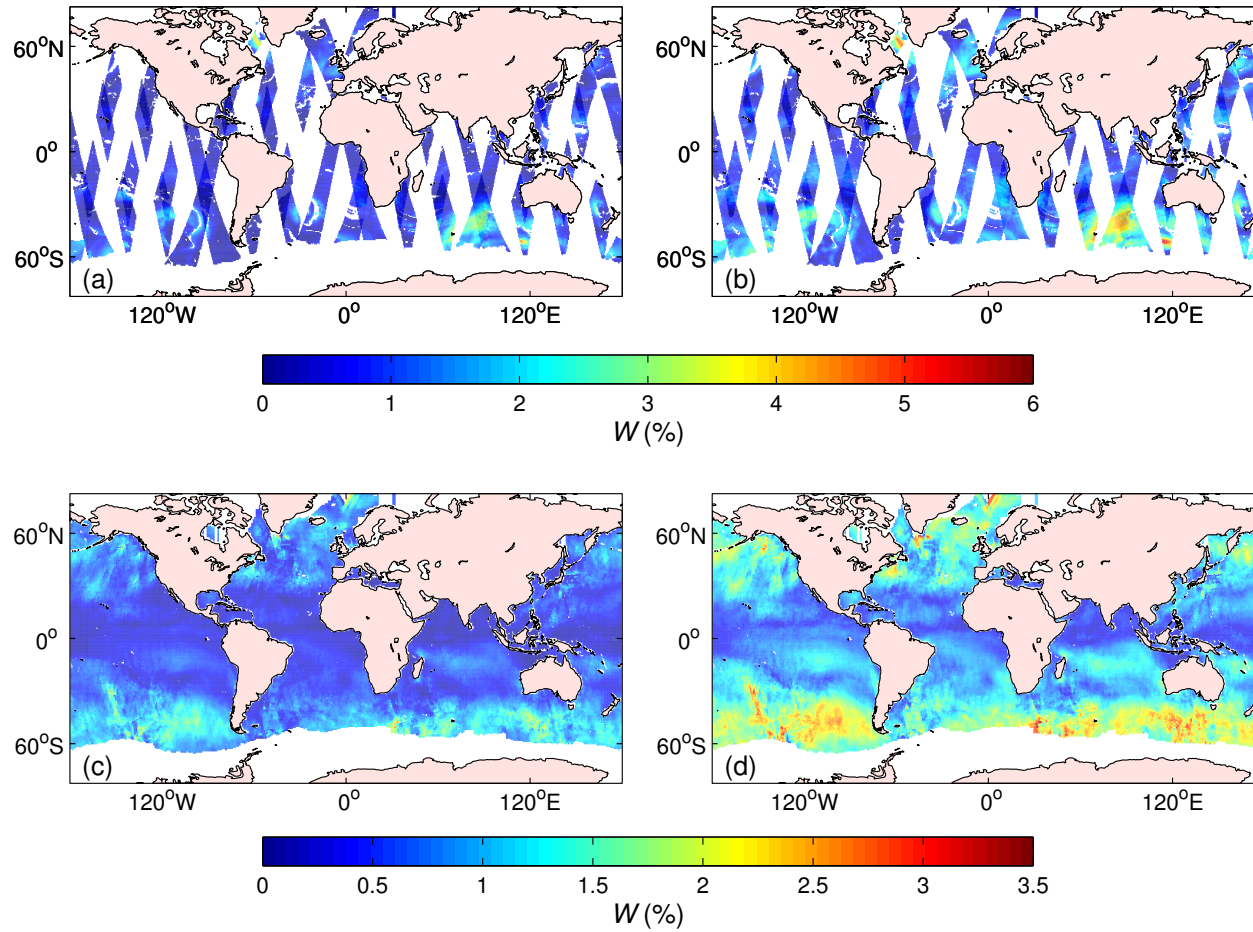
FIGURE 3.5: A daily map for 1st October 2006 of (a) W_{10} and (b) W_{37}, and a monthly composite map for October 2006 of (c) W_{10} GHz, and (d) W_{37}.

3.2.1.1   Error on W estimates

Explicit calculation of the error on individual W estimates is not currently available
due to the complex multi-variable nature of the $W(T_B)$ algorithm. However, where
applicable, we have used the statistics obtained during the gridding process to calculate
the root mean-square (rms) error, standard deviation σ_W, and count (the number of
individual swath samples averaged to obtain the daily mean W for the cell). These
statistics are subsequently used to screen for unreliable W estimates resulting from,
for example, a low count in a particular grid cell, or an exceptionally large spatial
variation between individual swath samples. In Figure 3.6 we show histograms (top
panels) of the relative standard deviation (RSD = σ_W/W) and associated cumulative
frequency histograms (bottom panels) for W_{10} and W_{37} estimates covering 2006. It
can be seen that the RSD of W_{10} and W_{37} estimates are similar, but a slightly larger
fraction of W_{37} estimates have a low RSD value (for example, $\sim$95% of W_{37} estimates
have $\sigma_W/W < 0.2$, whereas this value is $\sim$87% for W_{10}).
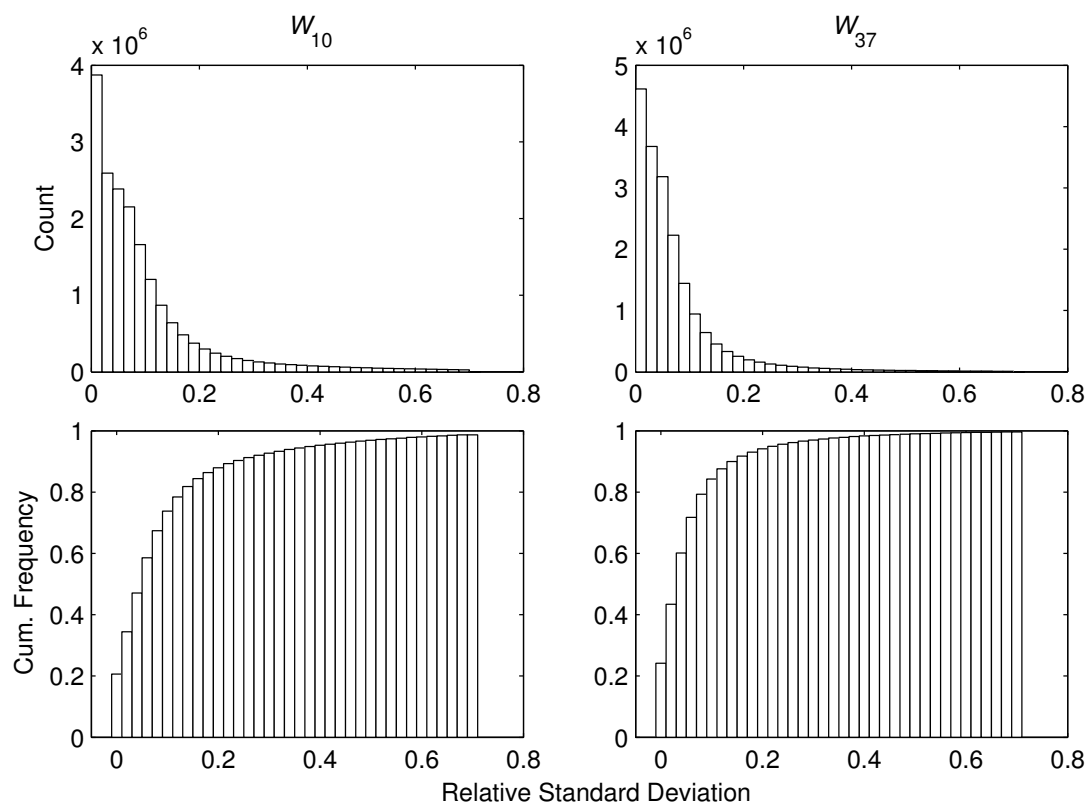
FIGURE 3.6: (Top) Histograms of relative standard deviation and (bottom) cumula-
tive frequency histograms for (left panels) W_{10} and (right panels) W_{37}.

3.2.2   Basic additional variables

Whitecap fraction data at swath resolution are matched in time and space with six meteorological and oceanographic variables; wind speed U_{10}, wind direction U_{dir}, SST, air temperature T_a, significant wave height H_s (defined as $4\sqrt{E}$, where E is total wave energy), and peak wave period T_p (defined as the period corresponding to the highest peak in the one dimensional frequency spectrum of the wave field). These basic additional variables are taken from different sources.

Wind vector (U_{10} and U_{dir}) is taken from the SeaWinds microwave scatterometer onboard the QuikSCAT satellite (http://winds.jpl.nasa.gov/missions/quikscat). The SeaWinds scatterometer measures backscattered pulses from the earth's surface; over the ocean the returned signal is related to the ocean surface roughness and hence the near-surface wind speed and direction. The matching criterion between WindSat and SeaWinds measurements is that the data were observed within 25 km and 60 minutes. The resulting spatial match is patchy (section 3.1.4) because the ascending and descending passes of the Coriolis and QuikSCAT satellites are out of phase.

When a SeaWinds matchup is not available, U_{10} and U_{dir} from the model output (every 6 hours) of the Global Data Assimilation System (GDAS) of the National Centers for Environmental Prediction (NCEP) is used. GDAS is the system used by NCEPs global forecast model to place myriad observations (including those of QuikSCAT) into a gridded model space for the purpose of initializing weather forecasts with observed data (http://www.ncdc.noaa.gov/model-data/global-data-assimilation-system-gdas). We use GDAS outputs closest in time and spatially interpolated to the location of the Wind-Sat data; this results in good spatial coverage along the WindSat swath. Data for SST and T_a (at 2 m above the surface) are also from GDAS. We follow Bettenhausen et al. [2006] in using different sources for the wind vector because the $W(T_B)$ algorithm uses the same roughness and atmospheric models employed by the WindSat retrieval procedure.

Data for H_s and T_p are from NCEPs Wave Watch III (WW3) model. We have used the historical archive of wave hindcast results produced with version 2.22 of WW3 at 3 hour intervals (http://polar.ncep.noaa.gov/waves/implementations.shtml). The input variables for WW3 are from GDAS. The WW3 model also gives peak wave direction, but it is not currently included in the database. The temporal and spatial matching

criteria for WindSat and WW3 data are as those for GDAS. Table 1 summarizes information for these variables, including their spatial resolutions, use, and access.

All these variables, matched up initially to WindSat data at swath resolution, are gridded in the same way as the W estimates (as described in section 3.2). Mean daily values, as well as statistics (root-mean-square error, standard deviation, and count), are obtained for each variable for each grid cell. The distribution of data (covering 2006) for these variables are shown in Figures 3.7 and 3.7.
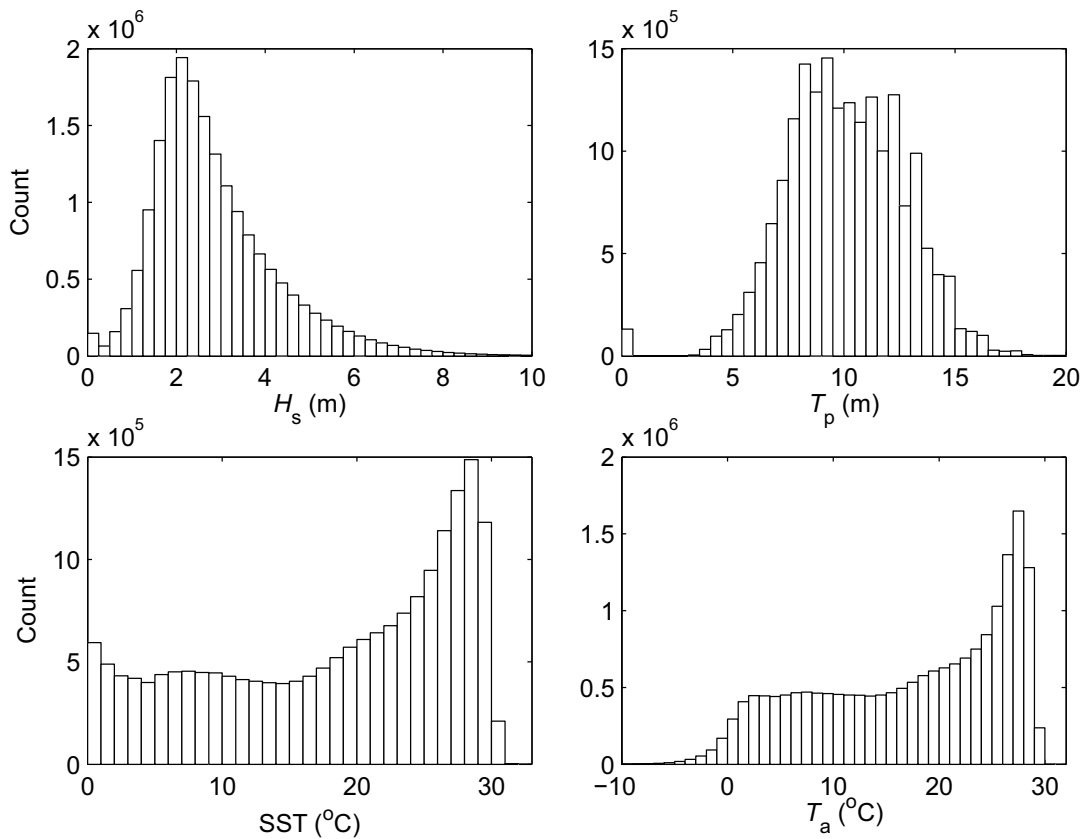
FIGURE 3.7: Histograms showing the distribution of database H_s, T_p, SST, and T_a entries covering 2006

3.2.2.1   Some notes on database wind vector data

As described above, database U_{10} estimates are obtained from either QuikSCAT or GDAS. A distinction needs to be made between database wind estimates and the actual (or true) wind speed, as would be measured in situ. True wind speeds are stability-dependent i.e., the atmospheric stratification alters the wind profile. Both QuikSCAT and GDAS provide estimates of the equivalent neutral wind at a 10-m

TABLE 3.1: Sources of database variables, with resolution and data access

Model/Sensor (Satellite) Access	Variable (units)	Grid resolution	Variable Use
Windsat (Coriolis) Naval Research Laboratory	Brightness temperature T_B (K)	0.5° x 0.5°	$W(T_B)$ algorithm
SSM/I (F13) Remote Sensing Systems [a]	Water vapor Cloud liquid water	0.25° x 0.25°	$W(T_B)$ algorithm
SeaWinds (QuikSCAT) PODAAC/JPL [b]	Wind speed U_{10} (m s^{-1}) [c] Wind direction U_{dir} (°)	0.25° x 0.25°	$W(T_B)$ algorithm & W database
GDAS/NCEP [d] CISL RDA [e]	U_{10}, U_{dir}, SST (°C) Air temperature T_a (°C)	1° x 1°	$W(T_B)$ algorithm & W database W database
WaveWatch III NOAA NCEP [f]	Significant wave height H_s (m) Peak wave period T_p (s)	1° x 1.25°	W database
World Ocean Atlas 2005 NASA GSFC [g]	Salinity (surface field)	1° x 1°	Expand W database
SeaWiFS OrbView-II NASA GSFC[h]	Chlorophyll a concentration (mg / m^{-3})	1° x 1°	Expand W database

[a] www.remss.com
[b] Physical Oceanography Distributed Active Archive Center at the NASA Jet Propulsion Laboratory (http://podaac.jpl.nasa.gov)
[c] Satellite wind estimates (such as those from QuikSCAT) are calibrated to equivalent neutral wind speeds [Kara et al., 2008]. Model winds are also corrected to neutral winds.
[d] Global Data Assimilation System, National Centers for Environmental Prediction (http://www.emc.ncep.noaa.gov/gmb/gdas/)
[e] Research Data Archive at Computational and Information Systems Laboratory (http://rda.ucar.edu/datasets/ds083.2/)
[f] National Centers for Environmental Prediction (http://polar.ncep.noaa.gov/)
[g] National Oceanographic Data Center (http://www.nodc.noaa.gov/OC5/WOA05/woa05data.html)
[h] NASA Goddard Space Flight Center (http://oceandata.sci.gsfc.nasa.gov/SeaWiFS/Mapped/Daily/9km/chlor/)

reference height U_{10EN}, rather than the *true* wind speed. U_{10EN} can be defined in several ways [Kara et al., 2008], but the definition provided by Tang and Liu [1996] is perhaps more applicable to this study as scatterometery (which actually measures surface stress) is used to obtain the satellite winds; the equivalent neutral wind is 'the wind speed calculated by using the stress and roughness length consistent with the observed atmospheric stratification but setting the atmospheric stratification term in the modified log-wind profile equal to zero.' These estimates are therefore not identical to the *true* U_{10} (unless the atmosphere's stratification is neutral). Satellite winds are also surface (rather than earth) relative, though the effect of surface motion is generally not accounted for. Throughout this work, database estimates for U_{10} are assumed to be representative of U_{10EN}, whereas in situ (ship-based) estimates of U_{10} are considered true/actual winds (despite often not being adjusted to account for flow distortion and surface currents). Where applicable, the implications of this difference are discussed.

To ensure that use of two different wind speed sources does not introduce bias, we explore the distribution of swath resolution U_{10} values from QuikSCAT and GDAS, for October 1, 2006 (Figure 3.8a). The shapes of the probability density functions for the two sources are similar. Differences of a few percent are visible at low wind speeds ($U_{10} < 5$ m s^{-1}) where QuikSCAT values are higher than those of GDAS; GDAS values are higher for $U_{10} > 11$ m s^{-1}. Note that this is not a comparison of paired QuikSCAT-GDAS values for U_{10} at a given location; at each point we have either a QuikSCAT or GDAS value. For the U_{10} values considered in Figure 3.8a, we find that in general GDAS has more counts at high latitudes and low latitudes, while in the mid latitudes, a larger count is from QuikSCAT values. It is therefore logical that GDAS gives higher probability for high winds than QuikSCAT, while QuikSCAT gives higher probability for low winds. Figure 3.8 shows a histogram of gridded wind speed values coupled with W data for 2006.

We expect some correlation between W_{10} and W_{37} values and the basic additional variables. The reason is that the same U_{10}, U_{dir}, and SST values used in the $W(T_B)$ algorithm at swath resolution (section 3.1.1) are also entries in the W database in gridded format. Some correlation is tolerated because there are no substantial gains in seeking different sources for U_{10}, U_{dir}, and SST data. For instance, we aim to use all available W estimates, of which there are more than 18 million; this would not have been possible with a more selective temporal and spatial match-up with direct
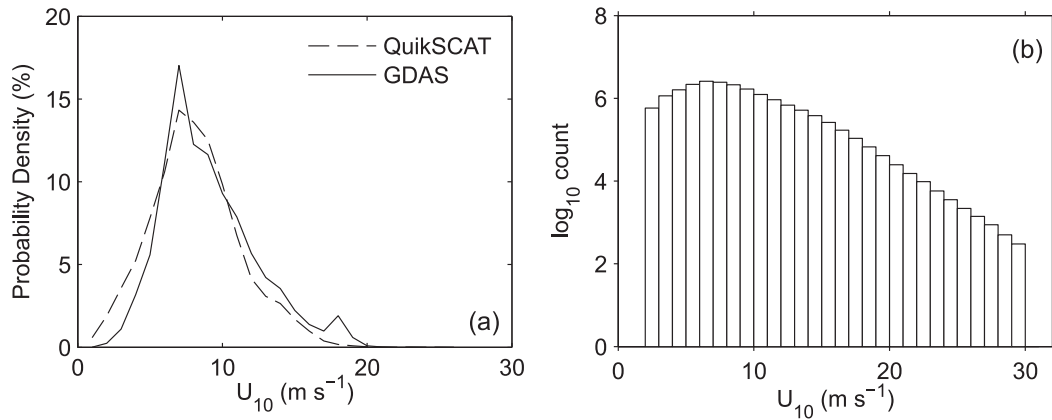
FIGURE 3.8: (a) Probability density function of swath resolution U_{10} values from QuikSCAT and GDAS for October 1, 2006. Panel (b) shows the number of individual gridded W estimates obtained for each 1 m s^{-1} wind speed bin over the course of 2006.

measurements from other satellites or buoys. Gains in using independent data would have also been limited if model outputs different from those provided by GDAS [e.g., use of the European Centre for Medium-Range Weather Forecasts (ECMWF)] were used, considering that assimilation of buoy and satellite measurements in any model is a common practice. Indeed, assimilation of the QuikSCAT data in ECMWF and NCEP have led to wind component values differing by at most 1.5 m s^{-1} [Chelton and Freilich, 2005].

Wind direction is one of the basic variables in the W database (Table 1), but in this study we do not analyse W as a function of U_{dir}. Brightness temperature used to obtain radiometric estimates of W varies with both wind speed and wind direction. This directional dependence comes from the non-uniform distribution of the foam and short (capillary) waves over the profile of the underlying large-scale waves, i.e., the face of a breaking wave has higher emissivity than its back [Wentz, 1992]. Attempts to model [Kunkee and Gasiewski, 1997] and measure [Padmanabhan et al., 2006] this azimuthal dependence of foam have been made. Knowledge and reliable modeling of it is important for the accuracy of geophysical retrievals [Johnson, 2006]. However, for parameterizing air-sea interaction processes in terms of W, an account for the effect of wind direction itself on W is not pertinent. Rather, the wind direction could be useful as a means of determining the fetch of the wind so that the history of the wave field can be inferred [Callaghan et al., 2008a]. Also, an increase or a decrease in whitecap fraction can be observed if the wind is aligned with or against the waves and/or currents

[Callaghan et al., 2008a; Sugihara et al., 2007]. To investigate such variability, one needs the relative direction between wind and wave field or currents. Meaningful information for the wave field directionality requires detailed spectral information, such as directional wave spectra [Sugihara et al., 2007], usually provided by models at specific regions but not on a global scale. At this stage of development, the W database does not contain information necessary for systematic study of directional W variability. Work on this topic, however, should be pursued as the W algorithm is further improved.

3.2.3   Additional data and derived forcing parameters

We expanded our set of six basic variables in the current whitecap database with two further parameters (i) estimates of ocean surface salinity Sal, and (ii) satellite estimates of chlorophyll a concentration (Chl a). Both products are regridded to match the resolution (0.5º x 0.5º) of the other database variables. For the salinity data, we use monthly mean salinity fields from the NOAA World Ocean Atlas 2005 (WOA05) (accessible online at www.nodc.noaa.gov/OC5/WOA05/pr_woa05.html). Chl a data is obtained from SeaWiFS sensor onboard the OrbView-II platform; we use daily global level-3 standard mapped images at 9 km resolution (accessible online at oceandata.sci.gsfc.nasa.gov/SeaWiFS/L3SMI). Note that in this study, satellite-derived Chl a fields (being readily available) are used as a proxy for biological productivity and therefore as an indicator of overall surfactant concentration, though it is acknowledged that the correlation between Chl a and surfactant concentration is complicated by several factors and that the relationship varies both temporally and from region to region.

In addition to the variables listed in Table 3.1 as entries in the W database, several further parameters are constructed to assess their influence on W. Atmospheric surface layer stability is indicated by the air-sea temperature difference $\Delta T = T_a - T_s$. The kinematic viscosity of water, ν_w, is calculated using a combination of daily SST fields and monthly mean salinity fields.

Two dimensionless wind-wave variables are considered. First, the breaking-wave Reynolds number, defined as

$$R_B = \frac{u_*^2}{\omega_p \nu_a}, \tag{3.4}$$
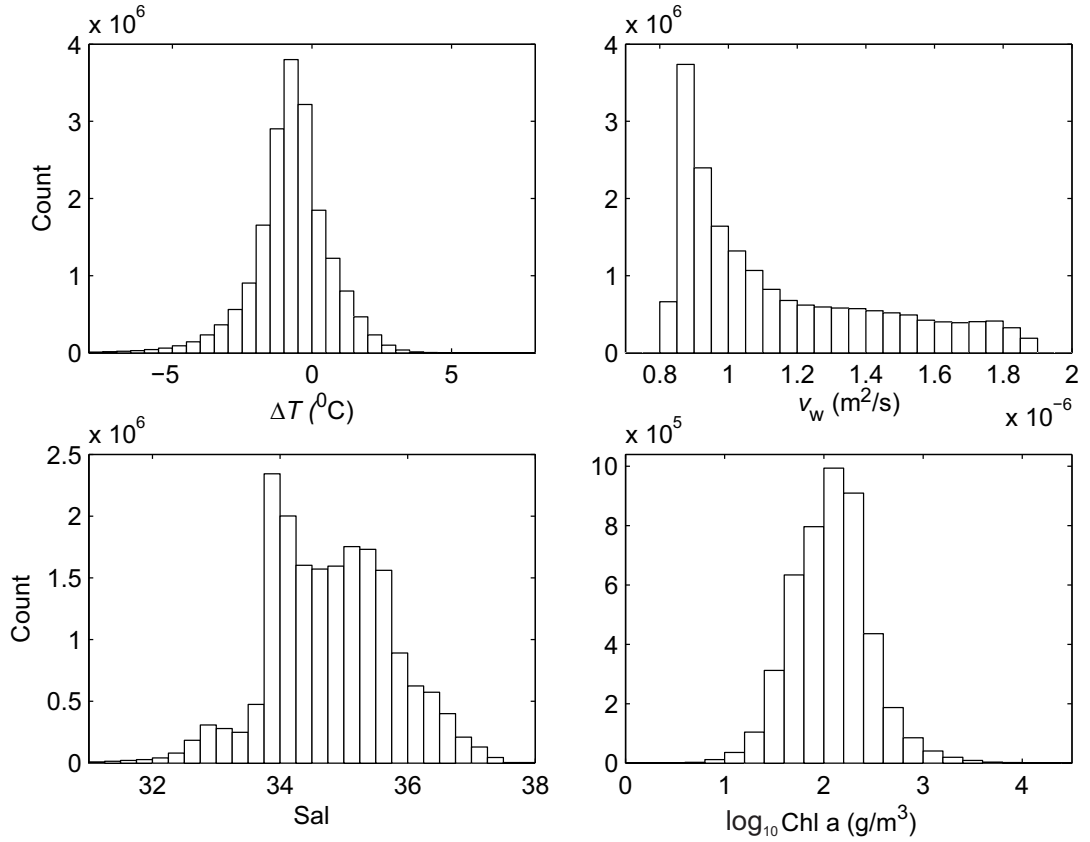
FIGURE 3.9: Histograms showing the distribution of database ΔT, ν_w, salinity, and Chl a estimates covering 2006

where ω_p is the spectral peak angular frequency of wind waves, and ν_a is the kinematic viscosity of air. The consideration of such a non-dimensional variable as an appropriate parameter to describe wave breaking dates back to the work of Toba and Chaen [1973], with R_B in its above form first suggested as a parameter to describe whitecap fraction by Toba and Koga [1986]. The roughness Reynolds number,

$$R_{Hw} = \frac{u_* H_s}{\nu_w}. \tag{3.5}$$

R_{Hw} is a slightly modified version of that of Zhao and Toba [2001], the only difference being use of the kinematic viscosity of water ν_w instead of ν_a, following the suggestion of Woolf [2005].

3.2.3.1   Measures of Wave Development

As summarised in section 2.5.1, recent in situ studies have strived to explicitly evaluate the role of the wave field on variability in W. Wave age Φ—defined as c_p/u_*, where

c_p is the wave phase velocity and u_* the air-side friction velocity—can be used to infer the stage of development of the sea. Φ can be expressed in terms of readily available parameters [Hanley et al., 2010] as

$$\Phi = \frac{gT_p}{2\pi\sqrt{c_d}U_{10}},\tag{3.6}$$

by using $c_p = gT_p/(2\pi)$ and $u_* = \sqrt{c_d}U_{10}$. Here, the drag coefficient c_d is calculated using the widely-used relationship of Large and Pond [1981]. A related wind-wave measure, fetch, has been used previously to infer the stage of wave development in analysis of in situ W data. At this stage, the database lacks important information (wave direction estimates) needed to estimate fetch, and so we proceed with use of wave age as a measure of sea state.

We also calculate the mean wave slope (or significant steepness) MWS, a dimensionless measure of the degree of wave development,

$$MWS = \frac{2\pi H_s}{gT_p^2}.\tag{3.7}$$

Note the use of the peak wave period in this formulation (the only available wave period measure), as opposed to the mean wave period. Although it has been shown that MWS alone cannot predict whether an individual wave will break [Holthuijsen, 2007], here we consider this quantity as a bulk measure of the wave field, combining the effects of H_s and T_p. Furthermore, this variable is not explicitly dependent upon wind speed, and so is included in our analysis of variability in W once the wind speed dependence has been accounted for. The dependence of W on MWS has not previously been considered.

3.2.3.2   Classification of wave field

A different approach to assessing the influence of the wave field involves categorizing W estimates by degree of wave development. Ideally, spectral wave data is analysed to reveal the presence (and relative intensity) of different regimes such as wind sea and swell (e.g., Callaghan et al. [2012]; Sugihara et al. [2007]).

It is, however, possible to use the two wave measures available in the current database (H_s and T_p), together with U_{10}, to attempt a broad classification of W estimates by the
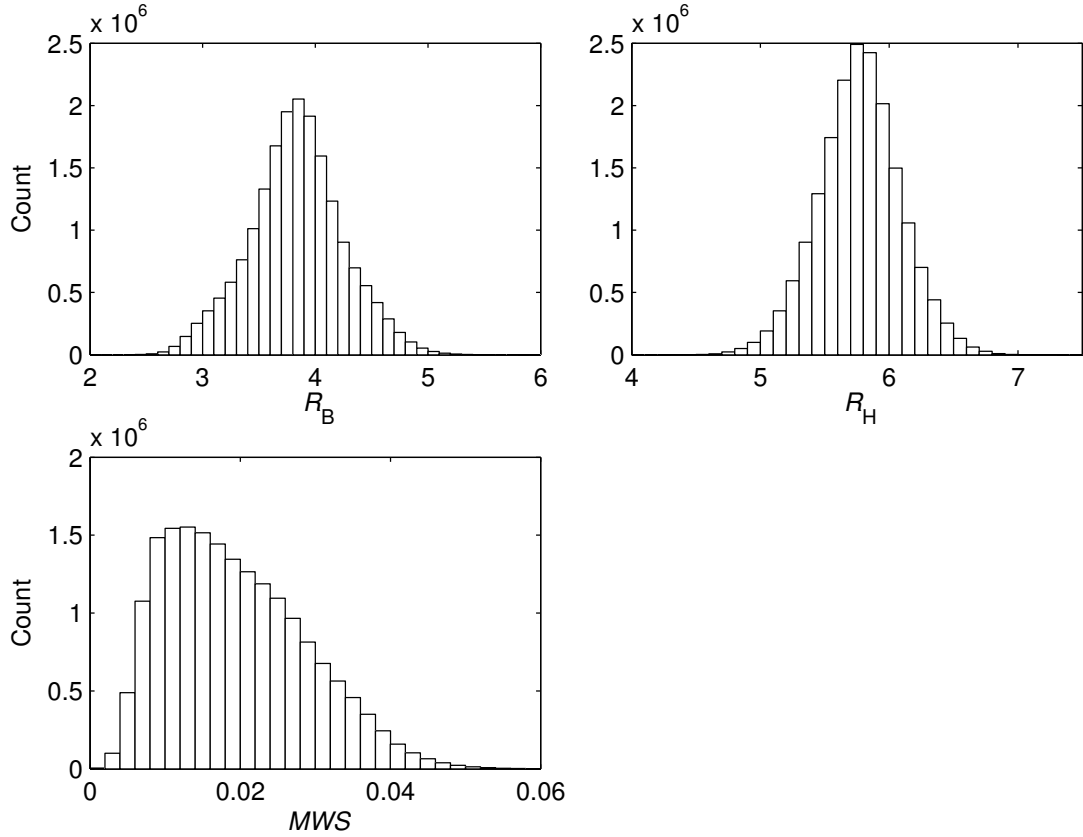
FIGURE 3.10: Histograms showing the distribution database R_B, R_H, and MWS entries covering 2006

stage of wave development. A similar approach was adopted in the study of Stramska and Petelski [2003], where U_{10} and H_s measurements were used to classify data into three groups; those obtained in undeveloped seas, those obtained in developed seas, and those obtained under conditions of decreasing winds. The authors note that whilst this criterion is not exact, it does allow an insight into the effects that sea state can have on W. Indeed, the authors modified the relationship slightly to reflect inaccuracies in their measurements of H_s, but stress that the qualitative conclusions should remain unchanged.

Classification by significant wave height is as follows. At each individual grid cell, the recorded value of H_s is compared with H_{fd}, the significant wave height that would be expected given a fully developed sea in equilibrium with the wind. H_{fd} is calculated from the wind-wave relation in the WAM model [Hasselmann et al., 1988],

$$H_{\text{fd}} = 1.614 \times 10^{-2} U_{10}^2; \quad 0 < U_{10} \leq 7.5,$$
$$H_{\text{fd}} = 10^{-2} U_{10}^2 + 8.134 \times 10^{-4} U_{10}^3; \quad 7.5 < U_{10} \leq 50. \tag{3.8}$$

This relationship defines the sea state as either *swell* when $H_s > H_{fd}$ or *wind sea* when $H_s < H_{fd}$. At the threshold level, where $H_s = H_{fd}$, it is assumed that the seas have just reached maturity.

Similarly, T_p can be used to partition W estimates. A relation predicting the peak wave period of a fully developed sea is given by Carter [1982] as:

$$T_{fd} = 0.785 U_{10}. \tag{3.9}$$
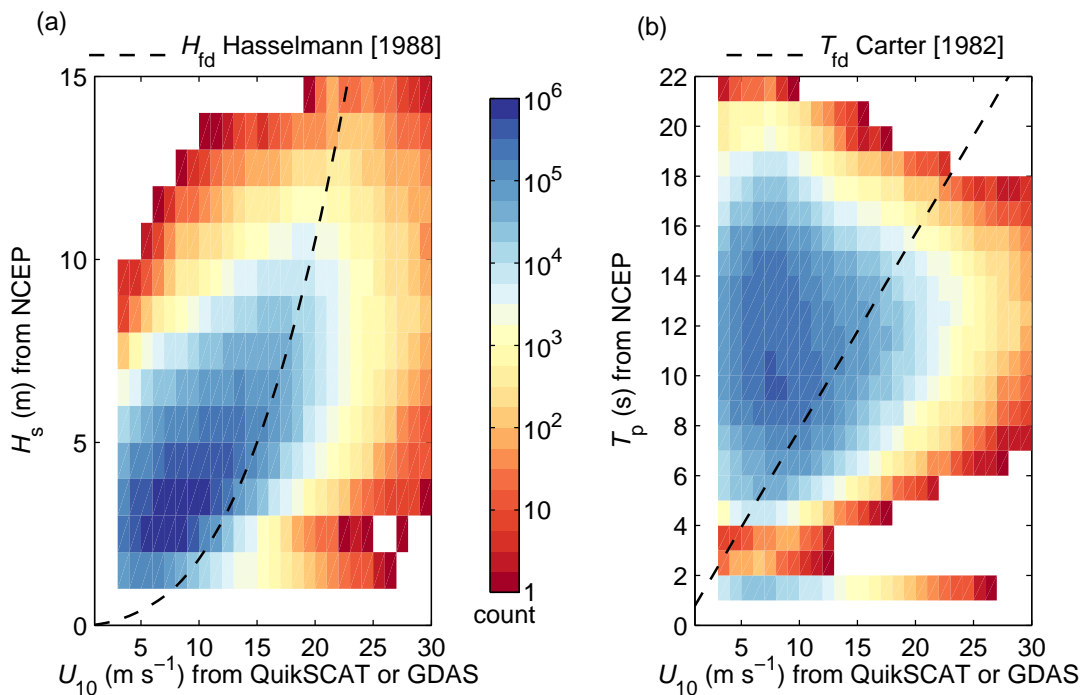
FIGURE 3.11: (a) Density plot of U_{10} and H_s for all W estimates from 2006. Also shown is the Hasselmann et al. [1988] theoretical relationship relating the two for a fully developed sea (black dashed line). (b) As (a), but for U_{10} and T_p estimates, and with the Carter [1982] relationship overlaid.

The frequency of occurrence of U_{10} and H_s is shown in Figure 3.11a. It is evident that the vast majority of data points lie above the threshold for a fully developed sea, indicating that a large portion of W estimates have been obtained in swell-dominated seas. The same conclusion can be drawn from Figure 3.11b, where T_p estimates are used to separate wind sea from swell cases using equation 3.9.

The results here echo those in the study of Chen et al. [2002], who note that there is a systematic swell dominance in the world's oceans, with swell occurring more than 80% of the time over vast areas. As such, this whitecap data set comprises mostly

W estimates obtained under swell affected/dominated conditions. This is in contrast to the many in situ data sets obtained in coastal or fetch-limited regimes. This is an important point, and should be noted when comparing findings from this study and those from previous in situ studies regarding the influence of the wave field on W (section 5.2.1.1).

3.3 Ship-based data

3.3.1 Overview of the UK-SOLAS SEASAW field campaign

This study draws upon measurements from the UK-SOLAS (Surface Ocean Lower Atmosphere Study) SEASAW (Sea Spray, Gas Flux and Whitecaps) project. The project involved two cruises in the North Atlantic on the NERC research ship RRS*Discovery*. The first, in November-December 2006 (D313), was a joint campaign with a related study—the Deep Ocean Gas Exchange Experiment (DOGEE). The first cruise encountered severe storm conditions with hurricane force winds, which meant many of the planned measurements were impossible to undertake. The second (D317) took place in March-April 2007. The cruise tracks for D313 and D317 are shown in Figures 3.12 and 3.13, respectively.
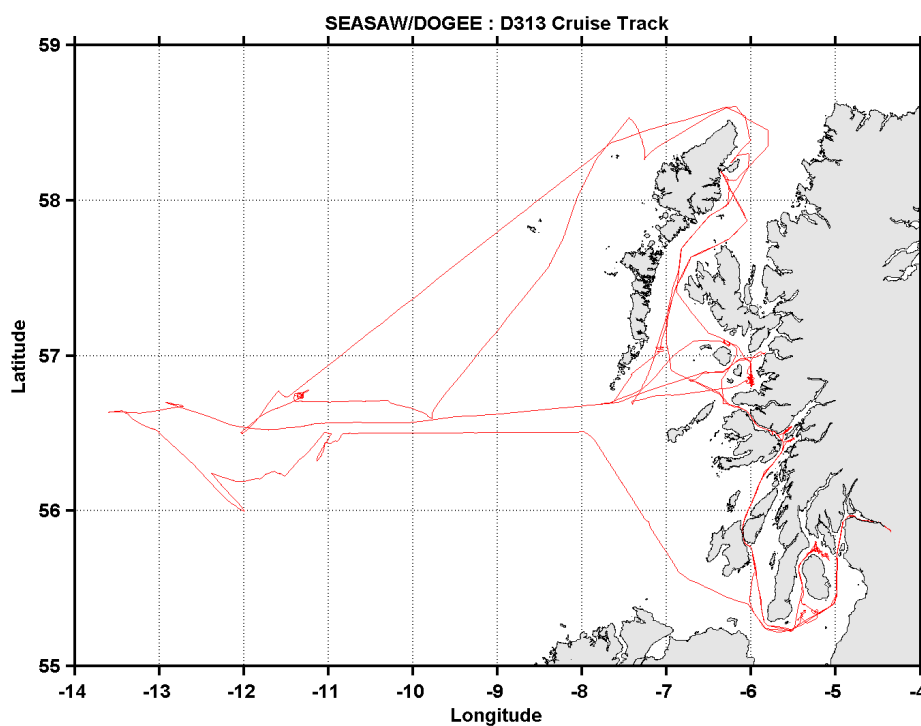
FIGURE 3.12: The D313 cruise track

The overarching goal of the UK-SOLAS projects was to understand the processes controlling physical exchanges at the air-sea interface [Brooks et al., 2009]. The SEASAW project incorporated a wide range of measurements with the general aim of obtaining
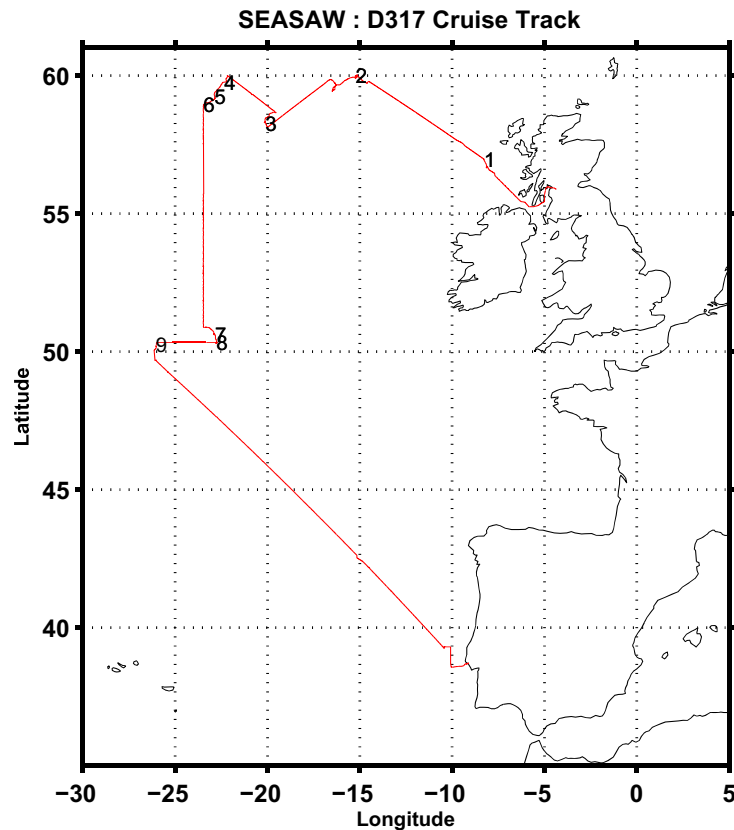
FIGURE 3.13: D317 cruise track with buoy deployments indicated by numbers

direct eddy covariance measurements of both sea spray and CO_2 fluxes [Brooks, 2007];
RRS *Discovery* was instrumented with

- an AutoFlux system [Yelland et al., 2009], with twin sets of annemometers and
  LICOR LI-7500 gas analyser units on the foremast platform;

- a second flux system including a CLASP (Compact Lightweight Aerosol Spec-
  trometer Probe) unit;

- a suite of instruments to measure background aerosol spectra and composition;

- a set of digital SLR cameras to obtain images of the sea surface at 30 second
  intervals.

In addition, one-dimensional wave spectra were obtained from a ship borne wave
recorder (SBWR) system, a tethered buoy used to make near-surface measurements of

bubble and aerosol spectra, and infrared-based systems measured air and water partial pressures of CO_2.

3.3.2 Photographic whitecap data

During both SEASAW cruises, images of the sea surface were taken in daylight hours by two Nikon Coolpix 8800 5 megapixel cameras looking directly abeam from the ship's bridge at a height of 13 metres and incidence angle of 22 degrees. Images with a resolution of five mega pixels were obtained every 30 seconds during daylight hours.

Processing such a large amount of data requires some sort of automation. Here we use the automated whitecap extraction (AWE) method [Callaghan and White, 2009] to obtain W estimates from the photographic data. First, the colour images are converted to greyscale. Next, a rectangular region from the centre of the image is selected to eliminate brightness effects due to either the horizon or the ship wake. To separate whitecaps from the background water, a suitable threshold intensity value unique to each image is determined by varying the threshold and examining the rate of change of resultant number of pixels selected. Once the threshold value is set, the area of the whitecap (corresponding to the number of pixels with a brightness above this threshold) can be obtained for each processed image. Figure 3.14 shows the typical output from processing an image from a camera aboard RRS $Discovery$ on March 24th 2007, during the D317 cruise.

The advantage of using the AWE method is that data processing is much faster than the manual methods previously employed to obtain W from photographic data. However, the quality control of processed images is still manual and therefore time-consuming. A flag is set to indicate whether or not the image passes quality control tests and so to determine whether or not it should be used in the subsequent analysis. Images are rejected for various reasons, such as if there is contamination from sun glint, sky reflection, seabirds, uneven illumination of the image, or raindrops on the bridge window. Due to the nature of these contaminants, several hours of contiguous data at a time (corresponding to hundreds of images) can be rejected.
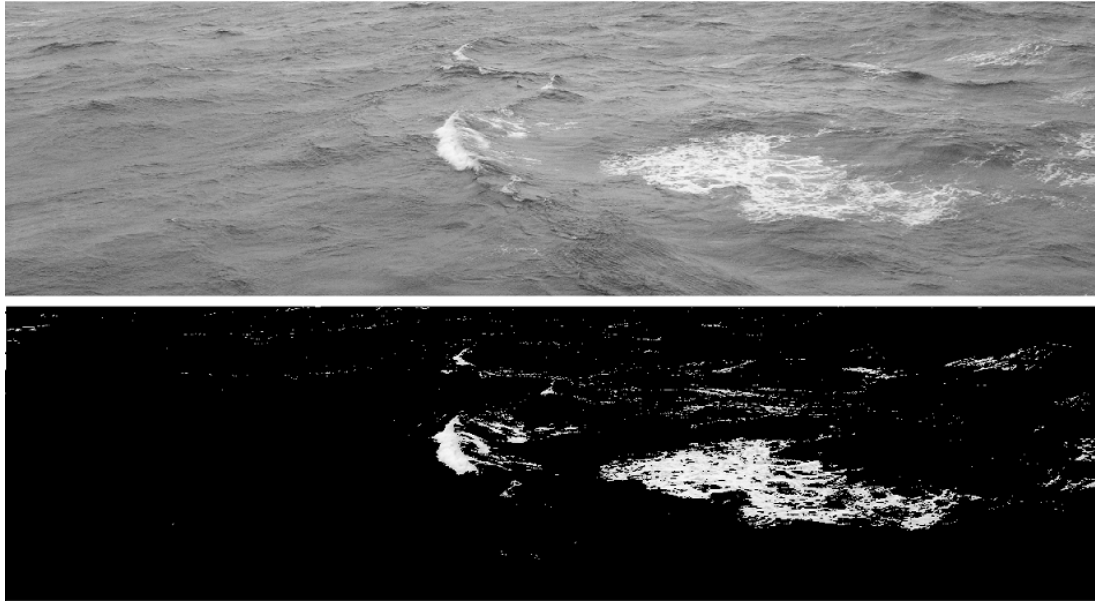
FIGURE 3.14: (Top) A digital image of the sea surface taken during the SEASAW (D317) cruise on RRS *Discovery*. (Bottom) The same image but after processing to isolate the whitecaps using the algorithm of Callaghan and White [2009].

3.3.3 Meteorological and oceanographic measurements

During both SEASAW cruises, mean meteorological measurements were obtained from the permanently installed instrumentation on RRS *Discovery* which includes—amongst various other instruments—anemometers to obtain wind speed and direction, temperature and humidity probes, and a barometer to obtain atmospheric pressure. The in situ wind speed estimates used chapter 4 of this study are provided by this system, with a time resolution of 30 seconds. Wind speed measurements are adjusted to a height of 10 m using the function of Large and Pond [1981]. Further, wind speed measurements are corrected for the airflow distortion created by the ship's hull and superstructure using the direction-dependent results of Yelland et al. [2002].

3.4 Additional data

In section 6.2.1.1, data from the European Centre for Medium-Range Weather Forecasts (ECMWF) operational archive is used to drive whitecap parameterisations. Modelled U_{10} fields (labelled the WIND parameter) for 2011 (consisting of 6-hourly records) are used at a spatial resolution of ($0.5^{\circ} \times 0.5^{\circ}$).

Chapter 4

Evaluation and validation of satellite-based W estimates

In their feasibility study, Anguelova and Webster [2006] discuss three methods by which the satellite estimates of W could be validated, namely:

- through comparison with individual estimates from historic photographic data sets,

- by comparing with estimates obtained from an existing $W(U_{10})$ parameterisation, or

- by performing a direct comparison of matched-up (i.e., simultaneous and collocated) satellite- and ship-based estimates.

The validation process is not as straight forward as it may first seem. The most direct method is through a comparison of satellite-derived estimates of W and in situ photographic estimates. In the first part of this chapter, a direct comparison is undertaken using ship-based photographic W estimates from two field campaigns. In the second part of this chapter, the wind speed dependence of satellite estimates is investigated and their global distribution and seasonal dependence is compared to those of W estimates derived using the widely used Monahan and O'Muircheartaigh [1980] $W(U_{10})$ parameterisation. We then discuss the results of these comparisons and comment on the use of in situ data to validate and evaluate the satellite observations of W.

4.1 A direct comparison of satellite-based W with in situ photographic estimates

4.1.1 Ship-based W estimates

Photographic W estimates were obtained by processing ship-based photographic data from both SEASAW cruises, as described in section 3.3.2). Although the ship-borne cameras were—for the most part—continually capturing digital images at a rate of two per minute, the number of usable images obtained over a given period can vary drastically. This is due to quality control stage, at which point images were rejected (based on human assessment) for a number of reasons; these include poor lighting conditions (such as sun glint), a questionable choice by the algorithm for the threshold brightness, or contamination of the image, for example, by water on the ship's windows. Estimates of W obtained by averaging photographs over a varying time window are shown in Figures 4.1 and 4.2. The figures illustrate variation in volume of data obtained, with Figure 4.1 representative of a 'good' day where a large proportion of the images passed the quality control tests, whereas Figure 4.2 is illustrative of a day when a much larger fraction of the images have been rejected.
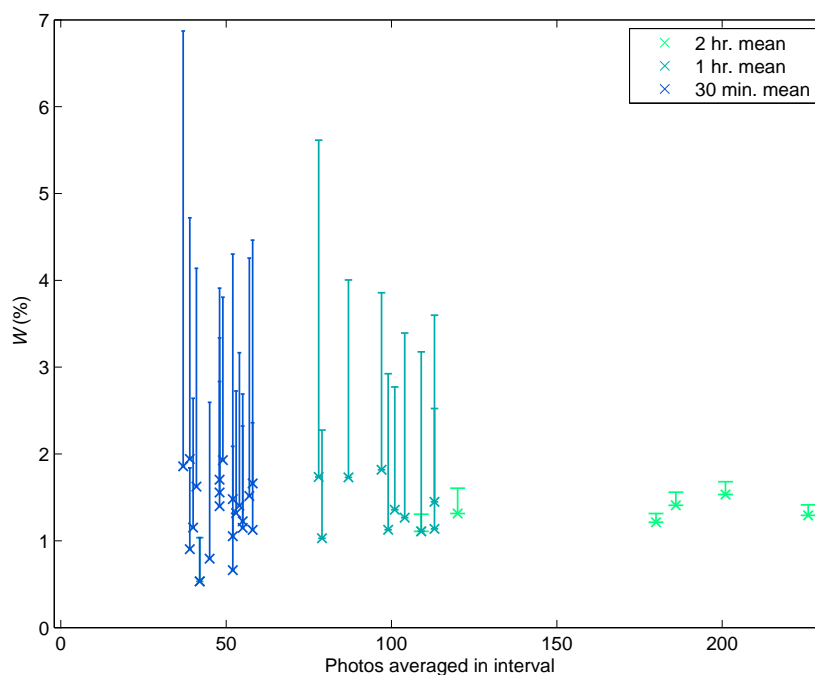
FIGURE 4.1: Time-averaged estimates of W against number of photos averaged for data obtained on 23rd March 2007 (Julian Day 082). Errorbars indicate the (positive only) standard error about the means.
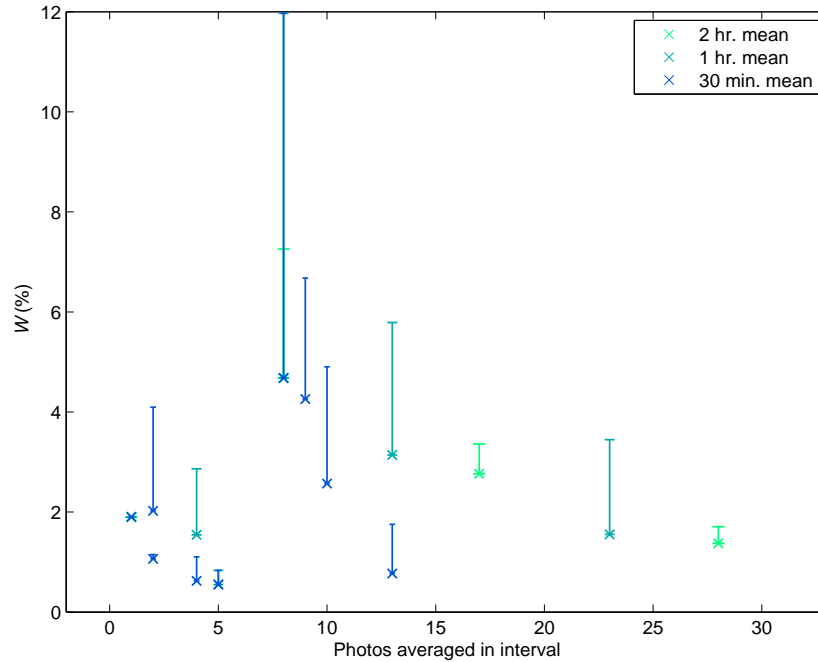
FIGURE 4.2: Time-averaged W means against number of photos averaged for data obtained on 30th November 2006 (Julian Day 334). Errorbars indicate the (positive only) standard error about the means.

Increasing the averaging period generally increases the number of images averaged, although in some cases variation in the quality of data throughout the day results in some estimates obtained from more photos averaged over a shorter time window. In both figures there is a trend of individual W estimates converging on a 'characteristic' value of W—which is likely representative of the true whitecap fraction—as the number of photographs averaged in a period increases. However, this will not always be the case as estimates spread more than several hours might diverge if conditions change over time. As expected, the error (represented here as the standard error on the mean) on an individual W estimate generally decreases as the number of photos averaged increases.

4.1.1.1 Wind speed dependence

We investigate the wind speed dependence of SEASAW W data by working with half-hour averaged estimates for W and U_{10}. W estimates are obtained by averaging individual W values (i.e., obtained by processing of a single photo) that pass the quality control stage. U_{10} estimates are obtained by averaging the corresponding U_{10} values for single photos; these are first obtained by averaging all 30 second U_{10} estimates that fall
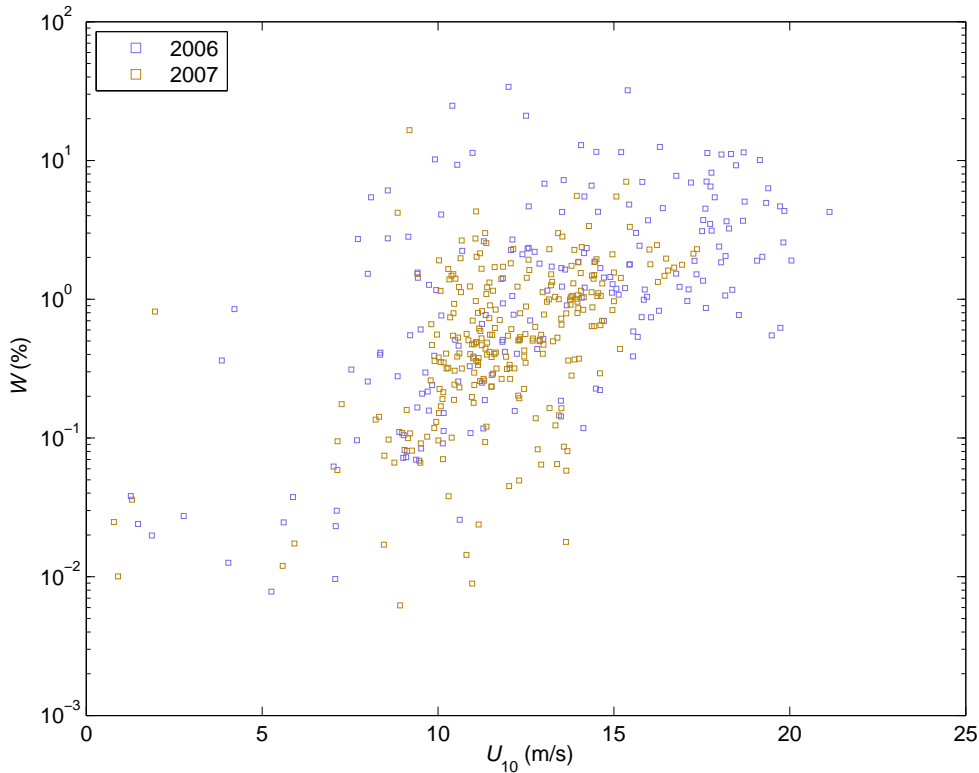
FIGURE 4.3: D313 (purple) and D317 (brown) half-hour averaged estimates of W and their corresponding U_{10} estimate.

in a ten minute window prior to the time the digital image is obtained. A histogram of the half-hour averaged U_{10} estimates is shown in Figure 4.4. Combining the D313 and D317 data sets results in U_{10} estimates that range from 1 m s^{-1} to 21 m s^{-1}, though the range of wind speeds encountered during D313 is much larger than the range for D317. A scatter plot (Figure 4.3) of W estimates against the corresponding estimate for U_{10} illustrates the characteristically large scatter in W estimates, spanning up to three orders-of-magnitude at a given wind speed.

We derive a $W(U_{10})$ parameterisation of ship-based W estimates from SEASAW by carrying out a non-linear regression to mean W estimates evaluated at each 1 m s^{-1} wind speed bin. The estimate of W for the range 20 m s$^{-1} < U_{10} \leq 21$ m s^{-1} is based on only one half-hour estimate and so is excluded from the fit. The resulting fit,

$$W_{\text{SEASAW}} = 3.6 \times 10^{-3} \times U_{10}^{2.42}, \tag{4.1}$$

is valid up to a maximum wind speed of 20 m s^{-1}. A comparison of the resulting parameterisation with several of those in the literature (Figure 4.5), shows that the
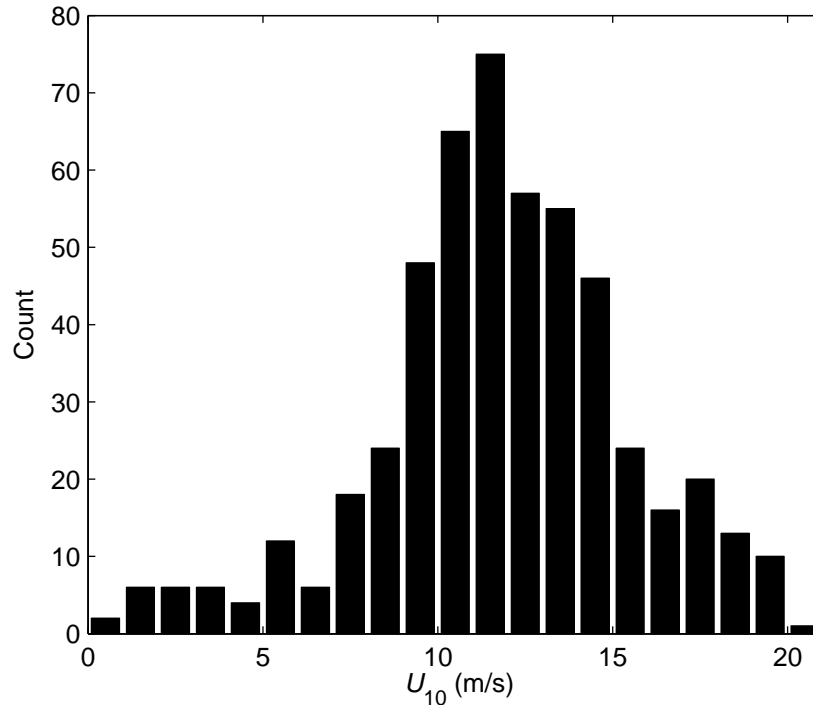
FIGURE 4.4: Distribution of U_{10} estimates corresponding to half-hour averaged means of W for D313 and D317 data.

SEASAW W estimates have a similar magnitude to those predicted by the relationship of Callaghan et al. [2008a] (equation 2.21), although their cubic wind speed dependence is stronger than that of the SEASAW data. This is interesting, as their relationship was derived from a set of measurements processed using the same AWE method, but made using different systems on different ships. Difference in the wind speed dependencies of the two parameterisations can be expected to arise due to the fact that the Cal08 relationship is formulated using U_{10} estimates that were not corrected for flow distortion. The relationships of Stramska and Petelski [2003] (SP03) and MM80 predict higher W than the SEASAW formulation over much of the wind speed range, and have a stronger wind speed dependence, resulting in larger deviations from SEASAW estimates in high winds (e.g., for $U_{10} > 12$ m s^{-1}).

4.1.2 Comparison of ship-based and satellite-based W

4.1.2.1 Method to obtain matchups

A spatial-temporal approach [Ichoku et al., 2002] is used to obtain matchups between in situ and satellite estimates of W. The first step is to determine validation points for
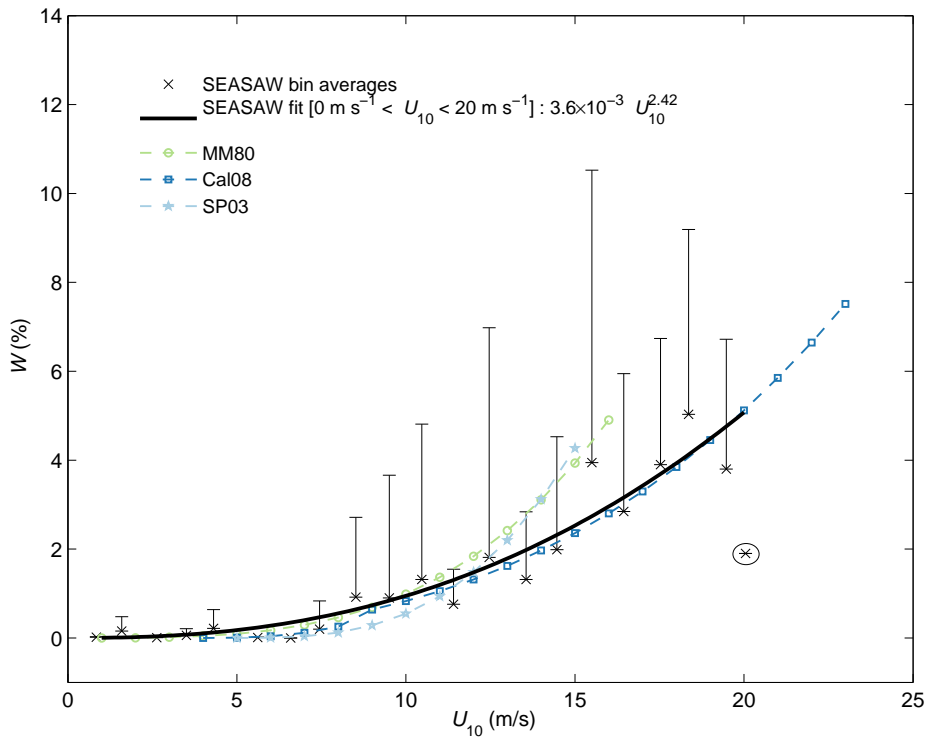
FIGURE 4.5: A comparison of the SEASAW derived $W(U_{10})$ relationship (solid black line) with several published parameterisations. Errorbars (positive only shown) show the standard deviation of the bin-averaged means of W. The outlier shown circled is excluded from the fit.

which collocated and simultaneous in situ and satellite W estimates exist, and then to obtain an estimate for satellite-based W; the procedure is as follows:

1. Determine approximately the latitude (lat) and longitude (lon) for each matching point;

2. Take an area of $N° \times N°$ degree centered at the validation point;

3. Find WindSat swath resolution data in this area;

4. Calculate a mean W by averaging all values in the box.

For each of the validation (matchup) points, each $N \times N$ box contains a certain number of spot samples from the WindSat swath (Figure 4.6), depending on the box size and its position within the swath; here, data at a swath resolution of approximately 40 km $\times$ 60 km is used. Distances between the samples in the center and in the wings of the swath are different. The average of all samples falling in the spatial box will
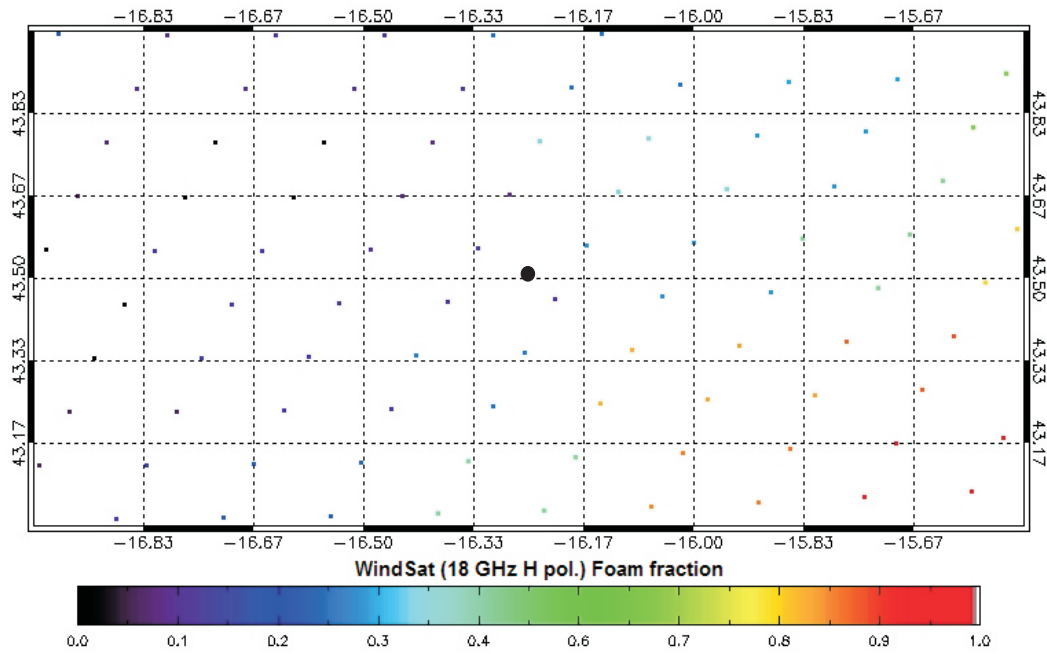
FIGURE 4.6: A sample box with WindSat swath spot W estimates (at 18 GHz, H pol.) from April 2007; the N×N box in this instance is 1° latitude by 1.5° longitude. Note that W is given as a fraction, rather than a percentage. Figure courtesy of M. Anguelova (NRL)

provide one satellite-based value of W for the matching point in the center (indicated by the black dot). An acceptable size of the box is an area commensurate with the footprint of the WindSat measurements at the working resolution i.e., approximately 0.5°× 0.5°. Here, we work with 1° latitude by 1.5° longitude boxes, though in some cases larger or smaller boxes are chosen depending on the number of WindSat spot samples (section 4.1.2.2).

Next, in situ photographic data must be temporally averaged to obtain a ship-based estimate of W. To determine over what time period the in situ data need to be averaged, the following considerations are taken into account: Winds with a speed of 10 m s^{-1} will traverse a ∼50 km distance in roughly 1.4 hours; assuming that other influencing factors change slowly over this distance, the wind field will generate a specific whitecap fraction over this area. For low winds (e.g., 5 m s^{-1}) the corresponding time period is 2.8 hours. For higher winds, 15 and 20 m s^{-1}, the time windows are 54 minutes and 42 minutes, respectively. It follows that to cover a wide range of wind speeds it seems reasonable to choose a time window of 3 hours over which to average in situ data. On the other hand, such long period of averaging may introduce bias toward lower winds and whitecap fraction. One other consideration for the length of

the time window concerns time of WindSat overpass. Ideally, the time window should be centered at the time of WindSat overpass. However, the WindSat equator crossing times are such that it passes in the areas of interest (i.e., the North Atlantic) in the morning or in the evening; thus, our time windows may cover periods of insufficient daylight during which the cameras were not collecting data. Thus, in the best case scenario, we have photographic W data covering this time period, which is centered at the time of WindSat measurement. In other instances, full coverage will not be obtained. Based on these considerations, we choose a 2 hour window period centered at the validation time in an effort to maximize the number of photographs obtained during the time window.

A corresponding ship-based U_{10} estimate is obtained by averaging U_{10} estimates (i.e., those corresponding to each individual photo) over the same time window.

4.1.2.2   Results

A summary of the matchup information for the D313 (5 matchups) and D317 (10 matchups) field campaigns is shown in Table 4.1, and a log-log 1:1 plot of matched-up pairs of in situ and satellite estimates of W is shown in Figure 4.13. Although a total of 15 matchups are identified, data for only 12 matchups are shown in the plot. For three of the matchup points (matchup 4 from D313 and matchups 6 and 11 from D317), W_{photo} is estimated to be zero after averaging a very small number of photos in each case (2, 8 and 3 photos, respectively). For this reason, we exclude these data from our analysis.

Despite the small number of data points, a general trend of overestimation of satellite W at low wind speeds, and underestimation at high wind speeds can be seen. The deviations ($W_{\text{sat}} - W_{\text{photo}}$) for W_{10} and W_{37} are plotted in Figure 4.8, bottom) for all matchups except matchup 1 from D313 which are deemed to be outlier values with large biases of -5.84 % for W_{10} and -5.01 % for W_{37}. The matchup deviations are also shown as a function of ship-based U_{10} measurements (Figure 4.8, bottom). In general, the deviations are larger as U_{10} increases, though the bias for matchups at the highest wind speeds ($U_{10} > 15$ m s^{-1}) are in fact smaller than several of those in the range 10 m s$^{-1} < U_{10} < 15$ m s^{-1}. Although no wind speed information goes into the estimates of W, it is interesting to compare the ship- and satellite-based estimates of

TABLE 4.1: A summary of information for the D313 and D317 matchups.

	Date	Overpass time	Ship location		WindSat area		Satellite measurements				In situ measurements		
	dd/mm/yy	(hh:mm:ss)	Lat (°N)	Lon (°W)	Lat (°N)	Lon (°W)	U_{10} (m s^{-1})	Count [a]	W_{10}	W_{37}	U_{10} (m s^{-1})	Count [b]	W_{photo}
D313													
1	10/11/06	17:53:22	56.38	11.25	56.13-56.65	11.75-10.75	15.1	18	2.19	3.02	15.1	57	8.03
2	11/11/06	17:35:49	56.25	12	55.4-55.9	12.5-11.5	13.3	20	1.5	2.55	18.4	38	1.43
3	12/11/06	17:18:49	56.7	13.25	56.45-56.9	12.4-13.9	15.9	35	2.4	2.9	16.1	79	1.78
4	25/11/06	06:59:31	57.7	9.25	57.3-57.9	10-8.6	5.6	22	0.23	0.62	12.6	2	0
5	26/11/06	18:14:26	56.75	11.5	56.5-57	12-11	15.7	10	2.38	3.01	10.6	15 1	0.63
D317													
1	22/03/07	17:47:23	59.83	15.73	57-58	10-8	5.4	65	0.20	0.6	5.2	8	0
2	24/03/07	17:13:36	58.5	20	59.5-60	16-15	16.0	42	2.47	2.89	15.2	149	1.88
3	27/03/07	18:00:49	58.5	20	58-59	21-19	9.4	78	0.74	1.62	11.5	11	0.32
4	27/03/07	18:00:52	59.83	22	58.75-59.75	19-17	8.5	75	0.61	1.4	11.5	11	0.32
5	27/03/07	18:00:55	59.83	22	58.25-59.25	20-18	7.3	73	0.43	1.09	11.5	11	0.32
6	28/03/07	17:43:33	57.5	9	58-59	21-19	17.3	85	0.41	1.13	9.3	3	0
7	30/03/07	18:49:16	59.25	18	60.33-59.33	23-21	11.5	66	1.06	1.8	13.1	18	0.42
8	31/03/07	18:31:29	58.75	19	60.33-59.33	23-21	14.0	73	1.68	2.50	14.2	125	0.64
9	08/04/07	08:01:28	48.5	24	49-48	25-23	4.5	100	0.13	0.49	7.7	17	0.01
10	08/04/07	08:01:39	47.5	22	48-47	23-21	4.1	78	0.11	0.43	7.7	17	0.01

[a] Number of spot samples falling within N×N box
[b] Number of photographs averaged to obtain an individual estimates of W_{photo}
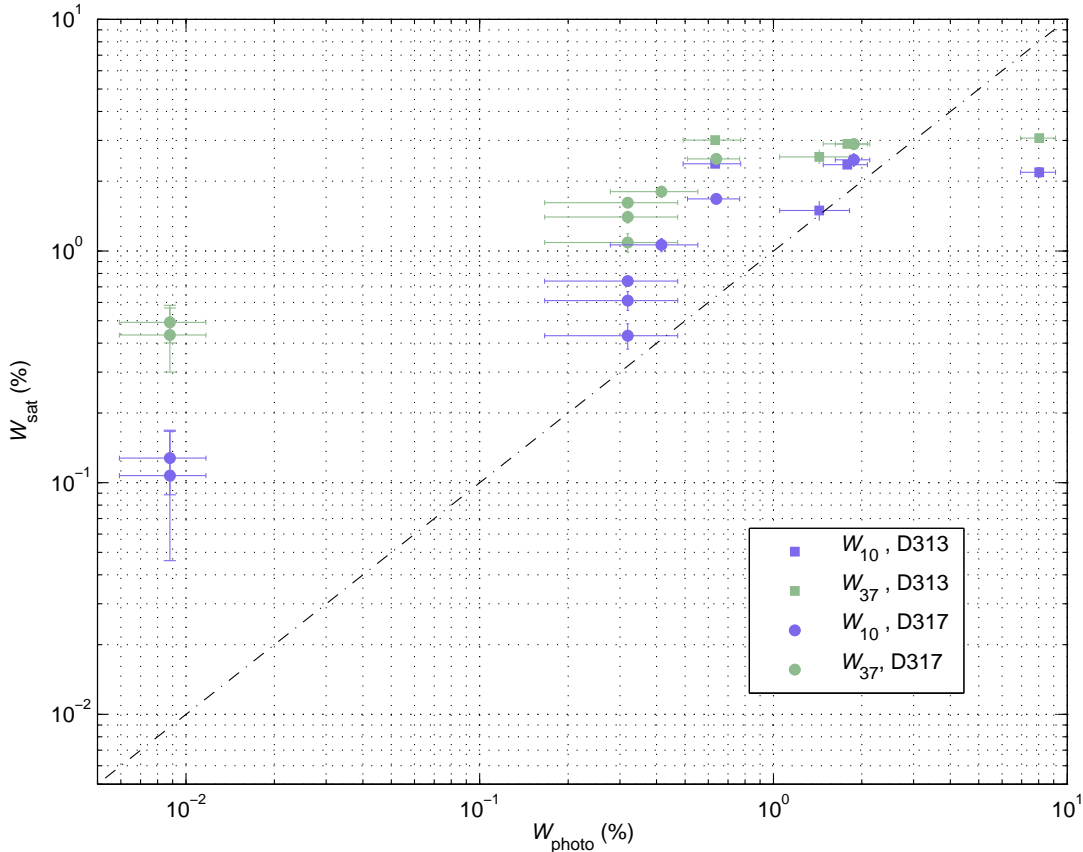
FIGURE 4.7: A 1:1 comparison of paired in situ and satellite W estimates. Matchup points for D313 are shown with squares, and those from D317 by circles.

U_{10} (Figure 4.8, top). Note that this figure compares QuikSCAT equivalent-neutral U_{10} to ship-based estimates of 'true' U_{10}. Though the paired U_{10} data show a reasonably high correlation ($R = 0.77$), differences between the two estimates can be as large as 55% (matchup 7). The bias between the paired U_{10} estimates are a result of (i) errors associated with ship-based and satellite estimation, (ii) errors associated with the temporal and spatial averaging and (iii) difference between stability-dependent and equivalent neutral wind speed estimates.

It is hard to draw any firm statistical conclusions from such a limited data set. However, it is worth noting that if a linear fit is applied to the 12 matchups, the resulting fits have the following form (all values in %):

$$W_{10} = 1.02 + 0.21 \times W_{\text{photo}}$$
$$W_{37} = 1.65 + 0.25 \times W_{\text{photo}},$$

(4.2)

indicating that although estimates of both W_{10} and W_{37} lie higher at low winds and
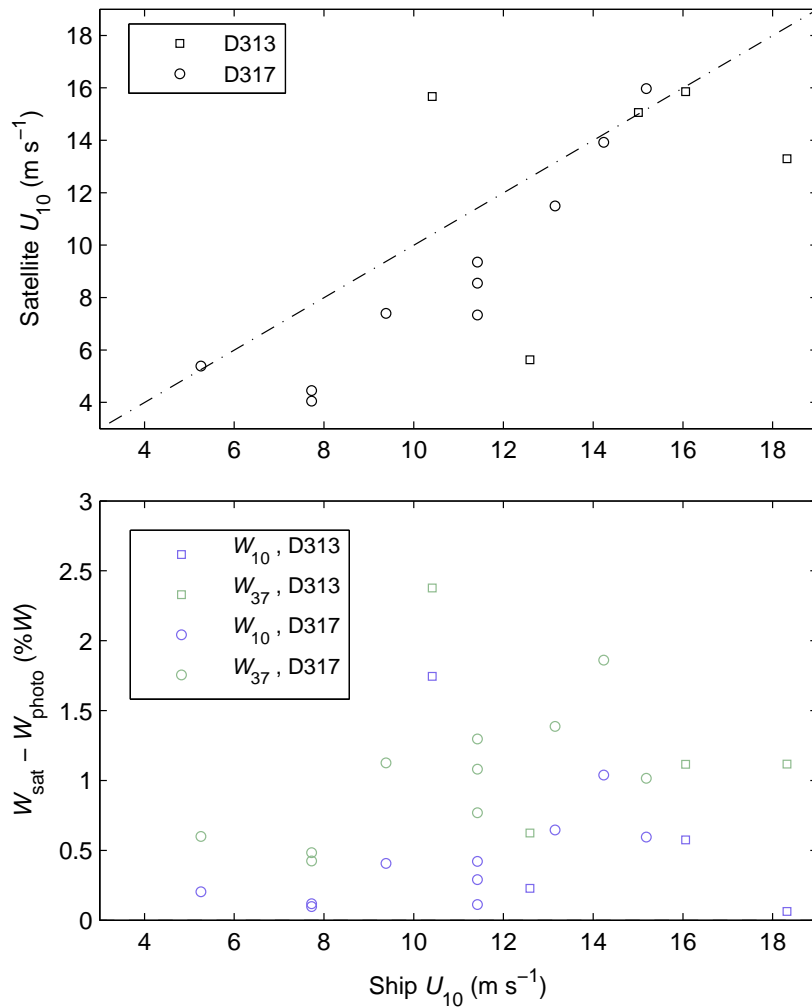
FIGURE 4.8: (Top panel) A 1:1 plot of satellite- and ship-based U_{10} estimates for all 15 matchups. (Bottom panel) Wind speed dependence of the matchup bias ($W_{\text{sat}} - W_{\text{photo}}$).

lower at high winds, the W_{37} estimates are more largely biased with respect to the 1:1 line. The correlation coefficient R between W_{photo} and W_{10} for the 12 data points is 0.52. For W_{37}, the value is 0.56. Removal of one data point (matchup 1, where W_{photo} is much higher than W_{10} and W_{37}) increases the correlation dramatically, to 0.83 for W_{10} and 0.81 for W_{37}.

4.1.3 Discussion

The results here are in line with the analysis of matchups with in situ data from the High Wind Air-Sea Exchanges (HiWASE) project, presented in Anguelova et al. [2009a], which also showed the same trend of overestimation of satellite-based W at

low winds, and underestimation at high winds. There are three plausible reasons for the overestimation of W_{sat} at lower whitecap fraction values. In situ data is fundamentally different, in that it represents the optically measured foam fraction, whereas the satellite estimates are radiometric. Specifically, W_{sat} estimates are—by the virtue of their principle of measurement—more sensitive to both active and residual whitecaps. Thus, a satellite-based method to measure whitecaps is prone to register more foam in places where optical observation may underestimate decaying foam. This sensitivity to the thickness (thus type) of the foam depends on the frequency, and so too therefore does the magnitude of the overestimation—being smaller at 10 GHz and increasing for 37 GHz. In this respect, it is worthwhile trying to ascertain what frequency (or combination of frequencies) is most representative of the optical measurement. A short discussion on this topic is presented in Anguelova et al. [2009a]. Second, expected deficiencies in the retrieving algorithm would most likely add to the overestimation at low whitecap coverage values. These include shortcomings of the atmospheric correction, difficulties in the modeling of the rough sea surface, and inadequate choice in the foam emissivity model [Anguelova et al., 2009a]. Finally, the estimates used to ground truth the satellite estimates are subject to large errors themselves (section 4.1.1). Errors will, in most cases, be relatively larger in low wind, low W conditions, where extraction of whitecap fraction from video records can be problematic. Once a larger number of matchups has been achieved, it may be worth quantifying the effect of comparing in situ W estimates paired with stability dependent wind speed estimates to satellite estimates of W paired with $U_{10\mathrm{EN}}$ values.

The direct validation exercise is limited by the small number of matchups, despite collating validation points from two field campaigns. This is due to the nature of satellite-ship matchups; if the ship's position is outside of the satellite swath, no matchup can be obtained. However, the spatial-temporal approach used here is perhaps the best possible method available for validating satellite-based observations using ship-based in situ data. Whilst satellite matchups provide the opportunity of direct validation of the retrieval estimates, it is not clear how spatially averaged satellite estimates should compare with temporally averaged in situ estimates. The effect of the averaging used in this method should be further evaluated, for example, by varying the temporal and spatial intervals used.

Further work on the direct validation of satellite-based W estimates using in situ

estimates should be pursued in order to minimise the error on radiometric estimates. The ship-satellite matchup approach can also clarify the source of differences between optical and radiometric estimates, including quantification of the level of uncertainty in the W estimates from both methods to ascertain whether it is appropriate to use photographic data to calibrate the retrieval. For the time being, the main approach to minimise error in satellite estimates of W is to develop the retrieval algorithm further [Anguelova et al., 2009a].

4.2 Indirect validation: Wind speed dependence of satellite-based W, and comparison with $W(U_{10})$ parameterisations

4.2.1 Correlation between satellite-based W and U_{10}

To investigate how well wind speed alone accounts for the variability in satellite-derived estimates of whitecap fraction, we consider the strength and spatial characteristics of the correlation between whitecap fraction (both W_{10} and W_{37}) and U_{10} from the whitecap database. We calculate a cell-by-cell Pearson product-moment correlation coefficient R from a series of W and wind speed pairs. The maximum number of individual W estimates used to calculate R for a grid cell is 317, the minimum is 3, and the average 140.

Figure 4.9 shows the correlation coefficient for W_{10} and wind speed is > 0.95 at over 95% of grid cells; for W_{37} over 89% of cells have $R > 0.95$. The small number of cells below these thresholds are generally either close to land, or have a low count rate over the year. Correlation with wind speed is higher for W_{10}, suggesting that more variability in W_{37} can be attributed to factors other than U_{10}. Furthermore, as R is a measure of the strength of a linear relationship, the correlations reported here may be biased low, more so in the case of W_{10} which has a more nonlinear dependence on wind speed.

Some spatial structure is evident in Figure 4.9. Correlation between U_{10} and W_{10} is highest in low-latitude regions, such as the equatorial Atlantic and eastern equatorial Pacific. Slightly lower values of R are found in the mid-latitudes, where the variability
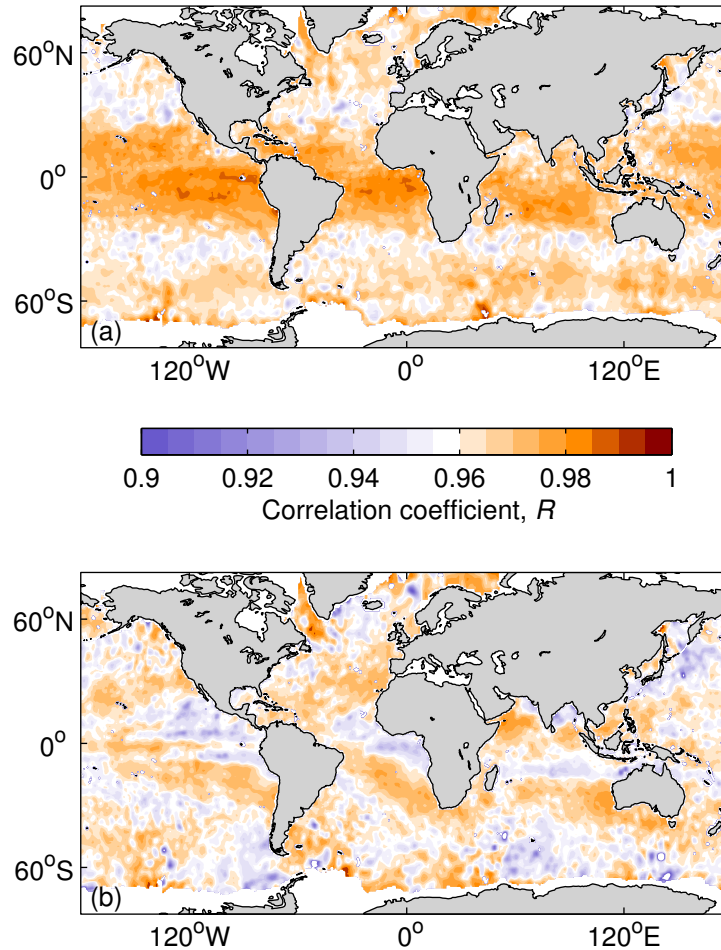
FIGURE 4.9: Global maps of cell-by-cell Pearson's correlation coefficient R for U_{10} and (a) W_{10}, and (b) W_{37}. Sources for W and U_{10} are listed in Table 3.1. Data comprises all estimates from 2006.

in wind speed (and wave field) is higher. Correlation is more variable for W_{37}, with areas of lower correlation found in both low average wind speed regions (equatorial Pacific) and regions where wind speed is on average much higher (Southern Ocean). We note that the spatial patterns in R are not explained by differences in the U_{10} range which has potential to distort the statistic.

4.2.2   Wind speed dependence of satellite W estimates

4.2.2.1   Comparison with traditional $W(U_{10})$ formulations

To explore the wind speed dependence of satellite-derived W, all estimates in the range $0 < U_{10} \leq 30 \text{ m s}^{-1}$ are averaged into wind speed bins of 1 m s^{-1} width. A histogram of the U_{10} values used was previously shown in Figure 3.8b. The wind speed bin-averaged

means of W_{10} (blue crosses) and W_{37} (green crosses) are compared to three $W(U_{10})$ parameterisations; that of Monahan and O'Muircheartaigh [1980] (MM80), Callaghan et al. [2008a] (Cal08), and Goddijn-Murphy et al. [2011] (GM11) in Figure 4.10a. It is apparent that both W_{10} and W_{37} have a weaker wind speed dependence than MM80 and Cal08 formulations based on in situ U_{10} values, indicative of overestimation of satellite retrieved W at low wind speeds, and underestimation at higher wind speeds. However, W_{10} is close to the GM11 formulation, which uses the same data set of W estimates as Callaghan et al. [2008a], but satellite (rather than in situ) U_{10} data. At $U_{10} > 20$ m s^{-1}, W_{37} begins to level off, causing W_{37} to fall lower than W_{10}. This behaviour is not physically viable given the interpretation of the two different estimates (section 3.1.2) and therefore points to an issue with the retrieval, one that should be explored in future work if this feature persists.
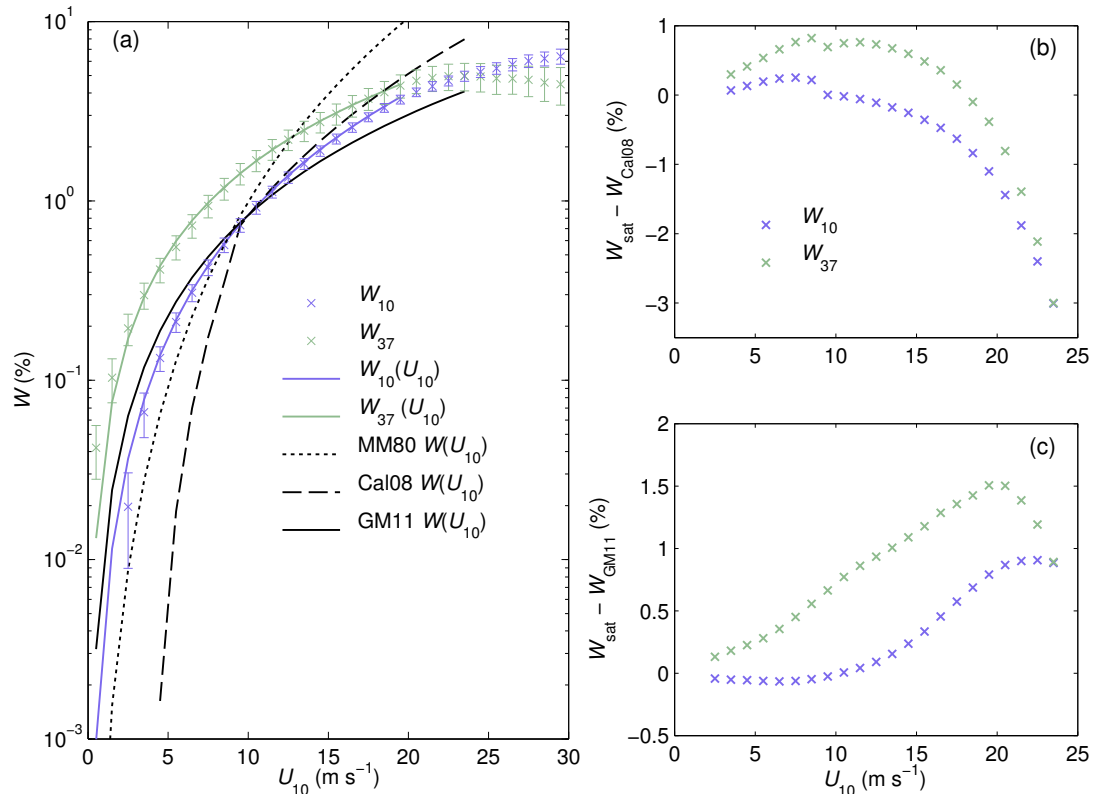
FIGURE 4.10: (a) Wind speed dependence of W_{10} and W_{37}, two $W(U_{10})$ parameterisations from in situ data—that of Monahan and O'Muircheartaigh [1980] (MM80) and Callaghan et al. [2008a] (Cal08)—and a $W(U_{10})$ parameterisation using satellite winds Goddijn-Murphy et al. [2011] (GM11). Error bars indicate the standard deviation on the bin-averaged means. The absolute difference between W_{10} and W_{37} and the Cal08 relationship is shown in panel (b). Panel (c) is as panel (b) but the comparison is made with the GM11 parameterisation.

At moderate wind speeds (7 m s^{-1} < U_{10} < 12 m s^{-1}), the satellite retrievals compare

reasonably well with the Callaghan $W(U_{10})$ parameterisation (Figure 4.10b). At the global average oceanic wind speed of $U_{10} = 7$ m s^{-1}, W_{10} is very close to W predicted by the Callaghan et al. [2008a] parameterisation, differing by only 0.2%, whereas for W_{37} the difference is 0.8% at this wind speed.

Figure 4.10c highlights good agreement between the satellite W estimates and those from the GM11 parameterisation. Absolute differences between W_{10} and GM11 are very close to zero for wind speeds lower than 12 m s^{-1}; beyond this point the difference grows, reaching 0.9% at $U_{10} = 24$ m s^{-1}. The difference between W_{37} estimates and those using GM11 grows with increasing wind speed to a maximum of 1.5% at $U_{10} = 20$ m s^{-1}.

At high wind speeds (i.e., $U_{10} > 20$ m s^{-1}) we must be cautious with regards to the comparison between satellite and in situ W estimates, due to the sparseness of in situ estimates. It is hard to judge the validity of the retrieval at high wind speeds by comparing with the two in situ $W(U_{10})$ formulations, one of which (MM80) has been extrapolated to wind speeds above those from which it was derived. The fact that the wind speed dependence of W_{10} and W_{37} is much closer to that of GM11 points to the importance of the wind speed source in formulating a $W(U_{10})$ parameterisation.

There is no signal for W_{10} below 2 m s^{-1}, whereas for W_{37} there is a small signal in the two bins below, the result of a handful of instances where foam has been detected. These winds speeds are below the suggested threshold for whitecapping of ~ 4 m s^{-1} [Callaghan et al., 2008a], a value obtained from analysis of photographic data. Whilst there is likely to be little (or no) wave breaking at these wind speeds, microwave radiometers may detect small amounts of residual long-lived foam from previous breaking events, which are typically missed in photographic analysis.

4.2.2.2   Wind speed parameterisations

To parameterise the satellite-based estimates of W in terms of U_{10}, a power-law relationship has been fitted to mean W estimates at each wind speed bin in the range $2 < U_{10} \leq 20$ m s^{-1}. We fit both W_{10} and W_{37} over the same wind speed range, thus excluding mean W_{37} values for the first two bins for which W_{10} estimates (and thus bin-averaged means) are always zero. The functions are valid up to a maximum

wind speed of 20 m s^{-1}; the decision to restrict the parameterisations to this range is based on considerations of data statistics and the validity of satellite-based estimates of W (and U_{10}) in high wind conditions (discussed further in section 4.2.3). The fits are given by

$$W_{10} = 4.6 \times 10^{-3} \times U_{10}^{2.26}; \;\; 2 < U_{10} \leq 20 \text{ m s}^{-1},$$
$$W_{37} = 3.97 \times 10^{-2} \times U_{10}^{1.59}; \;\; 2 < U_{10} \leq 20 \text{ m s}^{-1},$$

(4.3)

and are shown as coloured solid lines in Figure 4.10a. The shape of the functional forms of the above relationships differ from those of previous in situ parameterisations, the majority of which exhibit a roughly cubic dependence on wind speed. The W_{10} relationship is closer to those from in situ parameterisations, with an exponent of 2.26, whereas the exponent is 1.59 for W_{37}. Again, it is worth noting that the U_{10} estimates used to construct these parameterisations are equivalent neutral winds, and so the functions should be forced with values for $U_{10\text{EN}}$.

4.2.3 Discussion

The satellite retrieval of W_{10} is biased high with respect to the traditional $W(U_{10})$ parameterisations of Monahan and O'Muircheartaigh [1980] and Callaghan et al. [2008a] at low wind speeds, but falls below them for winds above about 10 m s^{-1}. W_{37} is even higher at low winds, but increases more slowly than W_{10}. At winds above 20 m s^{-1} W_{37} actually begins to fall with increasing U_{10} and fall below W_{10}; this behavior can be explained only by an unidentified issue in the retrieval algorithm. The general wind speed behavior is similar to that reported by Anguelova and Webster [2006] in spite of substantial modifications to the retrieval algorithm. Both W_{10} and W_{37} are closer to the parameterisation of Goddijn-Murphy et al. [2011]—which uses satellite winds with the same in situ whitecap imagery used by Callaghan et al. [2008a]—than to the purely in situ functions. Indeed, the exponent of GM11 (1.86) lies almost halfway between that of the W_{10} and W_{37} formulations presented here.

Potential sources of relative bias between the different functions are systematic differences in the estimation of whitecap fraction and wind speed via different techniques, and from averaging over different ranges or probability distributions of secondary factors. We note that the best agreement between all the different functions is for winds in the range 5–10 m s^{-1}, those most commonly encountered over the ocean [Ebuchi,

1999]. Both the satellite winds and whitecap fraction estimates are spatial averages, while in situ winds are time averages at a single point and in situ whitecap fractions are joint time and spatial averages, albeit over a much more restricted area.

The Goddijn-Murphy et al. [2011] function is even more strongly biased high (low) with respect to MM80 and Cal08 at low (high) wind speeds than W_{10}. This suggests that the differences between the different functions may depend as much, or more, on biases between the wind speed estimates as on the whitecap fraction measurements. A potentially significant factor here is that satellite winds are not estimates of the true 10-m wind speed, but of an equivalent neutral wind speed. There are also known issues such as the saturation of QuikSCAT for $U_{10} > 20$ m s^{-1} [Quilfen et al., 2007]. In situ winds are not necessarily without biases; ship-based measurements require correction of both their speed and effective altitude because of distortion of the air flow over the ship [Moat et al., 2006; Yelland et al., 2002], something only recognized relatively recently and not applied by earlier studies. Determining the correction is difficult however, and is not always undertaken even today—Cal08 do not correct their winds for flow distortion.

The accuracy of both the satellite-derived parameterisations and traditional in situ parameterisations at high wind speeds should be questioned; the validity of traditional parameterisations may suffer due to the sparsity of in situ W data in this range, whilst satellite-derived W parameterisations may suffer from errors in U_{10} values, due to for example, the known saturation of QuikSCAT at $U_{10} > 20$ m s^{-1} [Quilfen et al., 2007].

4.3 Global distribution and seasonal dependence of satellite-based W estimates

In this section, we use a full year (2006) of satellite estimates of whitecap fraction to assess the spatial distribution and seasonal dependence of W. We compare this global distribution with that derived from the MM80 parameterisation and discuss implications for models and retrieval algorithms.

To date, studies of global and seasonal distributions of whitecaps have been possible only by driving $W(U_{10})$ parameterisations with global wind distributions. Blanchard

[1963] showed the latitudinal variation of W by estimated zonal means for June–August and December–February; these varied from a minimum of $\sim 2\%$ in the tropics to $\sim 9\%$ at 45°S during June–August. The seasonal contrast was highly asymmetric. In the southern hemisphere, zonal means of W in summer were roughly 2% lower than winter values across the hemisphere with W peaking at around 45°S for both seasons. In the northern hemisphere, there was a strong seasonal cycle; W peaked just above 8% at 55°N in winter but had a near-uniform value of about 2% across the entire hemisphere in summer. It is worth noting that these results derived from a $W(U_{10})$ parameterisation based on an extremely limited data set of just five aerial photographs of the sea surface in the Caribbean, at wind speeds between approximately 4 and 20 m s^{-1}.

A monthly global climatology of W was presented by Spillane et al. [1986], based on a rate of wind work parameterisation of W and ship observations of surface wind speed and stability dependent drag coefficient. Highest W (3–4%) occurred in the North Atlantic in winter. The relatively lower values (1.5–2%) for the Southern Ocean even during the austral winter were attributed to undersampling of high wind conditions by the ships. At low to mid latitudes (up to 40°N and °S) W never exceeds 1%.

Erickson III et al. [1986] used the $W(U_{10})$ function of Monahan and O'Muircheartaigh [1980] (MM80) and global monthly mean winds at 5° resolution. They found a similar general seasonal distribution and highlighted geographic regions of persistently high whitecap fraction over periods of months, such as the Indian Ocean during the monsoon season and high-latitude storm-tracks.

4.3.1 Method

For a given grid cell, the number of estimates of W_{10} and W_{37} varies with the number of matchups between different source measurements; for calculation of seasonal means, this number ranges from 1 to 130, with an average of 34–40 depending on the season. Latitudinal variations are presented with zonal mean profiles of whitecap fraction. Zonal means were obtained by averaging all values within each 0.5° latitude band. Seasons are defined as northern hemisphere spring (March–May, hereafter MAM), summer (June–August, JJA), autumn (September–November, SON), and winter (December–February, DJF).

We compare satellite-based W estimates with those predicted by the $W(U_{10})$ relationship of MM80 (equation 2.20) We use (2.20) with U_{10} values from W database to obtain W_{MM80} values matched to each W_{10} and W_{37} estimate; these were similarly averaged. This parameterisation is chosen because it is widely used, forming part of the Monahan et al. [1986] sea spray source function and several others adapted from it, including those of Gong [2003] and Mårtensson et al. [2003], which are used to calculate sea spray aerosol source fluxes in many aerosol and climate models [Spracklen et al., 2005; Textor et al., 2006]. MM80 or similar formulations are also used in sea surface reflectance models for aerosol [Sayer et al., 2010] and wind speed [Harmel and Chami, 2012] retrievals.

4.3.2   Seasonal dependence of geographic distribution

The seasonal global distributions of W_{10} and W_{37} (Figure 4.11) follow similar patterns, with W_{37} always higher, as expected. Highest seasonal W occurs in bands centered around $50°$N and $50°$S, where mean wind speeds are highest [Sayer et al., 2010]. The southern hemisphere band is persistent, with $W_{10} > 1.5\%$ and $W_{37} > 2\%$ over much of the Southern Ocean throughout the year. This feature was apparent in the monthly maps of W presented in Spillane et al. [1986]. Over much of the low-latitude ocean (equatorward of $30°$N and S), seasonal means of W_{10} are usually $<0.5\%$ while W_{37} seasonal means are typically above 0.5%. Like Erickson III et al. [1986], we find enhanced W in the Arabian Sea during summer, with mean $W_{10} \approx 1.5\%$ and mean $W_{37} \approx 2\%$.

4.3.3   Latitudinal variation of zonal means

The latitudinal variation of W_{10} and W_{37} for the four seasons is shown in Figure 4.12, along with that for W_{MM80}. W_{10} and W_{37} follow roughly the same latitudinal trends, with zonal means of W_{37} larger than those for W_{10} by a factor of 1.5–2. In the equatorial region, W_{10} is consistently around 0.3%, with W_{37} at $\sim0.6\%$. There is a general trend of increasing W from the equator to high latitudes, and a consistent asymmetry between the two hemispheres. Interseasonal variations are much stronger in the northern hemisphere; at 50–$60°$N, where W peaks, W_{10} is a factor of three and W_{37} a factor of approximately two higher in DJF than in JJA. In the southern hemisphere,
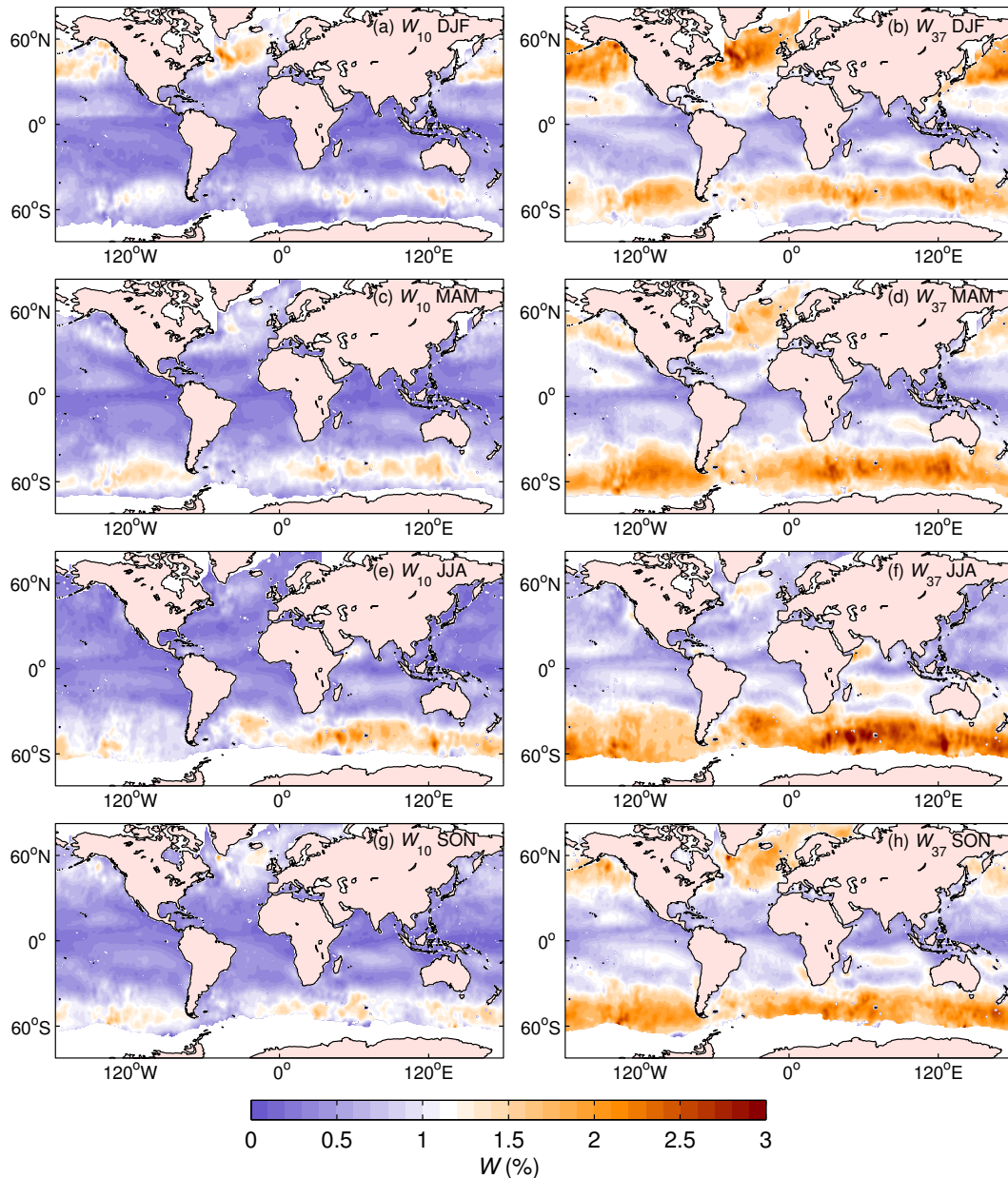
FIGURE 4.11: Seasonal means of W_{10} (left column) and W_{37} (right column).

W peaks around 50°S; here, W_{10} varies less than 30% and W_{37} less than 20% over the year. This result is in agreement with the findings of Blanchard [1963] and Erickson III et al. [1986]. The asymmetric distribution in mean W is a consequence of the larger seasonal variations of temperature and winds in the northern hemisphere (driven by the stronger response of land surface temperature) and persistent high winds and long fetches in the Southern Ocean, both of which result from the asymmetric distribution of land masses between the hemispheres.
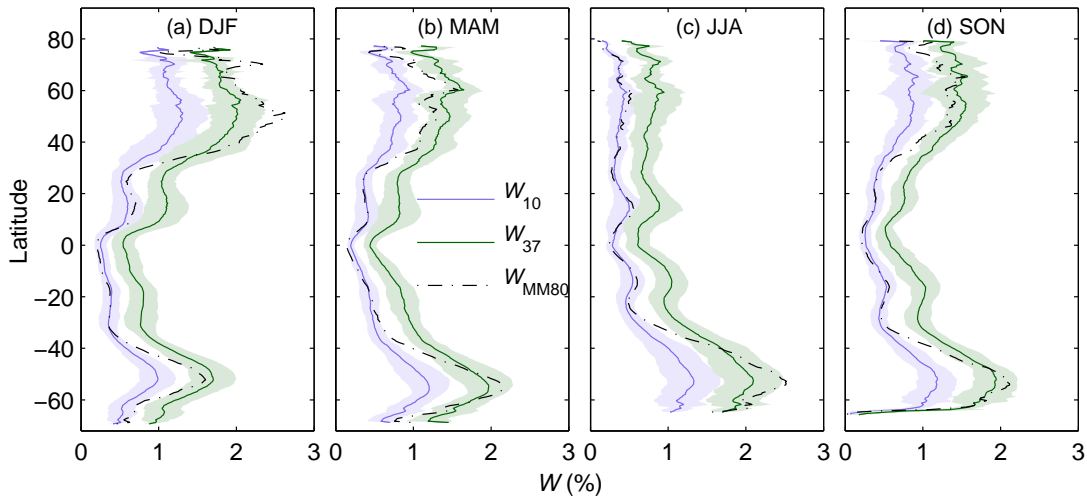
FIGURE 4.12: Latitudinally variation of seasonal means of W_{10}, W_{37}, and W_{MM80}. Shaded areas represent standard deviation on means.

4.3.4 Comparison of global distribution

Aggregating individual W estimates over the full year, we obtain the mean difference (MD) between W_{MM80} and both W_{10} and W_{37}, $\text{MD} = \overline{W} - \overline{W}_{\text{MM80}}$, together with the normalised mean difference (NMD), $\text{NMD} = 100 \times \text{MD}/\overline{W}_{\text{MM80}}$.
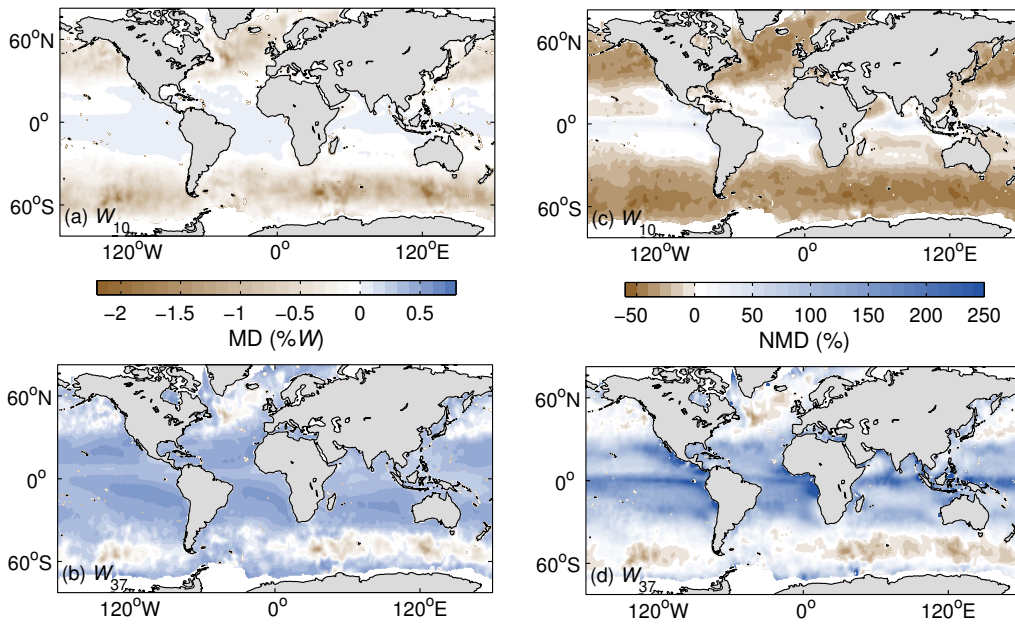
FIGURE 4.13: Mean difference ($\text{MD} = \overline{W} - \overline{W}_{\text{MM80}}$) and normalised mean difference ($\text{NMD} = 100 \times \text{MD}/\overline{W}_{\text{MM80}}$) between W_{MM80} and (a and c) W_{10} and (b and d) W_{37}.

The MD between W_{MM80} and both W_{10} and W_{37} are shown in Figures 4.13a and 4.13b. Over much of the mid and lower latitudes (between 30°N and 30°S) MD is close to zero

for W_{10}; for W_{37}, MD positive and reaches 0.8% in low wind speed regions. At higher latitudes, MD increases in magnitude, reaching -2.4% in regions of the Southern Ocean for W_{10}. These are high wind speed regions, where W_{MM80} is consistently higher than W_{10}. In these regions, MD for W_{37} is generally not as large because W_{37} estimates are higher than W_{10}.

Figures 4.13(c, d) show normalised mean differences between W_{MM80} and W_{10} and W_{37}, respectively. NMD for W_{10} lies between -50% and 50% over much of the oceans. A somewhat different behavior is seen for W_{37}; in equatorial regions and low latitudes, NMD can be as large as 240%, reflecting the large relative difference between W_{37} and W_{MM80}. The difference between the two frequencies results from the physically different nature of the properties they respond to—the foam in actively breaking waves, and the slowly decaying surface foam. This imposes both a large difference in mean W, and differences in response to environmental conditions.

4.3.5   Discussion

Latitudinal variations of W_{10} are in close agreement with W_{MM80} at low latitudes (Figure 4.12). At higher latitudes (poleward of 40°N and 40°S), W_{MM80} is much larger than W_{10}, particularly so in the winter. Large differences here are driven primarily by the difference in wind speed dependence between satellite estimates ($U_{10}^{2.26}$ and $U_{10}^{1.59}$ for W_{10} and W_{37}, respectively and MM80 ($U_{10}^{3.41}$). The extrapolation of MM80 to wind speeds beyond those from which it was formulated is likely the source of significant high bias in the resulting W estimates. Only during northern hemisphere summer are seasonal means of W_{10} and W_{MM80} in agreement at high latitudes. Zonal means of W_{37} are higher than W_{MM80} over much of the global ocean; the reverse is true during DJF in the high northern latitudes and in JJA at around 50°S.

The global distribution and seasonal dependence of whitecap fraction at two microwave frequencies (W_{10} and W_{37}) have been described. Seasonal means of the two estimates have similar geographical distributions, with W_{37} seasonal means a factor 1.5–2 higher than those for W_{10}. At low latitudes (equatorward of 30°N and S), seasonal means rarely reach 1% for W_{10} and 1.5% for W_{37}. Seasonal changes in mid to high latitudes are stronger in the northern hemisphere than in the southern hemisphere; this reflects the effects of the asymmetry in distribution of continental land masses between

the hemispheres. Highest seasonal W occurs in DJF in the North Atlantic and JJA Southern Ocean.

Differences between satellite-based estimates of W and those obtained from the widely used $W(U_{10})$ relationship of Monahan and O'Muircheartaigh [1980] are driven primarily by their differing wind speed dependence, which is weaker for the satellite-based estimates. This results in satellite estimates higher than those obtained from MM80 in the tropics, but lower than MM80 in high latitudes where mean wind speeds are higher. Overestimation of MM80 due to extrapolation beyond its range of validity is likely a key bias at high wind speeds. The satellite-based parameterisations are derived from W estimates on a global scale and so their wind speed dependence will in part reflect the influence of factors other than wind speed which co-vary with the wind geographically; for example SST, biological surfactant concentration, and fetch-dependent wave state.

Chapter 5

Variability in satellite-based estimates of whitecap fraction

As described in section 2.5, it has hitherto not been possible to extensively evaluate the influence of secondary forcings on W due the limitations of in situ data sets. The satellite-based approach to estimation of W provides a significantly larger volume of data which enables an assessment of global variability in whitecap fraction. In this chapter, we describe variability analyses that were performed to both qualitatively and quantitatively assess variability in W due to secondary forcing parameters associated with both the wave field and environmental conditions.

5.1   Analyses to investigate variability

Whitecap fraction representative of predominantly active plus partially residual white-caps (W_{10}), and total active plus residual whitecaps (W_{37}) is analysed in conjunction with seven basic variables (U_{10}, T_a, SST, H_s, T_p, S, Chl a) and six derived forcing parameters (ΔT, ν_w, R_B, R_{Hw}, Φ, and MWS). In the first analysis, variability in W due to various forcing factors is explored after first accounting for the dominant wind speed dependence (5.1.1). In the second analysis, the relative contribution of each forcing factor to variability in W is evaluated using principal component analysis (5.1.2) on both a global and regional scale.

5.1.1 Quantifying effects of various factors

To investigate sources of variability in W, the strong wind speed dependence must first be accounted for. Prior to this procedure (outlined below), we consider the gridding statistics, and omit all individual W estimates that have a relative standard deviation (σ_W/W) above 0.3. This cut-off value is somewhat arbitrary but as can be seen in Figure 3.6, this value is will into the 'tail' of the distribution for both W_{10} and W_{37}. W estimates with $RSD > 0.3$ mostly occur in low winds, close to the threshold value for whitecapping to occur (~ 4 m s^{-1}). We choose to work with all remaining W estimates for which 4 m s$^{-1} \leq U_{10} \leq 20$ m s^{-1}, thus excluding both very low and very high wind speed regimes, where data is much sparser and removal of a mean wind speed trend would be dubious.

Elimination of known gross influences is necessary to meaningfully investigate secondary effects on a given quantity. This can be done in many ways, but the simplest approaches to represent deviations of a quantity from some reference value (e.g., its mean) is by anomaly (difference) or by normalisation (scaling). An important difference between these two representations is the use of absolute verses relative deviations.

The removal of the wind speed trend is as follows. All accepted estimates from 2006 are first binned by wind speed. For this analysis, we use wind speed bins of width 0.5 m s^{-1} to reduce the sensitivity of W to changes in U_{10} over the range of each individual wind speed bin. A mean whitecap fraction $\overline{W}$ is calculated for each wind speed bin. Then, all W estimates in each of the 32 wind speed bins are further binned by the corresponding measurement for the variable under investigation, and a mean whitecap fraction $\overline{\overline{W}}$ is obtained for each-sub bin. Normalizing each sub-bin mean by $\overline{W}$ results in the ratio $\overline{\overline{W}}/\overline{W}$, essentially showing the deviation from the mean wind speed behavior over the range of each secondary forcing variable.

The decision to represent our results in terms of normalized whitecap fraction is made through two considerations. We know that W depends strongly on wind speed and expect that the effects of the secondary forcing parameters would be to either enhance or suppress the wind speed effect. The ratio above can represent well such enhancement or suppression of the wind speed influence by the secondary factors. When $\overline{\overline{W}}/\overline{W} > 1$, the secondary factor enhances whitecapping produced by the wind speed for which $\overline{W}$ is obtained. When $\overline{\overline{W}}/\overline{W} < 1$, the secondary factor suppresses whitecapping.

A second consideration is that at this intermediate stage of the whitecap database (section 3.2), use of relative, rather than absolute, values is more pertinent. As the $W(T_B)$ algorithm continues to develop and improve, the absolute values will likely change. Meanwhile, the trends seem to be robust considering that the observation of more uniform latitudinal distribution of W documented with the initial implementation [Anguelova and Webster, 2006] remains for satellite-based estimates W_{37}, that account for total (active plus residual) whitecap fraction.

In the following analysis of the influence of secondary factors (Figures 5.2, 5.4, 5.6, and 5.7), the panels for normalized W_{10} and W_{37} have the same y-scales for easy comparison. Two main features in all the figures are considered. One is the overall trend of normalised whitecap fraction $\overline{\overline{W}}/\overline{W}$ over the full range of possible values of each forcing variable and its deviation above and below unity. Another is the spread within a family of curves colour coded to show these deviations by wind speed bin.

5.1.2 Principal component analysis

Principal component analysis (PCA) is a statistical procedure that can be used to investigate the variance of a multivariate data set. Here, we use PCA to quantify how successful each forcing variable is in describing variability in W [Anguelova et al., 2010]. This can be achieved by comparing how much variance is 'explained' by the first principal component (PC1), which can be thought of graphically as the 'direction' of maximum variance. The PC1 score quantifies the amount (percentage) of variance explained by this direction; the higher the score, the more variance that is explained. For this analysis, all database entries covering 2006 are used.

PCA is first performed on data sets comprising W and each of the 13 forcing variables. Then, to ensure that the dominant U_{10} signal does not mask fully the variance explained by additional factors, PCA is also performed on data sets comprising W, U_{10}, and each forcing variable (eleven data sets). To perform PCA, it is first required that all data are standardized—a transformation is applied so that each dataset has a mean of zero and a variance of one [Preisendorfer and Mobley, 1988].

In additional to performing PCA on the global dataset, we repeat the analysis for three localised regions (Figure 5.1) over the same time period (2006). The selection of the

TABLE 5.1: The mean and standard deviation of U_{10}, H_s and SST for three different oceanic regions.

Region	U_{10} (m s^{-1})		H_s (m)		SST (°C)	
	Mean	Std. dev.	Mean	Std. dev.	Mean	Std. dev.
North Atlantic	9.40	3.85	3.43	1.72	14.74	4.23
Equatorial Pacific	7.03	1.92	2.32	0.51	27.68	1.37
Southern Ocean	10.54	3.69	4.16	1.47	5.52	4.55
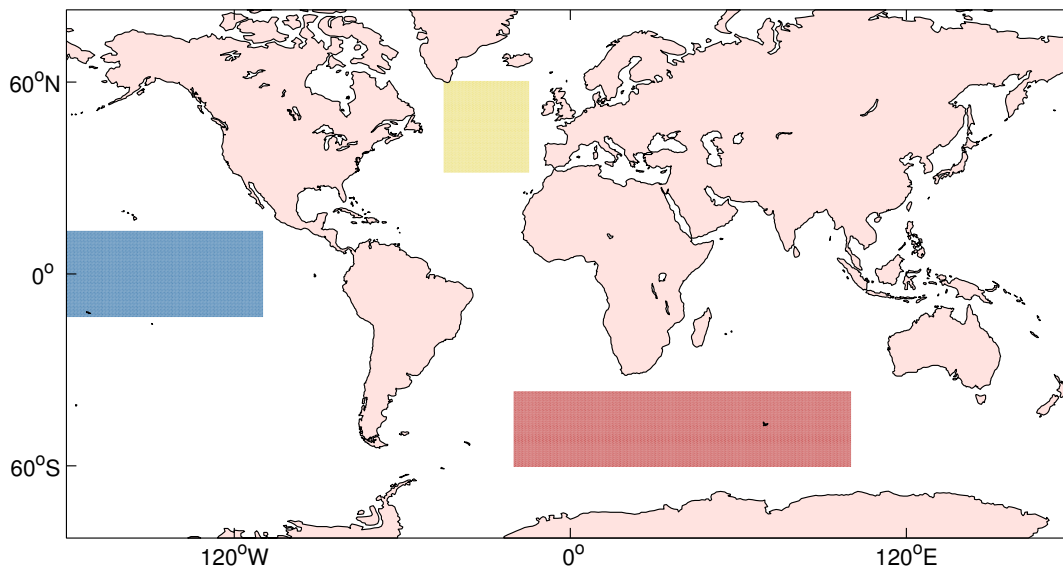
FIGURE 5.1: The three areas selected for the regional PCA study: North Atlantic (yellow region), Equatorial Pacific (blue region), and Southern Ocean (red region).

three regions is somewhat arbitrary, but each region is characterised by different wind, wave, and environmental conditions and their variability throughout the year. The mean and standard deviation of U_{10}, H_s, and SST for these regions are documented in Table 5.1. Both the North Atlantic and Southern Ocean regions have variable wind and wave regimes throughout the year in comparison to the Equatorial Pacific region, though the Southern Ocean region has on average a much lower SST than the North Atlantic. The Equatorial Pacific is characterised by relatively lower winds and wave heights, both of which are less variable, and a much higher mean SST than the other two regions.

5.2 Results

5.2.1 Dependence on secondary forcings

5.2.1.1 Dependence of whitecap fraction on wave variables

The variability of whitecap fraction as a function of wave parameters is assessed by plotting $\overline{\overline{W}}/\overline{W}$ as a function of H_s, T_p, and MWS (Figure 5.2). It is evident that the influence of secondary factors on W_{10} (Figure 5.2a, c, e) is much weaker than that on W_{37} (Figure 5.2b, d, f), in regards to both the magnitude of the trends observed and the spread in these trends with wind speed. Additionally, secondary influences are generally stronger with increasing U_{10}.

There is a small ($\sim$6%), approximately linear, increase in $\overline{\overline{W}}_{10}/\overline{W}_{10}$ over the range of H_s (Figure 5.2a). $\overline{\overline{W}}_{37}/\overline{W}_{37}$ increases much more with H_s, particularly in the range 2 m $< H_s <$ 6 m (Figure 5.2b). In the range 3 m $< H_s <$ 5 m (depending on the wind speed), there is a leveling off, or even reduction in $\overline{\overline{W}}_{37}/\overline{W}_{37}$ at low and moderate wind speeds, while at the highest wind speeds, $\overline{\overline{W}}_{37}/\overline{W}_{37}$ continues to increase, but at a much slower rate. The change in $\overline{\overline{W}}_{37}/\overline{W}_{37}$ increases from 15% to 20% over the range of H_s with increasing wind speed.

As for H_s, the influence of T_p is small for W_{10} (Figure 5.2c) but larger for W_{37} (Figure 5.2d). For normalized W_{10} there is little variation with T_p at low wind speeds, whereas at the highest wind speeds $\overline{\overline{W}}_{10}/\overline{W}_{10}$ shows a slight (5%) increase with T_p. Likewise, deviations from the mean for $\overline{\overline{W}}_{37}/\overline{W}_{37}$ over the T_p range are much more pronounced for high wind speeds; $\overline{\overline{W}}_{37}/\overline{W}_{37}$ can increase by as much as 20% as we move from a wave period of 5 s to 10 s. At lower wind speeds ($U_{10} < 12$ m s^{-1}), $\overline{\overline{W}}_{37}/\overline{W}_{37}$ peaks at $T_p = 11$ s. For $T_p > 13$ s, changes to normalized W are minimal.

Mean wave slope combines information for H_s and T_p, and so reflects joint changes in both variables. This variable serves as an indicator of the degree of wave development with MWS reducing as waves develop ($MWS > 0.03$), reach wind-wave equilibrium ($MWS \sim 0.03$), and finally become over-developed ($MWS < 0.03$) [Bourassa et al., 2001]. Again, variations in normalized W_{10} are small (Figure 5.2e). There is a clear peak in normalized W_{37} (Figure 5.2f) for a given wind speed, with the peak values occurring in the range $0.025 < MWS < 0.035$. At the lowest wind speeds, $\overline{\overline{W}}_{37}/\overline{W}_{37}$
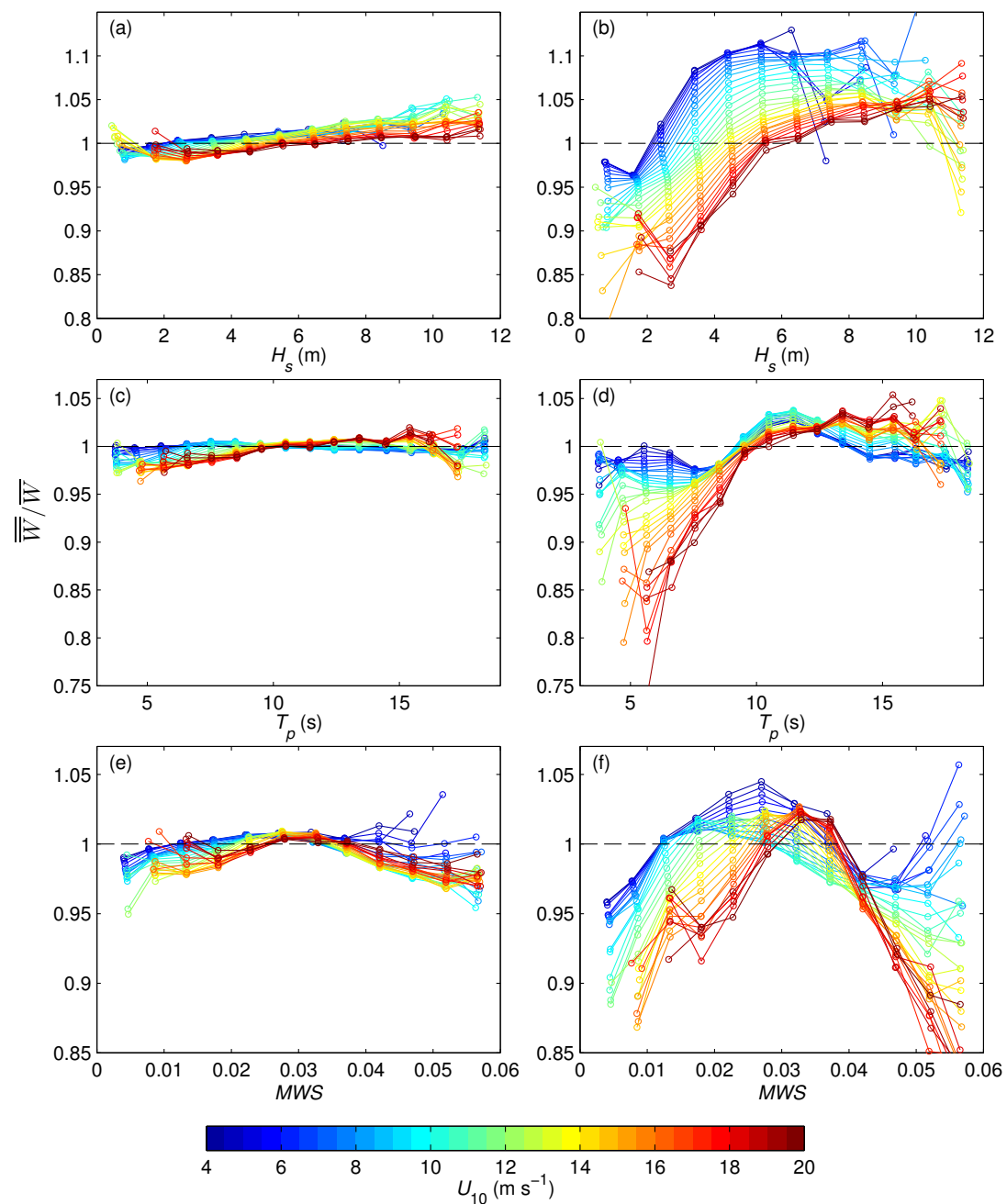
FIGURE 5.2: The dependence of $\overline{\overline{W}}_{10}/\overline{W}_{10}$ (a, c, e) and $\overline{\overline{W}}_{37}/\overline{W}_{37}$ (b, d, f) on significant wave height (top two panels), peak wave period (middle panels), and mean wave slope (bottom panels).

begins to rise again at $MWS > 0.045$. The peak in normalized W at or close to the threshold marking wind-wave equilibrium indicates that sea states in equilibrium with the wind result in the largest values of W at a given wind speed.

5.2.1.2 Degree of wave development

The results in the previous section provide a coarse assessment of changes to W due to the wave field, characterised by three different variables. We examine the dependence of W on H_s, T_p, and MWS again in Figure 5.4, but with further classification of the data as either wind sea (yellow/red curves) or swell (blue curves). To do so, the relationships in section 3.2.3.2 are used to form a classification system through which the influence of wave development on W can be assessed. W estimates are classified as representative of a fully developed sea if $(H_{\text{fd}} - 0.5) < H_s \leq (H_{\text{fd}} + 0.5)$, and $(T_{\text{fd}} - 1) < T_p \leq (T_{\text{fd}} + 1)$. Estimates are classified as wind sea cases if $H_s \leq H_{\text{fd}} - 0.5$ and $T_p \leq T_{\text{fd}} - 1$. Finally, W estimates are classed as swell if $H_s > H_{\text{fd}} + 0.5$ and $T_p > T_{\text{fd}} + 1$. There are a small number of cases where data cannot be classified as either swell or wind sea due to data being categorised as swell based on H_s and wind sea based on T_p, or vice-versa. The distributions of these select cases follow those for the unpartitioned data and so these data are most likely marginal cases (i.e., only just making one criteria or another) rather than extreme cases (e.g., limited to the lowest or highest U_{10} values only). These cases (approximately 10%) are omitted from the analysis.

In line with the analysis of Sugihara et al. [2007], we further partition the wind sea cases by the degree of wave development through grouping cases by the corresponding estimate of wave age (equation 3.6). Wave ages for wind sea cases have a range $5 \leq \Phi \leq 31$, with an almost symmetric distribution around the peak frequency of occurrence at $\Phi = 22$ (Figure 5.3). We divide the data classified as wind sea into three groups: $5 \leq \Phi < 20$, $20 \leq \Phi < 25$, and $25 \leq \Phi \leq 31$, so that the number of data in each group becomes approximately equal.

The trends in normalized W_{10} due to change in H_s are quite similar for wind sea and swell-dominated cases. For normalized W_{37} (Figure 5.4b), there is some evidence to suggest that the leveling off of normalized W with higher H_s is mostly confined to swell
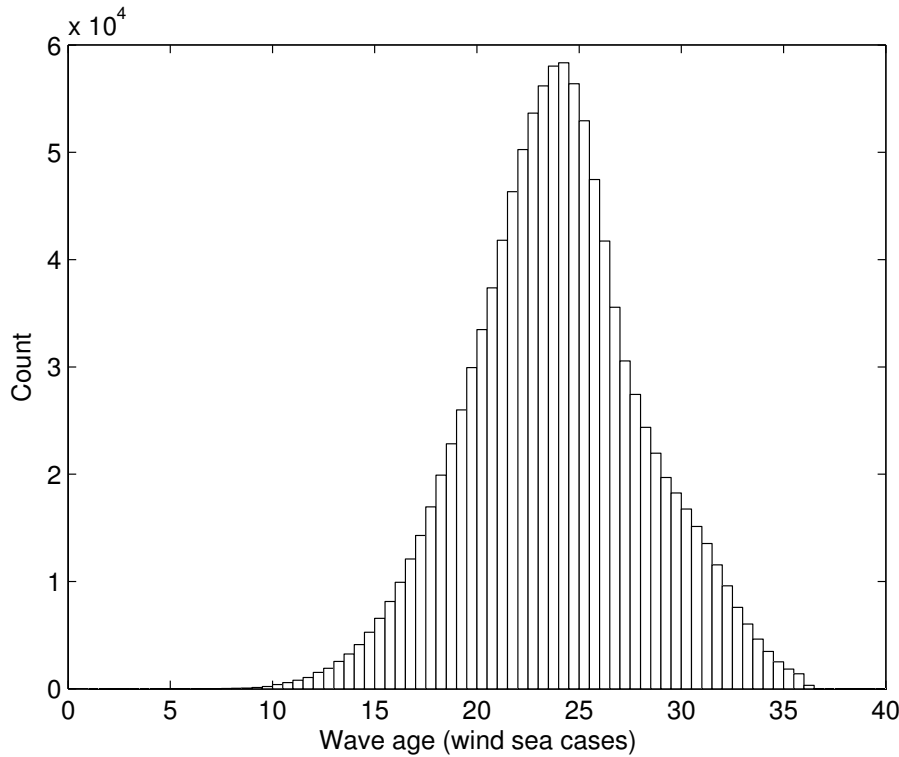
FIGURE 5.3: Distribution of wave age estimates for W estimates classified as wind sea.

cases, whereas for wind sea conditions, normalized W continues to increase although at a decreasing rate with increasing H_s.

Trends with T_p are somewhat harder to evaluate due to the grouping of wind sea data at low T_p, and swell at high T_p. The influence of T_p on W_{10} at a given wind speed is minimal in swell conditions. A trend of increasing $\overline{\overline{W}}_{10}/\overline{W}_{10}$ is seen for wind sea, whereas for swell there is little change. For W_{37} the largest deviations from the mean wind speed behavior can be seen for wind seas at $T_p < 8$ s, where seas are likely to be under-developed. Suppression of W_{37} is strongest in this regime at the highest wind speeds; under these conditions, seas will be significantly under-developed.

The results for MWS show that W_{10} is suppressed slightly for wind sea and swell cases either side of $MWS = 0.03$, but with no clear separation between the behavior of the two cases. In conditions where $MWS > 0.03$, nearly all W estimates are classified as wind sea. Here, normalized W_{37} increases with MWS at low winds, whereas at higher wind speeds there is a strong decrease with increasing MWS. The latter results in a large suppression of W_{37}; in such conditions, the magnitude of the wind in excess of equilibrium is at its largest [Bourassa et al., 2001]. We expect cases for which $MWS <$
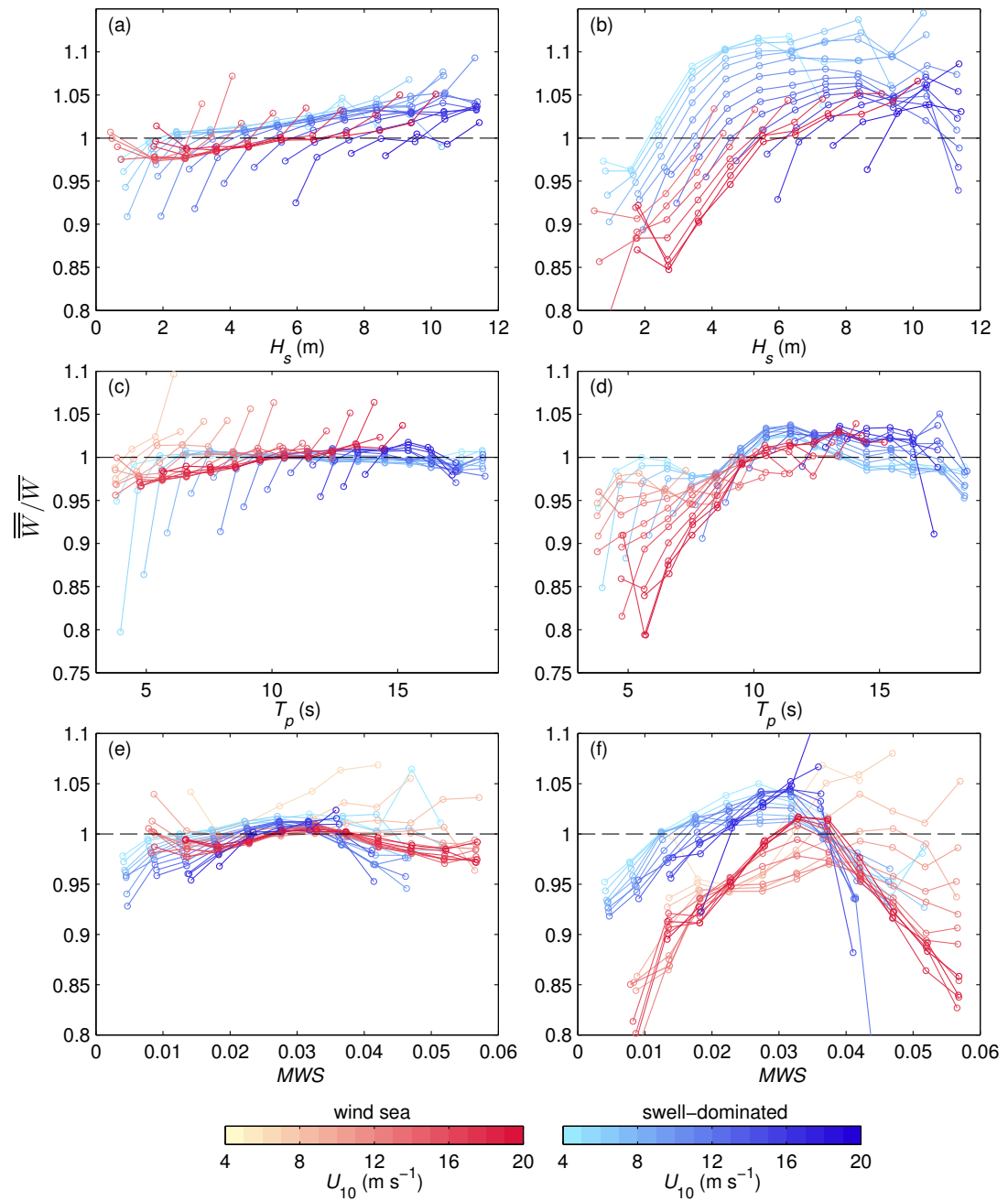
FIGURE 5.4: As Figure 5.2 but with data further classified into wind sea (yellow/red curves) and swell dominated cases (blue curves).

0.03 to correspond to well-developed seas; however, W estimates can still be classified as wind sea based on the classification using H_s and T_p values. In this MWS regime, there is a decrease in normalized W_{37} with decreasing MWS for both swell and wind sea cases, although this decrease is more rapid in wind seas.

We further assess the influence of the wave field in Figure 5.5 by classifying data as either swell, fully developed, or wind seas, with wind seas further classified by wave age (section 3.2.2). Using 1 m s^{-1} bins to increase the number of W estimates in individual bins, we calculate wind speed bin-averaged means, $\overline{W}$, for each of the classes. The ratios $\overline{W}/\overline{W}_{\text{fd}}$ are calculated for swell and three wave age ranges of wind sea to quantify enhancement or suppression of W, at a given wind speed, due to under-developed (wind sea) or over-developed (swell) wave states with respect to a fully developed wave field. These are shown in Figure 5.5a for W_{10}, and Figure 5.5b for W_{37}.

For W_{10}, deviations from W_{fd} in swell and wind seas are almost negligible for 9 m s^{-1} < U_{10} < 20 m s^{-1}. For 3 m s^{-1} < U_{10} < 7 m s^{-1}, there is enhancement of W_{10} for wind seas compared to fully developed sea states. However, this trend could be a result of the limitations of such a classification for low wind speeds; W estimates for U_{10} < 7 m s^{-1} are almost always classified as swell-dominated, with only 1–2% classified as fully developed. Therefore, calculation of $\overline{W}_{\text{fd}}$ at these wind speeds may suffer from poor statistics.

For W_{37} (Figure 5.5b), deviations from W_{fd} are generally larger. Over much of the wind speed range, W is enhanced in swell-dominated conditions, and suppressed in wind seas. Interestingly, for 7 m s^{-1} < U_{10} < 13 m s^{-1}, the largest suppression of W_{37} occurs in wind seas with highest wave ages ($25 \leq \Phi \leq 31$). At higher wind speeds (U_{10} > 14 m s^{-1}), W_{37} is suppressed most in the youngest wind seas ($5 \leq \Phi < 20$), with $\overline{W}$ ~10% lower than $\overline{W}_{\text{fd}}$.

5.2.1.3 Dependence on other environmental factors

The dependence of W upon SST and the viscosity of water are examined in Figure 5.6. The viscosity of water, although strongly related to SST, also takes into account the effect of salinity. This parameter may be considered to be more fundamentally related
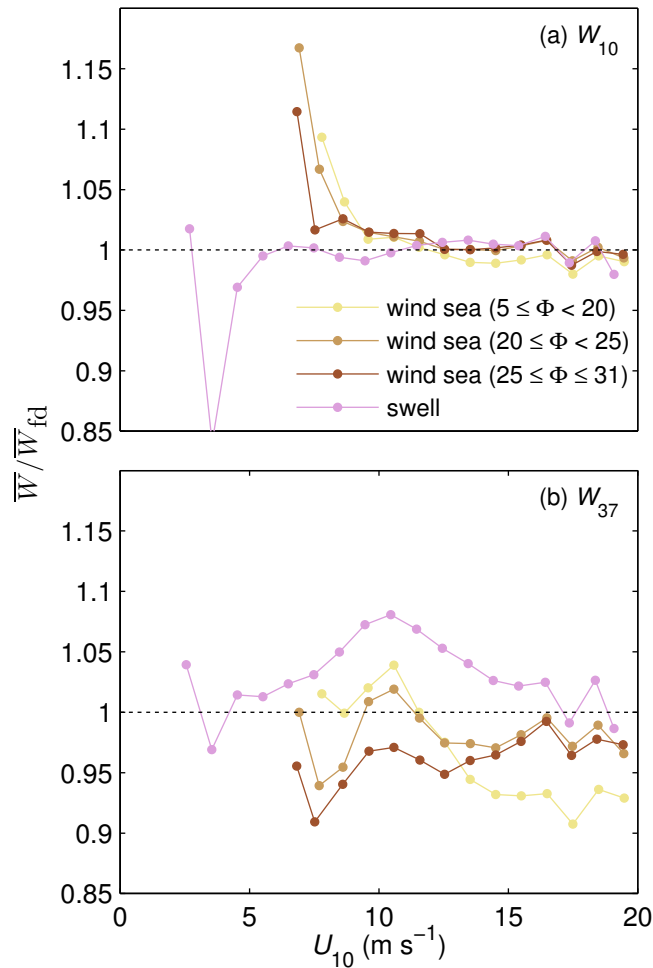
FIGURE 5.5: Ratio of wind speed averaged W_{10} (a) and W_{37} (b) to $\overline{W}_{\mathrm{fd}}$ for swell and wind sea cases, with wind sea further classified by wave age.

to the dynamic wave breaking process than SST itself, due to, for example, its role in determining the surface tension of the surface water.

The influence of SST on W_{10} is very small, with a slight reduction in $\overline{\overline{W}}_{10}/\overline{W}_{10}$ at the highest values of SST and for the highest wind speeds only (Figure 5.6a). Normalized W_{37} is near constant for SST $< 20^{\circ}$C, but drops off rapidly for SST $> 20^{\circ}$C (Figure 5.6b). Whitecap fraction is enhanced at a given wind speed by up to 12% at low temperatures. These deviations gradually decrease for SST ranging from 5 to 20°C. Whitecap fraction is suppressed by up to 25% for SST $> 20^{\circ}$C.

When plotted as a function of ν_w (Figure 5.6d), the effect on normalized W_{37} is as expected from the results for SST. We stress the relatively small influence these factors have (no larger than 5%) on normalized W_{10} (Figure 5.6c). There is however slightly
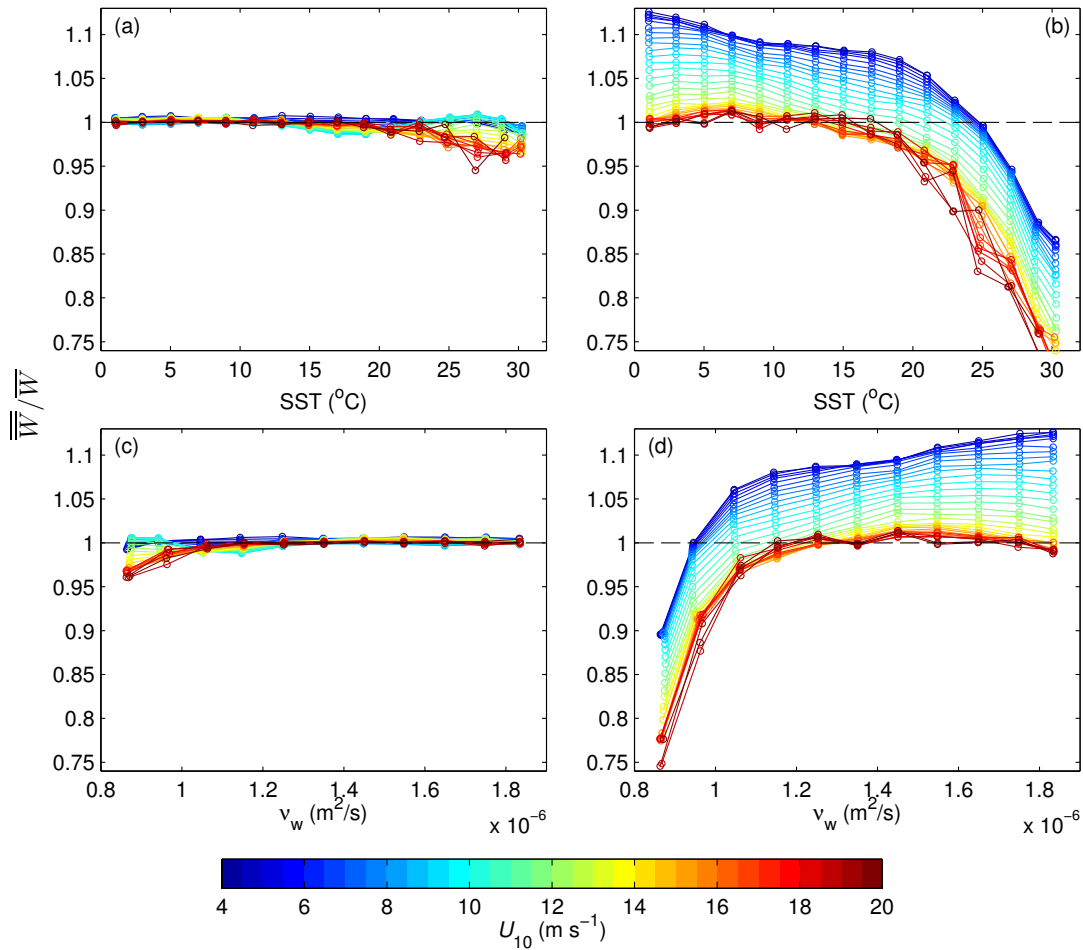
FIGURE 5.6: The dependence of $\overline{\overline{W}}_{10}/\overline{W}_{10}$ (a, c) and $\overline{\overline{W}}_{37}/\overline{W}_{37}$ (b, d) on SST, (top panels), and viscosity of water (bottom panels).

more uniform behavior between the trends in normalized W_{10} and W_{37} at the higher wind speeds (red), than that seen for SST.

We explore the dependence of W upon air temperature and the air-sea temperature difference, ΔT, in Figure 5.7. The trends in both W_{10} and W_{37} for T_a (Figure 5.7a, b) are very similar to those found for SST; this is most likely due to near surface air temperature coming into (near) equilibrium with SST over much of the ocean.

The influence of ΔT on W is less clear. The overall influence on W_{10} (Figure 5.7c) is again less than 5%; a slight peak in normalized W can be seen (at least for moderate to high wind speeds) just below $\Delta T = 0$, and a weak (5%) suppression for stronger unstable conditions. For W_{37} (Figure 5.7d), at moderate and high wind speeds, normalized W decreases as ΔT goes from unstable towards stable conditions. At the lower wind speeds, $\overline{\overline{W}}_{37}/\overline{W}_{37}$ shows enhancement for strongly unstable conditions, then falls off
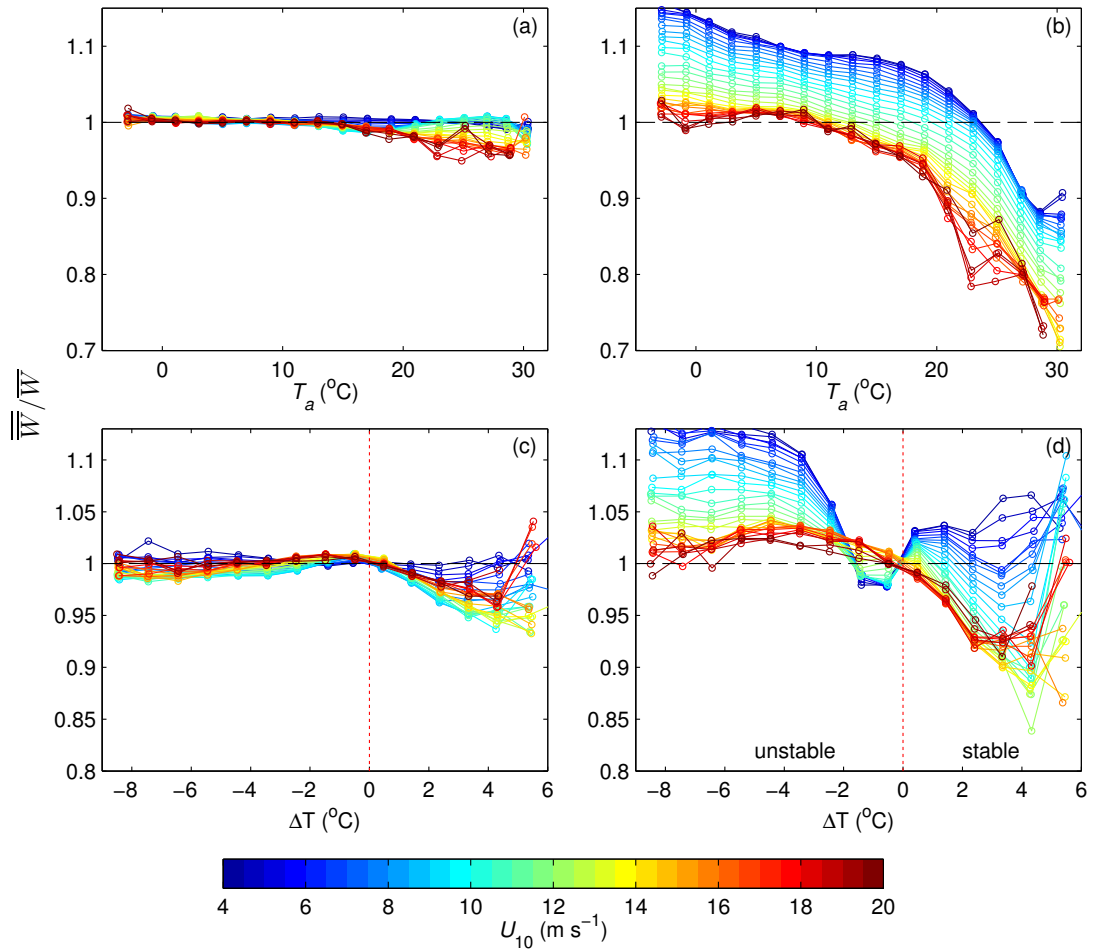
FIGURE 5.7: The dependence of $\overline{\overline{W}}_{10}/\overline{W}_{10}$ (a, c) and $\overline{\overline{W}}_{37}/\overline{W}_{37}$ (b, d) on T_a (top panels) and ΔT (bottom panels).

quickly as we go from unstable to near neutral conditions, but then increases slightly when ΔT becomes positive. In the most stable of conditions, normalized W_{37} is suppressed most at high wind speeds. The enhancement of normalized W_{37} is smaller in magnitude ($\sim 5\%$ at 14 m s^{-1}) than its suppression ($\sim 10\%$ at 14 m s^{-1}).

The influence of Chl a on W is shown in Figure 5.7. Note that for this variable, wind speed bins of width 1 m s^{-1} are used due to the relatively sparse availability of Chl a estimates—a consequence of loss of coverage due to sunglint contamination and atmospheric correction issues—in comparison to the majority of other database variables for which near global coverage exists on a daily basis. The influence of Chl a on $\overline{\overline{W}}_{10}/\overline{W}_{10}$ is dependent on the wind speed (Figure 5.8a); at low winds there is reduction in normalized W_{10} as Chl a increases, but as wind speed increases the trend turns positive. Trends in normalized W_{37} (Figure 5.8b) also vary greatly with wind speed. At low winds, $\overline{\overline{W}}_{37}/\overline{W}_{37}$ only begins to deviate from the mean wind speed
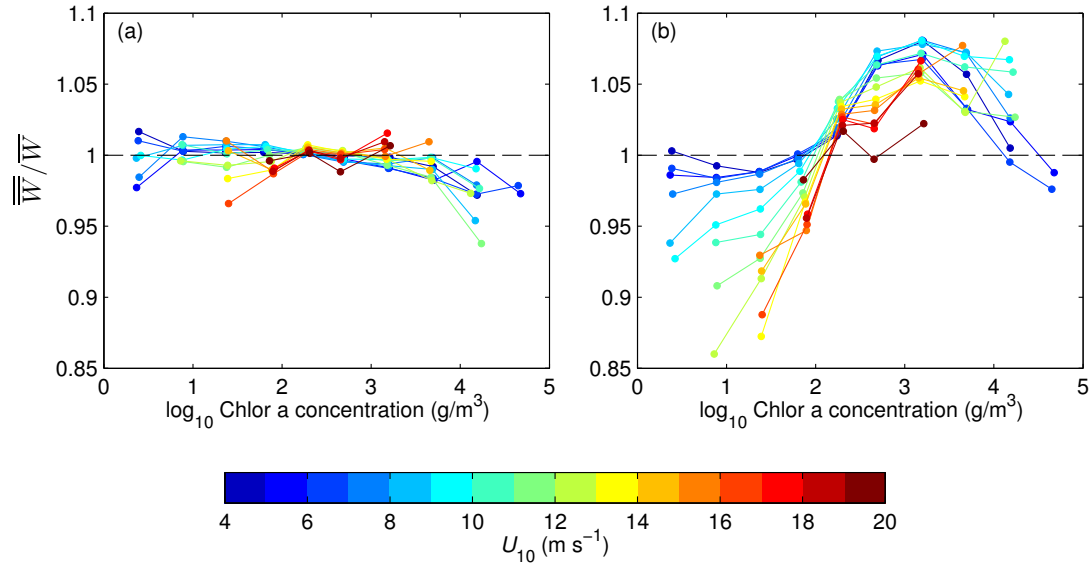
FIGURE 5.8: The dependence of $\overline{\overline{W}}_{10}/\overline{W}_{10}$ (a) and $\overline{\overline{W}}_{37}/\overline{W}_{37}$ (b) on Chl a.

behaviour at Chl $a \sim 2$ g m^{-3}, peaks at ~ 3 g m^{-3}, before falling off. At higher wind speeds, trends follow a linear increase in normalized W_{37} with increasing Chl a up until Chl a reaches ~ 3 g m^{-3}. The plateauing of $\overline{\overline{W}}_{37}/\overline{W}_{37}$ around this value of Chl a is reasonably robust with varying U_{10}. W_{37} can deviate from the mean wind speed behaviour by as much as 15% at moderate to high wind speeds (12 m s^{-1} $< U_{10} <$ 16 m s^{-1}).

5.2.2 Relative contribution of forcing factors

The relative contribution of the different factors to variability in W is evaluated using prinicipal component analysis. We show, for both W_{10} and W_{37}, the variance explained by the first principal component (PC1) for wave and wind-wave variables (Figure 5.9a), and other environmental factors (Figure 5.9b). All forcing parameters are considered, including those which have an explicit dependence on wind speed, such as the two Reynolds numbers. In the figures, variables are ordered by the percent variance explained by PC1.

The highest ranking variable is U_{10} for both W_{10} and W_{37}. Two of the wind-wave variables (the breaking-wave and roughness Reynolds numbers) perform almost as well, with significantly higher scores than the other wind-wave variables considered.
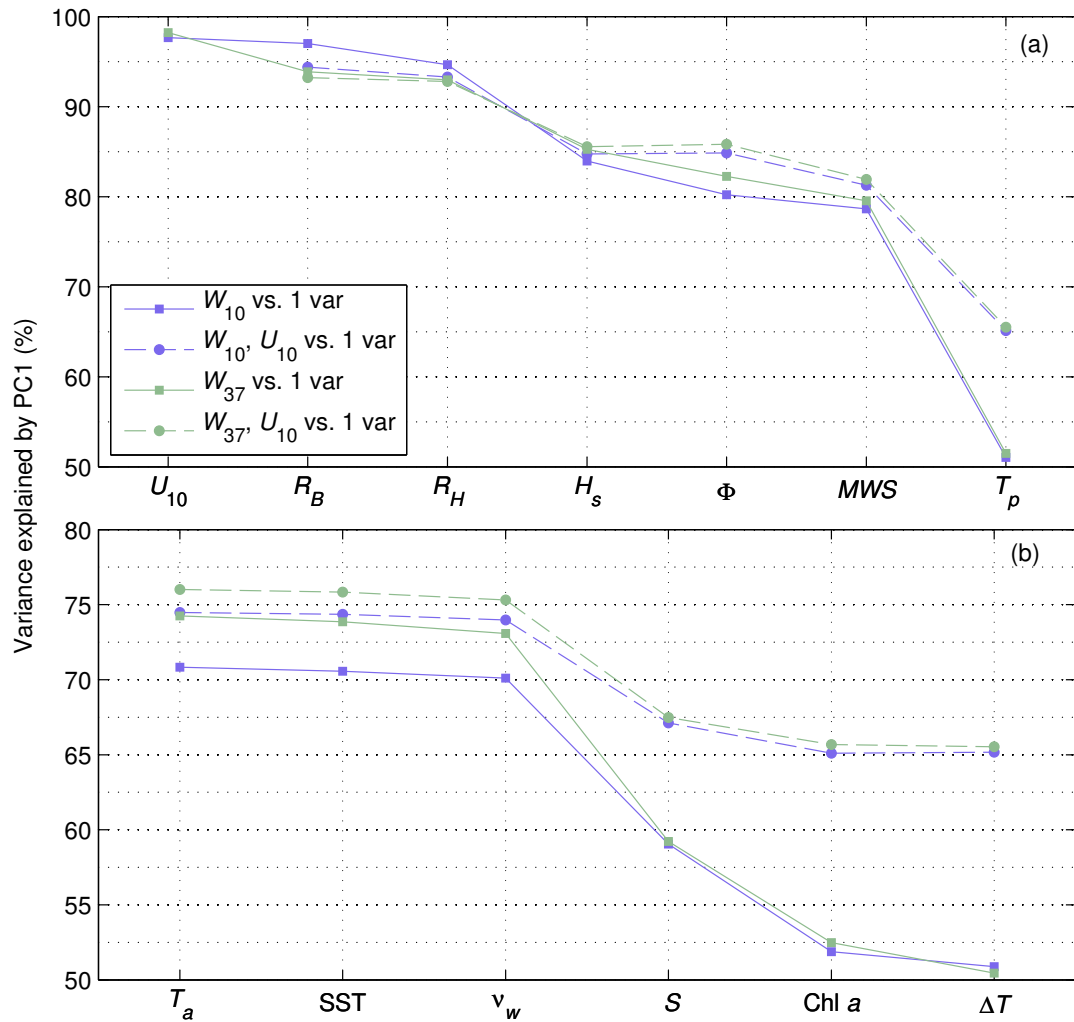
FIGURE 5.9: Percent variance explained by the first principal component PC1 for data sets combining W with various other factors (solid lines), and the corresponding data sets when wind speed is included (dashed lines).

The next best performing wave variable is H_s, followed by Φ, and MWS. T_p accounts for only 50% of the variance of both W_{10} and W_{37}.

T_a, SST, and ν_w all describe roughly the same percent variance. Notably, these three variables also show the biggest difference in variance explained by PC1 between W_{10} and W_{37}, accounting for $\sim$4% more variance in W_{37} than in W_{10}. This supports the findings in section 5.2.1.3 that SST (or viscosity of water) has a more pronounced impact on W_{37} than on W_{10}. Note that this difference is not as large as one might expect because here we consider estimates covering almost the whole globe, whereas large changes to W resulting from SST changes are probably confined to very warm waters (equatorial regions). In the case of the breaking wave Reynolds number and the roughness Reynolds number, variance explained by PC1 for W_{37} is slightly lower

than that for W_{10}. Because both Reynolds numbers combine information on the wind field and wave field, they may be better predictors of the variability of active foam (W_{10}), and not quite as successful when residual foam is included (W_{37}). The finding that the Reynolds numbers account for slightly less variance than wind speed alone is in stark contrast to a recent study of eddy covariance sea spray fluxes [Norris et al., 2013a], which found that a wave roughness Reynolds number explained up to twice the variance in the sea spray flux as wind speed alone. The slightly poorer performance of the Reynolds numbers here might result from inadequacies in model estimates of wave properties, the necessarily indirect estimate of u_*, or a degree of self-correlation between W and U_{10} introduced through the whitecap retrieval itself.

When wind speed is included in the data sets (dashed lines), the ranking of the percent variance explained by PC1 is preserved, despite changes in the absolute values. In general, inclusion of wind speed lifts the variance explained by PC1—confirming that combining individual variables with wind speed is more effective in describing variability in W than the variable alone is. This is not the case for the two Reynolds numbers, for which inclusion of wind speed slightly lowers the percent variance explained by PC1; this is likely due to the dependence of both Reynolds numbers on wind speed through the friction velocity.

5.2.2.1   Regional PCA results

Results for the regional PCA are shown in Figure 5.10. Note that for clarity, for the regional study PCA is performed on data sets comprising W and each of the 13 forcing variables only, i.e., the effect on PC1 scores of including U_{10} information is not considered. Through comparison of the top and bottom panels, it is clear that between regions variations in PC1 scores are much larger for environmental variables (bottom panel) compared to wave variables (top panel). For each wave variable, PC1 values vary by less than 10% between regions. PC1 scores for wave variables are especially close for the Southern Ocean and Equatorial Pacific regions, with PC1 lying slightly higher for numerous variables in the North Atlantic region.

For environmental variables, variations in PC1 scores between regions are as large as 25%, as is the case for T_a. Largest variation between regions exists for T_a, SST, and
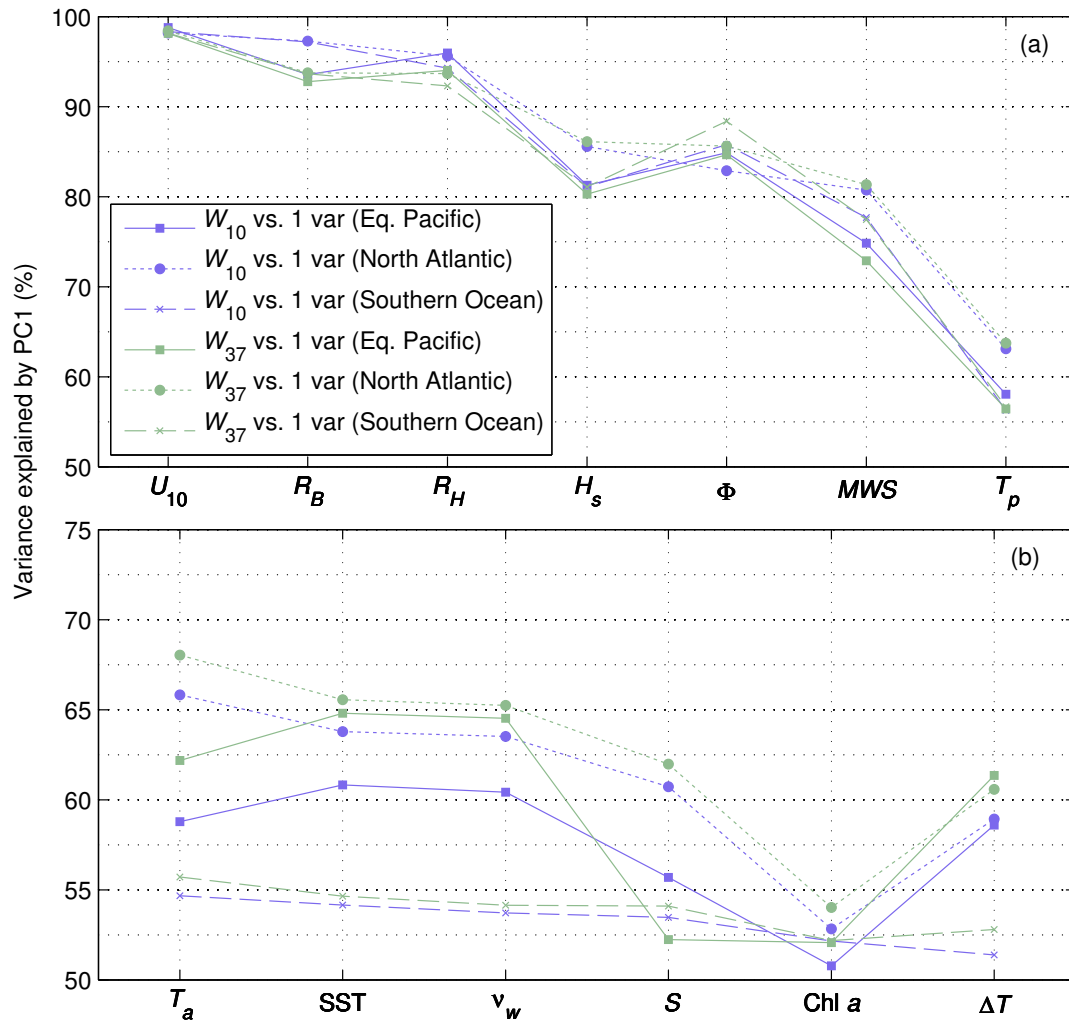
FIGURE 5.10: Percent variance explained by PC1 for data sets combining W with various other factors (solid lines).

ν_w. For both the Eq. Pacific and North Atlantic regions, the PC1 values for W_{37} are noticeably higher for W_{37} than W_{10}.

5.3   Discussion

5.3.1   Influence of secondary factors

Secondary factors may perturb the whitecap fraction from the mean for a given wind speed in several distinct ways: by changing the scale or frequency of wave breaking events, by modifying the bubble plume properties, and by modifying the surface foam

properties. In all the cases studied, W_{37} (active and residual foam) shows a stronger response to secondary factors than does W_{10} (predominantly active whitecaps).

Some care should be taken when interpreting Figures 5.2, 5.5, 5.6, 5.7, and 5.8. The ratio of the observed W at a given value of both wind and secondary factor to the mean for each wind speed are shown. The means are calculated from the individual contributing values and are thus dependent on the probability distributions of the secondary factors. Offsets between the lines at different wind speeds may occur purely because of differences in these probability distributions at different wind speeds—for example the range of significant wave heights observed is very different at high and low winds speeds, so that the mean W occurs at different values of H_s for different wind speeds. Relative trends in $\overline{\overline{W}}/\overline{W}$ are thus more informative than the absolute values.

5.3.1.1 Influence of the wave field on W

The results in Figures 5.2-5.5 relate the whitecap fraction to various measures of wave state. There exists considerable subtlety in the response of W to wave state, with W_{10} and W_{37} sometimes showing different behavior.

Both W_{10} and W_{37} are generally suppressed in developing wind seas (low H_s and/or T_p) (Figure 5.4a-d); the suppression is greatest when wind and waves are far from equilibrium as can be seen under conditions with moderate to high wind speed but very low T_p (Figure 5.4d). At low and moderate wind speeds, W peaks at $T_p \sim 11$ s; this peak shifts to higher T_p with increasing U_{10} for wind seas (Figure 5.4c, d).

W tends to be largest when the wind and waves are in, or close to, equilibrium with the local wind. This enhancement close to wind-wave equilibrium is most clearly observed when MWS is used to define the wave field; peak W occurs at ~ 0.03, corresponding to waves in equilibrium with the wind. In wind sea conditions, the peak shifts to higher MWS (less well developed waves) as the wind speed decreases. In wind seas at low wind speeds, W_{37} appears to continue to increase with MWS, but this may reflect a lack of data at sufficiently high MWS.

When we compare W with that for a fully developed sea state for the local wind (Figure 5.5), we find no appreciable differences in W_{10} over much of the wind speed range. However, we again find a general trend of suppression of W_{37} in wind seas; at

moderate wind speeds, largest suppression of W_{37} occurs in wind seas with highest wave age; at higher wind speeds largest suppression occurs in the youngest wind seas.

The results above are consistent with recent studies showing enhancement of W in developed seas relative to that in under developed seas [Callaghan et al., 2008b; Goddijn-Murphy et al., 2011; Stramska and Petelski, 2003], and of increasing W with wave age in wind seas [Sugihara et al., 2007].

Using MWS to characterise the degree of wave development, we find suppression of W at a given wind speed in well-developed seas ($MWS < 0.03$) (Figure 5.4e, f); this suppression increases as the waves become increasingly over-developed. This picture is consistent both with recent studies showing evidence for suppression of W in the presence of swell [Callaghan et al., 2008b; Sugihara et al., 2007].

However, when we classify W estimates based on comparison of H_s and T_p with those expected for fully-developed seas, we find that W_{37} is largest in swell-dominated seas (Figure 8b). This result may at first seem at odds with the results shown in Figure 5.4e, f. We must note the difference between use of MWS as an indicator of the wave state, and classification of W estimates based on comparing H_s and T_p to values expected for fully developed seas. The latter requires no information on local wind speed, and so cannot be judged as a definitive measure of the degree of wave development. In contrast, classification based on a comparison of H_s to H_{fd} and T_p to T_{fd} inherently considers the local wind speed. Different measures of wave development can give apparently contradictory impressions; this results from the partial picture provided by averaging different subsets of the data, suggesting the need for more detailed information on wave spectra to fully resolve the wave influences on whitecap fraction.

For wind sea dominated conditions, the increase in W with wave state is readily interpreted as resulting simply from larger waves and consequently either larger individual breakers or more frequent breaking events. For swell-dominated conditions, the behavior is more complicated with W having a more or less distinct peak at some mid-range of wave state, decreasing for both less well and better developed wave states. We speculate that this results from changes in wave-wave interactions between the wind sea and swell as a function of the difference between their respective wavelengths.

Both wind waves and swell are dispersive, and grow and break suddenly as a consequence of wave-wave interactions as individual waves pass through a wave group [Donelan and Pierson Jr., 1987]. The steepening of waves during such interactions is greatest when the wavelengths are similar, decreasing as the difference in wavelength increases. Swell dominated cases where the swell and wind waves are similar in wavelength would thus be expected to enhance wave breaking, while those where the wavelengths were very different would not. We note that W_{10} follows this pattern with T_p but not with H_s; we attribute this to the fact that T_p provides a better measure of separation on wind sea and swell scales, while the H_s results are averaged over a range of wave and swell scales combined.

We have considered the success of several wind-wave and wave variables in accounting for variability in W. Of these, the two Reynolds numbers perform best. It has been shown previously that the primary contribution to wave breaking and resulting whitecaps comes from the high frequency components of the wave spectrum, and not the dominant waves [Dulov et al., 2002; Gemmrich et al., 2008; Plant, 2012]. Therefore, the success of wind-wave variables in accounting for variability in W may be improved with use of wave measurements describing the wind sea part of the spectrum only, e.g., the peak wave period for wind-waves, rather than peak wave period of the total spectrum. This hypothesis could be tested with expansion of the database to include wave measures quantifying a partitioned spectrum.

5.3.1.2 SST and water viscosity effects

Both normalized W_{10} and normalized W_{37} show a clear decrease in whitecap fraction for SSTs greater than about 15–20ºC; the suppression is much stronger for normalized W_{37}. The findings could be explained following the argument of Monahan et al. [1983], namely that rise times of bubbles are longer in colder waters, resulting in longer whitecap lifetimes and hence greater values of W under the same meteorological conditions. However, Leifer et al. [2000] have shown that for clean bubbles the SST effect on the bubble rise velocity is size dependent. This suggests that SST would influence the whitecap fraction not just through the decay rate, but also by changing the bubble size distribution that contributes to the surface foam layer. Because Anguelova and Gaiser [2011, 2013] have shown that foam emissivity and thus T_B due to whitecaps

depends on the void fraction and thickness of the foam layers, one could expect W_{10} and W_{37} to be sensitive to such an influence. Studies of such intriguing connections would require data on bubble size distributions from regions with different seawater temperatures—this is only possible for in situ studies, not satellite based retrievals.

Our results for W_{37} could be further explained by a reduction in the decay time of residual foam patches with increasing SST [Bortkovskii and Novak, 1993], while those for W_{10} remain harder to explain. The relatively flat response to SST below 15–20°C is consistent with Stramska and Petelski [2003], who found no SST response between 2 and 13°C.

Another possibility is that the observed SST dependence is a result of a spatial correlation between SST and some other factor affecting whitecap properties such as the concentration of organic surfactants in the surface water (section 5.3.1.4). Finally, we cannot entirely exclude the possibility that uncertainty in the models used in the W algorithm may contribute to the observed temperature dependence.

The impact of viscosity largely reflects that of SST, although there is a little less scatter, particularly for W_{37}; this may result from the inclusion of salinity as well as temperature.

5.3.1.3 Atmospheric stability effects

The air temperature dependence of W_{10} and W_{37} follows that of the SST dependence. Since air and water temperatures do not usually differ by more than a few degrees Celsius over much of the ocean [Kara et al., 2007], it is likely that results are largely due to the SST dependence.

We find W_{10} is largest for weakly unstable conditions at most wind speeds; there is little change for $\Delta T < -3^{\circ}$C, but a decrease with increasing stability. W_{37} displays even more complex behavior; for U_{10} above about 13 m s^{-1}, the behavior is similar to that for W_{10}, with slight decrease for stronger instabilities and a greater decrease with increasing stability. At low wind speeds, W_{37} is generally lowest for weakly unstable conditions, with largest enhancement of W for the most unstable conditions.

Previous studies have found an increase in W for unstable conditions [Monahan and O'Muircheartaigh, 1986; Monahan and Woolf, 1988; Wu, 1988]. This is plausibly explained by an increase in u_* at a given wind speed because of the additional turbulence generated by convection. Some caution is needed when interpreting our results, however; the satellite winds used here are not true local values, but the equivalent wind under neutral conditions. Scatterometer backscatter depends on short surface waves, which respond rapidly to the local wind stress, rather than wind speed, and are calibrated to give the equivalent neutral wind that would provide the same wind stress [Tang and Liu, 1996]. Thus our measurements should not be expected to exhibit the same wind speed/stress dependence on stability as in situ measurements. The stability dependence of W_{10} and W_{37} must thus have some other cause.

We speculate that one possible cause is a change in the spatial distribution of wind stress with stability within the satellite footprint. Under unstable conditions, the superposition of large scale convective motions on the mean wind may lead to highly variable local surface winds, and wind stress, due to convergent flow at the base of updrafts at scales much smaller than the footprint of the brightness temperature measurement. This will lead to spatially variable whitecap formation, and because whitecap fraction is a highly nonlinear function of the local wind, the spatially averaged W will be higher than that for the same spatially averaged mean wind. The nature of the spatial variability will change with both the strength of the instability and with the mean wind speed, and may include more or less randomly distributed, isolated thermal plumes, organized cellular convection with open or closed cells, and linearly organized boundary layer rolls.

5.3.1.4 Surfactant concentration effects

The influence of surfactant concentration on W has been evaluated using satellite-based estimates of chlorophyll a concentration. It is interesting that at low wind speeds W_{10} decreases slightly with increasing Chl a. If this is a robust trend, it could indicate a possible influence of surfactant concentration on the active wave breaking process, mediated by either (i) surface tension effects, or (ii) changes to the bubble properties in active breakers that are sufficient to affect the retrieval algorithm.

Generally, W_{37} increases with increasing Chl a at a given wind speed, with the influence being larger for moderate and high winds. This is likely due to the influence of surfactant concentration (here quantified using Chl a) on the lifetime of residual decaying foam layers. Callaghan et al. [2013] confirmed that the presence of surfactants acts to stabilize surface bubbles and so increase whitecap decay times. For satellite-based observations, this would manifest as an increase in W_{37} (which captures the thinnest foam layers).

We cannot rule out the possibility that trends in Chl a are in fact due to the dependency of surfactant concentration on SST. In the open ocean, the primary source of natural surfactant compounds are phytoplankton exudates, which can be transported to the surface through diffusion and via rising bubbles [Žutić et al., 1981]. Surfactant concentrations tend to be higher in cooler waters where nutrients are more plentiful and primary production is higher. This inverse correlation between SST and phytoplankton concentration [Falkowski et al., 1998; McClain et al., 2004] might thus be expected to contribute to a relative reduction in the lifetime of residual foam in warm waters. It is also possible that covariation between the two actually results in the trends being mistakenly identified as due to Chl a when they are in fact due to water temperature effects.

5.3.2 Radiometric frequency dependence of W estimates

The operational radiometric frequency is an important aspect of satellite estimates of whitecap fraction, with different frequencies able to discriminate, at least approximately, between foam layers depending on their thickness (section 3.2). Our results show unambiguously that wind speed and secondary factors affect W_{10} and W_{37} differently.

Importantly, these differences can be plausibly explained with different influences of the secondary factors on foam layers associated with different whitecap lifetime stages. This lends support to the notion that W_{10} and W_{37} represent different mixes of active and residual whitecaps. This is also an independent confirmation of the conclusions regarding the frequency sensitivity to foam layer thicknesses which Anguelova and Gaiser [2011] obtained on the basis of purely physical considerations. Whitecap fraction is currently used to parameterise numerous bubble-dependent air-sea processes, but it

is expected that these parameterisations could be improved through use of measures of W that discriminate between active breakers and residual foam. As such, microwave measurements of whitecap fraction could prove beneficial to parameterisation of such processes.

Chapter 6

Improved representation of whitecaps for applications using whitecap fraction

A 'one-size-fits-all' approach has prevailed with regards to the use of W in both remote sensing and air-sea interaction applications. Simple wind speed only parameterisations of W have been used to quantify a variety of different processes including the production of sea spray aerosol, air-sea gas exchange rates, and changes to the ocean surface albedo due to the presence of whitecaps. Over previous decades, the focus much of the research on whitecaps has been on obtaining more accurate parameterisations of W, by increasing the accuracy and data volume of in situ estimates on which they are based. Despite these developments, the parameterisations remain inherently limited, and cannot be expected to predict W to the desired level of accuracy (section 2.4.1.2).

One a more fundamental level, questions regarding the complex relationship between observations of W and its determining factors have been asked. In particular, recent work by Callaghan and coworkers (see Callaghan [2013]; Callaghan et al. [2012, 2013]) has shown that W is largely determined by foam decay times, with decay rates controlled by bubble plume degassing and/or stabalisation of the surface bubbles. The results have implications for the parameterisation of air-sea exchange processes, for linking W to energy dissipation from breaking waves, and for the interpretation of measurements of whitecap fraction itself [Callaghan et al., 2012].

However, it remains the case that W provides a convenient approach to inferring information on important processes such as marine aerosol production and gas exchange [Woolf and Goddijn-Murphy, 2012], which are known to be dependent upon wave breaking and whitecapping. The significant amount of work involved with developing a novel satellite-based approach to estimation W is testament to the importance of the whitecap fraction as a measureable quantity. Whilst further development of the satellite-based approach is necessary, the technique is a significant improvement on the use of parameterisations based on a limited amount of photographic data.

In light of recent developments and results—regarding in situ and laboratory work, together with the analysis presented in this study—it is worth asking the question: how can we improve representation of whitecaps (for example, through relating W more closely to physical processes)? The most obvious first step is to explore possible approaches toward an improved understanding of the relationship between W and the different physical processes and mechanisms associated with whitecapping. This issue is explored in the first part of this chapter.

In the second part of this chapter, we reappraise use of W by the air-sea community, with focus on the prediction of SSA source fluxes, and bubble-mediated gas exchange, given the implications of both recent results and future operational use of satellite-based estimates of whitecap fraction.

6.1   Interpretation and measurement of whitecap fraction: Differentiating contributions from stage A and B whitecaps

Whitecaps provide a convenient visual expression of wave breaking. As such, W has been used to quantify various phenomena associated with breaking, ranging from dynamic processes such as bubble plume formation and ambient noise generation [Monahan and Lu, 1990], the production of spume droplets Mueller and Veron [2009], turbulent mixing and air-sea gas transfer, to climatically relevant processes such as the whitecap albedo effect [Frouin et al., 2001].

It has been argued that the majority of these air-sea interaction processes are likely more fundamentally linked to either (i) the energy dissipated by surface gravity wave breaking (visible or not) or (ii) parameters quantifying air-entrainment and bubble plume production. With regards to the former, W cannot be considered as a direct representation of the occurrence (frequency) and scale of surface wave breaking which—to first order—dictate the breaking contribution to energy dissipation rates. W, as currently estimated using either visible photographs or radiometric satellite-based measurements, remains an indirect, bulk representation of breaking. Further, W is not an unequivocal measure of total wave energy dissipation; in estimation of W, all information on the scales of the breaking waves contributing to W is lost, though the contributions are from breakers across the spectrum. This information is of fundamental importance for the development of more rational models of air-sea mass, momentum, and energy transfer and mixed layer dynamics [Kleiss and Melville, 2010]. Observations of W (using traditional methods) alone do not provide the level of information needed to more accurately quantify these air-sea interaction processes, and while important parameters pertinent to wave breaking, air entrainment, bubble plume evolution, and bubble bursting can be measured in the laboratory, this information is often not readily measurable and/or not applicable (or scalable) to open ocean conditions.

Alternatively, it may be possible to take advantage of recent advances in the measurement and modelling of W to better relate whitecap fraction to these physical processes. Specifically, there is a need to 'resolve' the different lifetime stages of whitecaps and quantify their contribution to W. As a first step towards this goal, there is a requirement to separate the contribution of whitecaps associated active breaking crests (W_A) from the total whitecap fraction W which is what is generally measured or predicted. This has been attempted previously using photographic data, according to the different visible signatures of stage A and B whitecaps. However, this is often a crude and inconsistent approach, and provides little insight into the relationship between whitecaps and the wave breaking process.

In this section, two approaches towards this goal, both presently the subject of development, are outlined and discussed: (i) a radiometric approach exploiting the dependence of the radiometric signature of foam on its thickness, and (ii) an approach based on the relationship between W and the statistics and dynamics of individual breaking

waves. For the second approach, we bring together recent results pertaining to the life-cycle of individual whitecaps and breaking wave statistics, which enables one to distinguish between estimates of total W, and the whitecap fraction resulting from actively breaking wave crests only, W_A.

6.1.1 Radiometric approach

The sensitivity of microwave frequencies to foam layer thicknesses has important implications for the remote sensing of (the surface expression of) whitecaps. Anguelova and Gaiser [2011] show that this sensitivity can be explained physically through consideration of radiometric and structural properties of sea foam, and that foam thickness depends on both the environmental conditions and the lifetime stage of the whitecaps. The results presented in chapter 5 on the different responses of W_{10} and W_{37} to secondary forcings, provide support to the idea that use of different radiometric frequencies in the $W(T_B)$ algorithm can crudely distinguish between different stages of foam lifetime.

The next step is to move from mere detection of the foam at different microwave frequencies, towards inferring further information on the foam layers [Anguelova and Gaiser, 2011]. The primary aim would be to qualitatively link the radiometric signature of the foam to its lifetime stage (active or decaying). Though it has been shown that as the radiometric frequency decreases from 37 GHz to 6 GHz its sensitivity to thinner foam decreases, the microwave signature is not a simple function of foam thickness. More work is needed to investigate the complex relationships between the physical and radiometric properties of oceanic foam and lifetime stage, before more assertive claims regarding this feature can be made.

The focus of this study is the end product of the satellite algorithm, W_{10} and W_{37}. Though it is clear that 'resolving' active and decaying whitecaps using the radiometric approach requires further work, including significant development of the retrieval algorithm, it is worthwhile comparing estimates of W at the two different microwave frequencies. Figure 6.1 shows maps of the ratio $\overline{W_{37}}/\overline{W_{10}}$, illustrating the varying relationship between the two W estimates for given forcing conditions (wind, wave, and environmental conditions) on a seasonal timescale. Therefore, variations in $\overline{W_{37}}/\overline{W_{10}}$
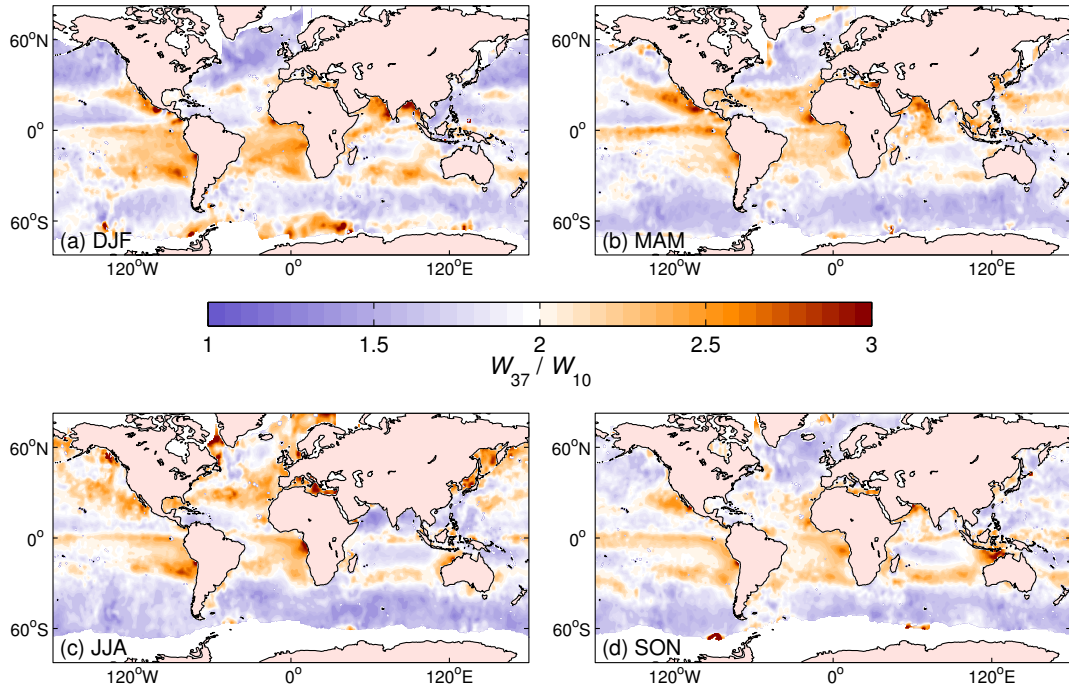
FIGURE 6.1: Seasonal maps of the ratio W_{37}/W_{10} for (a) December–February, (b), March–May, (c) June–August, and (d) September–November.

are related to the radiometric signature of the foam layers detected at the two frequencies. Following the arguments above, as the ratio increases, the area covered by thinner foam layers is increasing, relative to thicker foam layers. If one assumes that changes to the emissivity signal are driven primarily by foam layer thickness, the ratio of the two estimates is related to the persistence of the thinner foam layers.

$\overline{W_{37}}/\overline{W_{10}}$ is generally larger in mid latitude regions (especially along the Equator) where mean wind speeds are lowest. Localised regions, such as off the western coast of Mexico, where $\overline{W_{37}}/\overline{W_{10}} > 2.8$ throughout the year are apparent. Interestingly, the ratio is appreciably larger over much of the northern high latitude oceans for JJA than for the rest of the year. The ratio reaches its lowest value (approximately 1) in regions where mean wind speeds are highest, such as the Southern Ocean. Visual inspection of these maps reveals distinct patterns that could be related to a variety of factors including the distribution of mean values for U_{10}, SST, and perhaps even Chl a. The December–February mean wind speed ($\overline{U_{10}}$) dependence of $\overline{W_{37}}/\overline{W_{10}}$ as a function of seasonal mean SST is shown in Figure 6.2. $\overline{W_{37}}/\overline{W_{10}}$ is highest (reaching a value of $\sim$ 4) when SST is highest and $\overline{U_{10}}$ lowest. The ratio falls off as $\overline{U_{10}}$ increases, with a rate that is proportional to the mean SST; the higher mean SST is, the quicker the rate of fall off. In regions where mean wind speeds are highest ($U_{10} > 14$ m s^{-1}), the ratio
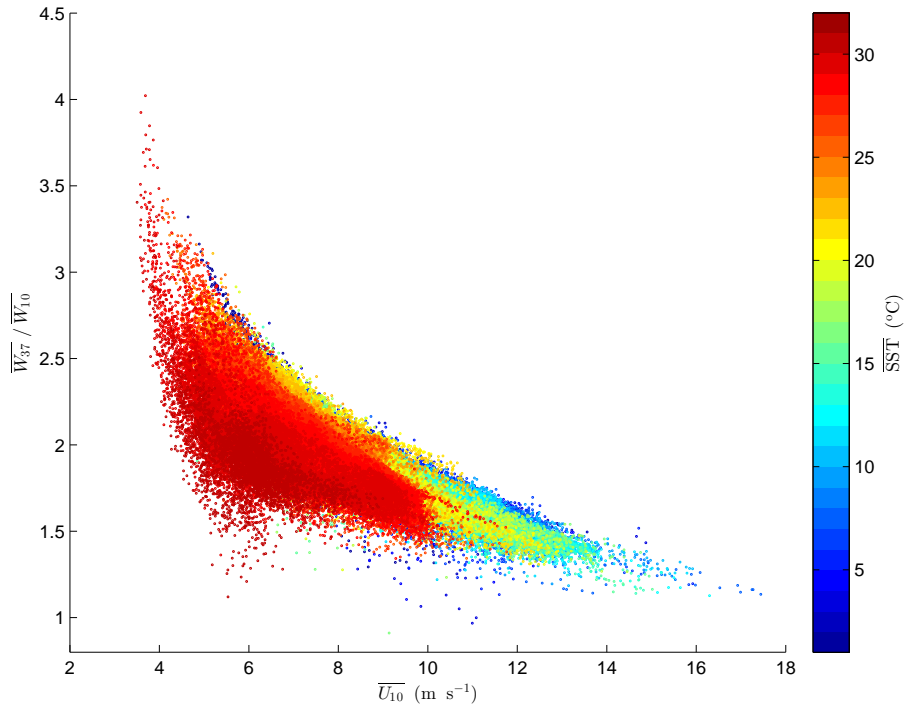
FIGURE 6.2: $\overline{W_{37}}/\overline{W_{10}}$ as a function of $\overline{U_{10}}$ for December–February, with data coloured by the mean SST over the period.

approaches 1. The exact cause(s) of this dependence should be investigated in future work. Specifically, more work is required to determine whether the enhancement of W_{37} relative to W_{10} in low wind, high SST conditions has a physical basis, for example, stabilisation of decaying foam by surfactants.

In summary, as a direct result of the radiometric frequency dependence of satellite-based observations of W, comparing the magnitude of W_{10} and W_{37} estimates (as the currently available end product of the $W(T_B)$ algorithm) may be related to the persistence of the thinnest foam layers. However, to achieve the overall goal of using a radiometric approach to accurately quantify the contribution to total whitecap coverage from foam layers in different life cycle stages and with different physical properties, it is likely that more fundamental, low-level, development of the $W(T_B)$ algorithm is required. In a recent experimental study [Savelyev et al., 2014], it was shown that there is a strong sensitivity of the rate of aerosol production from oceanic whitecaps to the brightness temperature polarization difference, a parameter obtained from radiometric measurements. This is a significant finding; an air-sea interaction processes (in this case SSA production) has been shown to be well correlated with a parameter related to brightness temperature, but not explicitly related to the areal coverage of

the surface foam layer (i.e., W). It is therefore possible that SSA source fluxes can be accurately parameterised using radiometric measurements of brightness temperature without converting T_B measurements to W estimates. Finally, radiometric measurements of oceanic whitecaps are not limited to visible and microwave frequencies; the possibility of using infra-red signature of whitecaps to infer further information on surface foam and wave breaking dynamics has previously been illustrated (e.g., Jessup and Phadnis [2005]; Marmorino and Smith [2005]. Importantly, the observed differences between the infrared signature of whitecaps in active and decaying stages are related to the distinct differences between the structure and evolution of the two foam types, and so can be used to distinguish between the two.

6.1.2   Approach based on a dynamical model of W

There has been renewed interest recently in relating W to breaking wave dynamics via the Phillips parameter, a statistical quantity characterising wave breaking (section 2.3.2.1), which is in turn can be related to the momentum flux and energy dissipation due to breaking [Duncan, 1981; Phillips, 1985]. The Phillips concept therefore provides means of obtaining information on wave breaking and energy dissipation using whitecap observations.

Recall from section 2.3.2.1, it was shown by Phillips [1985] that

$$W = T_{\text{Phillips}} \int_c c\Lambda(c)dc, \tag{6.1}$$

where T_{Phillips} is a time factor related to the bubble persistence time which was originally speculated by Phillips to be constant. The model was enhanced by Reul and Chapron [2003], who noted that T_{Phillips} is not a constant but rather depends on the scale (i.e., breaking speed) of the underlying breaker, with the breaker speed related to the period of the breaking wave, T. Indeed, choice of the factor determines the foam layers that contribute to the whitecap fraction as calculated using equation 6.1. In the following section, we relate T_{Phillips} to whitecap timescales (section 2.2.3.2), which are determined from a model for the areal evolution of an individual whitecap of a given scale. These whitecap timescales are then combined with the dynamical model for W to obtain estimates of W_A and W.

6.1.2.1 Modelling the time-evolution of an individual whitecap's area

A dynamical model $A(c,t)$ for the areal evolution of an individual whitecap over its lifetime is set out such that

$$A(c,t) = \beta(c)t \qquad \text{for } 0 \leq t \leq \tau_*,$$
$$A(c,t) = A_{\max} \exp\left(\frac{-(t-\tau_*)}{\tau}\right) \qquad \text{for } t \geq \tau_*. \tag{6.2}$$

where t is time and c is the speed of the breaking front. The model combines a linear growth phase (as observed by Callaghan [2013]; Kennedy and Snyder [1983]; Koepke [1984] amongst others) with the well-documented exponential decay phase, characteristic by the decay time τ. The active breaking duration τ_* marking the time of transition between the two phases. The model mirrors the dynamical model for foam layer thickness presented by Reul and Chapron [2003] but our interest is the areal coverage of whitecaps associated with individual breakers, rather than on the foam layer thickness, though the two are known to be related (section 2.2.3.1).

The scheme for the time evolution of whitecap area (equation 6.2) is illustrated in Figure 6.3, for whitecaps produced by breakers with different scales. In the top panel, the breaker has $c = 3$ m s^{-1} and $L = 2$ m, whereas the bottom panel shows the time evolution of a larger whitecap produced by a breaker for which $c = 5$ m s^{-1} and $L = 4$ m.

6.1.2.1.1 Growth phase

The key assumption in the above model is that the scale of a whitecap formed from a wave with breaking crest length L can be described using c only. $\beta(c)$ defines the rate of growth of an individual whitecap's area. Following the arguments of Kleiss [2009], the rate of growth of area $\beta(c) = cL$. Integrating this over the duration of active breaking (τ_*), at which time the whitecap obtains its maximum area $A_{\max}$, gives

$$A_{\max}(c,L) = cL\tau_*. \tag{6.3}$$

The parameter $\tau_*(c)$ is the duration of the breaking event and is therefore a function of the breaking front speed c. This parameter has been shown to be proportional to
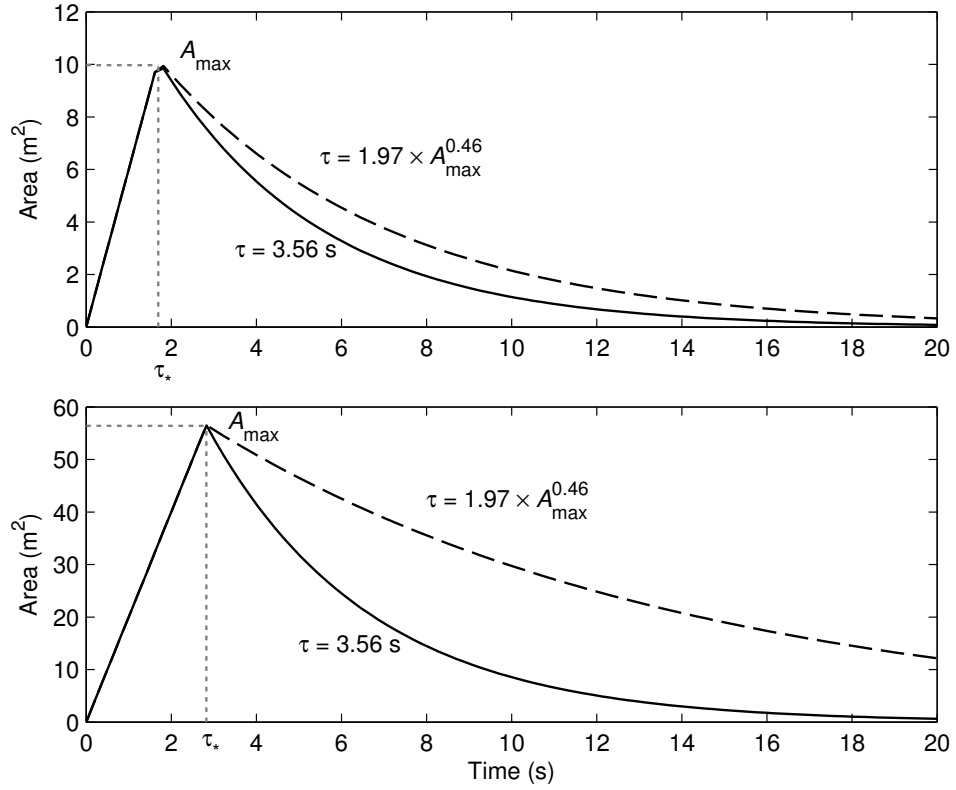
FIGURE 6.3: Schematic showing the growth and decay phases of two different white-caps, resulting from a breaking wave with breaking crest length of (top panel) 2 m and (bottom panel) 4 m, advancing at a speed of (top panel) 3 m s^{-1} and (bottom panel) 5 m s^{-1}. For the decay phase, the area evolution is characterised using either a constant or variable characteristic decay time τ)

the period of the underlying waves T [Melville and Matusov, 2002; Phillips et al., 2001; Rapp and Melville, 1990], such that

$$\tau_* = \alpha T, \tag{6.4}$$

where α is a constant of proportionality. Estimates for α generally range from 0.7 [Rapp and Melville, 1990] to 0.8 [Phillips et al., 2001]. Using the dispersion relation for gravity waves in deep water, the period of the wave can be related to c_p, the phase speed of the underlying carrier waves:

$$T = \frac{2\pi c_p}{g}, \tag{6.5}$$

so through combining the two equations;

$$\tau_*(c_p) = \frac{2\pi \alpha c_p}{g}. \tag{6.6}$$

The breaking speed c is not always equal to the phase speed of the carrier waves; it was shown by Stansell and MacFarlane [2002] that the two are related as $c/c_p = \gamma$ where $\gamma = 0.8$–0.95 depending on the nature of the breaking wave Substituting this in to equation 6.6, one obtains a final expression for the duration of the breaking event:

$$\tau_*(c) = \frac{2\pi\alpha c}{\gamma g},\tag{6.7}$$

where in this work $\gamma = 0.85$.

6.1.2.1.2 Decay phase

Two different decay times characterising the exponential decay phase in the model are considered: (i) a constant (scale-independent) decay time ($\tau = \tau_{\mathrm{Mon}} = 3.53$ s) [Monahan et al., 1982, 1986], and (ii) a scale-dependent τ. For the purpose of the above illustration, we obtain (ii) using the empirical relation of Callaghan et al. [2012]:

$$\tau(A_{\max}) = K_0 A_{\max}^{k_1},\tag{6.8}$$

where the exponent K_1 is 0.43 and the factor $K_0 = 1.97$. These values for K_1 and K_0 are the means of those reported by Callaghan et al. [2012] over four different measurement periods. Note that this is by no means a universal relationship. It does however, provide observational evidence that the characteristic decay time does indeed vary on a wave-by-wave basis, and so the result is at odds with use of a constant characteristic decay time, such as τ_{Mon}. The relationship dictates that the larger the maximum area of whitecap, the slower the rate of decay. This finding is intuitively reasonable, as it would be expected that larger whitecaps entrain bubbles deeper and thus have longer decay times. Importantly, Callaghan et al. [2012] also found that the mean value of τ also varies between observational periods i.e., under different wind-wave and environmental forcings. The issues associated with finding appropriate values (or a scaling relation) for τ is discussed in section 6.1.3.1.

6.1.3 Dynamical model for W and W_A using whitecap timescales

With a model for the time evolution of an individual whitecap, one can obtain an expression for W_A by considering only the contribution of individual waves during

the active breaking stage [Kleiss and Melville, 2010]. Replacing T_{Phillips} with our characteristic whitecap formation timescale τ_{form}, one obtains

$$W_A = \tau_{\text{form}} \int_c c\Lambda(c)dc, \tag{6.9}$$

where τ_{form} is defined by equation 2.3. Since the whitecap formation phase is linear, $\tau_{\text{form}}(c) = \tau_*(c)/2$. As this term is a function of c, equation 6.9 can therefore be written as

$$W_A = \int_c \frac{\tau_*(c)}{2} c\Lambda(c)dc, \tag{6.10}$$

so that with our definition of τ_* (equation 6.7), one obtains

$$W_A = \frac{\alpha\pi}{\gamma g} \int_c c^2 \Lambda(c)dc. \tag{6.11}$$

It follows that the stage A whitecap fraction is proportional to the second moment of the Phillips' parameter, based on the assumption that the formation time scales with the breaking front velocity c [Kleiss, 2009; Kleiss and Melville, 2010; Reul and Chapron, 2003].

Following the same argument, the total whitecap fraction W can be determined by replacing T_{Phillips} with τ_{wc}, to obtain

$$W = \tau_{\text{wc}} \int_c c\Lambda(c)dc, \tag{6.12}$$

where $\tau_{\text{wc}} = \tau_{\text{form}} + \tau_{\text{decay}}$ (section 2.2.3.2). As τ_{form} has already been obtained, the task is now to find an appropriate value for the timescale τ_{decay}, as defined by equation 2.4.

6.1.3.1   Choice of τ_{decay}

Referring back to our model for the time evolution of the area of an individual whitecap, there are two choices for the characteristic decay time τ. Note that τ is by definition equivalent to τ_{decay}—that is, our whitecap timescale *is* the characteristic decay time. In the first instance using a constant characteristic decay time $\tau_{\text{decay}} = \tau_{\text{Mon}}$, the combined timescale for growth and decay is

$$\tau_{\text{wc}}(c) = \frac{\alpha\pi c}{\gamma g} + \tau_{\text{Mon}} = \frac{\alpha\pi c}{\gamma g} + 3.53. \tag{6.13}$$

which when combined with equation 6.12 leads to

$$W = \frac{\alpha\pi}{\gamma g} \int_c c^2 \Lambda(c)dc + 3.53 \int_c c\Lambda(c)dc = W_A + 3.53 \int_c c\Lambda(c)dc, \qquad (6.14)$$

where the integral of the first moment of c is equivalent is an integration over the spectral rate of whitecap formation per unit area (s^{-1}).

In the second instance using a variable decay rate, the (generic) timescale for a whitecap produced by a breaker at advancing at speed c is:

$$\tau_{\text{wc}}(c) = \frac{\alpha\pi c}{\gamma g} + \tau_{\text{decay}}, \qquad (6.15)$$

where the exact form of τ_{decay} is yet to be specified, but it is in some way dependent on the scale of the breaking wave that produced the whitecap. As noted above, Callaghan et al. [2012] observed that τ_{decay} scales with the maximum area of a whitecap (equation 6.8) on a wave-to-wave basis. Interestingly, the authors actually found poor correlation between τ_{decay} and c, indicating that 'the decay time of whitecap foam may be independent of the speed of the breaker that formed the initial whitecap.' Due to the dependence of $A_{\max}$ on both L and c (equation 6.3), it is not possible to obtain an appropriate scaling relationship for τ_{decay} in terms of c alone.

In their calculations, Reul and Chapron [2003] did not consider τ_{decay} directly but rather assumed that the *total* persistence time for whitecap foam scales with the period of the breaking wave T, and therefore also c. Noting that the 'reported static-foam coverage should correspond to the sum of individual sea surface area swept by each breaking wave front during approximately 5 wave periods', the authors set $T_{\text{Phillips}} = 5T$ in their calculations. No evidence of experimental verification of this relationship is given by the authors, but the resulting durations are close to time scales characterising bubble injection depth as reported by Rapp and Melville [1990]. Note that this is the same scaling used to predict the active breaking time τ_* (equation 6.4), but with $\alpha = 5$, rather than 0.8. It is not clear what exactly the 'total persistence time' refers to, but here it is assumed that this is equivalent to the combined whitecap timescale for growth and decay:

$$\tau_{\text{wc}}(c) = \frac{5\pi c}{\gamma g}, \qquad (6.16)$$

and thus using this expression in equation 6.12, one obtains

$$W = \frac{5\pi}{\gamma g} \int_c c^2 \Lambda(c) dc = \frac{5}{0.8} \times W_A, \tag{6.17}$$

and the result that total W is linearly proportional to W_A. This should be true at least for constant environmental conditions [Leckler et al., 2013], and so the effects of varying environmental conditions on the lifetime of surface foam are not considered in the model for $\tau_{\mathrm{wc}}(c)$.

6.1.3.2   Choice for $\Lambda(c)$

The $\Lambda(c)$ distribution is directly related to the expected energy loss at a given scale [Phillips, 1985]. In wave models, this quantity is related to the dissipation source term in the wave action balance equation. Therefore, the Phillips distribution can be obtained in wave models via a wave spectrum definition [Leckler et al., 2013; Reul and Chapron, 2003], a feature of the most recent version of NCEP's WAVEWATCH III model. The distribution can also be measured empirically using video images of breaking waves. From the literature, field estimates of the Phillips $\Lambda(c)$ distribution are collated, and include those of Melville and Matusov [2002], Kleiss and Melville [2011], Gemmrich et al. [2008], and Callaghan et al. [2012] (Figure 6.4).

To obtain a $W(U_{10})$ formulation based on the Phillips parameter, one requires a functional form for $\Lambda(c)$ i.e., $\Lambda(c)(U_{10})$, rather than point measurements of the distribution corresponding to given wind and wave conditions. Therefore, we are forced to use either the empirical relation of Melville and Matusov [2002] or Kleiss and Melville [2011]. Both parameterisations were obtained from measurements made using a similar experimental method, and the parameterisations have the same functional form, with the distributions proportional to the cube of U_{10} and having an exponential dependence on the breaker speed c. The distribution of Melville and Matusov [2002] (MM02) is given by

$$\Lambda(c, U_{10}) = \left(\frac{U_{10}}{10}\right)^3 \times 3.3 \times 10^{-4} e^{-0.64c}, \tag{6.18}$$

and is used in the subsequent analysis. Though the e-folding scale is a constant in their parameterisation, Melville and Matusov [2002] predict that it is likely a function of fetch (or alternatively, the degree of wave development). Due to constant fetch
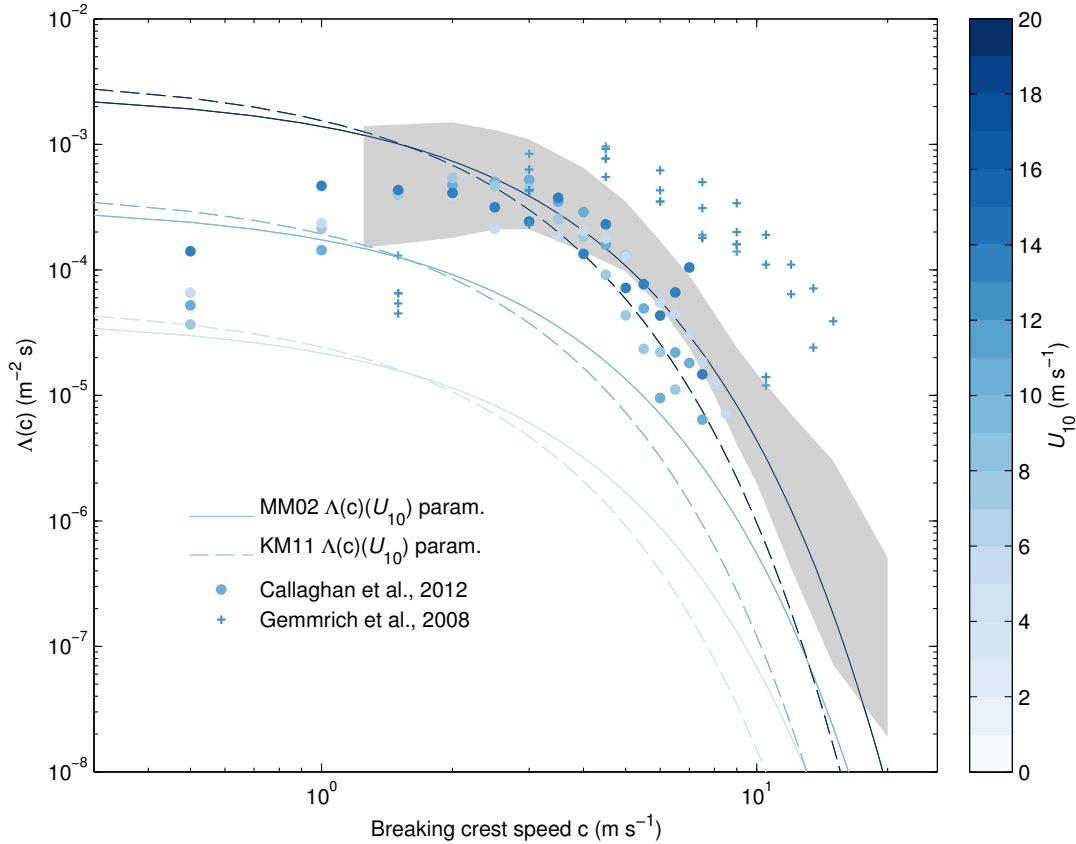
FIGURE 6.4: Published $\Lambda(c)$ from various authors, coloured according to the U_{10} value or range under which they were obtained / are applicable. The solid and dashed lines show the Melville and Matusov [2002] and Kleiss and Melville [2011] $\Lambda(c)(U_{10})$ parameterisations, respectively, evaluated at $U_{10} = 5$, 10, and 20 m s^{-1}. The grey area is from Kleiss and Melville [2011]. Gemmrich et al. [2008] and Callaghan et al. [2012] present individual estimates of Λ which are not parameterised in terms of U_{10}.

conditions in their study, this dependence was not built in to the function. In more recent work, scaling relationships for $\Lambda(c)$ in terms of both wind and wave variables have been suggested [Sutherland and Melville, 2013], based on the spread in estimates in $\Lambda(c)$ over much of the range of breaker speeds that contribute to W. This would be a significant step towards empirical or model parameterisation of breaking wave statistics as quantified by the Phillips distribution.

6.1.4   Results: Calculations to obtain W_A and W

Before equations 6.11, 6.14, and 6.17 can be evaluated using MM02, one needs to make choices for the integration limits $c_{\min}$ and $c_{\max}$. As MM02 was obtained in developed wave conditions, we set $c_{\max} = c_p$, the peak phase speed, where $c_p = gT_p/2\pi$. T_p can be calculated (for wind and waves in equilibrium) using the Carter [1982] relationship,

$T_p = 0.75U_{10}$. Therefore,

$$c_p(U_{10}) = \frac{0.75gU_{10}}{2\pi} \tag{6.19}$$

A constant lower limit for $c_{\min}$ is chosen as $0.1c_p$, which is a suitable lower limit for detectable breakers [Gemmrich et al., 2008]. As our focus is on prediction of W, this lower limit should restrict the scale of breakers to those that form whitecaps, even though including the microscale breaking range has a large effect on the value of $\Lambda(c)$ at low c [Sutherland and Melville, 2013] (this is somewhat evident in Figure 6.4). Sutherland and Melville [2013] state that visible (and infrared) measurements fail for breakers with speeds below 2–3 m s^{-1}, likely due to lack of air entrainment. Using this choice for $c_{\min}$ results in a value of approximately 1 m s^{-1} for $U_{10} = 9$ m s^{-1}, close to the lower limit of detected breaker speeds contributing to MM02 [Melville and Matusov, 2002].

Note that the integration window $[c_{\min}, c_{\max}]$ could be varied. This adds flexibility to the model because it has been shown that the scales over which breakers occur varies with the degree of wave development as measured relative to wind-wave equilibrium [Gemmrich et al., 2008].

In Figure 6.5, top, W_A predicted as a function of U_{10} from the dynamical model is compared with several $W_A(U_{10})$ relationships from the literature, together with $W_{10}(U_{10})$ (equation 4.2). Though lying slightly lower once U_{10} reaches ~ 8 m s^{-1}, predictions of W_A from the dynamical model are close to the $W_A(U_{10})$ relations of Monahan and Woolf [1988] and Asher and Wanninkhof [1998] which are based on photographic data. Though predictions from the $W_{10}(U_{10})$ parameterisation lie higher, the U_{10} exponent lies in between the quadratic dependence of the Monahan and Woolf [1988] $W_{10}(U_{10})$ formulation, and cubic dependence of the Asher and Wanninkhof [1998] parameterisation (note that this parameterisation goes as $W_A \propto (U_{10} - 1.77)^3$). The dynamical model, using the MM02 parameterisation of the Phillips distribution, predicts a stage A whitecap fraction of approximately 5% at $U_{10} = 20$ m s^{-1}.

The wind speed dependencies of predictions of W from the dynamical model (with both constant and variable decay rate) are compared with those of two in situ based $W(U_{10})$ parameterisations and of the $W_{37}(U_{10})$ relationship (equation 4.2) in Figure 6.5, bottom. There is good agreement between $W_{37}(U_{10})$ and predictions from the dynamical model with a variable decay rate, with regards to both the magnitude of estimates
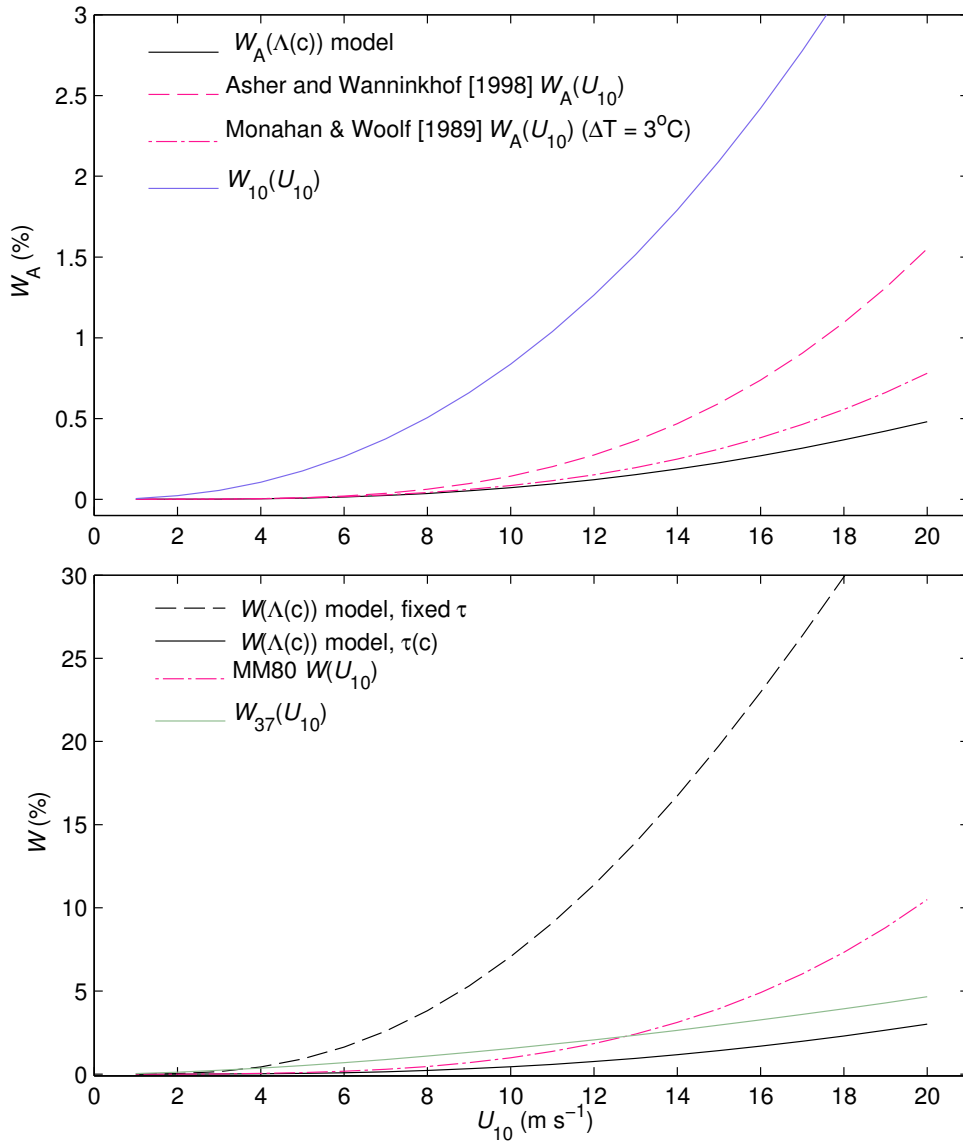
FIGURE 6.5: (Top panel) Comparison of the U_{10} dependence of W_A predictions from the dynamical model with two in situ based empirical formulations, and the W_{10} parameterisation. (Bottom panel) As top panel, but for total whitecap fraction W, and with the $W_{37}(U_{10})$ (rather than $W_{10}(U_{10})$) parameterisation shown for comparison.

and the U_{10} dependence. Predictions of W from MM80 lie slightly lie higher than those from the dynamical model with a variable decay rate, though the wind speed dependence ($U_{10}^{3.41}$) is much stronger.

It is interesting to see the disparity between predictions from the dynamical model using either a variable or fixed decay rate. The model with a fixed decay rate predicts values of W that seem unreasonably high, reaching $\sim 30\%$ at $U_{10} = 18$ m s^{-1}. The wind speed dependence is much stronger than that of the W_{37} parameterisation, that of MM80, and that of dynamical model using a variable $\tau(c)$. Recall that the dynamical

model is formulated using MM02, which has a cubic wind speed dependence; this is not, however, the sole factor determining the final wind speed dependence of the model predictions. Interestingly, the model with variable τ results in estimates and a wind speed dependence of W close to that of W_{37}.

The comparison is limited to $U_{10} < 20$ m s^{-1}. As noted in chapter 4, at higher wind speeds the validity of in situ parameterisations and satellite-based estimates is questionable. The same is true for the dynamical model, at least in its current usage, as the MM02 parameterisation of $\Lambda(c)$ was formulated from measurements in conditions where the mean $U_{10} < 14$ m s^{-1}. It is interesting to compare the results in Figure 6.5 to those of Holthuijsen et al. [2012], who presented results on the wind speed dependence of whitecap fraction well into the high wind (hurricane-like) regime. W showed a near cubic dependence on wind speed for $U_{10} < 24$ m s^{-1}. However, for wind speeds above this value the authors see no systematic dependency on wind speed, with W fluctuating around 4% for 24 m s$^{-1} < U_{10} > 46$ m s^{-1}. Though predictions for W from the dynamic model will continue to grow with U_{10} past this point (i.e., there is no built-in behaviour which would lead to the values 'plateauing'), the value of W predicted (using a variable decay rate) at this wind speed is 4.6%.

6.1.5   Discussion

A semi-empirical approach based on a dynamic model of whitecap formation and decay can be used to relate whitecap fraction to breaking wave statistics. The framework incorporates recent experimental results on the whitecap evolution and provides a more direct link between whitecap fraction and breaking waves. Though based on several assumptions, the framework can be further extended to link whitecap fraction to breaking-induced energy dissipation which is directly related to air entrainment and detrainment [Long et al., 2011], and therefore bubble-mediated air-sea gas transfer and (perhaps) SSA production via bursting bubbles.

In recent work, Leckler et al. [2013] used whitecap properties (areal coverage and foam thickness) to validate breaking wave statistics predicted by two different wave dissipation parameterisations in the spectral wave model WAVEWATCH III. The model is run and the Phillips distribution is obtained. The Phillips distribution was then used to compute a modelled total whitecap fraction via equation 6.1, with T_{Phillips} obtained

following Reul and Chapron [2003]. Finally, modelled W was compared to both radiometric estimates of W—the same as used here—and predictions from Monahan and Woolf [1988] in an attempt to provide a constraint on model dissipation source terms (which control the breaking wave statistics in the model).

In this work, a similar comparison has been performed, though here the aim of comparing predictions from the three different approaches is to explore the ability of the dynamical model (using an empirical parameterisation of the Phillips distribution) to make predictions of W_A and W by considering the scale-dependent areal evolution of individual whitecaps. In previous work, the growth phase of whitecaps has been shown to be dependent on the scale of the breaking wave (and therefore wave breaking speed). Quantifying the decay phase is far more complex; though well described by an exponential behaviour, the characteristic decay time varies considerably. Decay rates are controlled by the dynamics of subsurface (bubble-plume) processes (which are largely determined by the breaking event), and mechanisms (such as surface stabilisation of bubbles by surfactants) that are not directly related dynamical processes or to the scale or intensity of breaking. The relative contribution of these different mechanisms to whitecap decay rates is not yet fully understood; until these contributing factors can be separated out, the total whitecap fraction cannot be directly related to breaking wave statistics. Due to the importance of foam decay times in determining total W, estimates of W_A remain better indicators of the magnitude of dynamic processes associated with wave breaking. It follows that W_A estimates predicted by such a model are likely much more constrained than those for total W.

To enable a comparison with 'traditional' $W(U_{10})$ parameterisations, and those for W_{10} and W_{37}, a wind speed parameterisation of $\Lambda(c)$ has been used in the dynamical model; the resulting predictions are of course highly dependent on the choice one makes for the Phillips distribution. The model—using the Melville and Matusov [2002] parameterisation of $\Lambda(c)$—predicts W_A values that have magnitudes and a wind speed dependence in line with predictions from two $W_A(U_{10})$ parameterisations based on photographic data. The wind speed parameterisation for W_{10}, derived earlier in this work, has been shown for comparison given that it primarily quantifies thicker foam associated with active breaking; $W_{10}(U_{10})$ predictions are higher than those of the dynamical model and in situ parameterisations, and have a stronger wind speed dependence. As discussed in chapter 4, this is likely due to a combination of factors

including (i) the fundamentally different nature of the measurements (ii) the influence of secondary forcings which are inherent in estimates of W used to formulate the parameterisation, and (iii) W_{10} characterising some residual foam in addition to dynamic, stage A whitecaps. Predictions for total W from the model have been obtained using either a constant or scale-dependent decay rate. Use of a constant decay rate leads to estimates of W that are much higher than predictions from MM80, the W_{37} wind speed parameterisation, and the dynamic model using a variable decay rate.

6.1.5.1   Limitations and development of the dynamical model

The dynamical model relates the areal coverage of whitecaps to breaking wave statistics. The ultimate aim of this approach would be to develop a model that could predict the magnitude of air-sea processes (gas transfer coefficients, energy dissipation rates, etc.) from remotely sensed measurements of whitecaps. To achieve this goal, several limitations need to be addressed:

- The areal coverage of foam layers can only be related to breaking wave statistics (quantified using the Phillips distribution) via use of an appropriate time factor which accounts for the persistence time of foam on the surface. As demonstrated above, under certain conditions, the physical dependence of W on breaking wave statistics is distorted by foam lifetime effects. The relationship between foam decay times and breaking waves of different scales and intensities needs to be better understood through laboratory and, if possible, open ocean experiments.

- More measurements of the Phillips distribution are needed to better constrain it, and to eventually enable its parameterisation in terms of wind and wave variables. Given that the $\Lambda(c)$ distribution can be non-dimensionalised over a wind range of wind and wave conditions, if supplemented with detailed information on the wave field, breaking wave statistics could be parameterised in terms of readily measurable wind and wave quantities, without use of W.

- The Phillips framework not only relates whitecaps to breaking wave statistics, but further links these statistics to breaking wave energy dissipation. A relationship between whitecap fraction and wave energy dissipation is more direct than one in terms of wind speed. However, the Phillips concept relating the breaking crest

length distribution to energy and momentum dissipation is based on numerous assumptions and includes several poorly constrained parameters related to the breaking process [Schwendeman et al., 2014].

- If such a dynamical model is to be used to predict the magnitude of air-sea interaction processes, it needs to be expanded and combined with relevant parameters characterising the subsurface properties of breaking waves, such as bubble void fractions and size distributions. If such information is not attainable on a global scale, the radiometric remote sensing of whitecaps at different frequencies may provide a means by which information on subsurface properties of breaking waves can be 'extracted' from the radiometric signature of foam layers.

6.2 Use of W in air-sea interaction applications

W is used to quantify and parameterise physical air-sea interaction processes that are dependent upon the production and decay of whitecaps. Perhaps the most important of these processes from the standpoint of weather and climate are sea spray aerosol production via bubble bursting and bubble-mediated exchange of trace gases. Both of these mechanisms can be quantified following the 'whitecap method' in which the whitecap fraction (parameterised as a function of controlling variables) is used as a dimensionless scaling factor. This approach was initially formulated as a method to obtain the sea spray source flux (SSSF); its application remains the most viable method of determining interfacial SSA source fluxes on a global scale. (see section 2.7.2.2).

6.2.1 Prediction of sea spray aerosol source fluxes

An important application is the use of W to estimate the sea spray aerosol source flux (SSSF) in aerosol and climate models through application of the whitecap method. The source flux is obtained by scaling an estimate of the production flux per unit area whitecap $dF_{wc}(r_{80})$, often derived from laboratory measurements, by W. Traditionally, W is obtained at a given wind speed using a $W(U_{10})$ formulation, so that the source function as a function of radius and U_{10} is given by

$$\frac{dF_{int}(U_{10}, r_{80})}{d \log r_{80}} = W(U_{10}) \times \frac{dF_{wc}(r_{80})}{d \log r_{80}}. \tag{6.20}$$

Relevant to this study is the effect on SSA source flux estimates of changing the scaling term on the right hand side of equation 6.20, rather than exploring the effects of implementing a new shape function, $dF_{\text{wc}}(r_{80})$. The majority of SSSFs formulated using the whitecap method make use of the MM80 relationship (2.20). Use of MM80 results in fluxes with a $U_{10}^{3.41}$ dependence and potentially large uncertainties as uncertainty in W transfers directly to the flux estimates.

6.2.1.1   Modification of sea spray source functions

Satellite-based estimates of W can be incorporated into SSSFs by simply replacing the parameterised estimates of W (obtained using formulations such as MM80) by satellite-based estimates to obtain a modified source function:

$$\frac{dF_{\text{int}}(U_{10}, r_{80})}{d \log r_{80}} = W_{\text{sat}} \times \frac{dF_{\text{wc}}(r_{80})}{d \log r_{80}}. \qquad (6.21)$$

Presently, values for W_{sat} could be one of four possibilities: direct estimates of W_{10} or W_{37}, or alternatively estimates obtained using a parameterisation thereof. Wind speed parameterisations of W_{10} and W_{37} were presented in chapter 4, and in chapter 5 it was showed that variability in satellite-based estimates of W (at least those that make up the whitecap database as used in this work) is well described by U_{10} alone (section 5.2.2). If direct satellite-based estimates are not readily available, parameterisations of W_{10} and W_{37} can be easily implemented.

Predictions of the SSA source flux obtained using direct satellite-based estimates can be expected to be more realistic than those obtained using traditional $W(U_{10})$ formulations, as they are formulated from measurements of W on a global scale. Likewise, use of parameterisations of W_{10} or W_{37} in equation 6.21 should also lead to improvements to estimates of source fluxes as they are obtained using global source data for a full year; the parameterisations should capture major co-variations between U_{10} and secondary factors, and so are preferable to in situ based formulations derived from spatially and temporally limited measurements.

Evaluation of the benefits of using satellite-based W estimates in SSSFs obtained through implementation of the whitecap method is not straight forward. Some possible approaches are comparison with direct flux measurements, indirect estimates using

other methods, or via 'derived' quantities such as the integrated mass flux. However, the magnitude of the predicted fluxes scale linearly with W, and so with the shape function fixed, changes to the source flux (and derived quantities) are equivalent to changes to W. Therefore, changes to the magnitude and spatial distribution of estimated source fluxes can be visualised by comparing W estimates from MM80 and satellite-based parameterisations.
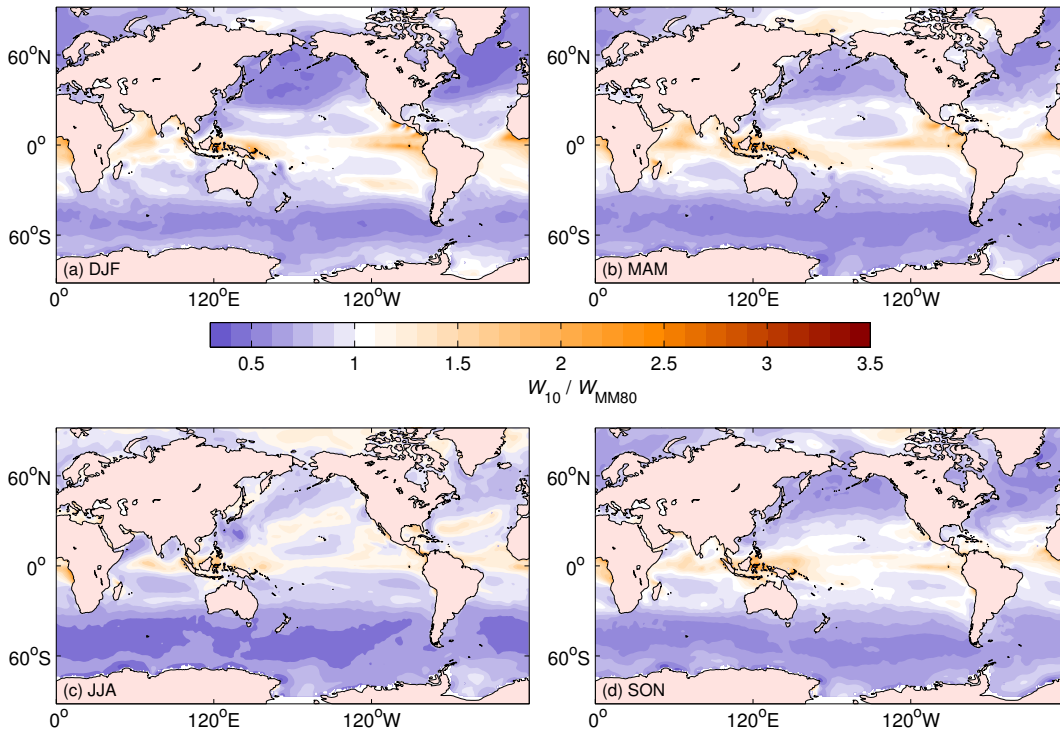
FIGURE 6.6: Seasonal maps of $\overline{W}_{10}/\overline{W}_{\mathrm{MM80}}$

To explore these effects, a comparison is made—on a seasonal timescale—between values predicted by MM80 and parameterised satellite-based W estimates obtained from the $W(U_{10})$ relationships (equations 4.3). Figure 6.6 shows the ratio of the two means $(\overline{W}_{10}/\overline{W}_{\mathrm{MM80}})$. The comparison is analogous to that detailed in section 4.3.1, though here the ratio (rather than differences) is considered, seasonal maps are presented (rather than a year map), and parameterised W_{10} estimates are used rather than direct daily estimates. Also note that W_{10} is used for the comparison, in preference to W_{37}. This decision is based on both the expected relationship between radiometric and traditional photographic estimates, and speculation on the applicability of the satellite-based estimates to parameterisation of air-sea processes. Finally, the parameterisations are driven by ECMWF operational mode global U_{10} fields at a 6-hourly time resolution, covering 2011. Use of modelled U_{10} fields provides additional coverage

than that provided by U_{10} entries in the W database, though the product is at the same resolution ($0.5^o \times 0.5^o$) as the database fields.

The resulting plots, as expected, lead to the same conclusions as those described in section 4.3.1. On a seasonal timescale, satellite W is higher, by up to a factor or 3.5, in regions where the mean wind speed is low (such as regions close to the equator), whereas in regions where mean wind speeds are moderate to high (Southern Ocean, North Pacific, and North Atlantic), W_{10} is as low as 30% of W_{MM80}. The distribution of the ratio changes with season, though the general pattern of enhanced satellite W in the low latitudes and lower satellite-based W in higher latitudes, is constant throughout the year.

6.2.1.2   Discussion

Though various SSSFs obtained using the whitecap method have been published in the literature over the past several decades, all are based on $W(U_{10})$ parameterisations, such as MM80, which are known to have several limitations. Although the satellite-based parameterisations are in terms of U_{10} alone, the wind exponents carry information for the geographical variations of whitecap fraction because equations 4.3—unlike MM80 and other in situ formulations—are based on W data covering meteorological and environmental conditions over the entire globe over a full year.

The highly non-linear wind speed dependence of SSSFs formulated using MM80 or similar parameterisations yields large source fluxes at high winds, and results in modeled sea salt number and mass concentrations typically higher than those measured [de Leeuw et al., 2011; Ovadnevaite et al., 2012]. Tsyro et al. [2011] found that model estimates based on the SSSFs of Mårtensson et al. [2003] and Gong [2003] overestimate atmospheric concentrations of Na by as much as 46% compared to observations. Similarly, through a comparison of modeled and ship measured sea salt mass concentrations, Witek et al. [2007] found that modeled concentrations were biased high—increasingly so with U_{10}. Jaeglé et al. [2011] found that the GEOS-Chem model consistently underestimates SSA concentrations in the tropics (SST $> 25°$C), and overestimates at higher latitudes (SST $< 10°$C).

That the uncertainty of the SSA flux drives substantial geographical biases has also been noted in model estimates of derived quantities. Using a lower limit for sea salt concentrations, Haywood et al. [1999] could not reconcile modelled and measured values of solar irradiance. Use of higher sea salt concentrations brought balance over much of the globe, but overestimation at high latitudes. Such overestimation at high latitudes for aerosol optical depth (AOD), accompanied with underestimation at low latitudes, persisted in models in which the SSSF uses the MM80 $W(U_{10})$ parameterisation [Chin et al., 2002]. Smirnov et al. [2011] found that modeled AODs south of 40°S are consistently higher than sunphotometer measurements; many of the models compared use the MM80 $W(U_{10})$ parameterisation as well.

Such biases in modelled sea salt concentrations and derived quantities cannot be solely attributed to biases in SSA source flux estimates—transport and removal processes also play a role, as does the quality of the wind speed data driving the parameterisation. However, the geographical biases outlined in section 3.2 are consistent with our findings regarding the differences between MM80 and satellite retrievals of W. In high-latitude regions such as the North Atlantic and Southern Ocean, where mean wind speed is highest, mean W_{10} is up to 60% lower than mean W_{MM80}, while mean W_{37} is up to 40% lower. In low-latitude regions where wind speeds are consistently low, the 1-year mean of W_{10} is up to 50% larger than W_{MM80} whereas mean W_{37} can be as much as 240% higher. As modeled SSA source fluxes scale linearly with W, use of satellite-based W estimates (either directly measured or parameterised) instead of MM80 in a SSSF would result, on average, in larger SSA fluxes in low wind speed regimes and smaller fluxes in high winds, by the factors shown in Figure 4.13. Because W_{10} and W_{37} capture the natural variability of whitecap formation and lifetime, our results imply that discrepancies between modelled and measured quantities can be, at least partially, reconciled with the use of satellite-based estimates of W.

With regards to the use of satellite-based estimates for obtaining SSA emissions using the whitecap method, we are not yet able to say whether W_{10}, W_{37}, or indeed some combination of both, is the most appropriate measure. One might presume W_{37} is a preferable measure, as it quantifies both active and residual whitecap stages, both of which involve bubble bursting and SSA production. However, a number of caveats hamper reliable characterisation of SSA production. Different production fluxes per unit area of whitecap in active and decaying phases are expected to be necessary,

since the bubble size distributions and rate of bursting will be different in each; these have not been characterised. Further, the relative contribution to the total production flux should be weighted by their respective decay times using W/τ [Monahan et al., 1982, 1986], but more measurements are necessary to quantify the decay times. In laboratory studies, Woolf et al. [1987] observed aerosol production to continue after the decay of a visible whitecap signature. This is likely the result of a small flux of bubbles small enough to remain in the water column for an extended period and which burst too rapidly at the surface for a foam layer to be maintained. Their concentration and size distribution ought, however, to be related to their rate of production and hence whitecap formation and W_{10}. Furthermore, the production flux per unit area whitecap is expected to change with the scale and intensity of individual breaking waves [Monahan et al., 1986]; recently Norris et al. [2013b] showed a sizeable wind-speed dependence of the production flux per unit area whitecap for small particles but no distinguishable change for large particles over individual whitecaps. It is also possible that the relevance of W_{10} and W_{37} could vary with emitted SSA particle size: smaller particles (produced by film droplets) are associated with the bursting of larger bubbles which rise to the surface rapidly and are thus more concentrated in recent/active breakers; on the other hand, larger particles (produced by jet droplets) are associated with smaller bubbles which can stay mixed in surface layer much longer, and may reach the surface over a longer period. Thus W_{10} may be more relevant to the production of smaller particles whilst W_{37} could be better related to production of larger particles. Finally, the stabilisation of bubbles by biological surfactants is a factor known to influence foam in its decaying stage [Callaghan et al., 2013], and so can be expected to affect W_{37} estimates and their SSA production rate more than the W_{10} estimates.

Consideration of all of the above factors suggests that use of the whitecap method to predict SSA source fluxes needs to be re-evaluated. In the meantime, if satellite-based W estimates are to be used to predict source fluxes, we suggest that use of W_{10} is preferable to W_{37}. This is based on (i) an assumption that the currently used production rates are more likely representative of thicker, active whitecaps (as quantified by W_{10}), and (ii) the closer agreement between the wind speed dependence of W_{10} and traditional parameterisations.

6.2.2   Bubble mediated gas-exchange

In a similar sense as above, the whitecap method has been applied to estimate the magnitude of bubble-mediated gas exchange. However, the method is not as well developed as it is for calculations of SSA source fluxes. First, it is not clear exactly what quantity should correlate best with whitecap fraction; in models and experimental data, W has been related to both the total gas transfer velocity (K) and the bubble-mediated component (K_b) alone. This reflects issues associated with separating contributions to the total transfer velocity from different processes; as noted by Zhao et al. [2003], 'In practical applications it is also difficult to distinguish the transfer mediated by turbulence and bubbles because both of them are proportional to wind speed.'

Assuming a hybrid-model that separates direct transfer from bubble-mediated transfer [Woolf, 1997], one can relate K_b to whitecap fraction:

$$K_{\mathrm{b}} = aW, \tag{6.22}$$

where a is a function of several variables. Such a model is implemented in the Coupled Ocean Atmosphere Response Experiment (COARE) bulk gas flux algorithm (COAREG3.1) [Fairall et al., 2011], with (total) W calculated using MM80 (equation 2.20). The proportionality factors are adjusted to allow 'calibration' of the model to observed fluxes.

6.2.2.1   Development of W-based models and use of satellite-based estimates of W

Issues related to the use whitecap fraction as a surrogate for the direct production and mixing of bubbles are well documented. Several alternative schemes, based on different forcing parameters, have been presented (see below). In the same way that U_{10} is an indirect factor affecting wave breaking and bubble plume production, W—specifying the *areal* coverage of foam—alone cannot be expected to quantify the enhancement of gas exchange to bubble plumes.

However, there is scope for development of whitecap-based models of bubble-mediated gas transfer. More physically-based models should be implemented; as a first step this

could involve relating K_b to W_A rather than total W. Although both W and W_A have been related to K_b, there is general agreement that W_A may be more applicable [Monahan and Torgersen, 1991; Zhang, 2012], based on consideration of typical coverages and bubble rise velocities of stage A and B whitecaps; approximately 98% of air entrained is vented through a whitecap in its active phase. W should be more explicitly linked to bubble processes, or combined with further information on the bubble plume. For example, in their study on the role of bubbles on air-sea heat and moisture exchange, Andreas and Monahan [2000] consider the spatially average flux of bubbles to the surface, which is the product of W with the air volume flux inside a unit area whitecap V_a. V_a can be estimated by integrating the product of the bubble rise velocity and the volume distribution of bubbles, though these quantities themselves need to be better linked to the energetics of the breaking process and environmental parameters.

Remotely sensed W provides a convenient approach to inferring gas transfer velocities (or at least the contribution associated with whitecapping). A move from parameterised values for W_A (or W) to use of direct measurements of W_{10}—or, if desired, W_{37}—in models for K_b should lead to improved agreement between models and observations. Though values for W predicted by the $W(T_B)$ algorithm will likely see some change as the algorithm develops, it is expected that values and the resulting spatial distribution of K_b obtained using satellite W should be more realistic because satellite-based estimates of W incorporate the effects of various secondary forcings. The supposed benefit should be verified through comparison of predicted gas transfer velocities using satellite-based W with field measurements, though isolating the 'bubbled-mediated' contribution to field measurements of gas transfer velocities remains a limiting factor.

The effect of using satellite-based estimates of W in equation 6.22, as far as changes to magnitudes and the spatial distribution go, will be analogous to the effect on SSA source fluxes described in section 6.2.1.1. This is because both models are linear in W, and the same $W(U_{10})$ relations that are used to specify W in many SSSFs are the same used to specify W in models for K_b. If one takes MM80 as the $W(U_{10})$ formulation, one can consider Figure 6.6 as representative of the seasonal distributions of the ratio of the predicted K_b values (i.e., satellite-based K_b estimate over predicted K_b using MM80).

At this stage, we speculate that W_{10} (rather than W_{37}) should be considered as a better representation of whitecaps suitable for the parameterisation of bubble-mediated gas transfer processes, based on (i) the wind speed characteristics of W_{10} and W_{37} (ii) their expected relation to stage A and B whitecap coverage as traditionally measured, (iii) the physical link between active breaking and bubble plume production, and (iv) the important roles that surface processes (such as stabilisation by surfactants) have on thinning foam layers (and thus W_{37}) which alter W but have no direct relation to air entrainment and bubble plume processes.

6.2.2.2 Use of alternative forcing parameters

The limitations of using W to parameterise gas transfer velocities (such as the spread in W estimates from traditional $W(U_{10}$ formulations) have led some to consider parameterisations in terms of other, more physically-based variables. Generally, interest remains focused on parameters that incorporate information on wind-wave coupling, such as the wind friction velocity. Zhao et al. [2003]—who suggest that 'the large uncertainties in the traditional relationship of gas transfer velocity with wind speed be ascribed to the neglect of the effect of wind waves'—proceed to parameterise the total gas transfer velocity in terms of the breaking wave Reynolds number R_B (equation 3.4) based on arguments relating the parameter to the intensity of turbulence induced by wind waves.

Woolf [2005] developed an existing W-based model for K_b by introducing Reynolds' number parameterisations for W. This approach—though not tackling the assumptions inherent to the $K_b(W)$ model—leads to a sea-state dependent K_b which could explain the diversity of transfer velocities at a given wind speed.

Various other possibilities enabling the inclusion of wave state in models for gas transfer are viable. One approach that may be favourable is use of wave energy dissipation estimates (either modelled or parameterised). As discussed in Fairall et al. [2011], a $K_b(\epsilon)$ model is physically viable because the rate of entrainment of air into water F_{ent} scales with ϵ [Long et al., 2011]. Another possibility involves relating K_b to breaking wave statistics via the Phillips distribution which is linked to the spectral rate of energy dissipation.

6.2.2.3 Summary

The full benefit of a move towards use of radiometric estimates of W in prediction of gas transfer velocities can only be realised if more refined models for air-sea gas-exchange are developed. Further information is needed to better relate breaking waves and bubble plume production to transfer coefficients. For example, wave information (wave height and slope) is required to better quantify transfer enhanced by wave breaking dissipation mechanisms. Likewise, bubble plume information (such as penetration depth, and bubble size distribution) needs to be considered for better representation of both exchange across bubble surfaces and exchange due to disruption of the surface microlayer by bubble surfacing and bursting.

Chapter 7

Summary and recommendations

7.1 Summary

This study has presented an analysis of whitecap fraction estimated from satellite-based radiometric observations at microwave frequencies of 10 GHz (W_{10}) and 37 GHz (W_{37}). Results and conclusions have been framed in the context of more traditional approaches to the measurement, interpretation, and parameterisation of W. By providing global coverage, along with a several order of magnitude increase in the number of individual estimates of W compared to historical in situ data, the satellite-based approach is unquestionably a significant step in the quest to obtain more accurate estimates of whitecap fraction which in turn will lead to improved representation of whitecaps in models and remote sensing applications.

W_{10} and W_{37} estimates have been directly validated against ship-based photographic estimates from two cruises. In situ W estimates were calculated by temporally averaging photographic data obtained from ship-borne digital cameras. Large day-to-day variation in the volume and quality of data was apparent; during several days it was not possible to obtain the number of photographs needed to converge on a statistically stable characteristic value of W over the time-averaging window. The wind speed dependence of the in situ estimates is similar to the Callaghan et al. [2008a] $W(U_{10})$ relationship, which was obtained using the same automated processing algorithm. Other published $W(U_{10})$ parametrisations, such as that of Stramska and Petelski [2003] and Monahan and O'Muircheartaigh [1980] predict higher W than the

SEASAW formulation over much of the wind speed range, and have a stronger wind speed dependence, resulting in larger deviations from SEASAW estimates in high winds (i.e., $U_{10} > 12$ m s^{-1}). To directly validate the retrieval, a spatial-temporal approach was used to obtain matchups between temporally-averaged in situ data and spatially averaged satellite data. Despite the small number of data points, (only fifteen ship-satellite matchups were identified), it was possible to determine that satellite-based W is biased high at low wind speeds (more so for W_{37}) and low at high wind speeds when compared to photographic W estimates. The bias between satellite and photo-based estimates is generally larger for W_{37} than for W_{10}, and generally increases as wind speed increases. Differences in U_{10} estimates (i.e., ship-based estimates of 'true' U_{10} versus the QuikSCAT equivalent-neutral U_{10} estimates paired with satellite W data) is likely the cause of some of the bias.

The global distribution and seasonal dependence of satellite-based W have been described. Seasonal means of the two estimates have similar geographical distributions, with W_{37} seasonal means a factor 1.5–2 higher than those for W_{10}. At low latitudes (equatorward of 30°N and S), seasonal means rarely reach 1% for W_{10} and 1.5% for W_{37}. Seasonal changes in mid to high latitudes are stronger in the northern hemisphere than in the southern hemisphere; this reflects the effects of the asymmetry in distribution of continental land masses between the hemispheres. Highest seasonal W occurs during the boreal winter (December–February) in the North Atlantic and during the austral winter months (June–August) in the Southern Ocean.

A comparison has been made between satellite-based W estimates and those obtained from the widely used $W(U_{10})$ relationship of Monahan and O'Muircheartaigh [1980] (MM80). Differences are driven primarily by their differing wind speed dependence, which is weaker for the satellite-based estimates. The weaker wind-speed dependence results in satellite estimates higher than those obtained from MM80 in regions (such as the tropics) where mean wind speeds are low ($U_{10} \leq 8$ m s^{-1}), but lower than MM80 in high latitudes where mean wind speeds are higher. Overestimation of MM80 due to extrapolation beyond its range of validity is likely a key bias at high wind speeds. These differences are robust if a comparison is made between MM80 W estimates and estimates from wind speed parameterisations of W_{10} and W_{37}. The satellite-based parameterisations have been derived from W estimates on a global scale and so their wind speed dependence will in part reflect the influence of factors other than wind speed

which co-vary with the wind geographically; for example SST, biological surfactant concentration, and fetch-dependent wave state. As the dataset of satellite-based W estimates is not yet freely available for use, the satellite-based $W(U_{10})$ parameterisations can be used in lieu of observed W_{10} and W_{37} estimates.

Estimation of satellite-derived whitecap fraction is dependent upon the retrieval's radiometric wavelength. Different frequencies are able to discriminate—albeit somewhat crudely—between foam layers depending on their thickness. Our results show unambiguously that wind speed and secondary factors affect W_{10} and W_{37} differently. Importantly, these differences can be plausibly explained with different influences of the secondary factors on foam layers associated with different whitecap lifetime stages. This lends support to the notion that W_{10} and W_{37} represent different mixes of active and residual whitecaps. This is also an independent confirmation of the conclusions regarding the frequency sensitivity to foam layer thicknesses which Anguelova and Gaiser [2011] obtained on the basis of purely physical considerations. Again it should be stressed that 'microwave radiometry is suitable for remote sensing of the surface foam layers which represent the horizontal extent of (i.e., the area covered by) the whitecaps. That is, passive microwave remote sensing measures predominantly the surface expression of breaking waves' [Anguelova, 2008].

Using collocated and concurrent measurements of a variety of physically relevant quantities in addition to wind speed, the influence of secondary factors on whitecap fraction has been quantified. At a given wind speed, variability due to secondary factors is more pronounced for W_{37} than for W_{10} with W_{37} changing by as much as 20% when wave height, wave period, or the mean wave slope are considered, and by up to 25% when SST or T_a are considered. This clear SST trend is largely due to the strong suppression of W_{37} in high SST (low viscosity) waters. The influence of the degree of wave development has also been assessed by partitioning the W estimates according to the relationship between the bulk wave parameters available as part of the database (signigicant wave height and peak wave period), and U_{10}. The results have been discussed in the context of the inconclusive findings of several previous studies using in situ data. At a given wind speed, satellite-based W is lower in conditions of a developing sea compared with a fully developed sea. The effect on W of the wave state in swell conditions is more complex; these findings require further investigation with more detailed wave

measurements including directional information, and ideally, measures quantifying the wind sea and swell parts of the wave spectrum separately.

Based on the magnitude of the influence of secondary forcing factors on W_{10} and W_{37}, we conclude that much of the variability in foam layer might be due to the behavior of the thinner, decaying foam patches, variability that is not captured by the retrieval using the 10 GHz channel. Variability in W is smaller for active whitecaps (W_{10}) and larger for total whitecap fraction which includes both active and residual whitecaps (W_{37}). Within each secondary dependence, the effect of the secondary parameter is, in most cases, stronger at higher winds than at lower, supporting the findings from the in situ studies of Callaghan et al. [2008a] and Goddijn-Murphy et al. [2011].

Principal component analysis has been used to assess the success of wind speed and secondary forcing parameters in accounting for variability in W. Though we show that the influence of secondary factors on W can be appreciable (especially for W_{37}), the PCA results suggest that wind speed alone accounts for most of the variability in both W_{10} and W_{37}. Interestingly, two Reynolds number parameters—combining measures of wind speed, wave height or period, and viscosity—perform almost as well as wind speed alone. Different measures of the degree of wave development (wave age and mean wave slope) can account for between 80 and 85% of variability in W. The first principal component for air temperature, SST, and the viscosity of water account for roughly the same level of variance in W; 71% for W_{10}, and 74% for W_{37}.

Whitecap fraction is currently used to parameterise numerous bubble-dependent air-sea processes, but it is expected that these parameterisations could be improved through use of measures of W that discriminate between active breakers and residual foam. As such, microwave measurements of whitecap fraction could prove beneficial to parameterization of such processes. It has been shown that use of $W(U_{10})$ parameterisations based on limited in situ data can lead to biases in the global distribution of W. This in turn leads to biases in predictions of the magnitude and spatial distribution of several bubble-dependent processes which are parameterised in terms of W. Such biases are consistent with recent results showing both general overestimation of modeled SSA concentrations in high latitudes and underestimation in the tropics. These biases can be reduced with use of satellite-based estimates of W to estimate SSA source fluxes. An improved representation of the spatial and temporal distribution of W will also

benefit parameterisations of air-sea interaction processes and the accuracy of remote sensing retrievals. Routine satellite observations of whitecap fraction can provide such improved spatial and temporal distribution of W.

Recent results on the time evolution of individual whitecaps have been combined with a dynamical model of whitecap fraction based on breaking wave statistics. The framework enables one to more closely relate whitecap fraction to the dynamics and statistics of breaking waves. It has been shown that such a semi-empircal approach may be favourable to constraining active whitecap fraction W_A which is thought to be more closely related to the dynamic processes associated with wave breaking (such as production of spume droplets) and bubble plume generation (such bubble-mediated gas exchange). Measured total W depends explicitly on the foam decay mechanism; in some situations—for example, when whitecap decay rates are controlled by surfactant stabilisation—estimates of W will be strongly influenced by factors that are not directly related to the active dynamics of the breaking waves. Consideration of both a constant decay rate and one that scales with properties of the breaking waves illustrates the large effect that different decay rate schemes have one estimates of total W (stage A and B whitecaps).

Though our discussion on the utility of satellite-based W estimates in predicting the magnitude of air-sea interaction processes focuses mainly on efforts to improve SSA source flux predictions, we stress that satellite-based estimates of W will also benefit modeling of other air-sea interaction processes associated with whitecaps. These include gas exchange, storm intensification, global radiation budget, and ocean albedo. It would also improve the accuracy of remote sensing retrievals of geophysical variables such as wind vector, sea surface salinity, and ocean color. Though whitecap fraction is an indirect, bulk measure of wave breaking, it provides a convenient approach to predicting the magnitude of bubble-related air-sea mechanisms. However, W needs to be more explicitly linked to these different processes; improved measurement and parameterisation of W needs to be complemented with a more refined understanding of the links between wave breaking, bubble plume production, formation and decay or surface foam layers, and related physical processes.

7.2   Recommendations

7.2.1   Recommendation 1: Continued development of the $W(T_B)$ algorithm

All satellite-based whitecap fraction estimates used in this study were obtained by running the $W(T_B)$ algorithm (v1.96), as described in chapter 3. The method of obtaining satellite-based W estimates is still in development. Continual development of various aspects of the retrieval algorithm, such as the foam emissivity model and atmospheric correction procedure, will lead to more accurate estimates of W.

It is anticipated that the features and trends illustrated here—such as the weaker latitudinal variation of W—are likely to persist, even as changes to the retrieval algorithm affect the magnitude of individual W estimates. The variability analyses carried out in this study should be applied to future (improved) satellite-based estimates of W, and the results compared to the findings presented here. On a related note, should the method of obtaining satellite-based estimates of W be pushed forward to operational use, or at least be routinely available as part of long-term reanalysis type data sets, the effect on predictions of SSA source fluxes, bubble-mediated gas exchange, ocean albedo and global radiation budget, should be evaluated.

7.2.2   Recommendation 2: Further investigation into variability of satellite-based W and improved parameterisations

In its current form, the $W(T_B)$ predicts W estimates that are well described by U_{10}, especially in the case of W_{10}. As shown in this study, wind speed parameterisations of W_{10} and W_{37} can be used in lieu of direct estimates with little loss in accuracy. It may be the case that the benefit of including secondary forcing parameters in parameterisations of satellite-based W is outweighted by the 'costs' involved with sourcing and matching-up data for these variables.

The findings presented here—specifically, the much larger influence of secondary forcings on W_{37} than W_{10}, and the trends seen for different forcing factors—should be further evaluated, for example on a regional basis. A more thorough evaluation of these influences can be achieved through expanding the current W database with

datasets for directional wave spectra, currents (speed and direction), and improved proxies for surfactant concentration. The utility of the database could be enhanced if supplemented with data for underwater bubble plumes and their characteristics, or sea spray production rates. All these additional data can be used to more specifically determine causes for variability in W, and can validate (or disprove) the hypotheses put forward in this work regarding the physical basis of such influences.

7.2.3   Recommendation 3: Further validation of satellite-based estimates of W

A larger scale direct validation of the satellite approach to obtaining W should be sought. Though data volume is limited due to the scarcity of ship-satellite matchups, such comparisons should be made. The recent Waves, Aerosol, and Gas Exchange Study (WAGES), includes three years of near-continuous measurements of W in different ocean regions, and therefore the possibility of obtaining significantly more ship-satellite matchups. The finer details regarding the relationship of radiometric estimates (at different frequencies) to photographic-based estimates need to be evaluated. Such a comparison will also lead to a better understanding of the dependency of W estimates on the measurement technique.

As an alternative or supplementary approach, satellite-based estimates can be compared to both radio radiometric and video estimates of W from aircraft measurements. Though there are practical issues associated with aerial measurements, they provide a half-way point between ship-based and satellite measurement insofar as measurement resolution, sampling area, and statistics are concerned.

Recent work to compare wave model predictions of W with radiometric estimates should be continued as the results can be illuminating. However, use of satellite-based (and traditional) estimates of W as a tool to constrain model dissipation source terms may be more valid and valuable one the relationship between breaking waves and their surface expression is better understood.

7.2.4 Recommendation 4: Re-evaluation of the use of whitecap fraction to predict air-sea processes

The validity of using W to quantifying wave energy dissipation and bubble-mediated processes should be further assessed in laboratory and field studies. Given the complex relationship between the whitecap fraction and its various determining factors—as illustrated in recent work—specific attention should be paid to evaluating the link between W and wave breaking on the scale of individual waves and for a given wave field under different environmental conditions. Laboratory and field studies should be used in combination with models to achieve this goal.

It is worth keeping in mind that W provides only a measure of the areal coverage of foam layers; wave breaking is a three-dimensional processes, but knowledge of the relationship between whitecaps and the dynamics and physical processes beneath the foam is limited. It may be the case that such 'information' needs to be used together with W to better parameterise different air-sea interaction processes. Alternatively, measurements at different radiometric frequencies can be exploited to provide a window on subsurface processes; changes to bubble plume dynamics and properties will manifest as changes to properties of the foam layer above; when these differences induce changes to the radiometric signature of foam, radiometric measurements can provide a window on subsurface processes. It may be the case that the method is developed to fully exploit this extra information carried by observations at different radiometric frequencies.

In theory, the whitecap method provides an effective and useful approach to determining the magnitude of processes driven by air-entrainment by breaking waves. The approach is routinely used to predict SSA source fluxes and can likewise be used to predict the magnitude of bubble-mediated gas exchange. Despite continual development by the marine aerosol community, the basic approach has remained the same since its inception. Despite inherent limitations of the method not being addressed by simply switching from use of traditional $W(U_{10})$ parameterisations to direct satellite-based estimates of W, this change will be a key development which should improve predictions obtained via the whitecap method.

In summary, our understanding of individual whitecaps, their contribution to the observed whitecap fraction, and the link between W and wave breaking needs to be better understood. Only then can more physically-based models of SSA production, bubble-mediated gas exchange, and breaking-induced energy dissipation be developed.

Bibliography

Andreae, M. and Rosenfeld, D. Aerosol-cloud-precipitation interactions. Part 1. The nature and sources of cloud-active aerosols. *Earth Sci. Rev.*, 89(1-2):13–41, 2008. doi: 10.1016/j.earscirev.2008.03.001.

Andreas, E. L. The temperature of evaporating sea spray droplets. *J. Atmos, Sci.*, 52: 852–862, 1995. doi: 10.1175/1520-0469(1995)052⟨0852:TTOESS⟩2.0.CO;2.

Andreas, E. L. and Emanuel, K. A. Effects of sea spray on tropical cyclone intensity. *J. Atmos, Sci.*, 58(24):3741–3751, 2001. doi: 10.1175/1520-0469(2001)058⟨3741: EOSSOT⟩2.0.CO;2.

Andreas, E. L. and Monahan, E. C. The role of whitecap bubbles in air-sea heat and moisture exchange. *J. Phys. Oceanogr.*, 30(2):433–442, 2000. doi: 10.1175⟨1520-0485(2000)030⟨0433:TROWBI⟩2.0.CO;2.

Andreas, E. L., Edison, J. B., Monahan, E., Rouault, M. P., and Smith, S. D. The spray contribution to net evaporation from the sea: A review of recent progress. *Bound.-Lay. Meteorol.*, 72(1):3–52, 1995. doi: 10.1007/BF00712389.

Andreas, E. L., Persson, P. O. G., and Hare, J. E. A bulk turbulent air-sea flux algorithm for high-wind, spray conditions. *J. Phys. Oceanogr.*, 38(7):1581–1596, 2008. doi: 10.1175/2007JPO3813.1.

Anguelova, M., Bettenhausen, M., and Gaiser, P. Passive remote sensing of sea foam using physically-based models. In *Proceedings of International Geoscience and Remote Sensing Symposium, (IGARSS) 2006, Denver, CO, USA*, pages 3676–3679. IEEE, 2006. doi: 10.1109/IGARSS.2006.942.

Anguelova, M. D. Complex dielectric constant of sea foam at microwave frequencies. *J. Geophys. Res.*, 113:C08001, 2008. doi: 10.1029/2007JC004212.

Anguelova, M. D. and Gaiser, P. W. Skin depth at microwave frequencies of sea foam layers with vertical profile of void fraction. *J. Geophys. Res.*, 116:C11002, 2011. doi: 10.1029/2011JC007372.

Anguelova, M. D. and Gaiser, P. W. Microwave emissivity of sea-foam layers with vertical profile of dielectric properties. *Remote Sens. Environ.*, pages 81–96, 2013. doi: 10.1016/j.rse.2013.07.017.

Anguelova, M. D. and Webster, F. Whitecap coverage from satellite measurements: A first step toward modeling the variability of oceanic whitecaps. *J. Geophys. Res.*, 111:C03017, 2006. doi: 10.1029/2005JC003158.

Anguelova, M. D., Bobak, J. P., Asher, W. E., Dowgiallo, D. J., Moat, B. I., Pascal, R. W., and Yelland, M. J. Validation of satellite-based estimates of whitecap coverage: Approaches and initial results. pages 11–15, 2009a. Paper presented at 16th Conference on Air Sea Interaction, AMS, 15–19 January, Phoenix, AZ (Available online: https://ams.confex.com/ams/pdfpapers/143665.pdf).

Anguelova, M. D., Gaiser, P. W., and Raizer, V. Foam emissivity models for microwave observations of oceans from space. In *Proceedings of International Geoscience and Remote Sensing Symposium, (IGARSS 2009), Cape Town, South Africa*, volume 2, pages II–274. IEEE, 2009b.

Anguelova, M. D., Bettenhausen, M., Johnston, W., and Gaiser, P. W. First extensive whitecap database and its use to study whitecap fraction variability. 2010. Paper presented at 17th Conference on Air Sea Interaction, AMS, 26–30 September, Annapolis, MD.

Asher, W. E. and Wanninkhof, R. The effect of bubble-mediated gas transfer on purposeful dual-gaseous tracer experiments. *J. Geophys. Res.*, 103(C5):10555–10560, 1998. doi: 10.1029/98JC00245.

Asher, W. E., Karle, L. M., Higgins, B. J., Farley, P. J., Monahan, E. C., and Leifer, I. S. The influence of bubble plumes on air-seawater gas transfer velocities. *J. Geophys. Res.*, 101(C5):12027–12041, 1996. doi: 10.1029/96JC00121.

Aziz, M., Reising, S., Asher, W., Rose, L., Gaiser, P., and Horgan, K. Effects of air-sea interaction parameters on ocean surface microwave emission at 10 and 37 GHz.

IEEE Trans. Geosci. Remote Sens., 43(8):1763–1774, 2005. doi: 10.1109/TGRS. 2005.848413.

Babanin, A. *Breaking and dissipation of ocean surface waves.* Cambridge University Press, 2011. doi: 10.1017/CBO9780511736162.

Bettenhausen, M., Smith, C., Bevilacqua, R., Wang, N., Gaiser, P., and Cox, S. A nonlinear optimization algorithm for WindSat wind vector retrievals. *IEEE Trans. Geosci. Remote Sens.*, 44(3):597–610, 2006. doi: 10.1109/TGRS.2005.862504.

Bigg, G. R. *The oceans and climate.* Cambridge University Press, 2003.

Blanchard, D. The electrification of the atmosphere by particles from bubbles in the sea. *Prog. Oceanogr.*, 1:73–112, 1963.

Blanchard, D. The production, distribution and bacterial enrichment of the sea-salt aerosol. In *Air-sea exchange of gases and particles*, pages 407–454. Reidel, Boston, USA, 1983.

Bobak, J. P., Asher, W. E., Dowgiallo, D. J., and Anguelova, M. D. Aerial radiometric and video measurements of whitecap coverage. *IEEE Trans. Geosci. Remote Sens.*, 49(6):2183–2193, 2011. doi: 10.1109/TGRS.2010.2103565.

Bondur, V. G. and Sharkov, E. A. Statistical properties of whitecaps on a rough sea. *Oceanology*, 22:274–279, 1982.

Bortkovskii, R. S. and Novak, V. A. Statistical dependencies of sea state characteristics on water temperature and wind-wave age. *Journal Marine Syst.*, 4(2):161–169, 1993.

Bortkovskii, R. *Air-Sea Exchange of Heat and Moisture During Storms.* Kluwer Boston Inc., Hingham, MA, 1987.

Bourassa, M. A., Vincent, D. G., and Wood, W. L. A sea state parameterization with capillary waves and non-arbitrary wave age. *J. Phys. Oceanogr.*, 2001. doi: 10.1175/1520-0485(2001)031⟨2840:ASSPWN⟩2.0.CO;2.

Bourassa, M. A., Gille, S. T., Jackson, D. L., Roberts, J. B., and Wick, G. A. Ocean winds and turbulent air-sea fluxes inferred from remote sensing. *Oceanography*, 23, 2010. doi: 10.5670/oceanog.2010.04.

Brooks, I. M. An overview of the SEA Spray and Whitecap (SEASAW) field study. In *15th Conference on Air-Sea Interaction*, 2007.

Brooks, I. M., Bloom, A. A., Brooks, B. J., Lingard, J. J. N., McQuaid, J. B., Norris, S. J., Smith, M. H., Smith, P. D., Yelland, M. J., Moat, B. I., et al. Physical exchanges at the air–sea interface: UK–SOLAS field measurements. *B. Amer. Meteorol. Soc.*, 90:629–644, 2009. doi: 10.1175/2008BAMS2578.1.

Callaghan, A., de Leeuw, G., Cohen, L., and O'Dowd, C. D. Relationship of oceanic whitecap coverage to wind speed and wind history. *Geophys. Res. Lett.*, 35(23): L23609, 2008a. doi: 10.1029/2008GL036165.

Callaghan, A. H. An improved whitecap timescale for sea spray aerosol production flux modelling using the discrete whitecap method. *J. Geophys. Res.*, pages 1–14, 2013. doi: 10.1029/2004JD005137.

Callaghan, A. H. and White, M. Automated processing of sea surface images for the determination of whitecap coverage. *J. Atmos. Ocean. Tech*, 26(2):383–394, 2009. doi: 10.1175/2008JTECHO634.1.

Callaghan, A. H., Deane, G. B., and Stokes, M. D. Observed physical and environmental causes of scatter in whitecap coverage values in a fetch-limited coastal zone. *J. Geophys. Res.*, 113(C5):C05022, 2008b. doi: 10.1029/2007JC004453.

Callaghan, A. H., Deane, G. B., Stokes, M. D., and Ward, B. Observed variation in the decay time of oceanic whitecap foam. *J. Geophys. Res.*, 117(C9):C09015, 2012. doi: 10.1029/2012JC008147.

Callaghan, A. H., Deane, G. B., and Stokes, D. M. Two regimes of laboratory whitecap foam decay: bubble-plume controlled and surfactant stabilized. *J. Phys. Oceanogr.*, pages 1114–1126, 2013. doi: 10.1175/JPO-D-12-0148.1.

Camps, A., Vall-llossera, M., Batres, L., Torres, F., Duffo, N., and Corbella, I. Retrieving sea surface salinity with multiangular l-band brightness temperatures: Improvement by spatiotemporal averaging. *Rad. Sci.*, 40(2), 2005. doi: 10.1029/2004RS003040.

Cardone, V. J. Specification of the wind distribution in the marine boundary layer for wave forecasting. Technical report, 69-1, 131 pp., Geophys. Sci. Lab., N. Y. Univ., New York., 1969.

Carter, D. J. T. Prediction of wave height and period for a constant wind velocity using the JONSWAP results. *Ocean Eng.*, 9(1):17–33, 1982.

Cavaleri, L., Fox-Kemper, B., and Hemer, M. Wind-waves in the coupled climate system. *B. Amer. Meteorol. Soc.*, 2012. doi: 10.1175/BAMS-D-11-00170.1.

Chelton, D. B. and Freilich, M. H. Scatterometer-based assessment of 10-m wind analyses from the operational ECMWF and NCEP numerical weather prediction models. *Mon Weather Rev*, 133(2):409–429, 2005. doi: 10.1175/MWR-2861.1.

Chen, G., Chapron, B., Ezraty, R., and Vandemark, D. A global view of swell and wind sea climate in the ocean by satellite altimeter and scatterometer. *J. Atmos. Ocean. Tech*, 19(11):1849–1859, 2002. doi: 10.1175/1520-0426(2002)019⟨1849:AGVOSA⟩2. 0.CO;2.

Chin, M., Ginoux, P., Kinne, S., Torres, O., Holben, B. N., Duncan, B. N., Martin, R. V., Logan, J. A., Higurashi, A., and Nakajima, T. Tropospheric aerosol optical thickness from the GOCART model and comparisons with satellite and sun photometer measurements. *J. Atmos, Sci.*, 59(3):461–483, 2002. doi: 10.1175/1520-0469(2002)059⟨0461:TAOTFT⟩2.0.CO;2.

de Leeuw, G., Moerman, M., Zappa, C. J., McGillis, W. R., Norris, S., and Smith, M. Eddy correlation measurements of sea spray aerosol fluxes. In *Transport at the Air-Sea Interface*, pages 297–311. Springer, Berlin, 2007. doi: 10.1007/ 978-3-540-36906-6_21.

de Leeuw, G., Andreas, E. L., Anguelova, M. D., Fairall, C. W., Lewis, E. R., O'Dowd, C., Schulz, M., and Schwartz, S. E. Production flux of sea spray aerosol. *Rev. Geophys.*, 49(2):RG2001, 2011. doi: 10.1029/2010RG000349.

Deane, G. B. and Stokes, M. D. Scale dependence of bubble creation mechanisms in breaking waves. *Nature*, 418(6900):839–844, 2002. doi: 10.1038/nature00967.

Dobbie, S., Li, J., Harvey, R., and Chýlek, P. Sea-salt optical properties and GCM forcing at solar wavelengths. *Atmos. Res.*, 65(3-4):211–233, 2003. doi: 10.1016/S0169-8095(02)00150-3.

Donelan, M. A. and Pierson Jr., W. J. Radar scattering and equilibrium ranges in wind-generated waves with application to scatterometry. *J. Geophys. Res.*, 92(C5): 4971–5029, 1987.

Drazen, D. A., Melville, W. K., and Lenain, L. Inertial scaling of dissipation in unsteady breaking waves. *J. Fluid Mech.*, 611:307–332, 2008. doi: 10.1017/S0022112008002826.

Dulov, V. A., Kudryavtsev, V. N., and Bol'Shakov, A. N. A field study of whitecap coverage and its modulations by energy containing surface waves. In *Gas Transfer at Water Surfaces*, pages 187–192. Wiley Online Library, 2002.

Duncan, J. H. An experimental investigation of breaking waves produced by a towed hydrofoil. *Proc. R. Soc. London, Ser. A*, 377(1770):331–348, 1981.

Ebuchi, N. Statistical distribution of wind speeds and directions globally observed by NSCAT. *J. Geophys. Res.*, 104(C5):11393–11, 1999. doi: 10.1029/98JC02061.

Erickson III, D. J., Merrill, J. T., and Duce, R. A. Seasonal estimates of global oceanic whitecap coverage. *J. Geophys. Res.*, 91(C11):12975–12977, 1986. doi: 10.1029/JC091iC11p12975.

Facchini, M., Rinaldi, M., Decesari, S., Carbone, C., Finessi, E., Mircea, M., Fuzzi, S., Ceburnis, D., Flanagan, R., Nilsson, E., et al. Primary submicron marine aerosol dominated by insoluble organic colloids and aggregates. *Geophys. Res. Lett.*, 35(17): L17814, 2008. doi: 10.1029/2008GL034210.

Fairall, C. W., Kepert, J. D., and Holland, G. J. The effect of sea spray on surface energy transports over the ocean. *Global Atmos. Ocean Sys.*, 2(2-3):121–142, 1994.

Fairall, C. W., Yang, M., Bariteau, L., Edson, J. B., Helmig, D., McGillis, W., Pezoa, S., Hare, J. E., Huebert, B., and Blomquist, B. Implementation of the Coupled Ocean-Atmosphere Response Experiment flux algorithm with CO_2, dimethyl sulfide, and O_3. *J. Geophys. Res.*, 116:C00F09, 2011.

Fairall, C. Interpretation of eddy-correlation measurements of particulate deposition and aerosol flux. *Atmos. Environ.*, 18(7):1329–1337, 1984. doi: 10.1016/0004-6981(84)90041-6.

Falkowski, P. G., Barber, R. T., and Smetacek, V. Biogeochemical controls and feedbacks on ocean primary production. *Science*, 281(5374):200–206, 1998. doi: 10.1126/science.281.5374.200.

Fitzgerald, J. W. Marine aerosols: A review. 25A(3-4):533–545, 1991. doi: 10.1016/0960-1686(91)90050-H.

Frouin, R., Iacobellis, S. F., and Deschamps, P. Y. Influence of oceanic whitecaps on the global radiation budget. *Geophys. Res. Lett.*, 28(8):1523–1526, 2001. doi: 10.1029/2000GL012657.

Fuentes, E., Coe, H., Green, D., de Leeuw, G., and McFiggans, G. Laboratory-generated primary marine aerosol via bubble-bursting and atomization. *Atmos. Meas. Tech.*, 3:141–162, 2010. doi: 10.5194/amt-3-141-2010.

Gaiser, P. W., St Germain, K. M., Twarog, E. M., Poe, G. A., Purdy, W., Richardson, D., Grossman, W., Jones, W. L., Spencer, D., Golba, G., et al. The WindSat spaceborne polarimetric microwave radiometer: Sensor description and early orbit performance. *IEEE Trans. Geosci. Remote Sens.*, 42(11):2347–2361, 2004. doi: 10.1109/TGRS.2004.836867.

Gantt, B., Johnson, M. S., Meskhidze, N., Sciare, J., Ovadnevaite, J., Ceburnis, D., and O'Dowd, C. D. Model evaluation of marine primary organic aerosol emission schemes. *Atmos. Chem. Phys.*, 12(18):8553–8566, 2012. doi: 10.5194/acp-12-8553-2012.

Garfinkel, C. I., Molod, A. M., Oman, L. D., and Song, I.-S. Improvement of the GEOS-5 AGCM upon updating the air-sea roughness parameterization. *Geophys. Res. Lett.*, 38(18), 2011. doi: 10.1029/2011GL048802.

Garrett, W. D. Stabilization of air bubbles at the air-sea interface by surface-active material. *Deep-Sea Res.*, 14(6):661–672, 1967. doi: 10.1016/S0011-7471(67)80004-4.

Gathman, S. and Trent, E. M. Space charge over the open ocean. *J. Atmos. Sci.*, 25:1075–1079, 1968. doi: 10.1175/1520-0469(1968)025⟨1075:SCOTOO⟩2.0.CO;2.

Geever, M., O'Dowd, C. D., van Ekeren, S., Flanagan, R., Nilsson, E. D., de Leeuw, G., and Rannik, U. Submicron sea spray fluxes. *Geophys. Res. Lett.*, 32(15):L15810, 2005. doi: 10.1029/2005GL023081.

Gemmrich, J. R., Banner, M. L., and Garrett, C. Spectrally resolved energy dissipation rate and momentum flux of breaking waves. *J. Phys. Oceanogr.*, 38(6):1296–1312, 2008. doi: 10.1175/2007JPO3762.1.

Goddijn-Murphy, L., Woolf, D. K., and Callaghan, A. H. Parameterizations and algorithms for oceanic whitecap coverage. *J. Phys. Oceanogr.*, 41(4):742–756, 2011. doi: 10.1175/2010JPO4533.1.

Gong, S. L. A parameterization of sea-salt aerosol source function for sub-and super-micron particles. *Global Biogeochem. Cy.*, 17(4):1097, 2003. doi: 10.1029/2003GB002079.

Gordon, H. R. and Wang, M. Influence of oceanic whitecaps on atmospheric correction of ocean-color sensors. *Appl. Opt.*, 33(33):7754–7763, 1994. doi: 10.1364/AO.33.007754.

Guan, C., Hu, W., Sun, J., and Li, R. The whitecap coverage model from breaking dissipation parametrizations of wind waves. *J. Geophys. Res.*, 112(C5):C05031, 2007. doi: 10.1029/2006JC003714.

Hanley, K. E., Belcher, S. E., and Sullivan, P. P. A global climatology of wind-wave interaction. *J. Phys. Oceanogr.*, 40(6):1263–1282, 2010. doi: 10.1175/2010JPO4377.1.

Hanson, J. L. and Phillips, O. M. Wind sea growth and dissipation in the open ocean. *J. Phys. Oceanogr.*, 29(8):1633–1648, 1999. doi: 10.1175/1520-0485(1999)029⟨1633:WSGADI⟩2.0.CO;2.

Harmel, T. and Chami, M. Determination of sea surface wind speed using the polarimetric and multidirectional properties of satellite measurements in visible bands. *Geophys. Res. Lett.*, 39(19), 2012. doi: 10.1029/2012GL053508.

Hasselmann, S., Hasselmann, K., Bauer, E., Janssen, P., Komen, G., Bertotti, L., Lionello, P., Guillaume, A., Cardone, V., Greenwood, J., et al. The WAM model:

A third generation ocean wave prediction model. *J. Phys. Oceanogr.*, 18:1775–1810, 1988. doi: 10.1175/1520-0485(1988)018⟨1775:TWMTGO⟩2.0.CO;2.

Haywood, J. M., Ramaswamy, V., and Soden, B. J. Tropospheric aerosol climate forcing in clear-sky satellite observations over the oceans. *Science*, 283(5406):1299, 1999. doi: 10.1126/science.283.5406.1299.

Hoffman, E. J. and Duce, R. A. Factors influencing the organic carbon content of marine aerosols: a laboratory study. *J. Geophys. Res.*, 81(21):3667–3670, 1976. doi: 10.1029/JC081i021p03667.

Holthuijsen, L. H. *Waves in oceanic and coastal waters.* Cambridge University Press, 2007. doi: 10.1029/2012JC007983.

Holthuijsen, L. H., Powell, M. D., and Pietrzak, J. D. Wind and waves in extreme hurricanes. *J. Geophys. Res.*, 117(C9), 2012. doi: 10.1029/2012JC007983.

Houghton, J. T., Ding, Y. D. J. G., Griggs, D. J., Noguer, M., van der Linden, P. J., Dai, X., Maskell, K., and Johnson, C. A. *Climate Change 2001: The Scientific Basis*, volume 881. Cambridge University Press, Cambridge, 2001.

Hwang, P. A. Temporal and spatial variation of the drag coefficient of a developing sea under steady wind-forcing. *J. Geophys. Res.*, 110(C7), 2005. doi: 10.1029/2005JC002912.

Hwang, P. A. Foam and roughness effects on passive microwave remote sensing of the ocean. *IEEE Trans. Geosci. Remote Sens.*, 50(8):2978–2985, 2012. doi: 10.1109/TGRS.2011.2177666.

Hwang, P. A. and Sletten, M. A. Energy dissipation of wind-generated waves and white-cap coverage. *J. Geophys. Res.*, 113(C2):C02012, 2008. doi: 10.1029/2007JC004277.

Hwang, P. A., Ocampo-Torres, F. J., and García-Nava, H. Wind sea and swell separation of 1D wave spectrum by a spectrum integration method. *J. Atmos. Ocean. Tech*, 29(1):116–128, 2012. doi: 10.1175/JTECH-D-11-00075.1.

Ichoku, C., Chu, D., Mattoo, S., Kaufman, Y., Remer, L., Tanré, D., Slutsker, I., and Holben, B. A spatio-temporal approach for global validation and analysis of MODIS aerosol products. *Geophys. Res. Lett.*, 29(12):8006, 2002. doi: 10.1029/2001GL013206.

Jaeglé, L., Quinn, P. K., Bates, T. S., Alexander, B., and Lin, J.-T. Global distribution of sea salt aerosols: new constraints from in situ and remote sensing observations. *Atmos. Chem. Phys.*, 11(7):3137–3157, 2011. doi: 10.5194/acp-11-3137-2011.

Jähne, B., Münnich, K. O., Bösinger, R., Dutzi, A., Huber, W., and Libner, P. On the parameters influencing air-water gas exchange. *Journal of Geophysical Research: Oceans (1978–2012)*, 92(C2):1937–1949, 1987. doi: 10.1029/JC092iC02p01937.

Janssen, P. A. E. M. Quasi-linear theory of wind-wave generation applied to wave forecasting. *J. Phys. Oceanogr.*, 21(11):1631–1642, 1991. doi: 10.1175/1520-0485(1991) 021⟨1631:QLTOWW⟩2.0.CO;2.

Jessup, A. and Phadnis, K. Measurement of the geometric and kinematic properties of microscale breaking waves from infrared imagery using a PIV algorithm. *Meas. Sci. Technol.*, 16(10):1961, 2005. doi: 10.1088/0957-0233/16/10/011.

Jessup, A., Zappa, C. J., and Yeh, H. Defining and quantifying microscale wave breaking with infrared imagery. *J. Geophys. Res.*, 102(C10):23145–23, 1997. doi: 10.1029/97JC01449.

Johnson, J. T. An efficient two-scale model for the computation of thermal emission and atmospheric reflection from the sea surface. *IEEE Trans. Geosci. Remote Sens.*, 44(3):560–568, 2006. doi: 10.1109/TGRS.2005.855999.

Kara, A. B., Hurlburt, H. E., and Loh, W.-Y. Which near–surface atmospheric variable drives air–sea temperature differences over the global ocean? *J. Geophys. Res.*, 112 (C5), 2007. doi: 10.1029/2006JC003833.

Kara, A. B., Wallcraft, A. J., and Bourassa, M. A. Air-sea stability effects on the 10 m winds over the global ocean: Evaluations of air-sea flux algorithms. *J. Geophys. Res.*, 113:C04009, 2008. doi: 10.1029/2007JC004324.

Keeling, R. F. On the role of large bubbles in air-sea gas exchange and supersaturation in the ocean. *J. Mar. Res*, 51(2):237–271, 1993. doi: 10.1357/0022240933223800.

Keene, W. C., Maring, H., Maben, J. R., Kieber, D. J., Pszenny, A. P., Dahl, E. E., Izaguirre, M. A., Davis, A. J., Long, M. S., Zhou, X., et al. Chemical and physical characteristics of nascent aerosols produced by bursting bubbles at a model air-sea interface. *Journal of Geophysical Research*, 112(D21):D21202, 2007.

Kennedy, R. M. and Snyder, R. L. On the formation of whitecaps by a threshold mechanism. Part ii: Monte Carlo experiments. *J. Phys. Oceanogr.*, 13(8):1493–1504, 1983. doi: 0.1175/1520-0485(1983)0132.0.CO;2.

Kleiss, J. M. *Airborne observations of the kinematics and statistics of breaking waves.* PhD thesis, University of California, San Diego, 2009.

Kleiss, J. M. and Melville, W. K. Observations of wave breaking kinematics in fetch-limited seas. *J. Phys. Oceanogr.*, 40(12):2575–2604, 2010. doi: 10.1175/ 2010JPO4383.1.

Kleiss, J. M. and Melville, W. K. The analysis of sea surface imagery for whitecap kinematics. *J. Atmos. Ocean. Tech*, 28(2):219–243, 2011. doi: 10.1175/2010JTECHO744. 1.

Koepke, P. Effective reflectance of oceanic whitecaps. *Appl. Opt.*, 23(11):1816–1824, 1984. doi: 10.1364/AO.23.001816.

Kondo, J., Fujinawa, Y., and Naito, G. High-frequency components of ocean waves and their relation to the aerodynamic roughness. *J. Phys. Oceanogr.*, 3(2):197–202, 1973. doi: 10.1175/1520-0485(1973)003⟨0197:HFCOOW⟩2.0.CO;2.

Kraan, C., Oost, W. A., and Janssen, P. Wave energy dissipation by whitecaps. *J. Atmos. Ocean. Tech*, 13:262–267, 1996. doi: 10.1175/1520-0426(1996)013⟨0262: WEDBW⟩2.0.CO;2.

Kunkee, D. B. and Gasiewski, A. J. Simulation of passive microwave wind direction signatures over the ocean using an asymmetric-wave geometrical optics model. *Radio Science*, 32(1):59–78, 1997. doi: 10.1029/96RS02434.

Lafon, C., Piazzola, J., Forget, P., Le Calve, O., and Despiau, S. Analysis of the variations of the whitecap fraction as measured in a coastal zone. *Bound.-Lay. Meteorol.*, 111(2):339–360, 2004. doi: 10.1023/B:BOUN.0000016490.83880.63.

Lafon, C., Piazzola, J., Forget, P., and Despiau, S. Whitecap coverage in coastal environment for steady and unsteady wave field conditions. *J. Mar. Syst.*, 66(1-4): 38–46, 2007. doi: 10.1016/j.jmarsys.2006.02.013.

Large, W. G. and Pond, S. Open ocean momentum flux measurements in moderate to strong winds. *J. Phys. Oceanogr.*, 11(3):324–336, 1981. doi: 10.1175/1520-0485(1981)011⟨0324:OOMFMI⟩2.0.CO;2.

Leckler, F., Ardhuin, F., Filipot, J., and Mironov, A. Dissipation source terms and whitecap statistics. *Ocean Modelling*, 70:62–74, 2013. doi: 10.1016/j.ocemod.2013.03.007.

Leifer, I., Patro, R. K., and Bowyer, P. A study on the temperature variation of rise velocity for large clean bubbles. *J. Atmos. Ocean. Tech*, 17(10):1392–1402, 2000. doi: 10.1175/1520-0426(2000)017⟨1392:ASOTTV⟩2.0.CO;2.

Lewis, E. R. and Schwartz, S. E. *Sea Salt Aerosol Production: Mechanisms, Methods, Measurements and Models: A Critical Review*. AGU, Washington, DC., 2004. doi: 10.1029/GM152.

Liss, P. S. and Merlivat, L. Air-sea gas exchange rates: Introduction and synthesis. In Buat-Menard, P., editor, *The role of air-sea exchange in geochemical cycling*, pages 113–127. Springer, 1986.

Long, M. S., Keene, W. C., Kieber, D., Erickson, D., and Maring, H. A sea-state based source function for size-and composition-resolved marine aerosol production. *Atmos. Chem. Phys.*, 11(3):1203–1216, 2011. doi: 10.5194/acp-11-1203-2011.

Marmorino, G. and Smith, G. Bright and dark ocean whitecaps observed in the infrared. *Geophys. Res. Lett.*, 32(11), 2005. doi: 10.1029/2005GL023176.

Mårtensson, E. M., Nilsson, E. D., de Leeuw, G., Cohen, L. H., and Hansson, H.-C. Laboratory simulations and parameterization of the primary marine aerosol production. *J. Geophys. Res.*, 108(D9), 2003. doi: 10.1029/2002JD002263.

Massel, S. R. *Ocean Waves Breaking and Marine Aerosol Fluxes*, volume 38 of *Atmospheric and Oceanographic Sciences Library*. Springer, New York, 2007. doi: 10.1007/978-0-387-69092-6.

McClain, C. R., Feldman, G. C., and Hooker, S. B. An overview of the SeaWiFS project and strategies for producing a climate research quality global ocean bio-optical time series. *Deep Sea Res. Pt. II*, 51(1):5–42, 2004. doi: 10.1016/j.dsr2.2003.11.001.

McGillis, W. R., Edson, J. B., Hare, J. E., and Fairall, C. W. Direct covariance air-sea CO_2 fluxes. *J. Geophys. Res.*, 106(C8):16729–16, 2001. doi: 10.1029/2000JC000506.

McGillis, W. R., Edson, J. B., Zappa, C. J., Ware, J. D., McKenna, S. P., Terray, E. A., Hare, J. E., Fairall, C. W., Drennan, W., Donelan, M., et al. Air–sea CO_2 exchange in the equatorial pacific. *J. Geophys. Res.*, 109(C8), 2004. doi: 10.1029/2003JC002256.

McNeil, C. and D'Asaro, E. Parameterization of air–sea gas fluxes at extreme wind speeds. 66(1):110–121, 2007. doi: 10.1016/j.jmarsys.2006.05.013.

Melville, W. K. and Matusov, P. Distribution of breaking waves at the ocean surface. *Nature*, 417(6884):58–63, 2002. doi: 10.1038/417058a.

Memery, L. and Merlivat, L. Modelling of gas flux through bubbles at the air-water interface. *Tellus B*, 37(4-5):272–285, 1985. doi: 10.1111/j.1600-0889.1985.tb00075.x.

Merlivat, L. and Memery, L. Gas exchange across an air-water interface: Experimental results and modeling of bubble contribution to transfer. *J. Geophys. Res.*, 88(C1): 707–724, 1983. doi: 10.1029/JC088iC01p00707.

Moat, B. I., Yelland, M. J., and Molland, A. F. Quantifying the airflow distortion over merchant ships. Part II: Application of the model results. *J. Atmos. Ocean. Tech*, 23(3):351–360, 2006. doi: 10.1175/JTECH1859.1.

Moat, B. I., Yelland, M. J., and Pascal, R. W. Oceanic whitecap coverage measured during UK-SOLAS cruises. Paper presented at 16th Conference on Air Sea Interaction, AMS, 15–19 January, Phoenix, AZ, 2009.

Modini, R. L., Russell, L. M., Deane, G. B., and Stokes, M. D. Effect of soluble surfactant on bubble persistence and bubble-produced aerosol particles. *J. Geophys. Res.*, pages 1–13, 2013. doi: 10.1002/jgrd.50186.

Monahan, E. C. Oceanic whitecaps. *J. Phys. Oceanogr.*, 1:139–144, 1971. doi: 10.11751520-0485(1971)001⟨0139:OW⟩2.0.CO;2.

Monahan, E. C. and Dam, H. G. Bubbles: an estimate of their role in the global oceanic flux of carbon. *J. Geophys. Res.*, 106(C5):9377–9383, 2001. doi: 10.1029/2000JC000295.

Monahan, E. C. and Lu, M. Acoustically relevant bubble assemblages and their dependence on meteorological parameters. *IEEE J. Ocean. Eng.*, 15(4):340–349, 1990. doi: 10.1109/48.103530.

Monahan, E. C. and O'Muircheartaigh, I. G. Optimal power-law description of oceanic whitecap coverage dependence on wind speed. *J. Phys. Oceanogr.*, 10:2094–2099, 1980. doi: 10.1175/1520-0485(1980)010⟨2094:OPLDOO⟩2.0.CO;2.

Monahan, E. C. and O'Muircheartaigh, I. G. Whitecaps and the passive remote sensing of the ocean surface. *Int. J. Remote. Sens.*, 7(5):627–642, 1986. doi: 10.1080/01431168608954716.

Monahan, E. C. and Spillane, M. C. The role of oceanic whitecaps in air-sea gas exchange. In Brutsaert, W. and Jirka, G. H., editors, *Gas transfer at water surfaces*, pages 495–503. Springer, 1984. doi: 10.1007/978-94-017-1660-4_45.

Monahan, E. C. and Torgersen, T. The enhancement of air-sea gas exchange by oceanic whitecapping. In *Air-Water Mass Transfer*, pages 608–617. ASCE, 1991.

Monahan, E. C. and Woolf, D. Comments on "Variations of whitecap coverage with wind stress and water temperature". *J. Phys. Oceanogr.*, 19:706–709, 1988. doi: 10.1175/1520-0485(1989)019⟨0706:COOWCW⟩2.0.CO;2.

Monahan, E. C. and Zietlow, C. R. Laboratory comparisons of fresh-water and salt-water whitecaps. *J. Geophys. Res.*, 74(28):6961–6966, 1969. doi: 10.1029/JC074i028p06961.

Monahan, E. C., Davidson, K. L., and Spiel, D. E. Whitecap aerosol productivity deduced from simulation tank measurements. *J. Geophys. Res.*, 87(C11):8898–8904, 1982. doi: 10.1029/JC087iC11p08898.

Monahan, E. C., Spiel, D. E., and Davidson, K. L. A model of marine aerosol generation via whitecaps and wave disruption. In Monahan, E. C. and Niocaill, G., editors, *Oceanic whitecaps*, pages 167–174. Springer, 1986. doi: 10.1007/978-94-009-4668-2_16.

Monahan, E., Fairall, C., Davidson, K., and Boyle, P. Observed inter-relations between 10m winds, ocean whitecaps and marine aerosols. *Quart. J. Roy. Meteorol. Soc.*, 109(460):379–392, 1983. doi: 10.1002/qj.49710946010.

Mueller, J. A. and Veron, F. A sea state–dependent spume generation function. *J. Phys. Oceanogr.*, 39(9), 2009. doi: 10.1175/2009JPO4113.1.

Munk, W. H. A critical wind speed for air-sea boundary processes. *J. Marine. Res.*, 6:203–218, 1947.

Nilsson, E. D. and Rannik, Ü. Turbulent aerosol fluxes over the Arctic Ocean 1. Dry deposition over sea and pack ice. *J. Geophys. Res.*, 106(D23):32125–32137, 2001. doi: 10.1029/2000JD900605.

Nilsson, E. D., Rannik, Ü., Swietlicki, E., Leek, C., Aalto, P. P., Zhou, J., and Norman, M. Turbulent aerosol fluxes over the Arctic Ocean 2. Wind-driven sources from the sea. *J. Geophys. Res.*, 106(D23):32139–32154, 2001. doi: 10.1029/2000JD900747.

Nordberg, W., Conaway, J., Ross, D., and Wilheit, T. Measurements of microwave emission from a foam-covered, wind-driven sea. *J. Atmos, Sci.*, 28:429–435, 1971. doi: 10.1175/1520-0469(1971)028⟨0429⟩MOMEFA⟩2.0.CO;2.

Norris, S. J., Brooks, I. M., Hill, M. K., Brooks, B. J., Smith, M. H., and Sproson, D. A. J. Eddy covariance measurements of the sea spray aerosol flux over the open ocean. *J. Geophys. Res.*, 117(D7), 2012. doi: 10.1029/2011JD016549.

Norris, S. J., Brooks, I. M., and Salisbury, D. J. A wave roughness reynolds number parameterization of the sea-spray source flux. *Geophys. Res. Lett.*, 40(16):4414–4419, 2013a.

Norris, S., Brooks, I., de Leeuw, G., Smith, M., Moerman, M., and Lingard, J. Eddy covariance measurements of sea spray particles over the Atlantic Ocean. *Atmos. Chem. Phys.*, 8(3):555–563, 2008. doi: 10.5194/acp-8-555-2008.

Norris, S., Brooks, I. M., Moat, B. I., Yelland, M. J., de Leeuw, G., Pascal, R. W., and Brooks, B. Near-surface measurements of sea spray aerosol production over whitecaps in the open ocean. *Ocean Science*, 9(1):133–145, 2013b. doi: 10.5194/os-9-133-2013.

O'Dowd, C. and de Leeuw, G. Marine aerosol production: a review of the current knowledge. *Philos. Trans. R. Soc. A*, 365(1856):1753–1774, 2007. doi: 10.1098/rsta.2007.2043.

O'Dowd, C., Facchini, M. C., Cavalli, F., Ceburnis, D., Mircea, M., Decesari, S., Fuzzi, S., Yoon, Y. J., and Putaud, J. P. Biogenically driven organic contribution to marine aerosol. *Nature*, 431(7009):676–680, 2004. doi: 10.1038/nature02959.

O'Dowd, C., Langmann, B., Varghese, S., Scannell, C., Ceburnis, D., and Facchini, M. A combined organic-inorganic sea-spray source function. *Geophys. Res. Lett.*, 35(1): 1–5, 2008. doi: 10.1029/2007GL030331.

Ovadnevaite, J., Ceburnis, D., Canagaratna, M., Berresheim, H., Bialek, J., Martucci, G., Worsnop, D. R., and O'Dowd, C. On the effect of wind speed on submicron sea salt mass concentrations and source fluxes. *J. Geophys. Res.*, 117(D16), 2012. doi: 10.1029/2011JD017379.

Padmanabhan, S., Reising, S. C., Asher, W. E., Rose, L. A., and Gaiser, P. W. Effects of foam on ocean surface microwave emission inferred from radiometric observations of reproducible breaking waves. *IEEE Trans. Geosci. Remote Sens.*, 44(3):569–583, 2006. doi: 10.1109/TGRS.2006.870234.

Padmanabhan, S., Reising, S. C., Asher, W. E., Raizer, V., and Gaiser, P. W. Comparison of modeled and observed microwave emissivities of water surfaces in the presence of breaking waves and foam. In *Geoscience and Remote Sensing Symposium, 2007. IGARSS 2007. IEEE International*, pages 42–45. IEEE, 2007. doi: 10.1109/IGARSS.2007.4422725.

Pandey, P. and Kakar, R. An empirical microwave emissivity model for a foam-covered sea. *IEEE J. Ocean. Eng.*, 7(3):135–140, 1982. doi: 10.1109/JOE.1982.1145527.

Peltzer, R. D. and Griffin, O. M. The stability and decay of foam in sea water. *Ocean Phys. Eng.*, 12(2):101–126, 1987.

Phillips, O. M. Spectral and statistical properties of the equilibrium range in wind-generated gravity waves. *J. Fluid Mech.*, 156(1):505–531, 1985. doi: 10.1017/S0022112085002221.

Phillips, O. M., Posner, F. L., and Hansen, J. P. High range resolution radar measurements of the speed distribution of breaking events in wind-generated ocean waves: Surface impulse and wave energy dissipation rates. *J. Phys. Oceanogr.*, 31(2):450–460, 2001. doi: 10.1175/1520-0485(2001)031⟨0450:HRRRMO⟩2.0.CO;2.

Pierson, W. J., Neumann, G., and James, R. W. *Practical methods for observing and forecasting ocean waves by means of wave spectra and statistics*, volume Publ. 603. U.S. Nav. Oceanogr. Off., Stennis Space Cent., Miss., 1955.

Plant, W. J. Whitecaps in deep water. *Geophys. Res. Lett.*, 39(16), 2012. doi: 10. 1029/2012GL052732.

Preisendorfer, R. W. and Mobley, C. D. *Principal Component Analysis in Meteorology and Oceanography*, volume 425. Elsevier, New York, 1988.

Quilfen, Y., Prigent, C., Chapron, B., Mouche, A. A., and Houti, N. The potential of QuikSCAT and WindSat observations for the estimation of sea surface wind vector under severe weather conditions. *J. Geophys. Res.*, 112(C9), 2007. doi: 10.1029/ 2007JC004163.

Quinn, P., Kapustin, V., Bates, T., and Covert, D. Chemical and optical properties of marine boundary layer aerosol particles of the mid-pacific in relation to sources and meteorological transport. *J. Geophys. Res.*, 101(D3):6931–6951, 1996. doi: 10.1029/95JD03444.

Rannik, Ü. and Vesala, T. Autoregressive filtering versus linear detrending in estimation of fluxes by the eddy covariance method. *Bound.-Lay. Meteorol.*, 91(2):259–280, 1999. doi: 10.1023/A:1001840416858.

Rapp, R. and Melville, W. K. Laboratory measurements of deep-water breaking waves. *Philos. Trans. R. Soc. A*, pages 735–800, 1990. doi: 10.1098/rsta.1990.0098.

Reddy, M., Boucher, O., Balkanski, Y., and Schulz, M. Aerosol optical depths and direct radiative perturbations by species and source type. 32(12):L12803, 2005. doi: 10.1029/2004GL021743.

Reising, S., Asher, W., Rose, L., and Aziz, M. Passive polarimetric remote sensing of the ocean surface: the effects of surface roughness and whitecaps. *Proceedings of the International Union of Radio Science*, 2002.

Resch, F. J., Darrozes, J. S., and Afeti, G. M. Marine liquid aerosol production from bursting of air bubbles. *J. Geophys. Res.*, 91(C1):1019–1029, 1986. doi: 10.1029/ JC091iC01p01019.

Reul, N. and Chapron, B. A model of sea-foam thickness distribution for passive microwave remote sensing applications. *J. Geophys. Res.*, 108(C10), 2003. doi: 10.1029/2003JC001887.

Rogers, D. Air-sea interaction: Connecting the ocean and atmosphere. *Rev. Geophys.*, 33:Suppl. 1377–1383, 1995. doi: 10.1029/95RG00255.

Romero, L., Melville, W. K., and Kleiss, J. M. Spectral energy dissipation due to surface wave breaking. *J. Phys. Oceanogr.*, 42(9), 2012. doi: 10.1175/JPO-D-11-072. 1.

Rose, L. A., Asher, W. E., Reising, S. C., Gaiser, P. W., St Germain, K. M., Dowgiallo, D. J., Horgan, K. A., Farquharson, G., and Knapp, E. J. Radiometric measurements of the microwave emissivity of foam. *IEEE Trans. Geosci. Remote Sens.*, 40(12): 2619–2625, 2002. doi: 10.1109/TGRS.2002.807006.

Ross, D. B. and Cardone, V. Observations of oceanic whitecaps and their relation to remote measurements of surface wind speed. *J. Geophys. Res.*, 79(3):444–452, 1974. doi: 10.1029/JC079i003p00444.

Salisbury, D. J., Anguelova, M. D., and Brooks, I. M. On the variability of whitecap fraction using satellite-based observations. *J. Geophys. Res.*, 118(11):6201–6222, 2013. doi: 10.1002/2013JC008797.

Salisbury, D. J., Anguelova, M. D., and Brooks, I. M. Global distribution and seasonal dependence of satellite-based whitecap fraction. *Geophys. Res. Lett.*, 41(5):1616–1623, 2014. doi: 10.1002/2014GL059246.

Saltzman, E. Marine aerosols. In *Surface Ocean - Lower Atmosphere Processes*, pages 17–35. AGU, Washington, D.C., 2009. doi: 10.1029/2008GM000769.

Savelyev, I. B., Anguelova, M. D., Frick, G. M., Dowgiallo, D. J., Hwang, P. A., Caffrey, P. F., and Bobak, J. P. On direct passive microwave remote sensing of sea spray aerosol production. *Atmos. Chem. Phys. Disscuss.*, 14(10):15363–15417, 2014. doi: 10.5194/acpd-14-15363-2014.

Sayer, A. M., Thomas, G. E., and Grainger, R. G. A sea surface reflectance model for (A)TSR, and application to aerosol retrievals. *Atmos. Meas. Tech.*, 3(2):1023–1098, 2010. doi: 10.5194/amt-3-813-2010.

Schwendeman, M., Thomson, J., and Gemmrich, J. R. Wave breaking dissipation in a young wind sea. *J. Phys. Oceanogr.*, 44(1), 2014. doi: 10.1175/JPO-D-12-0237.1.

Scott, J. C. The effect of organic films on water surface motions. In Monahan, E. and g. Niocaill, editors, *Oceanic whitecaps and their role in air-sea exchange processes*, pages 159–165. Springer, New York, 1986. doi: 10.1007/978-94-009-4668-2_15.

Sharkov, E. A. *Breaking Ocean Waves: Geometry, Structure and Remote Sensing*. Springer Praxis Books, 2007. doi: 10.1007/978-3-540-29828-1.

Smirnov, A., Holben, B., Giles, D. M., Slutsker, I., O'Neill, N. T., Eck, T. F., Macke, A., Croot, P., Courcoux, Y., Sakerin, S. M., et al. Maritime aerosol network as a component of AERONET - first results and comparison with global aerosol models and satellite retrievals. *Atmos. Meas. Tech.*, 4:1–32, 2011. doi: 10.5194/amt-4-583-2011.

Smith, P. The emissivity of sea foam at 19 and 37 GHz. *IEEE Trans. Geosci. Remote Sens.*, 26(5):541–547, 1988. doi: 10.1109/36.7679.

Snyder, R. L., Smith, L., and Kennedy, R. M. On the formation of whitecaps by a threshold mechanism. Part III: Field experiment and comparison with theory. *J. Phys. Oceanogr.*, 13(8):1505–1518, 1983. doi: 10.1175/1520-0485(1983)013⟨1505:OTFOWB⟩2.0.CO;2.

Spillane, M. C., Monahan, E. C., Bowyer, P. A., Doyle, D. M., and Stabeno, P. J. Whitecaps and global fluxes. In Monahan, E. and Niocaill, G., editors, *Oceanic whitecaps and their role in air-sea exchange processes*, pages 209–218. Springer, New York, 1986. doi: 10.1007/978-94-009-4668-2_19.

Spracklen, D. V., Pringle, K. J., Carslaw, K. S., Chipperfield, M. P., and Mann, G. W. A global off-line model of size-resolved aerosol microphysics: I. Model development and prediction of aerosol properties. *Atmos. Chem. Phys.*, 5(1):179–215, 2005. doi: 10.5194/acp-5-2227-2005.

Stansell, P. and MacFarlane, C. Experimental investigation of wave breaking criteria based on wave phase speeds. *J. Phys. Oceanogr.*, 32(5):1269–1283, 2002. doi: 10.1175/1520-0485(2002)032⟨1269:EIOWBC⟩2.0.CO;2.

Stogryn, A. The emissivity of sea foam at microwave frequencies. *J. Geophys. Res.*, 77(9):1658–1666, 1972. doi: 10.1029/JC077i009p01658.

Stramska, M. and Petelski, T. Observations of oceanic whitecaps in the north polar waters of the Atlantic. *J. Geophys. Res.*, 108(C3):3086–3095, 2003. doi: 10.1029/2002JC001321.

Sugihara, Y., Tsumori, H., Ohga, T., Yoshioka, H., and Serizawa, S. Variation of whitecap coverage with wave-field conditions. *J. Mar. Syst.*, 66(1-4):47–60, 2007. doi: 10.1016/j.jmarsys.2006.01.014.

Sutherland, P. and Melville, W. K. Field measurements and scaling of ocean surface wave-breaking statistics. *Geophys. Res. Lett.*, 40(12):3074–3079, 2013. doi: 10.1002/grl.50584.

Tang, W. and Liu, W. T. *Equivalent Neutral Wind.* Jet Propulsion Laboratory Publ. 96017, Pasadena CA, 1996.

Textor, C., Schulz, M., Guibert, S., Kinne, S., Balkanski, Y., Bauer, S., Berntsen, T., Berglen, T., Boucher, O., Chin, M., et al. Analysis and quantification of the diversities of aerosol life cycles within aerocom. *Atmos. Chem. Phys.*, 6(7):1777–1813, 2006. doi: 10.5194/acp-6-1777-2006.

Toba, Y. and Chaen, M. Quantitative expression of the breaking of wind waves on the sea surface. *Rec. Oceanogr. Works Jpn*, 12(1):11, 1973.

Toba, Y. and Koga, M. A parameter describing overall conditions of wave breaking, whitecapping, sea-spray production, and wind stress. In Monahan, E. and Niocaill, G., editors, *Oceanic Whitecaps and Their Role in Air-Sea Exchange Processes*, pages 37–48. Springer, New York, 1986. doi: 10.1007/978-94-009-4668-2_4.

Tsyro, S., Aas, W., Soares, J., Sofiev, M., Berge, H., and Spindler, G. Modelling of sea salt concentrations over Europe: key uncertainties and comparison with observations. *Atmos. Chem. Phys.*, 11(20):10367–10388, 2011. doi: 10.5194/acp-11-10367-2011.

Twomey, S. Aerosols, clouds and radiation. *Atmos. Environ.*, 25A(11):2435–2442, 1991. doi: 10.1016/0960-1686(91)90159-5.

Ulaby, F., Moore, R., and Fung, A. *Microwave Remote Sensing: Active and Passive, Vol. 1: Microwave Remote Sensing Fundamentals and Radiometry.* Addison-Wesley, Reading, Mass., 1981.

Vignati, E., Facchini, M. C., Rinaldi, M., Scannell, C., Ceburnis, D., Sciare, J., Kanakidou, M., Myriokefalitakis, S., Dentener, F., and O'Dowd, C. Global scale emission and distribution of sea-spray aerosol: Sea-salt and organic enrichment. *Atmos. Environ.*, 44(5):670–677, 2010. doi: 10.1016/j.atmosenv.2009.11.013.

Wanninkhof, R. and McGillis, W. R. A cubic relationship between air-sea CO_2 exchange and wind speed. *Geophys. Res. Lett.*, 26(13):1889–1892, 1999. doi: 10.1029/1999GL900363.

Wanninkhof, R., Asher, W. E., Ho, D. T., Sweeney, C., and McGillis, W. R. Advances in quantifying air-sea gas exchange and environmental forcing. *Ann. Rev. Marine Sci.*, 1, 2009. doi: 10.1146/annurev.marine.010908.163742.

Wentz, F. J. A model function for ocean microwave brightness temperatures. *J. Geophys. Res.*, 88(C3):1892–1908, 1983. doi: 10.1029/JC088iC03p01892.

Wentz, F. J. Measurement of oceanic wind vector using satellite microwave radiometers. *IEEE Trans. Geosci. Remote Sens.*, 30(5):960–972, 1992. doi: 10.1109/36.175331.

Wentz, F. A well-calibrated ocean algorithm for special sensor microwave / imager. *J. Geophys. Res.*, 102:8703–8718, 1997. doi: 10.1029/96JC01751.

Whitlock, C. H., Bartlett, D. S., and Gurganus, E. A. Sea foam reflectance and influence on optimum wavelength for remote sensing of ocean aerosols. *Geophys. Res. Lett.*, 9(6):719–722, 1982. doi: 10.1029/GL009i006p00719.

Witek, M. L., Flatau, P. J., Quinn, P. K., and Westphal, D. L. Global sea-salt modeling: Results and validation against multicampaign shipboard measurements. *J. Geophys. Res.*, 112(D8), 2007. doi: 10.1029/2006JD007779.

Woodcock, A. H. Note concerning human respiratory irritation associated with high concentrations of plankton and mass mortality of marine organisms. *J. Mar. Res.*, 7(1):56–62, 1948.

Woolf, D. and Goddijn-Murphy, L. The importance of whitecapping to air-sea interaction and earth observation approaches to its retrieval. In *ESA Special Publication*, volume 703, page 6, 2012.

Woolf, D. K. Energy dissipation through wave breaking and the air-sea exchange of gases. In Jähne, B. and Monahan, E. C., editors, *Air–Water Gas Transfer*, pages 185–195. AEON Verlag, 1995.

Woolf, D. K. Bubbles and their role in gas exchange. In Liss, P. S. and Duce, R. A., editors, *The Sea Surface and Global Change*, pages 173–206. Cambridge University Press, 1997. doi: 10.1017/CBO9780511525025.007.

Woolf, D. K. Parametrization of gas transfer velocities and sea-state-dependent wave breaking. *Tellus B*, 57(2):87–94, 2005. doi: 10.1111/j.1600-0889.2005.00139.x.

Woolf, D. K. and Thorpe, S. A. Bubbles and the air-sea exchange of gases in near-saturation conditions. *J. Mar. Res*, 49(3):435–466, 1991. doi: 10.1357/002224091784995765.

Woolf, D. K., Bowyer, P. A., and Monahan, E. C. Discriminating between the film drops and jet drops produced by a simulated whitecap. *J. Geophys. Res.*, 92(C5):5142–5150, 1987. doi: 10.1029/JC092iC05p05142.

Woolf, D. K., Leifer, I. S., Nightingale, P. D., Rhee, T. S., Bowyer, P., Caulliez, G., de Leeuw, G., Larsen, S. E., Liddicoat, M., Baker, J., et al. Modelling of bubble-mediated gas transfer: Fundamental principles and a laboratory test. *J. Mar. Syst.*, 66(1):71–91, 2007. doi: http://dx.doi.org/10.1016/j.jmarsys.2006.02.011.

Wu, J. Oceanic whitecaps and sea state. *J. Phys. Oceanogr.*, 9:1064–1067, 1979. doi: 10.1175/1520-0485(1979)009⟨1064:OWASS⟩2.0.CO;2.

Wu, J. Variations of whitecap coverage with wind stress and water temperature. *J. Phys. Oceanogr.*, 18(10):1448–1453, 1988. doi: 10.1175/1520-0485(1988)018⟨1448:VOWCWW⟩2.0.CO;2.

Yelland, M. J., Moat, B. I., Pascal, R. W., and Berry, D. I. CFD model estimates of the airflow distortion over research ships and the impact on momentum flux measurements. *J. Atmos. Ocean. Tech*, 19(10):1477–1499, 2002. doi: 10.1175/1520-0426(2002)019⟨1477:CMEOTA⟩2.0.CO;2.

Yelland, M., Pascal, R., Taylor, P., and Moat, B. AutoFlux: An autonomous system for the direct measurement of the air-sea fluxes of CO_2, heat and momentum. *J. Oper. Oceanogr.*, 2(1):15–23, 2009.

Yoon, Y. J., Ceburnis, D., Cavalli, F., Jourdan, O., Putaud, J. P., Facchini, M. C., Decesari, S., Fuzzi, S., Sellegri, K., Jennings, S., et al. Seasonal characteristics of the physicochemical properties of North Atlantic marine atmospheric aerosols. *J. Geophys. Res.*, 112(D4):D04206, 2007. doi: 10.1029/2005JD007044.

Yueh, S. Modeling of wind direction signals in polarimetric sea surface brightness temperatures. *IEEE Trans. Geosci. Remote Sens.*, 35(6):1400–1418, 1997. doi: 10.1109/36.649793.

Zábori, J., Matisāns, M., Krejci, R., Nilsson, E. D., and Ström, J. Artificial primary marine aerosol production: a laboratory study with varying water temperature, salinity, and succinic acid concentration. *Atmos. Chem. Phys.*, 12(22):10709–10724, 2012. doi: 10.5194/acp-12-10709-2012.

Zhang, X. Contribution to the global airsea CO_2 exchange budget from asymmetric bubble-mediated gas transfer. *Tellus B*, 64:17260, 2012. doi: 10.3402/tellusb.v64i0.17260.

Zhao, D. and Toba, Y. Dependence of whitecap coverage on wind and wind-wave properties. *J. Oceanogr.*, 57(5):603–616, 2001.

Zhao, D., Toba, Y., Suzuki, Y., and Komori, S. Effect of wind waves on air–sea gas exchange: proposal of an overall CO_2 transfer velocity formula as a function of breaking-wave parameter. *Tellus B*, 55(2):478–487, 2003. doi: 10.1034/j.1600-0889.2003.00055.x.

Žutić, V., Ćosović, B., Marčenko, E., Bihari, N., and Kršinić, F. Surfactant production by marine phytoplankton. *Mar. Chem.*, 10(6):505–520, 1981. doi: 10.1016/0304-4203(81)90004-9.